ANL-79-94

ANL-79-94

HIGH-PERFORMANCE BATTERIES FOR ELECTRIC-VEHICLE PROPULSION AND STATIONARY ENERGY STORAGE

Progress Report for the Period
October 1978—September 1979

MASTER

ARGONNE
NATIONAL
LABORATORY

ARGONNE NATIONAL LABORATORY, ARGONNE, ILLINOIS

Prepared for the U. S. DEPARTMENT OF ENERGY
under Contract W-31-109-Eng-38

DISCLAIMER

The facilities of Argonne National Laboratory are owned by the United States Government. Under the terms of a contract (W-31-109-Eng-38) among the U. S. Department of Energy, Argonne Universities Association and The University of Chicago, the University employs the staff and operates the Laboratory in accordance with policies and programs formulated, approved and reviewed by the Association.

MEMBERS OF ARGONNE UNIVERSITIES ASSOCIATION

The University of Arizona
Carnegie-Mellon University
Case Western Reserve University
The University of Chicago
University of Cincinnati
Illinois Institute of Technology
University of Illinois
Indiana University
The University of Iowa
Iowa State University
The University of Kansas
Kansas State University
Loyola University of Chicago
Marquette University
The University of Michigan
Michigan State University
University of Minnesota
University of Missouri
Northwestern University
University of Notre Dame
The Ohio State University
Ohio University
The Pennsylvania State University
Purdue University
Saint Louis University
Southern Illinois University
The University of Texas at Austin
Washington University
Wayne State University
The University of Wisconsin-Madison

NOTICE

This report was prepared as an account of work sponsored by an agency of the United States Government. Neither the United States Government or any agency thereof, nor any of their employees, make any warranty, express or implied, or assume any legal liability or responsibility for the accuracy, completeness, or usefulness of any information, apparatus, product, or process disclosed, or represent that its use would not infringe privately owned rights. Reference herein to any specific commercial product, process, or service by trade name, mark, manufacturer, or otherwise, does not necessarily constitute or imply its endorsement, recommendation, or favoring by the United States Government or any agency thereof. The views and opinions of authors expressed herein do not necessarily state or reflect those of the United States Government or any agency thereof.

Printed in the United States of America
Available from
National Technical Information Service
U. S. Department of Commerce
5285 Port Royal Road
Springfield, VA 22161

NTIS price codes
Printed copy: A12
Microfiche copy: A01

Distribution Category:
Energy Storage--Electrochemical-
Advanced Batteries (UC-94cb)

ANL-79-94

ARGONNE NATIONAL LABORATORY
9700 South Cass Avenue
Argonne, Illinois 60439

HIGH-PERFORMANCE BATTERIES FOR ELECTRIC-VEHICLE PROPULSION AND STATIONARY ENERGY STORAGE

Progress Report for the Period
October 1978—September 1979

D. L. Barney	Director, Advanced Battery Projects
R. K. Steunenberg	Manager, Lithium/Metal Sulfide Battery Program
A. A. Chilenskas	Manager, Advanced Battery Technology Development
E. C. Gay	Section Manager, Battery Engineering
J. E. Battles	Group Leader, Materials Development
F. Hornstra	Group Leader, Battery Charging Systems
W. E. Miller	Group Leader, Industrial Cell and Battery Testing
D. R. Vissers	Group Leader, Cell Chemistry
M. F. Roche	Group Leader, Calcium/Metal Sulfide Battery Development
H. Shimotake	Group Leader, Cell Development and Engineering
R. Hudson	Program Manager, Eagle-Picher Industries, Inc.
B. A. Askew	Program Manager, Gould Inc.
S. Sudar	Program Manager, Rockwell International

March 1980

Previous Reports

ANL-78-21	October—December 1977
ANL-78-45	January—March 1978
ANL-78-94	October 1977—September 1978
ANL-79-39	October 1978—March 1979

THIS PAGE
WAS INTENTIONALLY
LEFT BLANK

TABLE OF CONTENTS

TABLE OF CONTENTS (contd)

TABLE OF CONTENTS (contd)

TABLE OF CONTENTS (contd)

HIGH-PERFORMANCE BATTERIES FOR
ELECTRIC-VEHICLE PROPULSION AND
STATIONARY ENERGY STORAGE

Progress Report for the Period
October 1978—September 1979

ABSTRACT

This report covers the research, development, and management activities of the programs at Argonne National Laboratory (ANL) and at contractors' laboratories on high-temperature batteries during the period October 1978—September 1979. These batteries are being developed for electric-vehicle propulsion and for stationary energy-storage applications. The present cells, which operate at 400-500°C, are of a vertically oriented, prismatic design with one or more inner positive electrodes of FeS or FeS_2, facing negative electrodes of lithium-aluminum or lithium-silicon alloy, and molten LiCl-KCl electrolyte.

During this reporting period, cell and battery development work has continued at ANL and contractors' laboratories. A 40 kW-hr electric-vehicle battery (designated Mark IA) was fabricated and delivered to ANL for testing. During the initial heat-up, one of the two modules failed due to a short circuit. A failure analysis was conducted and the Mark IA program completed. Development work on the next electric-vehicle battery (Mark II) was initiated at Eagle-Picher Industries, Inc. and Gould Inc. Work on stationary energy-storage batteries during this period has consisted primarily of conceptual design studies.

SUMMARY

Industrial Contracts

Most of the cell and battery development, design, and fabrication was subcontracted to two industrial firms--Eagle-Picher Industries, Inc. and Gould Inc.

Eagle-Picher. In February 1978, Eagle-Picher was contracted to design, develop, and fabricate a 40 kW-hr lithium/iron sulfide battery (Mark IA) for testing in an electric van. In the cell development phase, Eagle-Picher fabricated about 130 multiplate Li-Al/FeS cells (assembled charged) of varying designs, which were tested at their own laboratories or ANL. In general, these cells consisted of three positive and four negative electrodes, BN fabric separators, and LiCl-KCl eutectic electrolyte. After testing of these developmental cells had been completed, the final design for the Mark IA cell was selected and testing indicated that they would meet our performance goals.

In the course of cell development, performance data were obtained for individually cycled cells, but virtually no cell interaction data were available for battery design. To this end, a cell-force test apparatus was designed and fabricated to determine the Mark IA cell characteristics when fully restrained; these data were used to define the maximum cell force that had to be restrained by the battery hardware during testing. In safety tests, the Budd Technical Center (under contract to Eagle-Picher) ruptured charged Mark IA cells at operating temperature, exposing the contents to room-temperature air, by two methods: pressing the cell until rupture and dropping a 50 kg weight onto the cell at 48 km/hr (30 mph). No signs of fire or chemical reactions were observed after rupture of these cells.

In conjunction with the cell development phase of the Mark IA program, Eagle-Picher constructed a small (6 V, 2 kW-hr) module consisting of five Mark IA cells connected in series and housed in a metal (Inconel 718) case insulated with vacuum-foil insulation. At Eagle-Picher, this module was operated for 10 cycles and exhibited acceptable performance. During cycles 3 and 5, the module was subjected to vibrations equivalent to 2.3 years of vehicle operation; the performance did not appear to be affected by the vibrations. Upon completion of these preliminary tests, the module was sent to ANL where it was used to test a charger/equalizer unit developed at ANL. Another small (6 V, 4 kW-hr) module was fabricated by Eagle-Picher for performance testing at ANL. This module was fabricated for the U. S. Army to determine the viability of this system for fork-lift applications and consisted of five parallel connected pairs of Mark IA cells. These five cell pairs were connected in series and thermally insulated by a stainless steel case with Min K insulation. Preliminary testing of this module at Eagle-Picher indicated that the performance was about as anticipated, and this module was then sent to ANL for lifetime testing.

In May, fabrication of the Mark IA battery was completed and it was shipped to ANL for vehicle testing. The battery consisted of two 20 kW-hr modules, each having 60 multiplate cells arranged in two rows of 30 cells and connected in series. These cells were retained by a stainless-steel tray and housed in a double-walled case of Inconel 718 insulated with multilayered foil in the evacuated space. Each module had provisions for thermal management (heating and cooling) and mica insulation to electrically isolate the cells from one another and other battery hardware.

<u>Gould Inc</u>. Over the past year, Gould fabricated and tested about forty-six Li-Al/FeS bicells (and seven multiplate cells). All of these cells had LiCl-KCl electrolyte and BN felt separators.

In general, the Gould cells have shown very good performance characteristics, but relatively short lifetimes. Post-test examinations indicated two main reasons for cell failure: extrusion of active material from the positive-electrode edges, and failure of the electrical feedthrough. A "picture frame" assembly has been reasonably successful in preventing extrusion of active material from the positive electrode. In the electrical feedthroughs of earlier cells, the reliability of the seal was poor, and frequent cell failure occurred as a result of cracks forming in the lower (Y_2O_3) and upper (Al_2O_3) insulators. Consequently, the feedthrough design was changed by the following modifications: replacement of the lower and upper insulator materials with BeO, replacement of the previous nickel terminal rod with a copper-filled stainless steel rod, and improved welding procedures. The recent feedthrough design appears to have resulted in the elimination of the feedthrough as a failure mechanism.

Initially, Gould cells were fabricated in the uncharged state. However, uncharged cells cycled during the past year have shown poor negative-electrode utilization and electrode swelling. Recently, therefore, cells have been assembled from electrodes in the half-charged state. One such cell showed little or no performance decline over an extended period of cycling. Testing of half-charged cells will be continued in FY 1980. Another improvement in the cell fabrication procedure was initiated at Gould in FY 1979. In the past, electrodes were formed by a hot-pressing operation in a glove box, which is time consuming and expensive. A much simpler technique, cold-pressing in a glove box, has recently been adopted to fabricate the half-charged positive and negative electrodes.

The Gould cell with the longest lifetime was a Li-Al/FeS bicell, which operated for about 350 cycles (six months) and maintained stable coulombic efficiency, capacity, and specific energy. In addition, the voltage *versus* cell capacity curves on charge and discharge were nearly identical at cycles 50 and 284, thereby indicating that the Gould cell has the potential for attaining long lifetimes.

Gould completed a preliminary analysis of the cost for the Mark II battery in mass production. The results indicated that the Mark II battery should cost $70 to 106/kW-hr in mass manufacture, and has commercialization potential for limited markets such as vans or buses.

Other Contractors. Three other contractors--Rockwell International, General Motors Corp., and the Institute of Gas Technology--conducted a variety of tasks for ANL. Rockwell tested fourteen Li-Si/FeS electric-vehicle bicells, evaluated the Li_3PO_4-Li_4SiO_4 powder separator for the Li-Si/FeS cell, and developed a conceptual design for a 100 MW-hr stationary energy-storage battery; General Motors Corp. investigated the discharge behavior of the FeS_2 electrodes; and IGT explored methods of boronizing low-carbon steel substrates for use as current collectors in FeS_2 electrodes.

Cell and Battery Testing at ANL

ANL Cells. Over the past year, ANL fabricated and tested over 50 engineering-scale Li-Al/FeS cells; most of these cells had a bicell design, BN felt separators, and LiCl-KCl (eutectic or LiCl-rich) electrolyte.

Preliminary results indicated that cell performance is improved by the use of a negative-to-positive (Li/S) theoretical capacity ratio greater than one. This result is consistent with observations that very little capacity loss occurred in most ANL Li-Al/FeS cells in which the Li/S ratio was about 1.3, whereas high capacity loss rates (about 20% in 200 cycles) occurred in Mark IA cells with a capacity ratio of 1.0. Two ANL bicells, M-8NP and SM8F08, were fabricated with the same design except for the Li/S ratios which were 1.0 and 1.4, respectively. Cell SM8F08 had about 50% less capacity loss per cycle than Cell M-8NP. In addition, the specific energy of Cell SM8F08 at current densities of 37 to 110 mA/cm^2 was 10 to 20% higher than that of Cell M-8NP. Studies of capacity density of the positive electrode over a range of 1.0 to 1.6 A-hr/cm^3 in a series of five Li-Al/FeS bicells indicated that the best performance is obtained at 1.4 A-hr/cm^3.

Efforts by the materials group at ANL identified two potential alternative collector materials--nickel and iron-based alloy of Fe-5 wt % Mo. These two materials along with iron were each tested in an engineering-scale Li-Al/FeS bicell. After more than 400 cycles, the cells with the iron and nickel collectors are showing similar positive-electrode utilizations (60%), capacity loss (5%), and resistance (3.8 mΩ at full charge). The cell with the iron-based alloy has been operated for more than 245 cycles and shown similar positive-electrode utilization and capacity loss but higher resistance (4.4 mΩ at full charge) than those of the other two cells; testing of this cell is continuing. In other cell tests, 9.1 mol % LiF-62.7 mol % LiCl-28.2 mol % KCl (liquidus, 397°C) has been found to be an acceptable alternative to LiCl-rich electrolyte (liquidus, ∿425°C), and the addition of 10 wt % TiS_2 to the positive electrode has been found to lower the cell resistance by more than half.

Two Li-Al/FeS multiplate cells with BN felt separators were fabricated and tested. Both showed better performance than that of similar bicells. One of the multiplate cells developed a short circuit in the feedthrough, and operation was terminated after 42 cycles. The other one operated for over 200 cycles with stable capacity.

Gould Cells. Over the past year, Gould Inc. fabricated 20 Li-Al/FeS bicells with BN felt separators and positive-electrode additives of iron, carbon, and cobalt or molybdenum for testing at ANL. The first ten such cells had theoretical capacities of 165 to 175 A-hr and were assembled in the uncharged state. Most of these cells had very short lifetimes: short circuits in the electrical feedthroughs and internal hardware problems were responsible for cell failure. Subsequent cells have been fabricated in the half-charged state, and some of the internal hardware was redesigned. To assess the status of the Gould cell design, Gould fabricated ten identical Li-Al/FeS bicells for testing at ANL. These cells were assembled half-charged and had theoretical capacities of 117 A-hr for the positive electrode and 154 A-hr for the negative electrode. These cells have shown excellent performance characteristics: capacities of 56 to 82 A-hr and energies of 66 to 97 W-hr. After 200 to 1150 hr of cycling, these ten cells are still in operation.

In another effort, Gould fabricated four Li-Al/FeS bicells of similar designs to evaluate the following current-collector materials for the positive electrode: iron, nickel, copper and Hastelloy B. These cells had BN fabric separators and positive-electrode additives of iron, cobalt and carbon powder. Tests at ANL showed that the best performing cell was the one with the nickel collector. Subsequently, four Gould cells with nickel collectors and no positive-electrode additives were tested at ANL; the cell with the additives showed a much higher capacity than that of the cells without.

Eagle-Picher Cells and Batteries. During the cell development stage of the Mark IA program, it was discovered that the Eagle-Picher multiplate cell (1) frequently failed due to swelling of the cell can which resulted in extrusion of active material from the positive electrode, (2) showed significant capacity decline with cycling (about 20% in 200 cycles), and (3) had a lower output than that required by the Mark IA goals. In regards to the first difficulty, investigations at ANL revealed that the melting of the electrolyte in the Eagle-Picher cells resulted in a pressure surge that was largely dependent upon the available void space in the cell prior to electrolyte melting; therefore, for the cells used in the Mark IA battery, the amount of electrolyte added to the cells was closely regulated. For the second difficulty, the following probable mechanisms for capacity fading were proposed based on cell-testing data: partial freezing of electrolyte or possibly negative-electrode poisoning, and overutilization of the negative electrode either through exclusion of electrolyte or through sintering and consequent agglomeration of Li-Al in the negative electrode. Methods of improving the capacity retention of the Eagle-Picher cell are being investigated. The third difficulty was resolved by improving the welded connection between the electrode leads and bus bars as well as adding a copper layer to the cell top to lower the resistance of the path between the negative-electrode bus bar and the intercell connector.

Other Eagle-Picher cells produced for the Mark IA program were tested at ANL to determine the effect of continued cycling after cell failure and simulated driving conditions. These tests indicated that the Mark IA battery could continue to be cycled even after some of the cells had shown a marked decline in coulombic efficiency and that the Mark IA cell should produce acceptable power under severe acceleration conditions without adverse effects to the cell.

During the past year, Eagle-Picher fabricated two small battery modules (6 V)--one as part of the Mark IA program and the other for the U. S. Army to determine the feasibility of the Li/FeS system for fork-lift trucks. The former module consisted of five cells in series and was operated at ANL for over 60 cycles with stable capacity. However, operation was terminated on cycle 70 due to the development of short circuits in two feedthroughs. The other battery module consisted of five pairs of cells connected in series and was operated for 23 cycles before failure. The failure was also due to feedthrough failure. The feedthrough failure in these modules was thought to be caused by the stress that the positive terminal transmitted through the rigid intercell connectors; more flexible intercell connectors are under investigation.

The Mark IA electric-vehicle battery, which consisted of two 20 kW-hr modules, was fabricated by Eagle-Picher and delivered to ANL for testing in May 1979. During startup heating prior to electrical testing, a short circuit developed in one of the modules, which resulted in complete failure of the module. The initial indication of difficulty was a small drop in the voltage of several cells, followed by short circuits in the balance of the cells and localized temperatures above 1000°C. The other module was unaffected by the failure. A team consisting of ANL and Eagle-Picher personnel conducted a detailed analysis as the failed module was disassembled, and the other module was examined for purposes of comparison. The general conclusion was that the short circuit was initiated (1) by electrolyte leakage and the resulting corrosion in the nearby region which formed metallic bridges between cells and the cell tray, or (2) by arcing between cells and the cell tray through the butt joints in the electrical insulation. The above two mechanisms were also believed to be responsible for failure propagation. Based upon the Mark IA failure analysis, design recommendations for future batteries have been made, and experiments to further evaluate the failure have been initiated. Future battery development and scale-up will proceed in a stepwise manner, stressing cell and hardware reliability.

Cell Performance and Lifetime Summary

Tests are being conducted on Li-Al/FeS bicells and multiplate cells to obtain performance and lifetime data on at least six similar cells of each type. The bicell design chosen for the status tests was the same as that of a state-of-art bicell which had been previously fabricated and tested at ANL; fourteen Mark IA multiplate cells fabricated by Eagle-Picher will be used for other tests.

A statistical analysis was conducted on the electrical performance of the Li/FeS_x cells tested in the past year. In general, these data indicated that the specific energy of multiplate cells was higher than that of bicells (99.4 *vs.* 52.4 W-hr/kg), but the decline in specific energy per cycle for the multiplate cells was over four times higher than that for bicells.

Post-test examinations have been completed on 30 multiplate cells (fabricated by Eagle-Picher) and 30 bicells (fabricated by ANL and industrial contractors). Of the multiplate cells, the primary causes of cell failure were extrusion of active material from the positive electrode (10 cells) and short circuits in the electrical feedthroughs (6 cells). The following general observations were made from the examinations of the multiplate cells: the typical negative electrode expanded in thickness by 20 to 25%, the separators and negative electrodes were deficient in electrolyte, and varying degrees of Li-Al agglomeration occurred in the negative electrodes. Post-test examinations of the bicells indicated that the major causes of cell failure in the past--extrusion of active material, cutting of separators by current collector, and cell assembly difficulties--appear to have been resolved by modifications in cell design and better quality control. The cell tray and some of the cells were examined from the failed module of the Mark IA battery; these results were then used in the failure analysis.

Cell Development

Engineering modeling studies were conducted at ANL with the objective of developing empirical equations that relate cell performance and lifetime to the physical and chemical characteristics of the cell and the mode of cell operation. Very general equations have been developed to fit FeS and FeS_2 bicells and multiplate cells; the coefficients in the equations were determined by multiple regression analysis. Good agreement has been obtained between predicted and actual cell performance and lifetime. The model will be very useful in the optimization of the electric-vehicle cell design. In another effort, a mathematical model, based on one developed at Globe-Union Inc. for lead-acid plates, is being used to predict the optimum current collector weight for the Li/FeS cell. The results of this effort demonstrated that this model has potential for optimizing the current collector weight of the Mark II cell. In a related program, the reaction distributions within the porous electrodes of the Li/FeS cell were calculated from a one-dimensional mathematical model. Physical phenomena described by this model include ohmic potential drop and diffusion potential within the electrolyte; changes in porosity and electrolyte composition due to electrochemical reactions;

local reaction rates and their dependence on local composition and potential; and diffusion, convection, and migration of electrolyte.

Small-diameter (~3 mm) reference electrodes are being developed for polarization measurements in engineering cells and for basic electrochemical investigations. Long-term stability tests have been completed on five electrode systems--Ag/AgCl/Cl^-, Ag/Ag_2S/$S^=$, Ni/Ni_3S_2/$S^=$, Fe/Li-Al/Li^+, and Al/Li-Al/Li^+--and the Ni/Ni_3S_2/$S^=$ system was found to be the most suitable. Measurements will be made with reference electrodes in three sizes of cells: large (~100 A-hr) and intermediate (5-15 A-hr) prismatic cells, and small tubular cells. Preliminary investigations with an engineering-scale Li-Al/FeS ANL cell having reference electrodes have indicated that there are large potential gradients across the surfaces of the positive and negative electrodes, probably caused by nonuniform current distribution developed during cycling. The use of a reference electrode in a Li-Al/FeS bicell with Mark IA-type electrodes indicated that the power is limited by the positive electrode at all states of charge, and that the cell capacity is limited by the negative electrode during discharge and the positive electrode during charge. Testing of these cells is continuing.

Means of optimizing cell performance were investigated through tests with laboratory (<10 A-hr) test cells. A Li-Al/FeS test cell using a 9.1 mol % LiF-62.7 mol % LiCl-28.2 mol % KCl electrolyte, which has a liquidus point of 397°C, attained a utilization of over 80% at 435°C. Test cells with additions of LiBr or NaCl (<10 mol %) to the LiCl-KCl electrolyte were also cycled, but did not attain as high a utilization as that of the above cell. This electrolyte is being tested in an engineering-scale cell. The test cells were also operated with 0, 5, 10 and 30 wt % TiS_2 added to the positive electrode to improve its conductivity. The 10 wt % TiS_2 addition was found to result in the optimal cell resistance and is presently being tested in an engineering-scale cell.

The ionic conductances of BN felt (porosity, 88% and 94%) and MgO powder (porosity, 41.8% and 85%) were measured with an experimental apparatus specially designed for this purpose. The results showed a conductivity of 1.022 $m\Omega^{-1}$-cm^{-1} for the 94% porous BN felt and 0.923 $m\Omega^{-1}$-cm^{-1} for the 85% porous MgO powder. These values were then used to predict cell resistance. In another effort, a special cell design consisting of 0.32-cm^2 electrodes has been developed for evaluations of electrodes.

Materials and Components Development

Electrode Development. Investigations are under way on the formation of agglomerated Li-Al in the center of the negative electrode during the operation of multiplate FeS cells. For these studies, cells were fabricated with small working electrodes of solid aluminum and large counter electrodes of porous Li-Al; the results so far indicate that Li-Al agglomeration is at least partly responsible for the rapid capacity decline observed in Li-Al/FeS multiplate cells.

In investigations of the FeS electrode, two 2 A-hr Li-Al/1 A-hr FeS cells (eutectic electrolyte) were operated to determine the potential at which $LiK_6Fe_{24}S_{26}Cl$ (J phase) forms during cycling. Preliminary results indicate that J phase transforms to FeS at 1.6 V during charge and 1.4 V during discharge. Cyclic voltammetry studies were completed on the FeS electrode in electrolytes of LiCl-KCl eutectic and 63.8 to 74.4 mol % LiCl-KCl at temperatures of 400 to 500°C. The results of these studies indicated that increasing the operating temperature or the LiCl content of the electrolyte should improve the reaction kinetics of the FeS electrode (*i.e.*, suppress J-phase formation). On the basis of thermodynamics, six reactions were proposed to account for the phases formed during cycling of the Li-Al/FeS cell. Subsequently, the transition potentials as a function of temperature were determined for each reaction.

In studies of the FeS_2 electrode, powders of Li_2S, Li_2FeS_2, Fe and FeS_2 were equilibrated with LiCl-KCl molten salt at 450°C; the information from this experiment was used to refine our understanding of the Li-Fe-S phase diagram. In a continuing effort to understand the electrochemistry of the FeS_2 electrode, three 4 A-hr Li-Al/1 A-hr FeS cells were cycled at a current density of 25-30 mA/cm^2 for ten cycles, and then cell operation was stopped after trickle charging at a selected cutoff voltage (1.64, 1.786, and 1.85 V) for about 18 hr. The results indicated that it is not possible to form FeS_2 at a potential of 1.76 V, which is the emf observed for the upper voltage plateau in Li-Al/FeS_2 cells. Cyclic voltammetry studies were completed on the FeS_2 electrode in LiCl-KCl eutectic and 55 mol % LiCl-KCl. These studies showed that the discharge reaction on the upper voltage plateau is more complex in the FeS_2 electrode with eutectic than with the 55 mol % LiCl electrolyte. In addition, it was found that the addition of graphite powder to the FeS_2 electrode improved the reaction kinetics.

Designing the thermal management of a cell requires knowledge of entropic heat effects, and hence of the cell reactants and products. In cell-chemistry studies, estimated values were calculated for the absolute entropies of Li_2FeS_2, $LiK_6Fe_{24}S_{26}Cl$, and $Li_3Fe_2S_4$, which are not available in the literature. These estimates were made by established procedures. Good agreement was found between the calculated values and those obtained from emf *vs.* temperature curves from experimental cells.

Separator Development. Carborundum Co. is fabricating BN felt for use as separators. These felts can be produced in any thickness and are typically 92-94% porous. These felts have been successfully tested in engineering-scale cells and will be used in the cells for the first phase of the Mark II program.

Procedures have been developed for the fabrication of porous, sintered ceramics of Y_2O_3 and MgO for separator applications. Such plates were prepared with porosities up to 60% and good mechanical properties. Separators of sintered MgO and Y_2O_3 have been tested in 50 A-hr cells, which have shown acceptable performance.

Current Collector. At present, nickel and three iron-based alloys developed at ANL (Fe-4.5 wt % Mo, Fe-10 wt % Mo-20 wt % Ni, and Fe-15 wt % Mo-30 wt % Ni) are under investigation for use as current collectors in FeS electrodes. All three iron-based alloys have shown very low corrosion rates in static corrosion tests and small cell (50 A-hr) tests. However, of the three alloys, Fe-4.5 wt % Mo showed the best combination of properties with regard to corrosion rate, resistivity, and potential for low cost; therefore, it is being tested in engineering-scale cells. Although nickel has shown low corrosion rates in static corrosion tests, small-scale cell tests have produced conflicting results. In cells assembled in the semi-charged or uncharged state, post-test examinations of the nickel current collector showed severe localized intergranular attack; but no evidence of this type of attack was observed in cells that were assembled fully charged. Studies are continuing in an effort to determine the mechanism for this unusual behavior.

Efforts are also being directed toward the development of conductive ceramics for use as a coating material on inexpensive metallic current collectors in FeS_2 electrodes. During the past year, static corrosion tests were conducted to determine the compatibilities of the following materials with the FeS_2 electrode: TiN, TiC, and TiB_2 formed by hot pressing; TiN, TiC, TiCN and TiB_2 applied by chemical vapor deposition to substrates; MoS_2 and $MoSi_2$ applied by RF sputtering to substrates; and duplexes of TiC plus TiN applied by chemical vapor deposition to substrates. The only materials found to be completely compatible with the FeS_2-electrode environment were the hot-pressed TiN and TiC. Of the coated samples tested, the TiN showed the most promise. The common mode of failure for the coated samples was cracking and spalling at the sample edges followed by rapid corrosion of the substrate by the sulfide. Studies are continuing to identify techniques to prevent spalling and cracking of the coatings.

Systems Design and Cost Analysis

In 1978, a conceptual design of a 100 MW-hr stationary energy-storage (SES) battery having Li-Al/FeS or Li-Si/FeS cells was developed as a result of a joint effort between ANL and Rockwell. In this design, the submodule, which was the basic replaceable unit for the battery, consisted of ninety-six 2.5 kW-hr cells. However, a study by Rockwell indicated that the cost for the battery hardware, \$60-88/kW-hr, was too high. In the above design, a significant portion of the cost was contributed by the electronic charge-equalization scheme, which was the same as that developed for electric-vehicle (EV) batteries. In this report period, a conceptual design for an alternative method of equalization, in which fixed resistance shunts are used on each cell, was developed. This equalization scheme adds little equipment cost to the system and only sacrifices about 4% of the coulombic and energetic efficiencies. Along with this new equalization scheme, three different sizes for the submodules were investigated: a 120 kW-hr submodule of 100 cells, a 1,020 kW-hr submodule of 408 cells, and a 30 kW-hr submodule of one cell. The cost of battery hardware for these three new designs was estimated to be \$20 to 40/kW-hr; some questions remain on the assumed capabilities of the cells and the feasibility of the battery hardware for these designs.

In 1976, an estimate was made of the cost to mass-manufacture an SES cell (Li-Al/FeS). During 1979, the cost for this type of cell was updated and used as the basis for estimating the cost to mass-manufacture Li-Al/FeS and Li-Al/FeS_2 cells for EV applications. This recent analysis indicated that the mass-manufacturing cost will be \$31 to 55/kW-hr for EV cells and \$24 to 41/kW-hr for SES cells. The total materials cost for each cell was found to contribute about 52 to 65% of the total cell cost. It should be noted that the above cost estimates are preliminary and may require further refinement as development of the advanced battery progresses.

The Li/FeS batteries under development for EV propulsion will be tested in the laboratory under a variety of modes, including computer-simulated road conditions, prior to in-vehicle tests. Preliminary in-vehicle testing at ANL using a van as a test bed will be followed by extensive in-vehicle testing by outside contractors and vehicle manufacturers. In order to evaluate battery performance under road-load conditions, an instrumentation package has been developed by ANL that is compact and can be installed in a van or automobile. The on-board package includes a microprocessor-controlled data acquisition and recording system, a signal integrator/display unit, a signal level monitor/alarm unit, and an operator visual/audible driving schedule meter. This equipment logs measurements of battery and vehicle performance on magnetic tape, while displays furnish an immediate visual indication of battery charge and energy transfer, as well as vehicle speed and range. The off-board support system provides a graphical display of recorded road-test data as a function of battery operating time on a cathode ray tube terminal. To obtain preliminary test data on vehicle operating characteristics and test procedures, a Volkswagen Van, which was powered by lead-acid batteries, was operated on a circular test track at ANL. In addition, to determine battery/controller interaction of the Li-Al/FeS system, the 6-V Mark IA module was placed in series with the lead-acid batteries of the van and tested. In general, there were no measurable changes in response time of the chopper current waveforms.

A charging system has been developed and fabricated for EV batteries. This system provides individual cell-capacity equalization with very close control of individual cell voltages, and can be preset to charge battery systems containing one to six cells. This charge unit was successfully tested with the 6-V Mark IA battery.

Calcium/Metal Sulfide Battery Development

The objective of this effort is to develop calcium alloy/metal sulfide cells for inexpensive, high-performance batteries. The electrodes and electrolyte for these cells are being developed and optimized through cyclic voltammetry studies, cell tests, and out-of-cell experiments.

In out-of-cell experiments, the solubility of CaS (one of the active materials in the positive electrode of uncharged calcium cells) in LiCl-NaCl-$CaCl_2$-$BaCl_2$ electrolyte was found to be a factor of ten lower than that of Li_2S in LiCl-KCl electrolyte (lithium cell), and the vaporization rate of sulfur from CaS_2-FeS_2 mixtures in the quaternary electrolyte was found to be significantly lower than that of the Li_2S-FeS_2 mixtures in LiCl-KCl.

Tests were conducted on small-scale cells having positive electrodes of either NiS_2, FeS_2, or FeS_2-CoS_2. The maximum utilizations of the NiS_2 and FeS_2 electrodes were satisfactory (64%), and CoS_2 additive improved the utilization of the FeS_2 electrode by 8%. Voltammetry studies of these three metal disulfide electrodes in an electrolyte of LiCl-KCl and LiCl-NaCl-$CaCl_2$-$BaCl_2$ indicated that the FeS electrode with the binary electrolyte should exhibit the best performance characteristics.

Three engineering-scale Ca-Si/FeS_2 bicells were cycled during this report period. The highest specific energy achieved by these cells was 67 W-hr/kg at the 5-hr rate, but a doubling of the resistance (8 to 16 mΩ) during the early cycles of these cells and a fading capacity limited the lifetime to about 2000 hr. The specific energy of the cells declined by about 25% per 1000 hr of operation. Post-test examinations identified two lifetime-limiting mechanisms: (1) reaction and compaction of the separator near the negative electrode to form a dense layer, and (2) formation of a nonadherent reaction layer, probably an iron silicide, on the negative current collectors. Preliminary tests have indicated that alternative negative electrodes such as $CaAl_2$ or $CaMg_2Si$ might solve both of the above problems. These alternatives will be tested in large cells in future experiments.

I. INTRODUCTION

Lithium alloy/iron sulfide batteries are being developed by Argonne National Laboratory (ANL) and its contractors for use as (1) an energy source for electric-vehicle propulsion, and (2) stationary energy-storage applications such as load leveling on electric utility systems or storage of energy produced by solar, wind, or other intermittent sources. The widespread use of electric vehicles would conserve petroleum fuels, since the electrical energy for charging the batteries could be provided by coal, nuclear, hydroelectric, or other energy sources; a side-benefit would also be realized in decreased air pollution in congested urban areas. The use of stationary energy-storage batteries for load leveling could save petroleum by reducing the need for gas turbines to meet peak power demands and by facilitating the use of alternative energy sources.

The battery cells that are currently under development consist of Li-Al or Li-Si negative electrodes, FeS or FeS_2 positive electrodes, and molten LiCl-KCl electrolyte. The melting point of the electrolyte at the eutectic composition (58.2 mol % LiCl) is 352°C, and the cells are operated at temperatures of 400 to 500°C.

The cell designs currently being developed all have a prismatic configuration with one or more positive electrodes and facing negative electrodes. The cells can be fabricated in a charged, uncharged, or partially charged state by using various combinations of reactants and products in the electrodes. Both the positive and the negative electrodes are normally fabricated by cold- or hot-pressing methods. A key cell component is the electrode separator, a porous material that provides electrical isolation of the electrodes but permits the migration of lithium ions between the electrodes. In most cell designs, it is also necessary to use screens or other structures to retain particulate material within the electrodes. To enhance the electronic conductivity of the electrodes, metallic current collectors are used to provide a low-resistance current path between the active material and the electrode terminal.

The overall electrochemical reaction for the Li-Al/FeS cell can be written as follows:

$$2LiAl + FeS \xrightleftharpoons{2e^-} Li_2S + Fe + 2Al \qquad (1)$$

The theoretical specific energy for this reaction is about 460 W-hr/hg, and the voltage *vs* capacity curve has a voltage plateau at about 1.3 V. The reaction is actually more complex than shown; for example, an intermediate compound, $LiK_6Fe_{24}S_{26}Cl$ (J phase), is formed through an interaction with the KCl in the electrolyte. The overall reaction for the Li-Al/FeS_2 cell can be written as:

$$4LiAl + FeS_2 \xrightleftharpoons{4e^-} 2Li_2S + Fe + 4Al \qquad (2)$$

The theoretical specific energy for reaction (2) is about 650 W-hr/kg. The voltage *vs* capacity curve has two voltage plateaus at approximately 1.6 and 1.3 V, respectively. Some Li-Al/FeS_2 cells are designed to operate only on the 1.6 V plateau and are referred to as "upper plateau" cells. Reaction (2) also involves several intermediate compounds (generally ternary compounds of lithium, iron, and sulfur). Although cells having FeS_2 electrodes offer a higher specific energy and voltage than those with FeS electrodes, the higher sulfur activity leads to high corrosion rates and long-term instability of the electrode.

The major requirements for an electric-vehicle battery are high specific energy (W-hr/kg), high volumetric energy density (W-hr/L), and high specific power (W/kg). Economic considerations require a minimum battery lifetime of about 3 yr (∿1000 deep discharge cycles or equivalent) and a cost goal of about \$50-60/kW-hr.* Stationary energy-storage batteries have somewhat less stringent specific-energy and specific-power requirements, but this application demands a longer lifetime (∿10 years and 3000 cycles) and a cost goal of \$45-55/kW-hr. As a result of these requirements, considerably different approaches are being taken in the designs of cells and batteries for these two applications.

The program on the electric-vehicle battery involves the development, design, and fabrication of a series of full-scale lithium/iron sulfide batteries, designated Mark IA†, II and III. The main purpose of the Mark IA battery was to evaluate the overall technical feasibility of the lithium/iron sulfide system for the electric-vehicle application and to identify potential problem areas. The Mark II battery has somewhat higher performance goals than Mark IA, but the major objective is to develop designs and materials that will permit low-cost manufacture in mass production. It is anticipated that the Mark II battery may have commercial potential for certain limited applications. The Mark III battery is planned as a high-performance prototype suitable for evaluation and demonstration in a passenger automobile. The performance and lifetime goals for the Mark IA, II, and III batteries are presented in Table I-1.

The Mark IA battery, which consisted of two 20 kW-hr modules containing 60 cells each, was fabricated by Eagle-Picher Industries and delivered to ANL for testing in May 1979. During startup heating prior to testing, a short circuit developed in one of the modules, which resulted in complete failure of the module. A detailed analysis of the failure was conducted; the results of the analysis will be covered more extensively in a separate report. The other module, which was alongside and connected in series, was unaffected by the failure. This module was disassembled to provide cells for failure analysis experiments and for additional testing of single cells and small battery configurations. No additional work will be done on the Mark IA system. As a result of the Mark IA experience, the strategy for the Mark II battery development has been revised somewhat. The first phase of the Mark II program will stress the development of high-reliability cells and will involve the fabrication and testing of 10-cell modules. This phase will conclude with qualification tests of these modules. The second phase of the program will then consist of the development of inter-connected modules and full-scale (50-60 kW-hr) batteries.

---

*Costs given in 1979 dollars throughout this report unless otherwise indicated.

†The original plan was to develop a series of Mark I batteries (IA, IB, and IC); however, a decision was made to proceed directly from Mark IA to Mark II in the development program.

Recent effort on the stationary energy-storage cells has consisted primarily of conceptual design studies of a 100-MW-hr utility load-leveling battery employing Li-Al/FeS cells. In 1978 the conceptual design for this battery included the same electronic charge equalization scheme that has been developed for electric-vehicle batteries. In 1979, an alternative method of equalization was found, thereby permitting major changes in the battery concept. As a result, studies of two new battery concepts were performed, and the estimated cost of the battery hardware (exclusive of cells) was brought down to a range of $30-40/kW-hr from an earlier estimate of $80/kW-hr (1978 dollars). Some feasibility questions remain on the battery hardware and on the assumed capabilities of the cells.

A major objective of this program is to transfer the technology to interested commercial organizations as it is developed, with the ultimate goal of a competitive, self-sustaining industry for the production of Li/FeS batteries. To this end, most of the cell and battery development, design, and fabrication is subcontracted to two industrial firms--Eagle Picher Industries and Gould Inc. A contract is under negotiation with the Carborundum Co. for the preparation of BN felt for separators and the development of production processes for this material. Other contractors currently participating in the program include the Energy Systems Group of Rockwell International, General Motors Research Laboratories, and the Institute of Gas Technology.

The in-house program at ANL consists of cell chemistry studies, materials engineering, component development, fabrication and testing of state-of-the-art status cells, testing of contractors' cells and batteries, development of battery auxiliary systems, and potential applications and cost studies. Facilities are now available at ANL for laboratory and on-board testing of electric-vehicle batteries, and lifetime and performance testing of cells. Another small effort at ANL is directed toward the development of calcium alloy/metal sulfide cells, which are believed to have a potential for low cost in mass production.

Table I-1. Program Goals for the Lithium/Metal Sulfide Electric-Vehicle Battery

Goal	Mark IA	Mark II	Mark III
Specific Energy,[a] W-hr/kg			
Cell (Average)	80	125	160
Battery	60	100	130
Energy Density, W-hr/liter			
Cell (Average)	240	400	525
Battery	100	200	300
Peak Power,[b] W/kg			
Cell (Average)	80	125	200
Battery	60	100	160
Battery Heat Loss,[c] W	400	150	125
Lifetime			
Deep Discharges	200	500	1,000
Equivalent Kilometers	32,000	95,000	240,000
Equivalent Miles	20,000	60,000	150,000

[a] Calculated at the 4-hr discharge rate.

[b] Peak power sustainable for 15 sec at 0 to 50% state of discharge; at 80% discharge, the peak power is 70% of the values shown.

[c] The values shown represent the heat loss of the battery through the insulated case; under some operating conditions, additional heat removal may be required.

II. INDUSTRIAL CONTRACTS*

Most of the cell and battery development, design, and fabrication was subcontracted to two industrial firms: Eagle-Picher Industries and Gould Inc. The cells fabricated by these contractors are tested either at their own facilities or ANL. In the past year, Eagle-Picher fabricated the Mark IA battery and two smaller (6 V) batteries and delivered them to ANL for testing. Also, development work on the Mark II battery was initiated at Gould and Eagle-Picher. The other contractors performed a variety of tasks for ANL.

A. Eagle-Picher Industries, Inc.

(R. Hudson)

Eagle-Picher Industries, Inc. entered into the lithium/metal sulfide battery program in May, 1975, as one of the first industrial firms to associate with ANL's battery program. Initial efforts were directed at developing engineering-scale bicells (*i.e.*, one positive and two facing negative electrodes) for electric-vehicle and utility load-leveling applications. Development progressed in these areas such that the fabrication of full-scale lithium/metal sulfide batteries was feasible. In February, 1978, Eagle-Picher was awarded a contract for the design, development, and fabrication of the first full-scale (40 kW-hr) lithium/metal sulfide battery.

1. Cell Development for the Mark IA Program

(E. B. Cupp, J. W. Buchanan, L. W. Aupperle)

As part of the cell development phase of the Mark IA program, Eagle-Picher fabricated four consecutive series of cells (designated Matrix A, B, C, and D). In general, these cells consisted of the following: three FeS positive electrodes with Cu_2S additives, four Li-Al negative electrodes, BN fabric separators, cloth (Y_2O_3 or ZrO_2) particle retainers, iron-honeycomb current collectors, and LiCl-KCl eutectic electrolyte. However, within the four matrixes, many different cell design and material variations were tested. The normal operating temperature for these cells was 450-465°C, and the discharge and charges rates were 4 hr and 8 hr, respectively. After completion of this development effort, the final design for the Mark IA cell was selected, and production of the required cells for the battery initiated. During the year, 430 cells were fabricated and tested. Allocation of these cells is as shown in Fig. II-1. The developmental cell matrices are discussed below.

a. Matrix A Cells

The purpose of the first test matrix was to determine the feasibility of building multiplate Li-Al/FeS cells and to pinpoint any manufacturing problems associated with the multiplate design. The nineteen Matrix A cells had four positive plates and five negative plates with dimensions of 12.7 x 17.8 cm. The following design variables were studied: type of particle barrier (ZrO_2, Y_2O_3, and none), Cu_2S additive to the positive active material, and metallic copper and iron as additives to the positive active material.

---

*The authors listed in this section of the report are from the contractors.

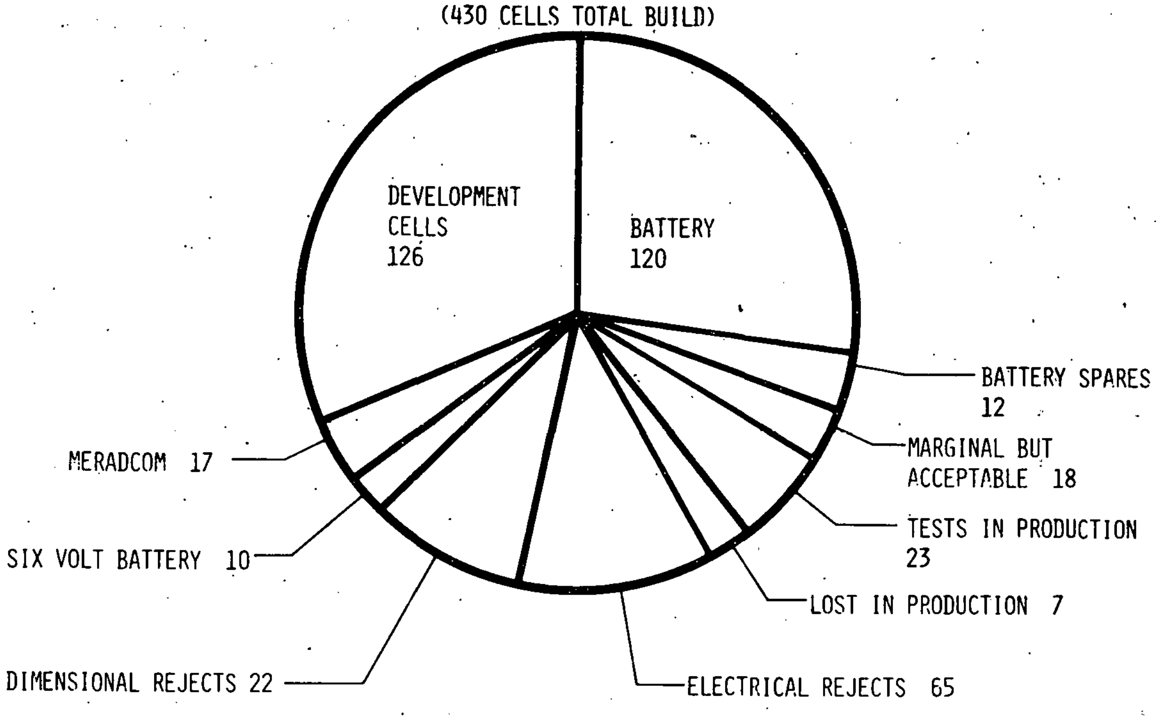

Fig. II-1. Cells Fabricated by Eagle-Picher for Various Program Efforts

Table II-1 shows the design variables, cycle life and maximum capacity attained by these cells. In general, the cells tested in this matrix gave good initial capacities, and the initial positive-electrode utilization appeared to be affected by the quantity of Cu_2S added. However, the high utilization was usually not permanent. In most cells, the higher initial utilization corresponded with higher rates of capacity decline with cycle life. In general, the positive-electrode utilization faded to about 70% regardless of the initial value.

b. Matrix B Cells

The Matrix B cells (Cells EPMP-7-20 through -36) had three positive and four negative electrodes with dimensions of 17.8 x 17.8 cm. These cells were fabricated to test the effects of Cu_2S additive, Y_2O_3 cloth as a particle barrier, lithium chloride additive to the eutectic electrolyte, and current collector material type and thickness.

Table II-2 shows the performance of the Matrix B cells. In general, these cells exhibited good performance characteristics. All cells tested except Cell EPMP-7-36 gave positive-electrode utilizations higher than 80% initially. However, all cells showed significant capacity decline during cycling. In almost all instances, the capacity fade was marked, to a degree, to a drop in coulombic efficiency. The lower coulombic efficiency was probably due to the formation of high-resistance short circuits within

Table II-1. Performance Data for Matrix A Cells

Cell No.	Capacity, A-hr FeS	 Max.	Cycle Life	Design Variables
EPMP-5-1	275	367	8	None
EPMP-5-2	293	377	5	None
EPMP-5-3	405	367	60	b
EPMP-5-4	405	377	47	b
EPMP-5-5	383	373	94	a(10 wt %)
EPMP-5-6	383	375	100	a(10 wt %), c
EPMP-5-7	370	334	40	a(15 wt %), c
EPMP-5-8	370	384	68	a(15 wt %), c
EPMP-5-9	320	346	75	a(15 wt %), b, d
EPMP-5-10	320	351	74	a(15 wt %), c, d
EPMP-5-11	370	33	h	a(15 wt %), b, g
EPMP-5-12	350	337	8	a(20 wt %)
EPMP-5-13	350	312	h	a(20 wt %), b
EPMP-5-14	350	248	h	a(20 wt %), b
EPMP-5-15	350	326	h	a(20 wt %), c
EPMP-5-16	405	277	56	b, d, e
EPMP-5-17	383	311	190	b, f(10 wt %)
EPMP-5-18	370	320	68	b, f(15 wt %)
EPMP-5-19	350	314	36	b, f(20 wt %)

[a] Cu_2S added to the positive electrode (wt % given in parentheses).

[b] Y_2O_3 cloth particle barrier.

[c] ZrO_2 cloth particle barrier.

[d] Iron powder added to the positive electrode.

[e] Cu powder added to the positive electrode.

[f] $CuFeS_2$ added to the positive electrode.

[g] Carbon black added to the positive electrode.

[h] Failed after only a few cycles due to equipment malfunction.

Table II-2. Performance Data on Matrix B Cells

Cell No.	Capacity, A-hr FeS	Capacity, A-hr Max.	Cycle Life	Design Variables
EPMP-7-20	409	329	45	c, d(0.0762 mm)
EPMP-7-21	409	332	65	c, d(0.0762 mm)
EPMP-7-22	350	320	87	a, c(20 wt %), d(0.0762 mm)
EPMP-7-23	350	310	72	a, c(20 wt %), d(0.0762 mm)
EPMP-7-24	370	334	32	a, c(15 wt %), d(0.0762 mm), g
EPMP-7-25	370	321	65	c(15 wt %), e
EPMP-7-26	370	278	58	a, c(15 wt %), e
EPMP-7-27	370	346	87	a, c(15 wt %), e
EPMP-7-28	370	333	70	a, c(15 wt %), d(0.127 mm)
EPMP-7-29	370	shorted	-	a, c(15 wt %), d(0.127 mm), h
EPMP-7-30	370	340	59	b, c(15 wt %), d(0.127 mm)
EPMP-7-31	403	339	191	b, d(0.127 mm), f
EPMP-7-32	403	376	61	b, d(0.127 mm), f
EPMP-7-33	403	-	-	b, d(0.127 mm), f
EPMP-7-34	403	shorted	-	b, e, f, h
EPMP-7-35	403	353	102	b, e, f
EPMP-7-36	403	353	78	b, e, f,

[a] Y_2O_3 cloth particle retainer on positive electrode.

[b] Y_2O_3 cloth retainer on positive and negative electrodes.

[c] Cu_2S in positive electrode (wt % given in parentheses).

[d] Iron current collector (honeycomb ribbon thickness given in parentheses).

[e] Nickel current collector (0.0762-mm thick ribbons)

[f] Lithium chloride-rich electrolyte (67 mol % LiCl).

[g] Carbon added to positive electrode plate (17 g).

[h] Separators prewetted with $LiAlCl_4$.

the cells. This condition occurred after different numbers of cycles for the cells and did not appear to correlate with any of the variables being tested. The test did indicate a slight improvement in performance with the iron current collectors (0.127-mm thick ribbons) and LiCl-rich electrolyte.* However, these cells were tested at 465 to 475°C, while the cells with the eutectic electrolyte were tested at 450°C.

c. Matrix C Cells

The negative electrodes of the Matrix C cells (EPMP-7-37 to -66) all had 46 at. % Li-Al alloy. The variables studied included particle retention (with and without), Cu_2S additive to the positive electrode (none and 15 and 20 wt %), and LiCl content of the electrolyte (eutectic or LiCl-rich). The design variables and capacities of these cells are listed in Table II-3. Not mentioned in this table is that Cells EPMP-7-41, -43, -45, -46, -47, -61, -62, -63, -64, -65, and -66 had 15 wt % Cu_2S added to the positive electrode. These tests indicated that the highest positive-electrode utilization was obtained in cells with 15 wt % Cu_2S in the positive electrode, eutectic electrolyte, and Y_2O_3 particle retainers.

Table II-3. Performance Data for Matrix C Cells

Cell No.	Capacity, A-hr FeS	Capacity, A-hr Max.	Cycle Life	Design Variables
EPMP-7-37 to -42	373	323.4	15.6	e
EPMP-7-43 to -48	373	342.4	72	-
EPMP-7-49 to -54	359	334	39	a
EPMP-7-55 to -57	403	334	218	b, c
EPMP-7-58 to -60	403	327	87	b, c, f
EPMP-7-61 to -66	373	351	151	d

[a] 20 wt % Cu_2S added to the positive electrode.

[b] No Cu_2S.

[c] LiCl-rich electrolyte (67 mol % LiCl).

[d] Eagle-Picher eutectic electrolyte.

[e] No particle barrier.

[f] Nickel current collector (0.003 mm-thick ribbons).

---

*Unless otherwise indicated, this term refers to 68 mol % LiCl in the electrolyte.

Three types of LiCl-KCl electrolyte were tested in these cells: Anderson eutectic,* Eagle-Picher eutectic, and Anderson LiCl-rich. The effects of these salts on the capacity are shown in Table II-4.

Table II-4. Effect of Salt on Capacity

	Anderson Eutectic	Anderson LiCl-rich	Eagle-Picher Eutectic
Positive Utilization, %	83	79	85.3
Ave. Cycle Life[a]	67	134	142
Capacity Fade, A-hr/cycle	0.78	0.59	0.59

[a] Cycles completed free of short circuits.

d. Matrix D Cells

The final test matrix consisted of 37 cells. Originally these cells were to be all replicates containing 15 wt % Cu_2S added to the positive electrode, eutectic electrolyte, Y_2O_3 cloth only on the positive electrode for retention, and iron current collectors. However, in an effort to obtain additional information, five cells were built with 15 wt % Cu_2S in the positive electrode and LiCl-rich electrolyte added during the electrolyte filling operation, and seventeen cells were built with no Cu_2S additive and LiCl-rich electrolyte added during the electrolyte filling operation. These 22 cells were sent to ANL for testing. Table II-5 shows the weight of the active materials used in the electrodes for the Matrix D cells.

Table II-5. Active Material and Electrolyte Weights for Matrix D Cells

	Materials for Pos., g			Materials for Inner Neg., g		Materials for Outer Neg., g	
Cell No.	FeS	Cu_2S	Electrolyte[a]	LiAl	Electrolyte[a]	LiAl	Electrolyte[a]
EPMP-7-67 to -81	193	34	34	204	10	102	5
EPMP-7-82 to -96	193	34	34	204	10	102	5
EPMP-7-97 to -111	231	0	34	204	10	102	5

[a] Anderson eutectic was used in all electrode plates.

---

*Prepared by the Anderson Physics Laboratories, Inc., Champaign, IL.

The Matrix D cells tested at Eagle-Picher showed very good performance characteristics, indicating that multiplate cells could be built that would meet the Mark IA goals. In addition, cells operated at 465°C showed better performance than those operated at 450°C.

Upon completion of testing the Matrix D cells, the final design for the Mark IA cell was selected. For this design, the cell has dimensions of 19 x 18 x 3.9 cm and weighs about 4 kg. The negative electrodes consist of 46 at. % Li-Al with a theoretical capacity of 440 A-hr, and the positive electrodes consist of FeS and 15 wt % Cu_2S with a theoretical capacity of 410 A-hr. The electrolyte composition is LiCl-KCl eutectic. Other cell components include current collectors of AISI 1010 carbon steel, separators of 0.175-cm thick BN cloth, particle retainers of Y_2O_3 cloth for both the positive and negative electrodes, a crimp-type electrical feedthrough with a BN powder seal, and a cell container of AISI 1008 and 1010 carbon steel with a material thickness of 0.57 cm. A total of 265 such cells were fabricated, at a maximum rate of ten cells per day. In general, the production run went smoothly, although the cylinder of the 500-ton press used to fabricate electrodes was out of operation for about four weeks. After fabrication, each cell was tested for acceptability, and 120 cells were chosen for the battery along with 12 spares.

2. Cell Experiments

(K. Gentry, J. W. Miller, M. M. McGinty)

a. Cell Force Testing

In the course of the development phase for the Mark IA program, many data were obtained on single-cell performance, but virtually no cell interaction data was available for battery design from this specific testing. To aid in this area, a cell-force test apparatus was designed and fabricated to determine the characteristics of fully restrained cells. This information, obtained with force-test equipment which was designed and fabricated at Eagle-Picher, was used in determining the final design for the Mark IA battery. Force tests with small battery modules (*e.g.*, 10 cells in series) were not pursued due to schedule and cost restraints. Figure II-2 shows the Mark IA cell force versus state of charge. Data obtained were used to define the maximum cell force that had to be restrained by the battery hardware during testing. Further work is currently planned for this force determination approach.

b. Cell Crashworthiness Testing*

As a part of the Mark IA program, a crashworthiness test was conducted on four Mark IA cells.

A static load was applied to two cells, EPMP-7-065 and-072, to determine their crush resistance. Figure II-3 shows the crush resistance of Cell EPMP-7-072. As can be seen, this cell has two distinct phases of crush resistance, with an inflection point at about 20,000 lb. The first phase is probably the force required to compress the voids (*i.e.*, separator,

---

*Crashworthiness Testing was performed by the Budd Technical Center, Ft. Washington, Pennsylvania.

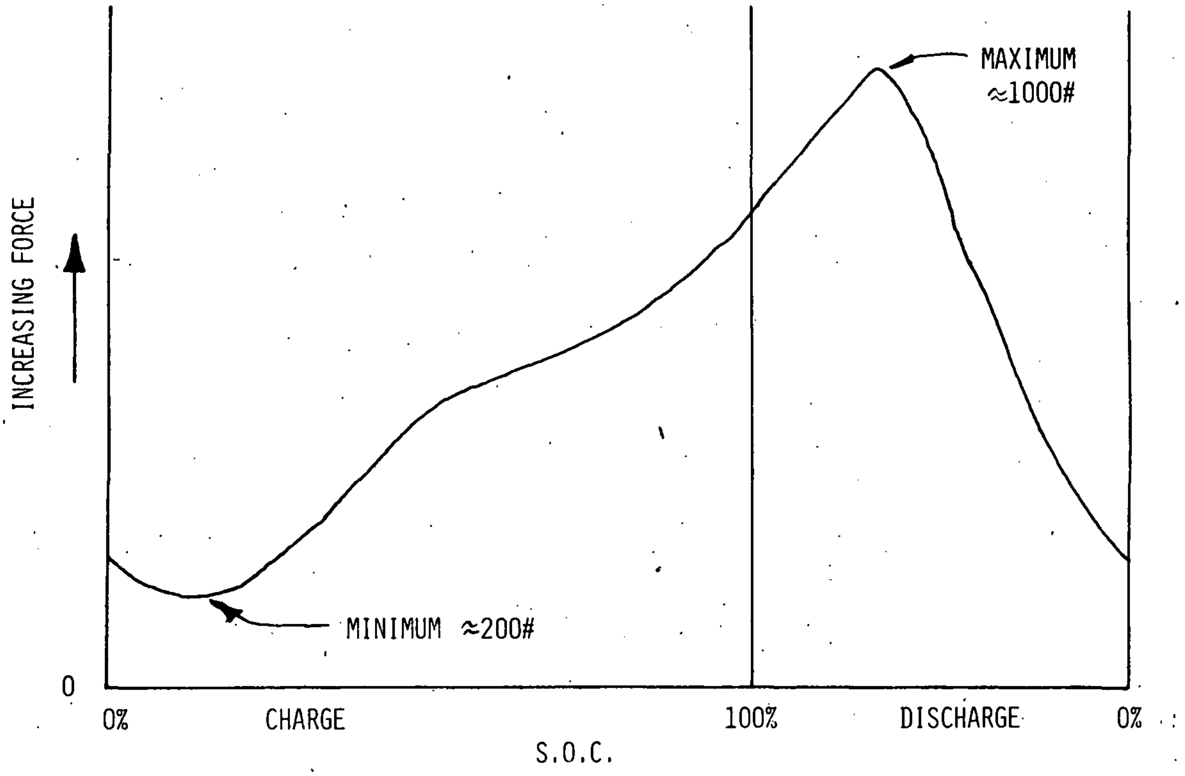

Fig. II-2. Cell Force *vs.* State of Charge of Mark IA Cell

electrolyte, etc.) and the second is probably compression of the honeycomb current-collector structure in the electrodes. The atmosphere in the vicinity of the cell was monitored for H_2 and H_2S, and only a minute reading of H_2 (0.057%) was obtained directly above the cell. Although not detected, a very faint odor of H_2S or SO_2 was also detected.

Two additional cells, EPMP-7-076 and -102, were tested to determine their rigidity, average crush force, and absorbed energy to a simulated 54 km/hr (30 mph) barrier crash. These cells were fully charged and at operating temperature (450°C) when a 49 kg weight was dropped on them with an impact velocity of about 54 km/hr. Table II-6 is a chart presenting the data obtained for both cells. The conclusions drawn from this testing indicated that no significant quantity of H_2 or H_2S gas was emitted at cell rupture and/or reaction with the air. No electrical effect such as arcing (or fire) was evident when the cell ruptured on impact. The data also indicated that, when integrated into an electric vehicle, it may be required to either restrain the battery or attenuate the energy with supplementary absorbers. This type of testing for both cells and batteries should be continued in future designs to assure safety of the entire system.

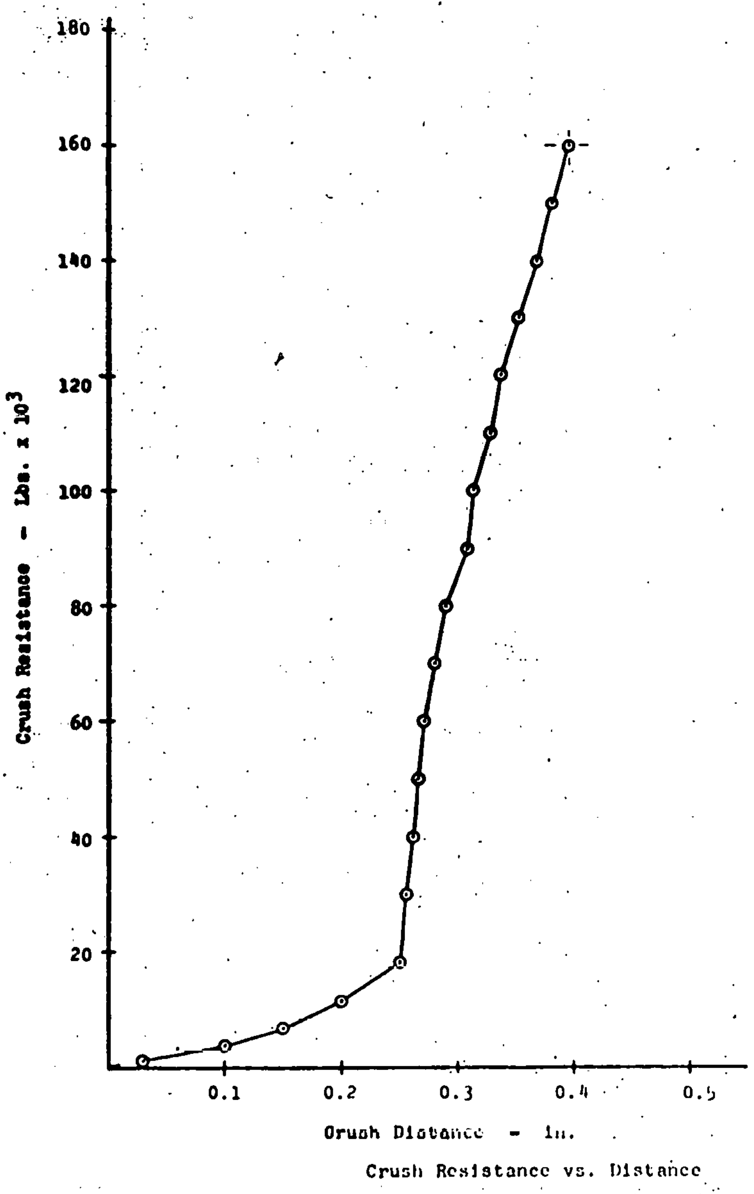

Fig. II-3. Static Crush Test of Cell EPMP-7-072

Table II-6. Barrier Impact Test Results of Budd Co.

	Cell EPMP-7-73	Cell EPMP-7-102
Impact Velocity, ft/sec	44	43.1
Kinetic Energy Absorbed, ft-lb	2958	3033
Crush Distance, in.	0.49	0.55
Average Crush Force, lb	76875	-

3. Mark IA Battery Development

(K. Gentry, J. W. Miller, M. M. McGinty)

a. Insulating Cases for Mark IA

Eagle-Picher contracted Thermo Electron Corp. and Budd Technical Center to fabricate a prototype stainless-steel case and two Inconel 718 cases for the Mark IA battery. The design for these cases consisted of double-walled corrugated metal with multifoil* in the evacuated space for insulation (Fig. II-4).

After fabrication, the prototype case underwent testing to ascertain its leak-tightness and ruggedness. To determine the conditions required to simulate road vibrations, a Volkswagen Transporter van powered by lead-acid batteries (the vehicle obtained by ANL to conduct in-vehicle tests of the Mark IA battery) was driven under road conditions. Driving conditions included typical urban and rural roads, railroad crossings, intersection bumps, and rough pavement. Results indicated that appropriate vibrational levels are a minimum of ±1.5 g's at a frequency of 30 Hz for 10^6 vibrational cycles.

For the vibrational tests, the prototype case was loaded with battery hardware and aluminum blocks (simulated cell weight), brought to operating temperature, and subjected to road vibrations equivalent to more than four years of vehicle operation. Test results indicated no degradation in thermal losses due to the vibrations and sufficient strength in the structure to ensure no mechanical problems during testing. Thermal losses of this case, however, were much higher than the design goal (160 *vs.* 82 W). An analysis revealed hot spots at certain areas (front flange, rear support pin, and bottom aft side of the vessel); therefore, a modification in the assembly procedures was instituted for the two Mark IA cases.

b. The 6-V Mark IA Battery

Prior to construction of the Mark IA battery, Eagle-Picher fabricated a small (6 V) Li-Al/FeS battery. This battery consisted of five Mark IA-type cells connected in series, restrained by a cell tray, and thermally insulated by a case of the type described above. Figure II-5 is a

---

*A trademark of Thermo Electron Corp.

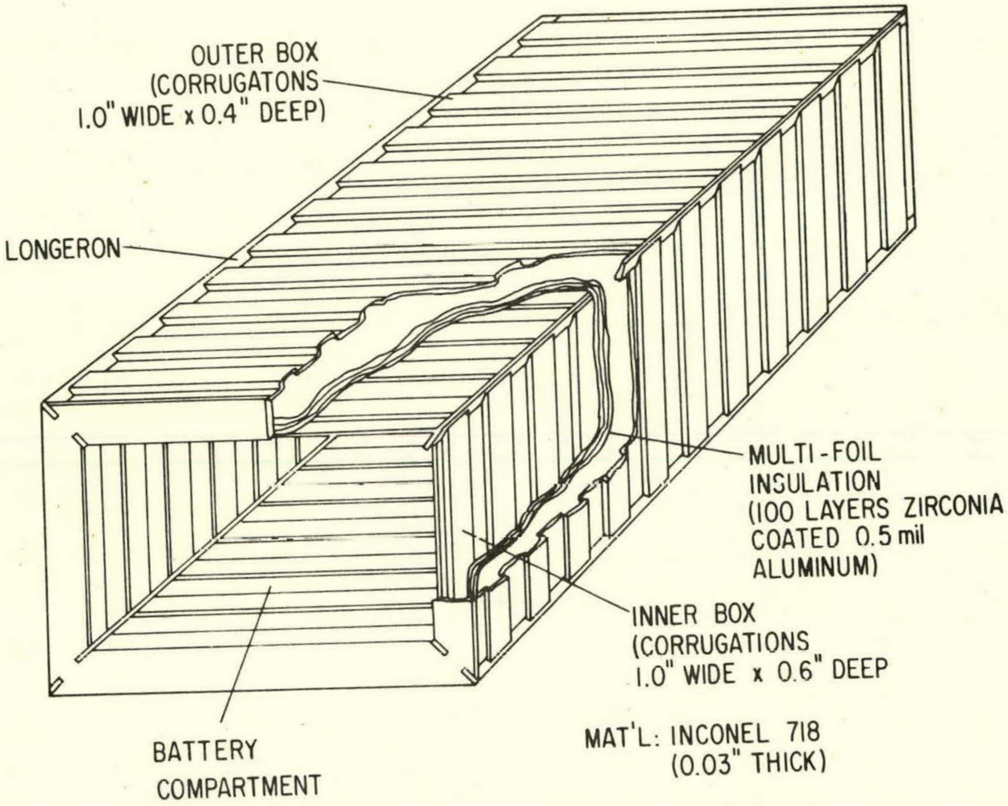

Fig. II-4. Schematic of the Insulating Case for Mark IA

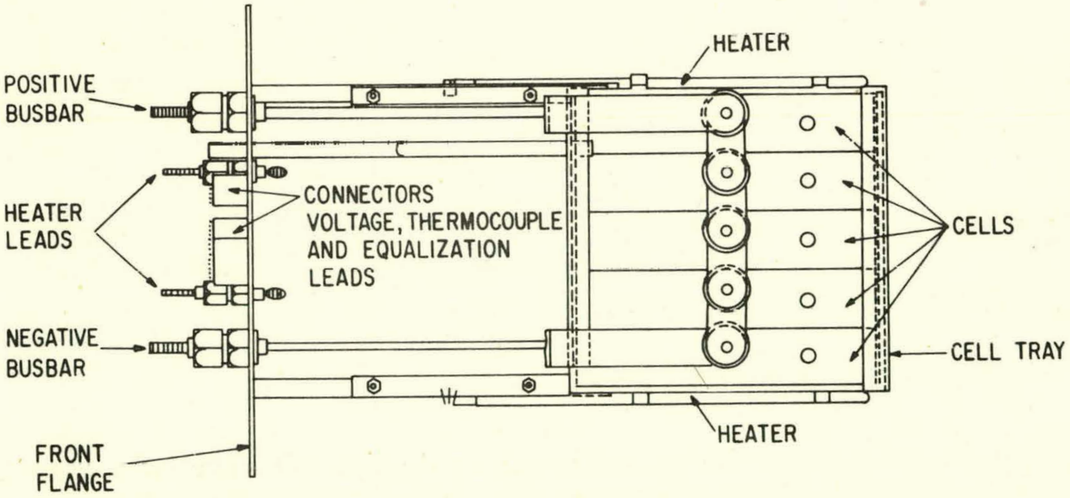

Fig. II-5. Six-Volt Mark IA Battery

schematic of the 6-V Mark IA battery. This unit was used to obtain experience with respect to the design, fabrication, and testing of the Mark IA battery. The testing program undertaken with this battery included operability, energy storage, thermal performance, and vibration compatibility.

The battery performance during qualification testing at Eagle-Picher was quite acceptable, showing good performance in all areas of testing. Table II-7 shows the performance of the battery. The energy storage achieved, 2.1 kW-hr, was somewhat higher than the design goal (1.9 kW-hr). A coulombic efficiency of over 99% was observed. The thermal loss of the battery was 190 W, the design goal being 120 W. The vibration testing was successfully performed on the 6-V battery to simulate an actual in-vehicle lifetime of 2.3 years. The test results indicated some areas of design change for the Mark IA battery. Upon completion of all qualification testing the battery was cooled to room temperature, examined, and shipped to ANL for life testing; this testing is reported in Section III.C.

Table II-7. Six-Volt Battery Tests

Attained Capacity, kW-hr	2.1
Specific Energy,[a] W-hr/kg	40
Heat Loss, W	190

[a] Measured at 6-hr rate.

c. The Mark IA Battery

In May, fabrication of the Mark IA battery was completed and it was shipped to ANL for testing (reported in Section III.C). A photograph of one of the modules is shown in Fig. II-6. The cells within each module were connected in series and arranged in two rows of thirty Mark IA cells each, the two cell rows being supported by a cell tray (see Fig. II-7). Each module had provisions for thermal management (heating and cooling) and insulation to electrically isolate the cells from one another and other battery hardware. Table II-8 shows a list of the materials of construction for the battery.

The largest success of this year's effort was not only the fabrication of the first full-scale Li-Al/FeS battery, but also the development of processes, procedures, and assembly techniques required to fabricate such a battery.

4. MERADCOM 6-V Battery

(M. M. McGinty, R. Hudson, J. W. Buchanan)

Eagle-Picher was also contracted to design and fabricate a small (6 V, 4 kW-hr) LiAl/FeS battery for the U.S. Army (MERADCOM*). The purpose was to demonstrate performance feasibility of the LiAl/FeS system for

---

*Mobility Equipment Research and Development Command, Fort Belvoir, N.J.

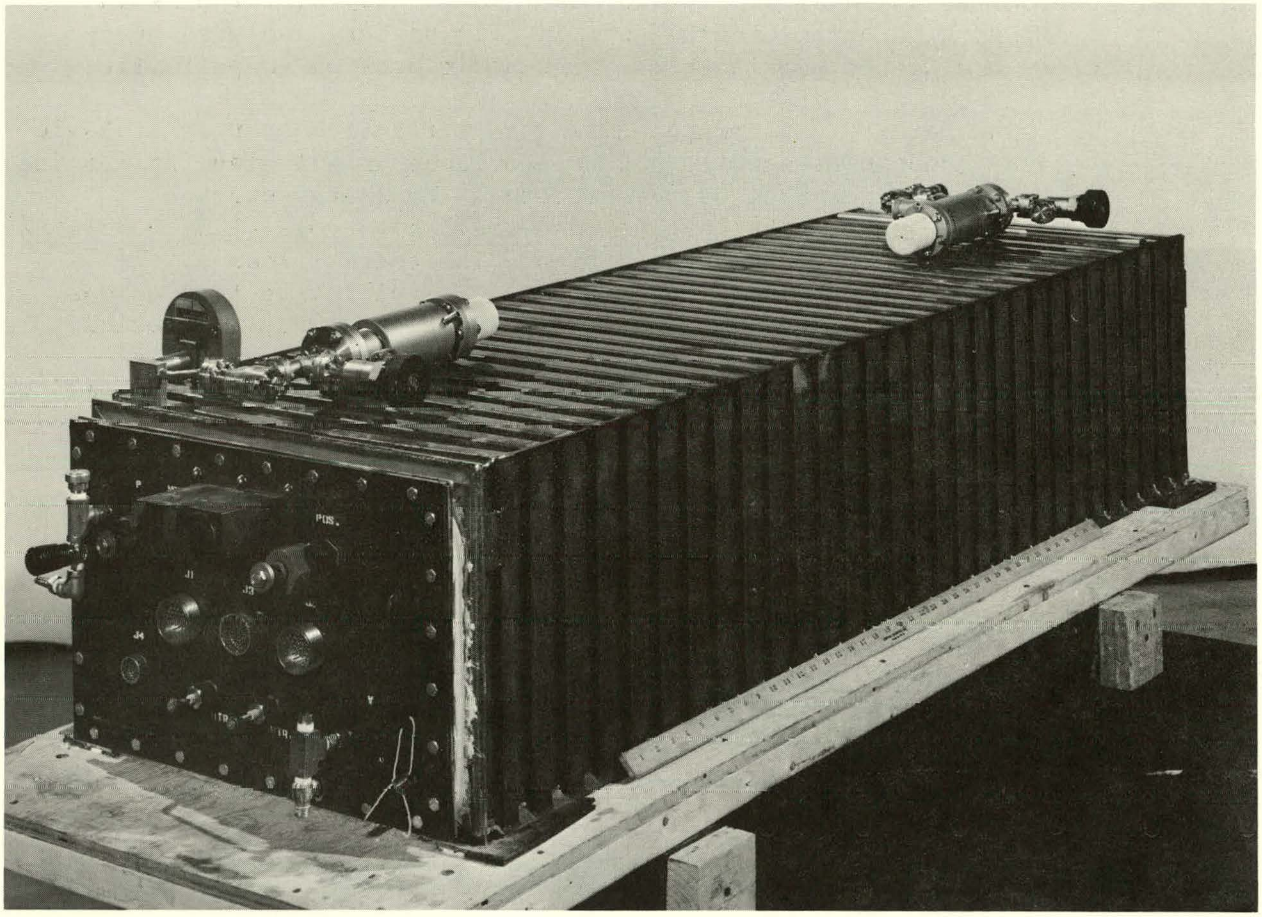

Fig. II-6. Photograph of Mark IA Module.
ANL Neg. No. 301-79-411.

fork-lift truck applications. If feasible, this would then lead to the fabrication of a full-scale (48 V, 26 kW-hr) battery which would be used in the performance demonstration of a standard capacity (2,000 lb) U. S. Army lift truck. Design goals were set to demonstrate the specific energy, specific density, and peak power capabilities of the current LiAl/FeS technology with respect to this type of application. These parameters then dictated geometry, size, weight and thermal management characteristics of the proposed system.

The MERADCOM battery consisted of five pairs of Mark IA cells, each pair connected in parallel. Cell pairs were selected to yield low resistance and high capacity (>750 W-hr at 6-hr rate). These five cell pairs were then connected in series to obtain the required capacity. The cells were restrained by a cell tray and were thermally insulated with a stainless steel case and a 5-cm thick layer of Min-K insulation (Johns Manville, Corp.). When assembled, this battery weighed 77.11 kg (volume, 55.34 L) and had dimensions of 51.4 x 29.0 x 35.4 cm. Instrumentation was added for thermal management and cell equalization.

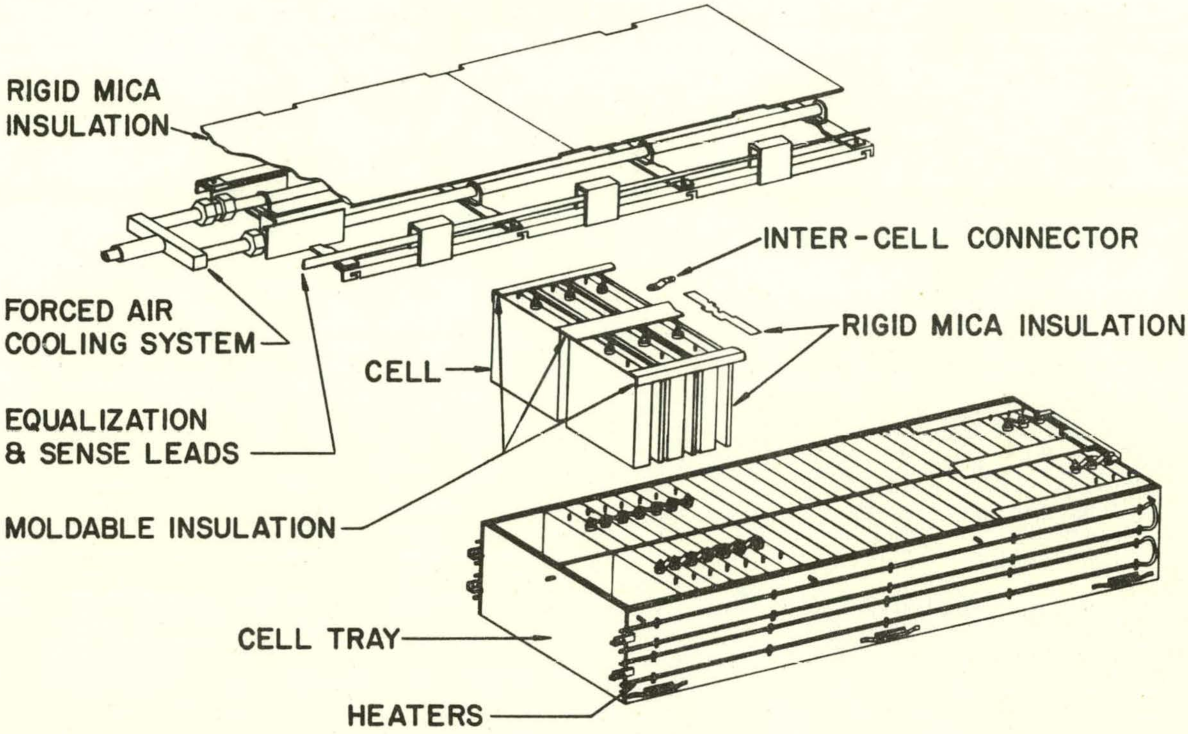

Fig. II-7. Cell Tray and Electrical Insulation for Mark IA Battery Module

Table II-8. Material Used for Mark IA Battery Hardware

Battery Hardware	Material
Tray[a]	304 SS
End Plates	Inconel 718
Cooling Tubes	300 Series SS
Insulation	
cell-cell, cell-tray, cell-case liner	Vitrabond mica 27-08
cell-tray angle, cell-"T" bar	Raybestos RM 1776
wires (equalizer, voltage sense)	SAMOX
thermocouples	Fiber glass braid
front plug	Min K
Wires	
equalizer, voltage sense	Nickel clad copper
thermocouples	Chromel-alumel
Intercell Connectors	Nickel clad OFHC copper
Wrap for Min-K and Wire Bundle	Glass cloth
Braze Flux	Airco Flux #12

[a] This include a "T" bar and peripheral angle to provide further restraint.

A battery test station was set up to cycle the 6-V unit at the 6-hr rate with individual cell equalizing capability. The unit was then operated for three characterization cycles, one qualification cycle, and one simulated forklift cycle. Results of this test as well as the design goals are shown in Table II-9. After this preliminary testing, the unit was then delivered to ANL for additional testing (Section III. C).

Table II-9. MERADCOM Battery Performance

Parameter	Proposed	Projected	Achieved
Energy Storage,[a] kW-hr	4	3.840	3.984
Voltage Profile, V			
end of charge	8.25	8.25	7.86
nominal operating	6.0	6.0	6.0
end of discharge	5.0	5.50	5.34
Heat Loss (on standby), W	500	539.57	250
Specific Energy,[a] W-hr/kg	50-55	55.37	51.67
Energy Density,[a] W-hr/L	55-60	69.39	72
Peak Power,[b] kW	2-3	2-3	2-3

[a] Measured at 6-hr rate.

[b] Measured during 3-sec power pulse.

5. Quality Assurance

(J. R. Todd, R. S. Repplinger, R. Harris)

Quality Assurance played a major role in all activities in the Eagle-Picher LiAl/FeS programs. The quality assurance activities were accomplished in accordance with a Quality Assurance Program Plan. A Quality Control Engineer, Quality Control Supervisor, and a Quality Control Technician were assigned to the project by, and reported directly to, the Product Assurance Manager. They were a part of the Project Team and, therefore, supported the needs and requests of the Program Manager. At no time was there any conflict between product assurance directive policies and the quality philosophy of the engineering department. The effort to fabricate the batteries described above involved control of both R & D and production fabrication. The cells fabricated in these programs had various design modifications, and each was thoroughly documented and configuration controlled. The writing and approving of procedures by Quality Control was a significant involvement. Quality personnel either authored, or coauthored six material specifications and twelve manufacturing and inspection procedures. Trips were taken by quality personnel to sub-tier suppliers. These visits were for numerous reasons, ranging from audits to source inspection. On-site inspection was essential several times throughout the year to expedite delivery of numerous components.

Quality Control personnel participated in cell selection for each of the Mark IA modules. The cells with functional deficiencies such as low capacity, shorting conditions, and high resistance were eliminated. The engineering personnel then selected cells based upon performance parameters such as capacity, voltage profiles, internal resistance, and charge-discharge efficiency. When the final cell designation for each battery module was approved by both engineering and quality control personnel, it was then submitted to Argonne for further evaluation. The documentation was reviewed on each cell from its final test data to receiving inspection data in order to ensure that no outstanding deficiencies were left unnoticed.

The assembly of each battery module fabricated at Eagle-Picher received 100% quality control inspection. The electrical insulation resistance (cell-to-cell and cell-to-container) was verified during assembly and prior to final battery closure. Cell resistances were checked, and each heater lead and cell lead was checked. All electrical and insulation parameters were repeatedly inspected and verified acceptable before the cell tray was inserted into the insulating case.

B. Gould Inc.

(B. A. Askew)

The Energy Research Laboratories of Gould have been involved with the advanced battery program of ANL since 1975. During the past year, they have fabricated 47 Li-Al/FeS bicells and 7 multiplate Li-Al/FeS cells. Most of these cells had separators of BN felt and current collectors of nickel for the positive electrode and iron for the negative electrode. The basic design for the bicell is shown in Fig. II-8 and that of the multiplate cell in Fig. II-9. These cells had many variations in components and materials, including the following: thickness and porosity of the electrodes, LiCl content of the electrolyte, charge state of the active materials for cell assembly, density and thickness of the positive current collector and felt separator, and additions to the FeS in the positive electrode. Appendix A shows these variations as well as the performance and lifetime for each cell tested. Overall, the cell tests show that Gould has made significant improvements in the performance, reliability, and mass-production capability of the Li/MS cell system. The cell development and testing performed at Gould over the past year are summarized below. The Gould cells tested at ANL are discussed in Section III. B.

1. Cell Component Development

(L. A. Eaton)

a. Feedthrough Development

The feedthrough design used in cells during 1978 is shown in Fig. II-10. The reliability of the seal was poor, and frequent cell failure occurred as a result of cracked ceramic components and subsequent electrolyte leakage. The first improvement of the seal incorporated two design changes. The Y_2O_3 lower ceramic bushing was replaced with a BeO component (manufactured by the 3M Company), which reduced the length of the feedthrough and reduced fracture-induced failure. In addition, a copper-filled stainless steel post was used to replace the nickel post; this change resulted in an improved reliability, although seal failures were not totally eliminated.

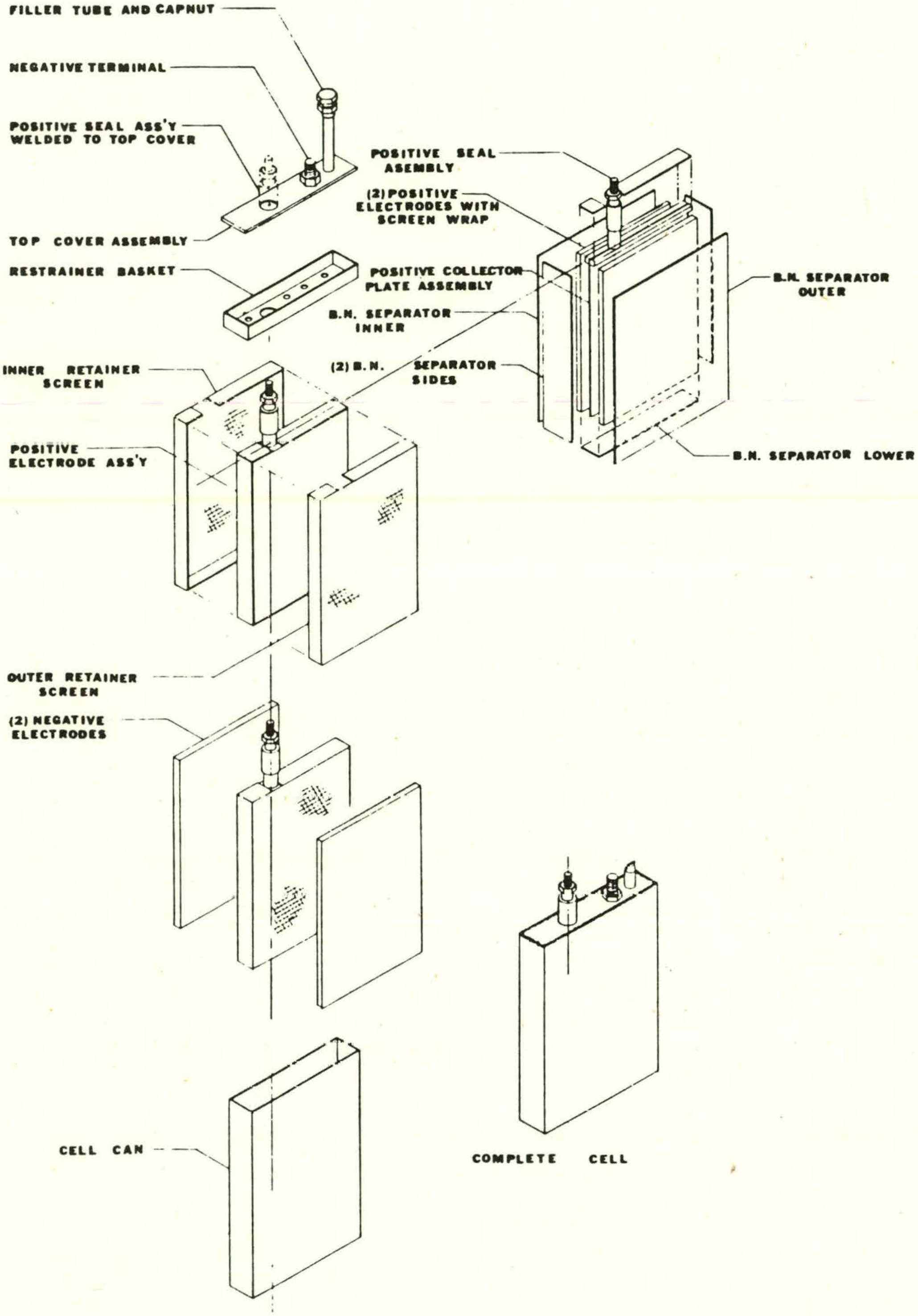

Fig. II-8. Gould Bicell

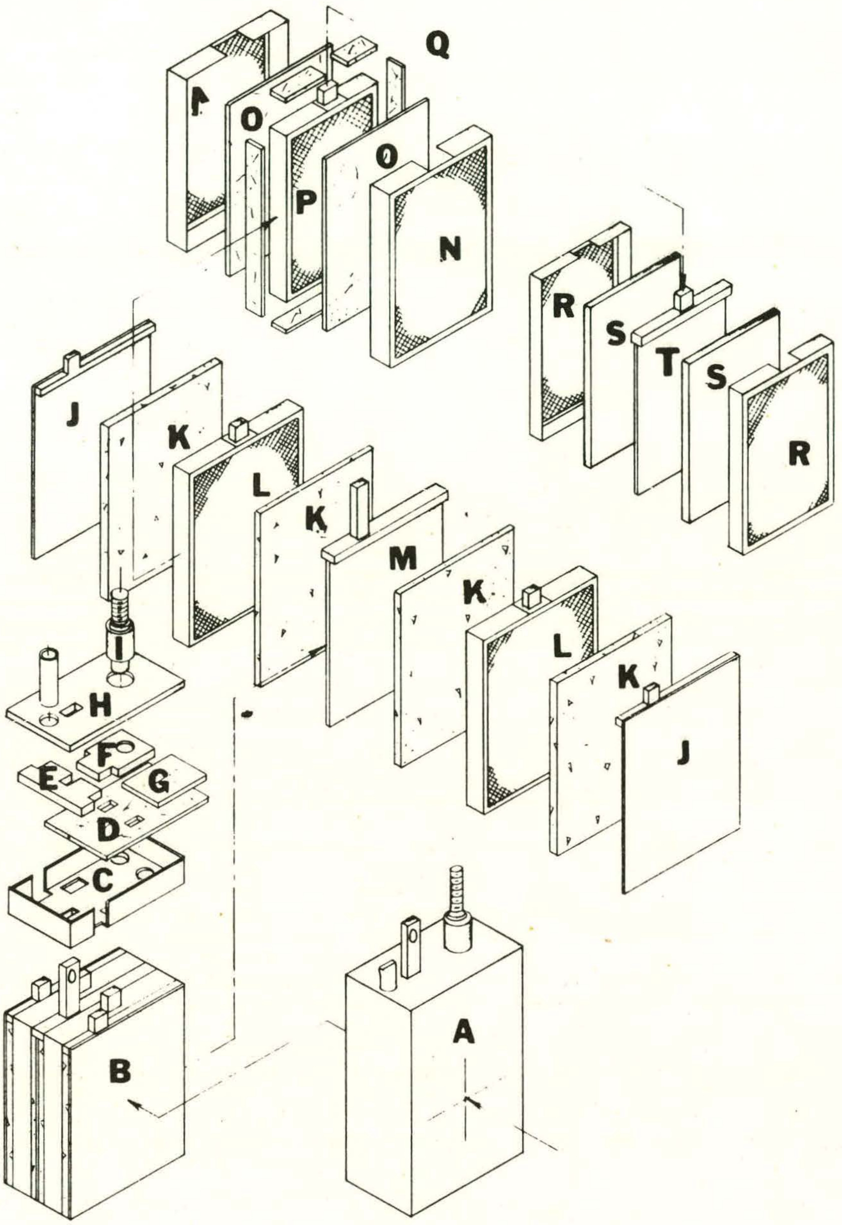

Item	Description
A	Complete Mod 02 Multiplate Cell
B	Mod 02 Cell Package
C	Top Retainer Basket
D	BN Top Insulator
E	Neg. Distribution Bus
F	Pos. Distribution Bus BN Insulator
H	Cover Assembly
I	Seal-Feed Through Assembly
J	End Wall Neg. Collector-Bus
K	Negative Electrode

Item	Description
L	Positive Package
M	Neg. Center Collector-Bus
N	Negative Retainer Basket
O	BN Face Separator
P	Positive Electrode Package
Q	BN Side Insulators
R	Positive Retainer Basket
S	1/2 Positive Electrode
T	Collector-Bus Assembly

Fig. II-9. Gould Multiplate Cell

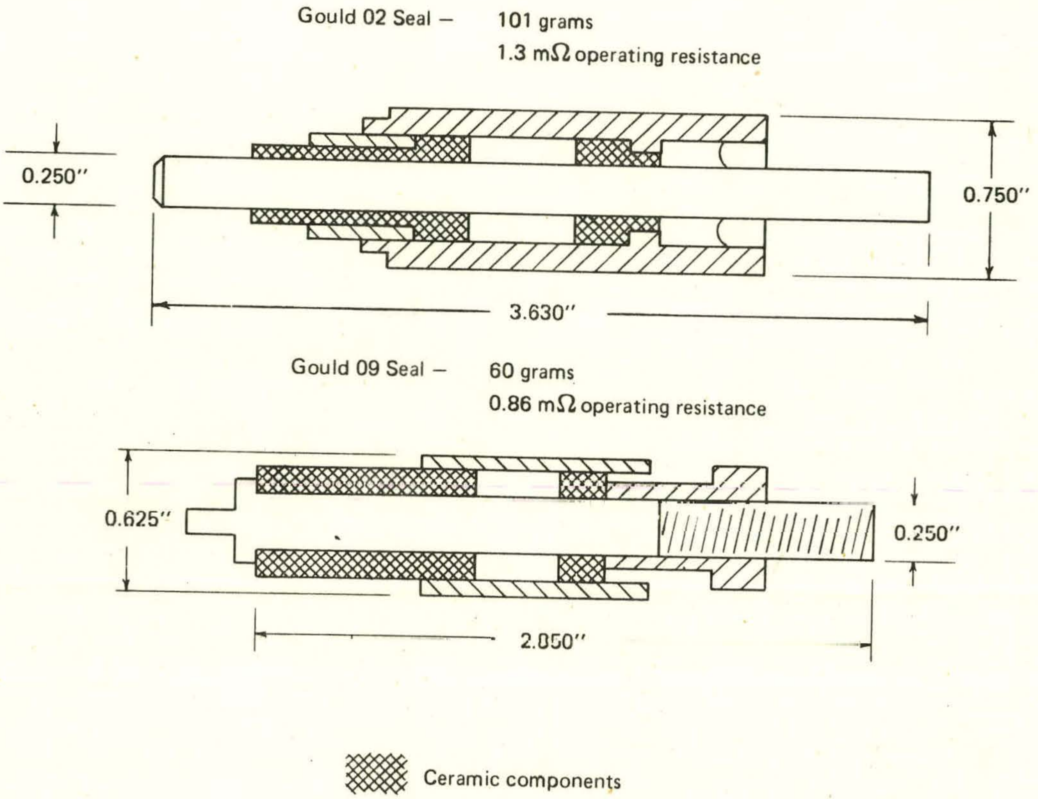

Fig. II-10. Initial Feedthrough Design

Three further modifications were subsequently made (see Fig. II-11):

1. The Al_2O_3 upper ceramic bushing was replaced by BeO; the ceramic component was eliminated because it could become electronically conducting when exposed to lithium-saturated molten salt.

2. The mechanism for securing the assembly and applying pressure to the packed BN powder bed seal was changed by the inversion of the design and by welding the positive distribution plate to the center post.

3. The standard welding practice of heating the seal body to achieve a bond to the cell cover caused overheating (to 800°C) of the ceramic components. This caused relaxation of the powder bed on cooling and allowed the possibility of the ceramic bushings fracturing. A more careful welding practice was therefore followed, reducing the maximum seal temperature from 800 to 450°C.

The present feedthrough design appears to have eliminated feedthrough failures and is currently employed in all bicell and multiplate cells.

REVISIONS			
ISSUE	DESCRIPTION	DATE	APPROVAL

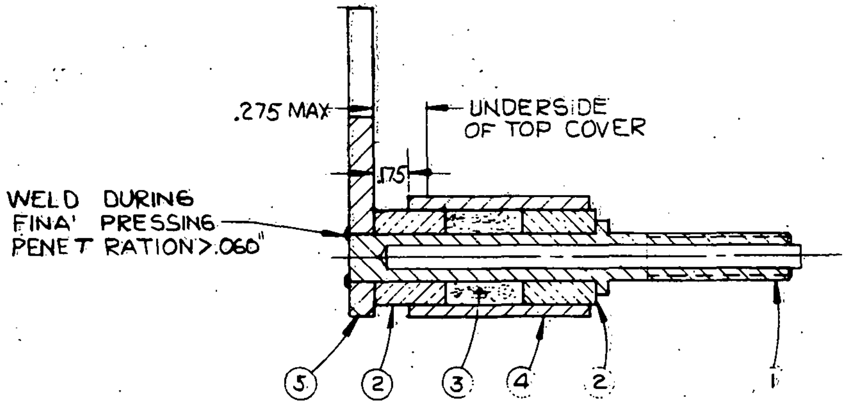

ITEM NO.	PART NUMBER	NAME
1	MIII/4331-02-201	CENTER POST ASSEMBLY
2	MIII/3354-01-200	BERYLLIA BUSHING
3.	MI/1330-20-204	POWDER SEAL
4	MIII/3330-02-201	SEAL BODY
5		DISTRIBUTION PLATE

TOLERANCES: UNLESS OTHERWISE SPECIFIED
FRACTION = ± ANGLES ±
.XX = ±
.XXX = ±
SCALE 2X
GOULD INC. HAS PROPRIETARY RIGHTS IN THIS MATERIAL
DO NOT SCALE THIS DRAWING

DRAWN I. RAKE DATE 5-29-79
CHECKED DATE

GOULD
GOULD LABORATORIES
ROLLING MEADOWS, ILL.60008

TITLE SEAL ASSEMBLY POSITIVE TERMINAL
DRAWING NUMBER B MIII/4330-02-200
ISSUE

Fig. II-11. Modified Feedthrough Design

The total feedthrough resistance is 0.8 mΩ at 450°C, the weld contribution being 0.15 mΩ. A heavier version of the feedthrough has been designated for future four-positive plate (450 A-hr) cells.

b. Positive Electrode Containment

In early bicell designs, the positive electrode was contained by the BN felt separators (both faces) and a frame of felt strips lining a negative retainer basket. The positive-electrode screen wrap was fabricated from 230-mesh stainless steel. A frequent mode of cell failure with this design was extrusion of positive material through the felt at corners of the positive electrode, which resulted in short circuits at the negative electrode. The use of a retainer-screen basket, where the BN felt was sandwiched between the inner and outer basket, was reasonably successful in preventing this mode of failure. One of the first cells of this type, X-77, operated for 350 deep discharge cycles. In a more recent iteration, a 0.152-cm steel-strip overlap forming a "picture frame" gave further support at the edges and corners of the positive electrodes (Fig. II-12). This design has been shown to be the most reliable to date in both bicells and multiplate cells.

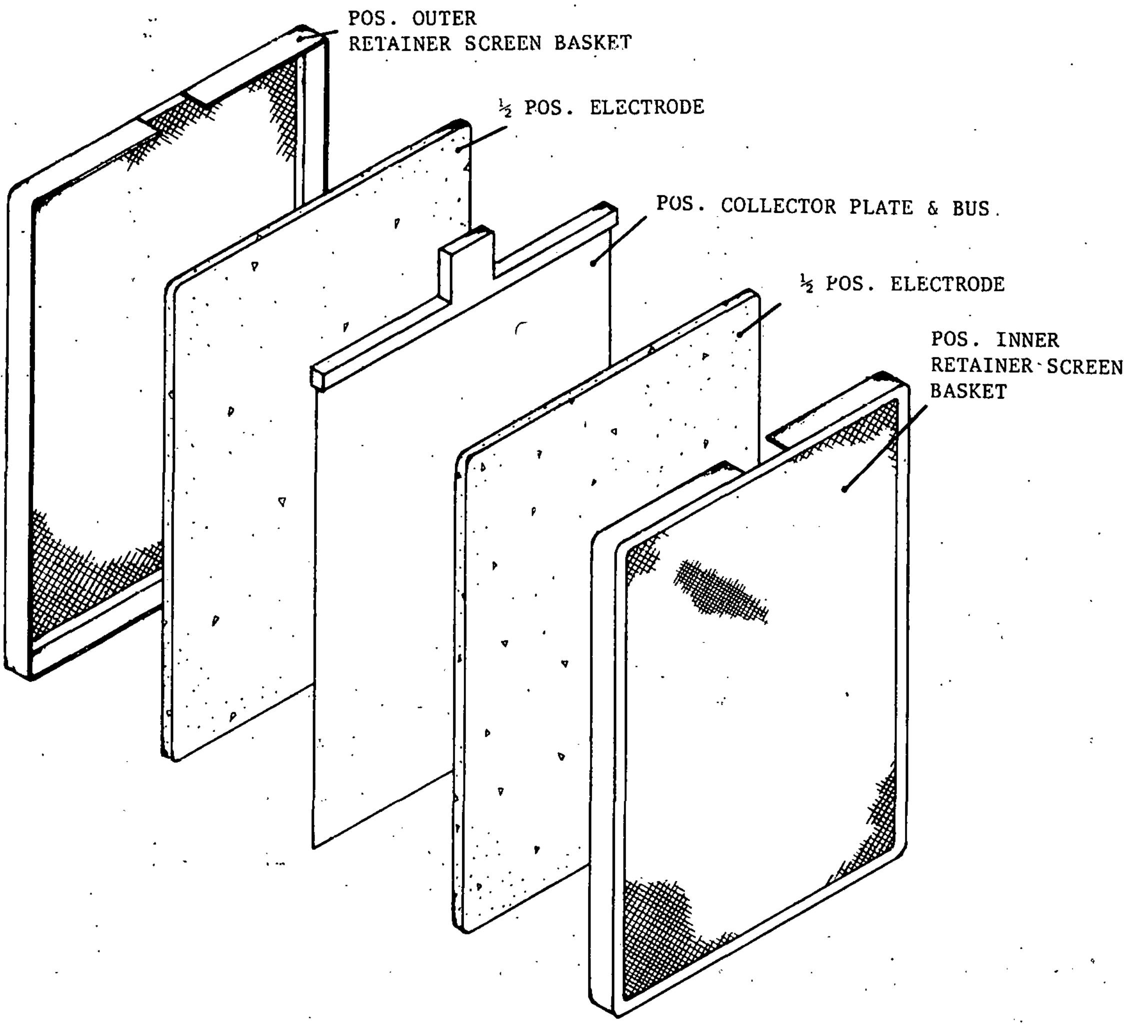

Fig. II-12. Containment Assembly for Positive Electrode

However, this basket assembly has certain inherent disadvantages:

1. The assembly process is cumbersome and difficult to adapt to mass manufacture.

2. The BN separator must be butt-jointed at locations between the screen baskets, providing a potential source for internal short circuiting.

3. The positive and negative electrodes must have different sizes, allowing nonuniform expansion of the negative electrode at the edges.

4. The negative electrode is not contained at the edges, allowing significant electrode growth in these regions which could also result in short circuiting.

A simple multiplate design is being developed where positive and negative electrodes are each contained within a "picture frame" assembly (see Fig. II-13). In this cell design (Fig. 14) strips of felt material are placed at the base and sides of the cell container to prevent short circuiting. This design is expected to have the following advantages:

1. The increased physical separation of materials of opposite polarity should greatly reduce their susceptibility to short circuiting.

2. Swelling of the negative electrode into unconstrainted regions of the cell should be eliminated.

3. Cell assembly should be greatly facilitated, with consequent reduction in damage to the fragile BN felt separator.

4. The design is suited to the use of alternative particle retainer systems and separators.

c. Electrode Current Collector

In past Li-Al/FeS bicells, nickel and iron current collectors have been tested in the electrodes. The most recent design for the positive current collectors consists of a solid nickel bus bar with a nickel collector plate welded to it. Since the latest feedthrough has a stainless steel post, an iron-to-nickel transition points exists in these cells. The lowest electronic resistance was achieved with a steel tab centrally located on the collector plate and welded to the nickel bus (using No. 61 alloy weld rod). The offset distribution plate was fabricated from steel to form part of the feedthrough assembly. The tab location provides for the maximum area of nickel-to-iron weld interfaces.

An iron current collector and bus bar have been developed for the negative electrode to minimize cell resistance. The use of a negative bus bar and a separate negative terminal provides a simple and effective means of current collection, eliminating the need for additional conducting material at the cell lid.

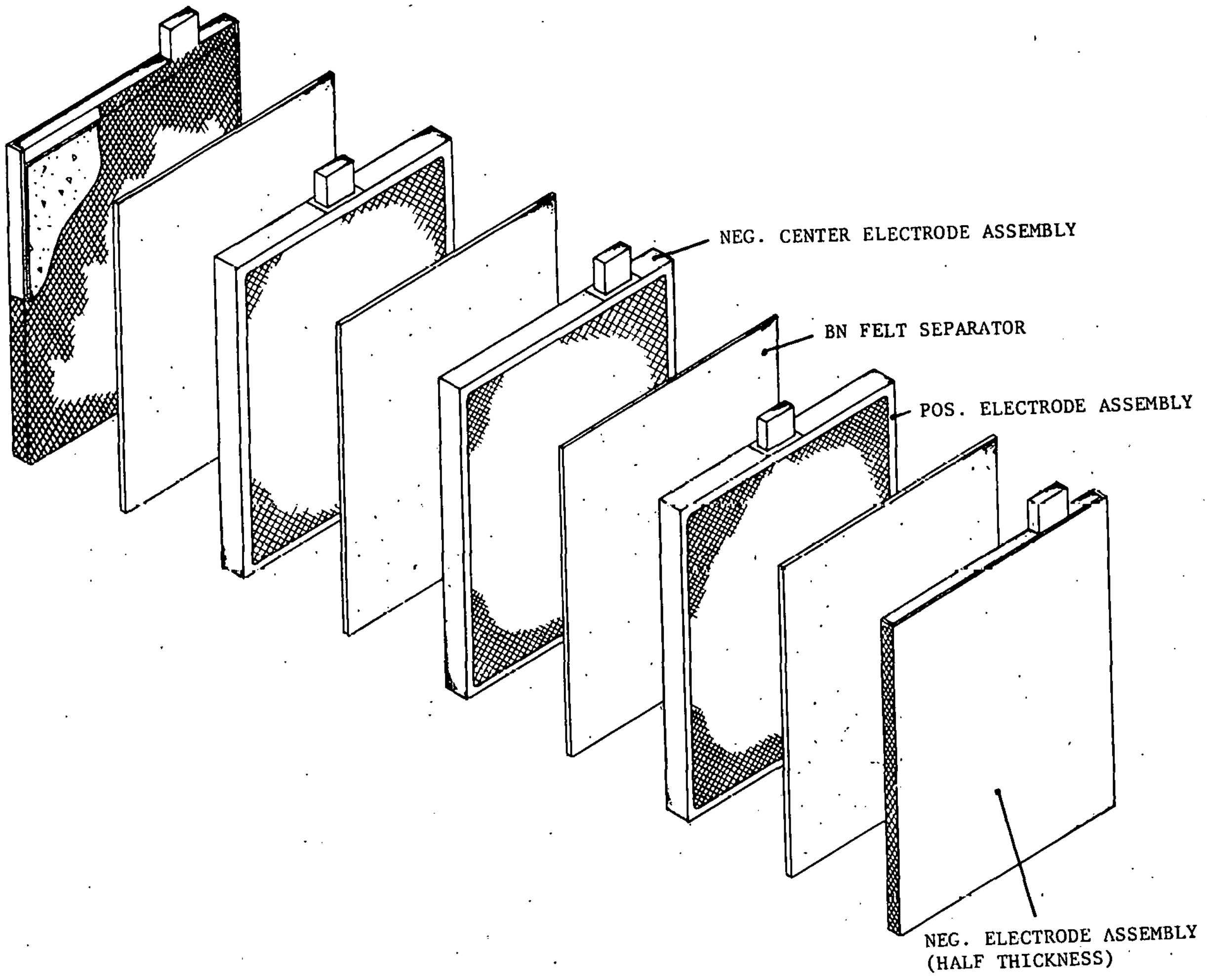

Fig. II-13. Electrode-Component Assembly for Multiplate Cells

2. Electrode Development

(P. Dand, R. E. Thompson)

a. Positive Electrode

The positive electrode for the cells was initially fabricated by hot pressing the appropriate mix of active materials in the uncharged state. The mix contained lithium sulfide, iron powder, electrolyte and other additives. The pressing operation consisted of spreading the mix evenly in a mold and then pressing at temperatures above the electrolyte melting point. A rigid control of pressure and temperature was necessary to obtain reproducible positives plates. However, dimensional constraints placed on electrode fabrication in the uncharged state (identified via computer cell design modeling) led to fabricating cells with half-charged active materials. Testing of Cells X-53 and X-54 provided evidence that the half-charged

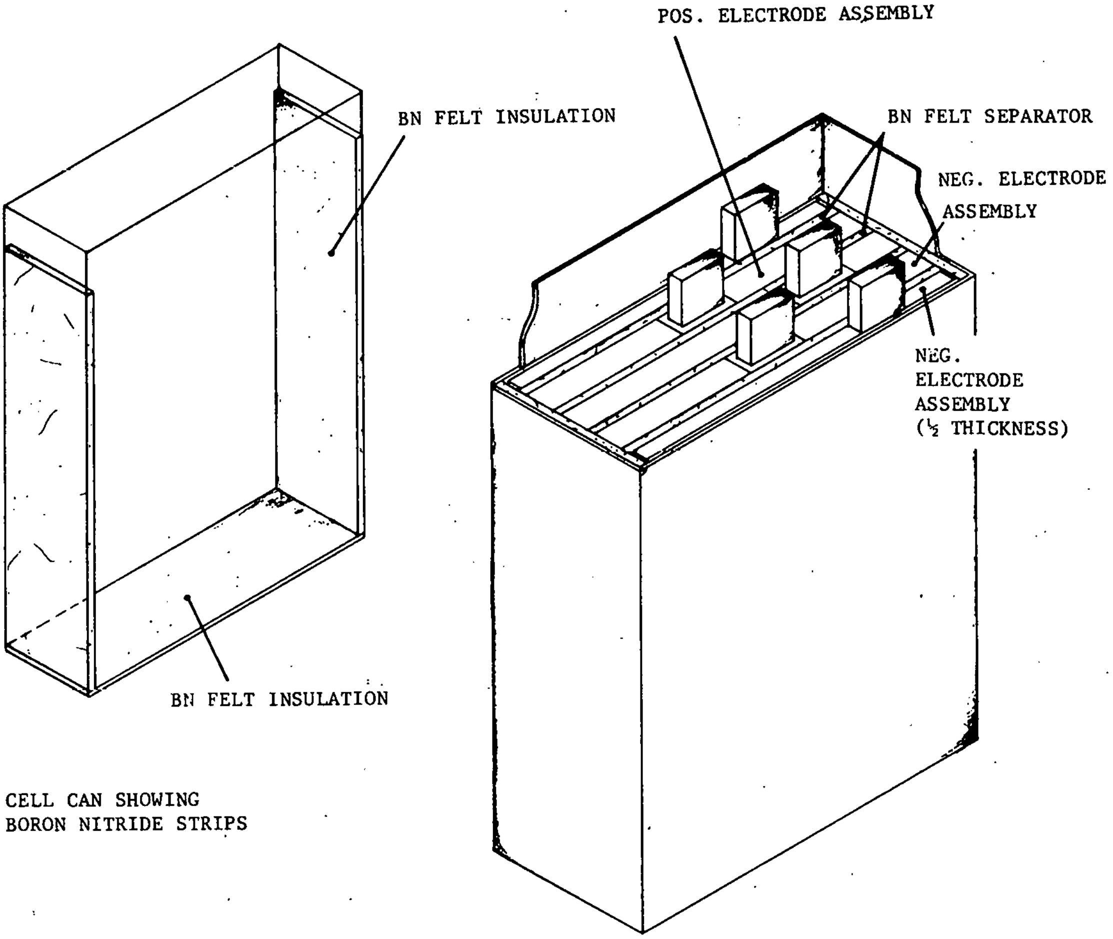

Fig. II-14. Multiplate Cell Showing Inserted Electrode Assembly

electrode fabrication technique was a viable alternative. Furthermore, the amount of "excess iron" (in excess of stoichiometric iron) required in the positive electrodes was decreased from 100 wt % (uncharged cell) to 10 wt % (half-charged cell).

In the positive electrodes of Cells X-41 to X-70, many different positive electrode additives were tested, including cobalt, molybdenum, chromium, vanadium, zirconium, and ZrO_2. Additions of molybdenum or cobalt and carbon were found to produce the highest active-material utilizations of the positive electrode. However, since cobalt is a scarce material and expensive, it was decided to only use additions of molybdenum and carbon. Consequently, hot-pressed, half-charged positive electrodes with additives of 10 wt % iron in excess of the stoichiometric iron as well as 1 vol % molybdenum, and 2 vol % carbon were fabricated and tested in experimental bicells X-78, X-83 to -90, and E-1 to E-4. Testing of these cells revealed marked improvements in active material utilization and specific energy, especially at high discharge current densities, and cell resistances at least as low as those of comparable cells fabricated in the uncharged condition.

The cells described above were all fabricated using hot-pressed positive electrodes. However, this fabrication method is slow and expensive. It was therefore decided to evaluate cold pressing of positive electrodes. The cold-pressing operation can be completed considerably faster than hot pressing, and may be carried out in a dry-room atmosphere. Initial experiments demonstrated that the pressure requirements for cold-pressing were in the range of 210 to 280 MPa (30,000 to 40,000 psi). At the time, Gould did not have a sufficiently large press to cold press full-size electrodes. Hence, the positive electrode was made in segments. Cell X-77 was the first cell constructed using cold-pressed positive electrode segments. This cell exhibited the longest life (349.5 cycles, 4512 hr) and the most stable performance ever achieved with the Gould Li/MS system. However, it was later shown that cold pressing produced fragile electrode plaques. Considerable differences in the density of the components of the half-charged positive mix were also likely to result in nonuniform material distribution. Fusion of the positive active material was therefore investigated to acquire better mixing and improve compaction characteristics. For this fusion process, the active material powder was mixed using a ball-mill in a dry-room atmosphere, fused under vacuum at a temperature of 450°C, and then ground to -40 mesh particle size. In preliminary experiments, cold compaction of this powder produced electrodes having the same porosity as hot-pressed positive electrodes. In addition, they were less brittle and, therefore, easier to handle during cell assembly. A 750-ton press has been recently installed at Gould and will be used to press full-size positive electrodes. Furthermore, experiments are planned in improving and optimizing the fusion process and powder characteristics for high-rate production of positive electrodes.

The FeS used for the X-series cells usually had a purity of 88.25%,* and the excess iron additive was coarse cast iron particles. Therefore, a series of cells was tested to evaluate the effect of impurities in the positive electrode. Cell E-1 contained the usual 88.25% pure FeS, E-2 possessed 84.5% pure FeS, and Cells E-3 and E-4 contained 99% pure FeS. All three cells had 10 wt % excess iron (pure grade). All cells performed very favorably, although Cell E-2 (lowest purity FeS) operated at a lower level of performance than the others. It was also apparent that reduction of excess iron in positive electrodes (100% down to 10%) was possible due to the replacement of coarse cast iron particles with higher-purity fine iron particles and/or the capability of fabricating electrodes in the half-charged state.

b. Negative Electrode

Earlier in the program, when cells were constructed in the uncharged state, the feasibility of extruding or casting negative electrodes having a low lithium content (5.25-8.18 wt %) was evaluated. However, electrodes fabricated from extruded and cast material exhibited serious polarization problems on discharge. In addition, cold pressing resulted in nonuniform electrodes with high porosity that were difficult to handle. Hot pressing was therefore adopted as the standard electrode fabrication technique for uncharged cells.

---

*Impurities were primarily iron oxide and silica.

With the decision to assemble cells in the half-charged condition, the possibility existed of fabricating negative electrodes by the cold compaction of a mixture of 20.5 wt % lithium-aluminum alloy and pure aluminum power. Experiments have been conducted using different particle size distributions of Li-Al powder (20 to -325 mesh) and aluminum powder (-40 to +200 mesh). These two powders were prepared in the ratio of 59 to 41, giving a half-charged composition of 12 wt % lithium containing alloy. These electrodes were formed at pressures of 175 MPa (25,000 psi); as a result, electrodes with a 20% porosity that were easy to handle during cell assembly were formed. The electrodes have been evaluated using reference electrodes in experimental bicells E-2, E-3, and E-4 and multiplate cells D-2 and D-4 and showed virtually no difference in performance; no polarization was observed during cycling. Experiments will be continued with other mixtures of Li-Al and aluminum, and the possibility of replacing the mixture with the exact half-charged composition of Li-Al will also be evaluated.

c. Separator

The most crucial consideration for the achievement of reliability in LiAl/FeS cells is the availability of an acceptable separator and the development of a technique to successfully incorporate the separator in the cell. Initially, the cells were fabricated with salt-bonded felt formulated at Gould. Boron nitride felt made at Carborundum Co. became available later; and, after considerable experimentation, particle retainer systems and cell assembly techniques compatible with the fragile felt were developed. Long-life cells with these separators were demonstrated in the recent past.

Gould cells have been shown to be exceptionally resistant to capacity decay with cycling. Continual electrode performance improvements have led to such high utilizations that efforts to further improve the performance are viewed as not being worthwhile. Under these circumstances, the separator thickness is crucial in achieving the optimal volumetric and gravimetric energy and power. Table II-10 illustrates the effect (via computer cell model design) of this parameter on cell specific energy, when the dimensions of the rest of the components remain constant.

Table II-10. Effect of Sparator Assembly Thickness on Cell Specific Energy

Felt Assembly Thick., cm	Cell Can Thick., cm	Cell Weight, kg	Specific Energy, W-hr/kg
0.101	5.537	6.023	125
0.127	5.740	6.165	122
0.152	5.944	6.306	119
0.178	6.147	6.448	116
0.203	6.350	6.589	114
0.211	6.411	6.632	113

Almost all the bicells tested at Gould had separators of unstabilized BN felt made from 6- to 7-μm dia fibers, little other felt material being available. Stabilized felt made from smaller diameter fibers is expected to have a different compressibility and compressive strength, thereby necessitating a redesign of the separator assembly to accommodate the new material.

3. Cell Testing and Post-Test Analysis

(R. E. Thompson, F. Marikar)

It is not practical to discuss the performance of each of the 53 cells tested during the past 12 months (see Appendix A). Therefore, a more detailed description of the performance obtained with a long-life bicell (X-77) and a multiplate cell (D-4) is given below. The performance of the Gould cells tested at ANL is given in Section III.B.

Cell X-77 (uncharged) was the first cell to be assembled in a dry room (instead of a glove box) at Gould. It was also the first cell to utilize a cold-pressed (segmented) positive electrode. A standard hot-pressed negative electrode was used. The positive electrode additives for this cell were excess iron (10 wt %), cobalt (2 vol %) and carbon (1 vol %). The iron used for this cell was a pure, fine iron powder, not the coarse-particle cast iron used in most other similar cells. After start-up, this cell was discharged at a current of 17 A (60 mA/cm^2).

The voltage *vs.* time graphs of this cell for cycles 50 and 284 (selected at random) are shown in Fig. II-15. The profiles obtained during these two cycles are virtually identical; this demonstrates the high degree of reversibility and stability of the LiAl/FeS cell, thereby indicating that

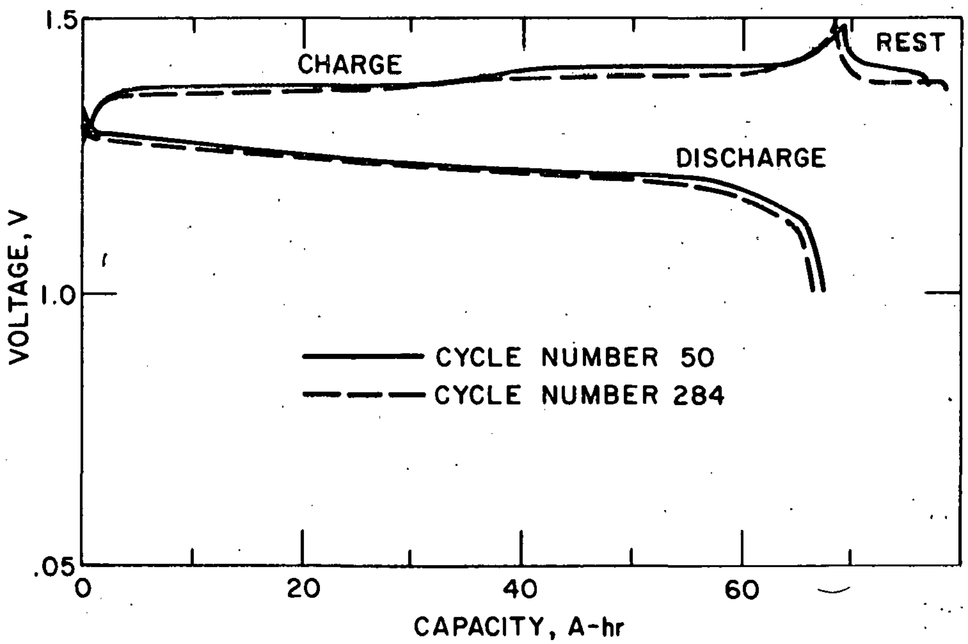

Fig. II-15. Voltage *vs.* Capacity of Cell X-77 on Cycles 50 and 284 the system is capable of extremely long-life operation with a stable performance. However, the elimination of intermittent internal short-circuiting, prevalent in most Gould cells, will be necessary before long cell lifetimes can be obtained in practice. The resistance for this cell was about 5 mΩ (t = 15 sec). The effect of current density on sulfur utilization (percent of theoretical capacity) is shown in Fig. II-16. The change in slope at around 60 mA/cm^2 is a common feature of these cells and is not fully understood. It may be associated with partial freezing of one of the electrolyte constituents at increasing current densities. It might also be the point at which the negative electrode becomes the limiting electrode. Further investigation of this behavior with reference electrodes will be conducted. Plots of coulombic efficiency, cell capacity and specific energy as a function of cycle number are shown in Fig. II-17. The first sign of cell failure was a slight decline in coulombic efficiency after some 270 deep discharge cycles; however, no capacity decline was detected until after 340 cycles. This is indicative of a partial short circuit during the charge cycle only. The cell operated for a total period of about 6 months.

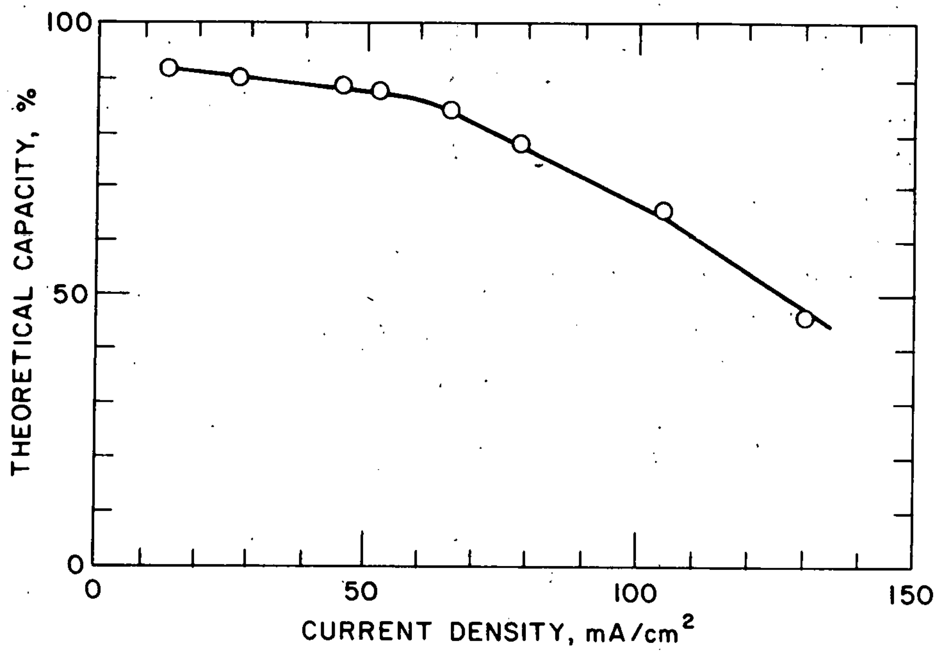

Fig. II-16. Capacity Curve for Cell X-77 at Various Current Densities

Metallographic examination after testing of Cell X-77 showed no corrosion of the nickel current collector as well as only surface attack of the retainer screen. It is believed that the corrosion found in some cells is associated with the use of coarse iron in the positive electrode. There are supporting arguments for this:

1. Cells with coarse iron are slow to form, *i.e.*, to reach full capacity during initial low-rate cycling. However, those containing fine iron rapidly achieve full capacity. It is very likely that in

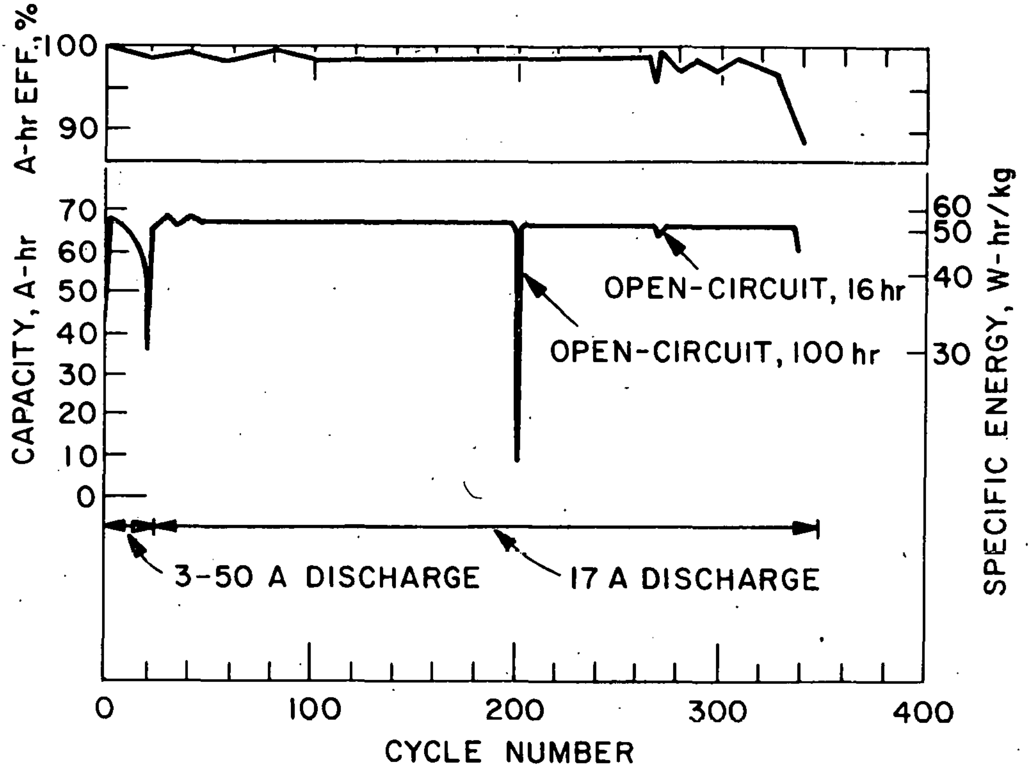

Fig. II-17. Performance Plot for Cell X-77 (charge rate, 10A).

cells containing coarse iron, the nickel current collector and steel screen provide the necessary active material for reaction with Li_2S during the charge cycle. Indeed, even after many cycles, considerable quantities of coarse iron are found within the positive electrode structure, indicating that they have not participated in any electrochemical reaction.

2. Cell X-77 was assembled in a dry room and undoubtedly contained more moisture than cells assembled in an argon glove box. However, no corrosion was observed in X-77, even after 350 cycles. It is, therefore, most unlikely that differences in moisture content account for the corrosion.

3. All cells were cycled between the same cutoff voltages (1.0 to 1.6 V); therefore, overcharge was not a contributing factor to corrosion.

The 232.3 A-hr multiplate cell, D-4, has operated for over 23 cycles. Performance data of this cell are shown in Fig. II-18. At a discharge current density of 60 mA/cm^2, Cell D-4 has attained a capacity of 210 A-hr and a specific energy of 108 W-hr/kg. The coulombic efficiency remained at 98% and the cell resistance at 2.5 mΩ. Further effort is needed to improve the cycle life of the multiplate cell.

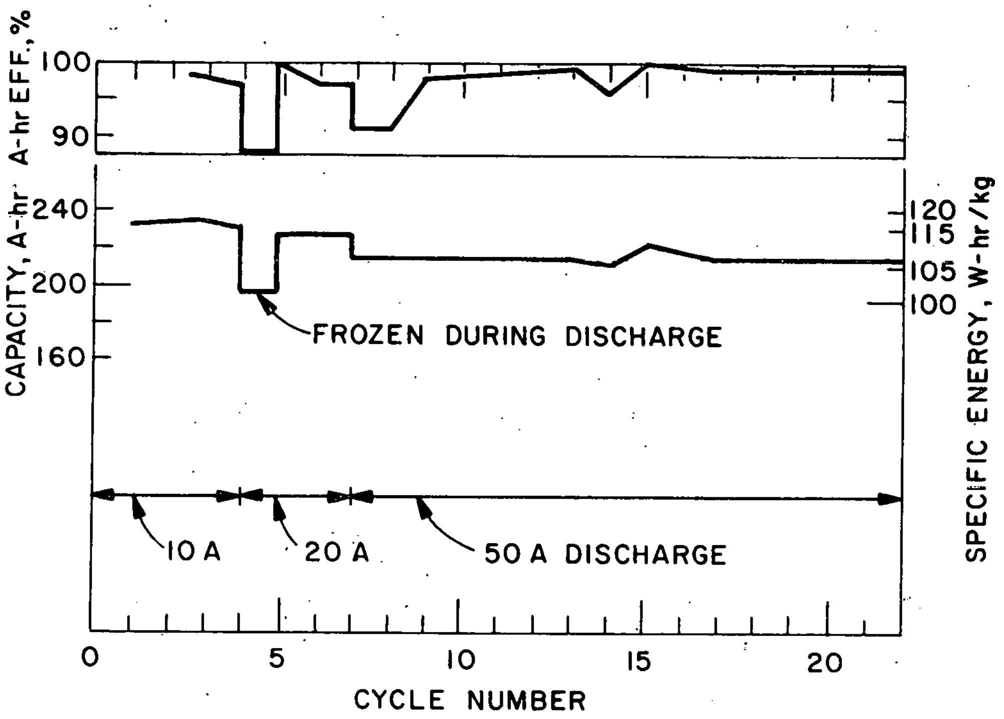

Fig. II-18. Performance Plot for Cell D-4
(charge rate, 6 to 20A)

4. Post-Test Cell Examinations

(F. Marikar)

The post-operative facility at Gould is housed in a dry room and is equipped to prepare and observe cell and electrode sections at high magnification using optical microscopy. Tested cells have usually been cycled until a fall in coulombic efficiency indicated a short-circuit. When the differential between charge and discharge capacity exceeded about 15 A-hr, the cell was classified as failed and cooled to room temperature for examination. The cold resistance of the cell was usually found to be less than 10 Ω. Monitoring the cold resistance of normal (*i.e.*, non-short-circuited) regions of the cell has been particularly valuable in determining the adequacy of material retention in the electrodes.

During the last year, failure analysis was performed on 36 cells, 11 of which failed due to short-circuiting of the feedthrough. Owing to a recent design change explained above, this problem appears to have been overcome. Table II-11 summarizes the failure analysis of some recent Gould cells.

Figure II-19 shows photomicrographs of sections from Cell X-77. Figure 19a shows a cross section of the negative electrode along its entire thickness, from the inside of the container can to the steel screen adjacent to the separator. The uniform fine structure of the Li-Al and the lack of any agglomeration are clearly observable. Figure 19b shows the central region of the positive electrode including the nickel current collector, which is totally free from corrosion. Figure 19c shows some reaction of the positive electrode screen and partial penetration of the BN felt separator by iron particles. Figure II-20 shows the uniform distribution of sulfides, iron and electrolyte in the positive electrode of Cell E-1 (operating time 27 cycles).

Table II-11. Results of Post-Test Examination of Six Gould Cells

Cell No.	Cycle Life	Cold Resistance, Ω	Cause of Failure	Separator Thickness, mm	Felt Face Density, mg/cm^2
X-77	350	2.3	Positive electrode extrusion through ruptured screen	1.60	69
E-1	27	0.2	Positive screen basket squeezed open along side, causing damage to BN felt	1.82	66
E-2	15	0	Positive Material extrusion along top weld to bus bar	1.02	34
D-1	18	0.6	Negative screen lifted and contacted positive bus at the top	1.52	67
D-2	14	0.7	Penetration and overall degradation of separator	0.89	35
D-3	3	0.2	Feedthrough short-circuit	1.35	67

5. Design and Cost Study

(F. Marikar)

A cost and design study of Mark II batteries was conducted; the objectives of this study were to

1. define the optimum cell and battery configuration;
2. evaluate the various materials of construction and manufacturing techniques;
3. estimate the manufacturing cost of electric-vehicle batteries in a 250 MW-hr/yr pilot facility and a 2000 MW-hr/yr manufacturing plant;
4. identify the areas of development critical to achieving the battery performance, cycle life, and cost goals.

The following sources of information were used in the study: cell development experience gained in the program, scientific and technical literature, suppliers and potential suppliers of materials and components, and manufacturing expertise of Gould personnel and consultants.

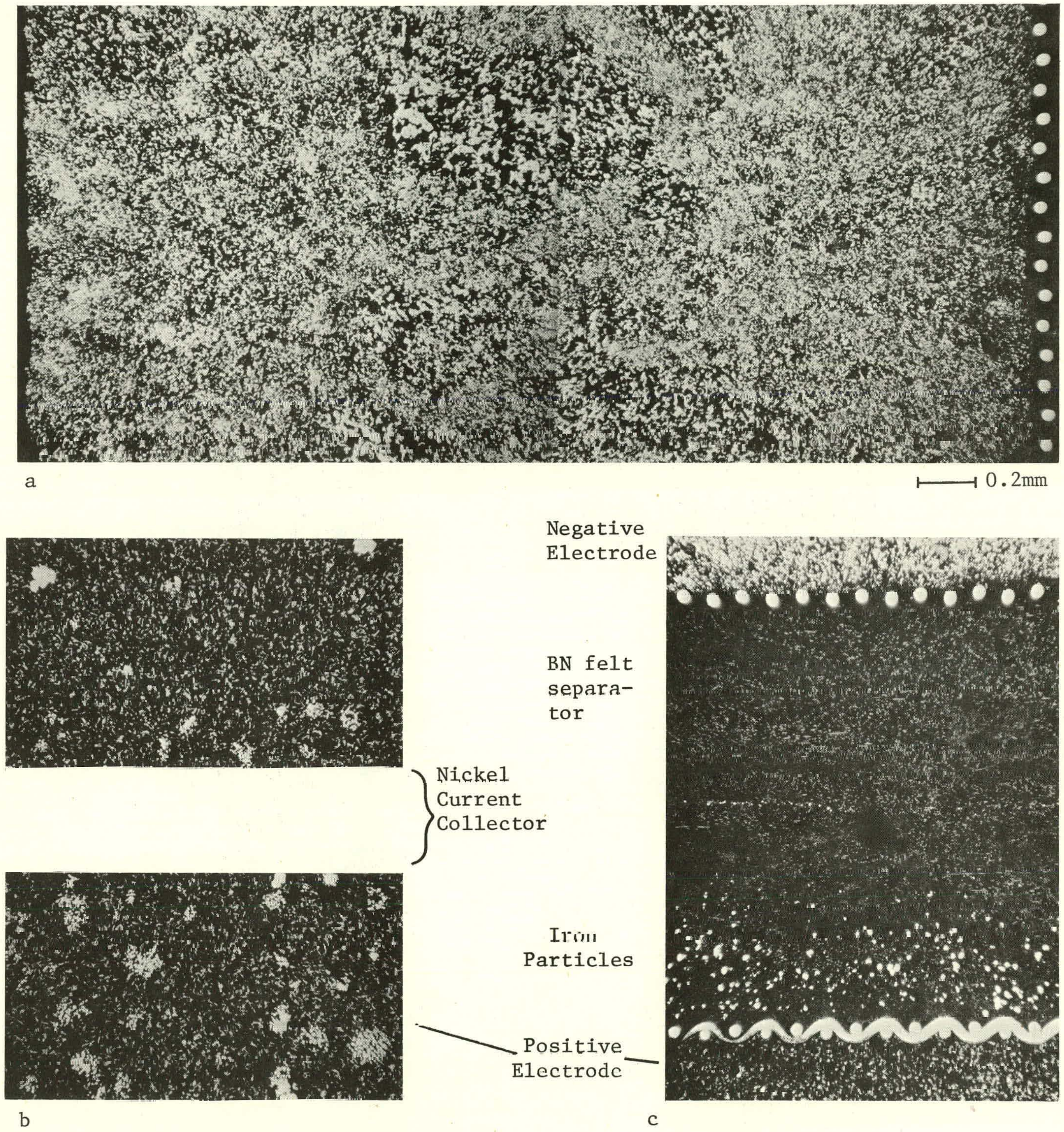

Fig. II-19. Photomicrographs of Cell X-77
a. Cross Section of Negative Electrode.
b. Cross Section of Positive Electrode (current collector in center).
c. Cross Section of BN Felt Separator (negative electrode on top and positive electrode on bottom).

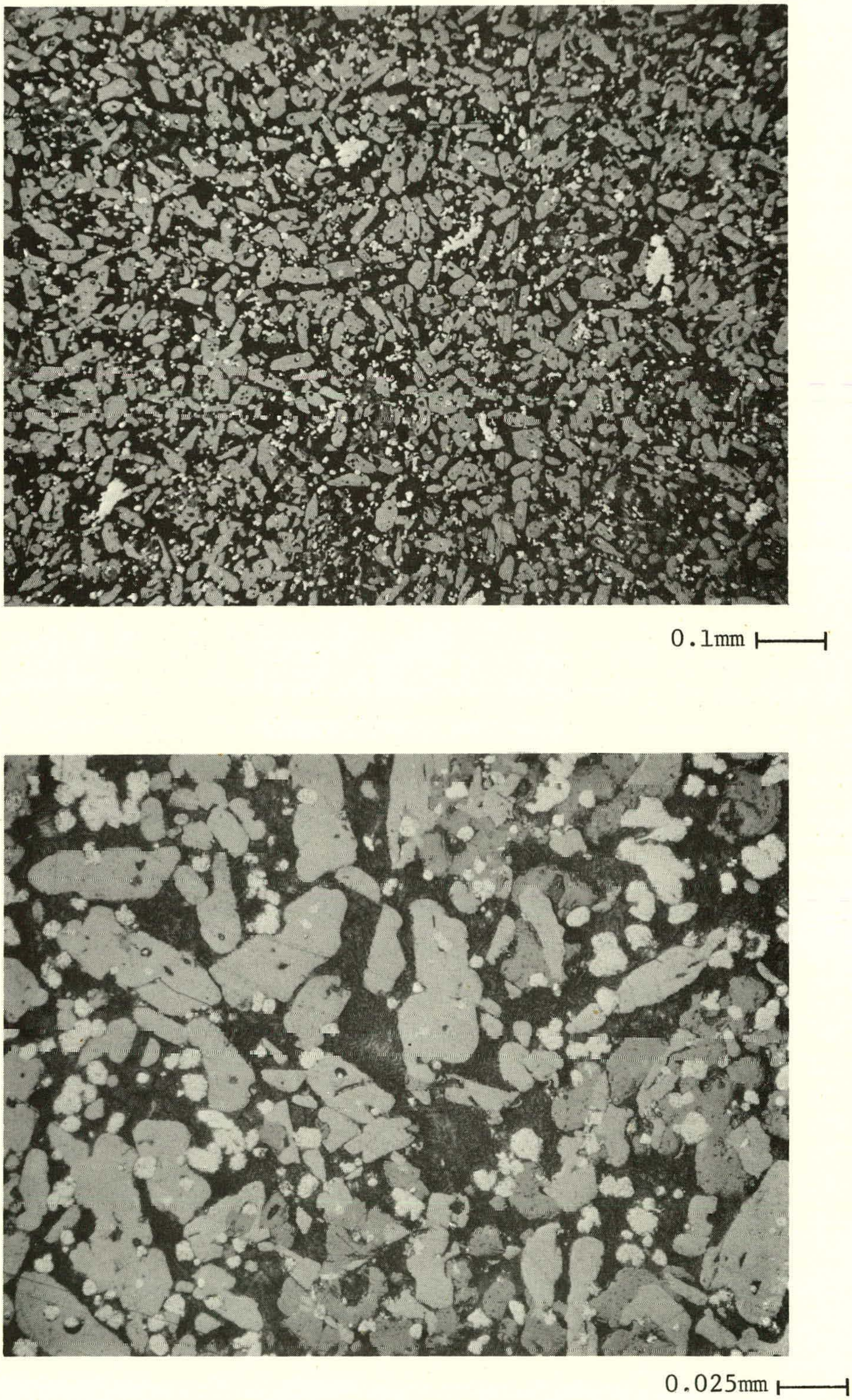

Fig. II-20. Photomicrographs of Positive Electrode from Cell E-1

a. Approach and Methodology

The first step of the study was the evaluation of the various active materials possible within the lithium alloy/metal sulfide system and the separator material alternatives. This analysis considered the basic materials' characteristics, compatability with other cell material, and commercial availability. Subsequently, a computer-aided analysis of cell design was conducted to identify and quantify the effects of design factors upon projected performance of cells. The computer program permitted evaluation of thirty cell design factors and gave projected performance, component weight breakdown, and certain dependent component dimensional characteristics. These efforts resulted in selection of the optimum design and materials for the Li/MS Mark II cell.

For the second phase of the study, material and component requirements were established for the fabrication of Li/MS batteries in pilot and manufacturing plants. Requests for cost quotations or cost estimates were made to suppliers and potential suppliers of components and materials. Fully developed manufacturing processes were assumed for these costs, and the following factors were taken into consideration: electrode manufacturing technique (by hot pressing, cold pressing, or extrusion of charged, half-charged, or discharged materials as applicable), cell assembly, electrolyte processing and cell-filling (flooded and starved conditions) operations, battery assembly, materials handling, quality control, and environmental control. Manufacturing processes and alternative processes were considered as individual manufacturing operations or functions. For each operation or function, estimates of capital equipment (amortized over 10 years), electrical power, floor space, labor and production rates were made. A total facility cost was then estimated based upon a representative combination of processes and functions and estimates for site, building, environment control equipment, and operating staff. By combining the manufacturing operations and functions with estimates of material and component costs, the manufacturing costs of electric-vehicle batteries were determined.

The conclusions derived from the study are to be considered the best estimates based on information available when the study was performed. The manufacturing costs estimated are believed to be conservative, and significant cost reduction should result from design optimization by a well-directed developmental program.

b. Results

The cell design analysis indicated that Li-Al is preferable to Li-Si as the negative electrode material, FeS is preferable to FeS_2 or other metal sulfides as the positive electrode material, and BN felt is the preferred separator (MgO as an alternative). Half-charged electrode fabrication was believed to be preferable to charged or uncharged fabrication. Development of a "starved electrolyte" cell was identified as an important advantage on the basis of reduced materials costs, simplified cell manufacturing, and increased specific energy. The computer-aided analysis of cell design indicated that the five most important factors with respect to gravimetric and volumetric specific energy are sulfide and lithium utilizations, positive and negative electrode porosities, and separator thickness.

An evaluation of cell or battery operating lifetime was not attempted as available data are insufficient to permit meaningful trade-off studies.

From the cell design study, a representative cell design was established, and materials and components costs for this cell when produced by a manufacturing plant were estimated. The basic materials cost (provided by potential suppliers) in mass-production quantities were estimated to be \$19.60/kW-hr for an uncharged cell, \$23.68 for a half-charged cell, and \$27.42/kW-hr for a charged cell. The major material costs were associated with LiAl and Li_2S. Carborundum Corp. provided cost projections for BN felt separator material of \$4 to 8/kW-hr in large quantities. For MgO powder separators, the materials costs projected were somewhat lower. It was also concluded that positive electrode additives could significantly affect costs; for example, the use of cobalt as a positive additive would cost about \$2.94/kW-hr. Information acquired concerning the costs for prefabricated metal cell components pointed to the need for much attention in this area. The total cost for metal components was projected to be \$38.50/kW-hr. Particle retainer screens were identified as a critical item, with a projected cost of \$15.17/kW-hr; this is partly due to the fact that one battery manufacturing plant would alone consume one-third to one-half the total output of the metal screen industry. It is believed that significant savings can be achieved in this area by simplifying the cell design.

The insulating case for high-temperature batteries is obviously an important component. Therefore, the Linde Division of Union Carbide Corp. made projections of the cost for such a case. Linde is a leader in the field of vacuum-foil insulated cases and has been contracted by DOE to develop a load-bearing insulation for high-temperature batteries. Their conclusions were that mass-produced vacuum-foil battery cases (non-load bearing) should have a cylindrical configuration and would cost about \$9/kW-hr in mass production. If a load-bearing insulation can be developed, a rectangular battery case would have the lowest cost, \$6/kW-hr in mass production.

The above costs for materials and components appear to be realistic, with the possibility of some improvement. The cost study indicated that price reductions in critical items (such as BN felt, Li_2S, LiAl) will not occur until large quantities are available from pilot manufacturing plants. Thus, materials costs during the cell development stage will be high. For example, a 60 kW-hr battery such as Mark II or III will require $\sim$4.5 ft^2 of separator material per kilowatt-hour; at \$30/ft^2 for BN felt (present cost), this amounts to \$8100 for the separator (\$135/kW-hr). These critical materials costs must be reduced so that statistically significant numbers of developmental cells and batteries can be tested in order to achieve the confidence required to invest in pilot facilities.

The fabrication and assembly costs for mass-manufactured batteries were projected to total \$6.44/kW-hr. The high-cost process was the electrolyte filling and electrode formation steps, projected at \$3.57/kW-hr. The estimated facility costs (buildings, equipment, and installation) were \$28.3 million and \$9.4 million, respectively, for pilot-plant facilities and manufacturing plants. The estimates for battery fabrication and assembly were based upon fully automated manufacturing processes in commercial dry-room environments. The various electrode manufacturing processes were also evaluated on the basis of compatibility with the materials to be used. Cold rolling and cold pressing were found to be viable for all negative-electrode materials, with cold pressing being the most economical at large scales. Cold-press sintering and hot pressing appear viable for all positive-electrode compositions. Cold rolling does not appear possible, and hot rolling does not appear practical. Hot extrusion of half-charged to full-charged positive materials appears viable if such processes can be developed. It was concluded that significant process development efforts will be required for each stage of electrode and cell fabrication.

From the above cost study, it was concluded that the projected cost for the Mark II battery will be $86 to $128 per kilowatt hour for pilot-plant facilities and $70 to $106 per kilowatt-hour for manufacturing plants.

It is anticipated that the Mark II battery may have commercial potential for limited markets such as buses or vans. Hence a study was conducted on the near-term market for electric vans. The performance requirements for such a vehicle battery were found to be a capacity of 60 to 65 kW-hr, a peak power of 70 to 80 kW, and a maximum continuous power of 30 to 40 kW.* At present, there is a market for about 20,000 electric vans per year, which could double in a very short time. Thus, electric vans are a potential market for the Mark II battery if an economically practical method of penetrating this relatively small market can be identified.

C. Rockwell International

(S. Sudar)

The Energy Systems Group of Rockwell International performed a variety of cell tests, conducted studies of ceramic separators, and carried out a system design study of an 100 MW-hr energy storage plant for load leveling.

1. Electric-Vehicle Cells

(R. C. Saunders, L. R. McCoy)

In electric-vehicle cells fabricated at Rockwell, the positive electrodes are 12 x 17 cm and have one of two basic structures--dual faced or split rib (see ANL-78-94, p. 67). The dual-faced structure consists of 100- or 200-mesh nickel screen that is diffusion-bonded to vertical ribs spaced 3 mm apart. The split-rib structure has a central-sheet current collector of copper laminated between nickel facing sheets (0.3-mm thick) to which vertical ribs are welded about 6 mm apart. Nickel screen is also diffusion-bonded to the rib edges to provide constraint. These structures are loaded with a dry powder mixture of Li_2S and iron powder to a density of 0.8 A-hr/cm^3. A cap plate of nickel is TIG welded in place after the electrodes are loaded with the active material. Copper overlayed with nickel sheet to protect it from corrosion was employed in some electrodes for added current conductivity.

---

*These values must be viewed with some caution since the electric van characteristics and manner of battery-to-vehicle integration have yet to be defined.

In previous cell tests, the corrosion resistance of the nickel sheet and nickel retainer screen used in the positive electrodes was found to vary greatly. Occasionally, severe attack was noted in some areas of the electrode, while other areas were virtually unaffected. This type of corrosion was also observed on the positive electrode of a cell heated to operating temperature, but not filled with electrolyte. This finding suggests that the attack on nickel was chemical rather than electrochemical in origin.

A small cell having a positive electrode (5 x 5 cm) with a current conductor of copper was operated, and post-test examination showed that the copper had been attacked rapidly in less than 40 cycles. A similar cell with a positive electrode of nickel-plated copper exhibited good coulombic efficiency for over 500 cycles, indicating that this coating may provide satisfactory protection for copper.

Fourteen electric-vehicle Li-Si/FeS bicells (REVC series) were built and/or operated within this period. The positive electrodes used in these cells are the same as those discussed above. The negative electrodes (12.7 x 17.8 cm), which were grounded to the case, had a Type-430 stainless steel honeycomb core which was diffusion-bonded to a current-conductor back plate. After loading with 40- to 80-mesh $FeSi_2$ (uncharged cell) or Li_2Si (partially charged cell), the electrodes were sealed by welding an 80-mesh screen to the honeycomb structure. Separators consisted of fine (<200 mesh) or coarse (-40, +80 mesh) AlN; ZrO_2 and/or Y_2O_3 ceramic cloths were sometimes used over the positive and negative electrodes, respectively, for particle retention. The electrolyte contained either 55 or 50 wt % LiCl and KCl.

These cells were cycled routinely at current densities of 30 mA/cm^2 on charge and 60 mA/cm^2 on discharge, with variations in the discharge current density from 30 to 90 mA/cm^2. The upper cut-off voltage was 1.7 V, and lower cut-off voltage was 1.0 V. The operating temperatures ranged from 450 to 500°C.

Performance data on the 14 cells tested are presented in Table II-12. The discharge capacities of these cells were found to be highly temperature dependent, with stable results being obtained only at a temperature in excess of 450°C. A significant improvement in positive electrode utilization was achieved at all temperatures when the 55 wt % LiCl electrolyte was used. The use of heavy copper current conductors (1B) or the presence of excess iron or nickel powder (12A and 2B) in the positive electrode offered little, if any, apparent benefit to cell performance. Cell resistances (t=0 sec) varied from 50 to 4 mΩ, with cells 10A and 2B exhibiting the highest values.

The poor performance of 2B, assembled with a sintered lithium silicate phosphate separator, was the most difficult to explain. Initially attributed to the relatively dense separator, the low utilization observed at a very low current density discharge (5 mA/cm^2) indicated that poor electrical contact with one negative electrode was the probable cause. The relatively high active-material depth of the positive electrode (0.48-cm half-thickness) is believed to have been the principal cause of poor positive utilization.

Table II-12. Performance Data on Cells Fabricated by Rockwell International

	Design Characteristics					Lifetime		
Cell No.	Pos. Elect.	Sep.	Electrolyte	Coulombic Eff.,[a] %	Pos. Utiliz.,[b] %	Cycles	Days	Comments
1A to 6A	Dual-face	Fine AlN	55 wt % LiCl	-	-	0	0	Four cells failed during startup; two cut up for inspection.
7A	Dual-Face	Fine AlN, Y_2O_3 cloth on neg.	55 wt % LiCl	89	-	28	10	Short circuit, tested at ANL.
8A	Dual-face	Coarse AlN, Y_2O_3 cloth on neg. and ZrO_2 on pos.	55 wt % LiCl	93(75)	40-55	281	164	Subjected to six thermal cycles without apparent effect.
9A-1	Dual-face	Coarse AlN, ZrO_2 over pos.	55 wt % LiCl	91(180)	40-50	255	121	Damaged by overcharge.
9A-2	Dual-face	Coarse AlN, ZrO_2 over pos.	50 wt % LiCl	95(187)	30-35	284	136	None.
9A-3[c]	Dual-face	Coarse AlN, ZrO_2 over pos.	50 wt % LiCl	98(92)	30-35	92	36	Voluntarily terminated.
10A[d]	Dual-face	Lithium silicate phosphate	55 wt % LiCl	90(52)	20-25	73	27	Failure in positive electrode.
11A	Dual-face	BN felt	55 wt % LiCl	-	-	-	-	Short circuit found in electrolyte.
12A	Dual-face	Coarse AlN, ZrO_2 on pos.	55 wt % LiCl	90(103)	50-55	149	45	Assembled partially charged. Nickel powder added to positive.
1B	Split-rib	Lithium silicate phosphate	55 wt % LiCl	98(91)	40-45	120	53	Assembled partially charged. Heavy central copper current collector. Short circuit in ZrO_2 cloth.
2B	Split-rib	Lithium silicate phosphate	55 wt % LiCl	98(118)	15-25	208	50	Assembled partially charged. Forty-three percent excess Fe added to positive. Voluntarily terminated.

[a] Numbers in parentheses are cycles at which coulombic efficiency began to decline at accelerated rate.

[b] Approximate range at 465-475°C.

[c] Tested at ANL and returned to Rockwell; data for Rockwell testing only.

[d] Rebuilt after initial failure; data shown for subsequent test only.

The use of partially-charged negative electrodes (*i.e.*, substitution of Li_2Si for $FeSi_2$) in Cells 12A, 1B, and 2B increased their average voltages from 1.22 to 1.34 V (60 mA/cm^2 discharge current density). Figure II-21 shows the voltage curves for one of these cells (12A) along with that for a cell assembled with uncharged negative electrodes (9A-1).

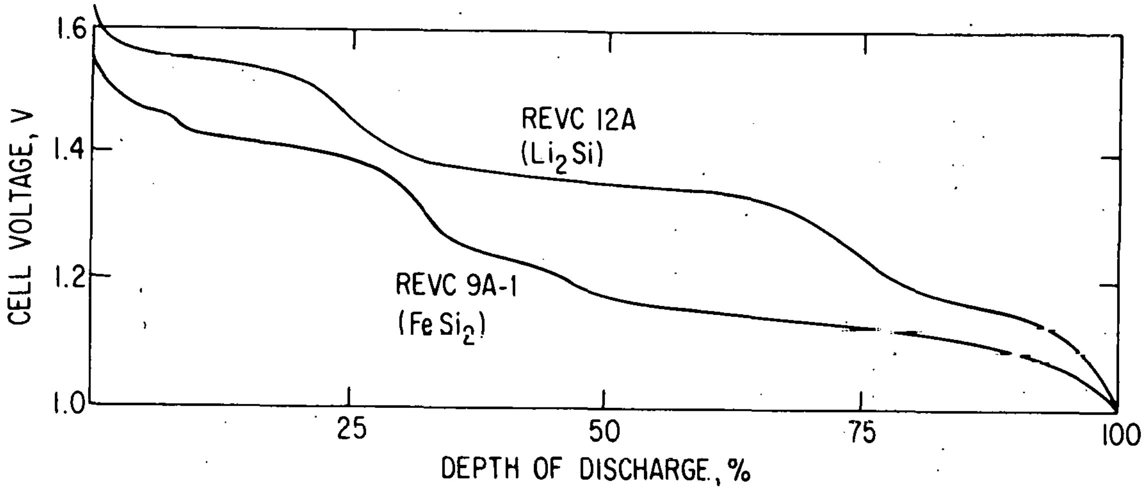

Fig. II-21. Voltage Curves for Two Rockwell Cells.

2. Ceramic Separator Development
(H. Lee, R. Saunders)

Work has continued on the development of separators containing Li_3PO_4 and Li_4SiO_4, which were first described by Hu, Raistrict, and Huggins as lithium ion-conductive.[1] The optimum resistance to attack and good ionic conductivity were found with compositions containing 25 to 30 mol % Li_3SiO_4 and the balance of Li_3PO_4 (ANL-78-94, pp. 70-71). Sintered plates were prepared using this composition range (2 mm thick, 45 to 50% porosity). Small cells (5 x 5 cm electrodes) using these separators sustained over 300 cycles without significant loss in coulombic efficiency.

In view of this early indication of stability in the cell environment, the decision was made to perform experiments to determine whether the ion-conductive properties of the lithium-silicate-phosphate material offered a practical reduction in cell resistance and/or an increased positive-electrode utilization. Therefore, powder separators of 70 mol % Li_3PO_4- 30 mol % Li_4SiO_4 were tested in Li-Al/FeS and Li-Si/FeS cells; cells with powder separators of MgO, which is not lithium-ion conductive, were used for comparison purposes. The test cells had the design shown in Fig. II-22. The positive electrodes were hot-pressed mixtures of electrolyte, FeS, Fe powder, and Li_2S loaded into a steel pan coated with 12 μm of electroless nickel; these electrodes were 54% charged in their initial state. The negative electrodes were LiAl or Li_xSi alloys in a corresponding state of charge and contained in a steel pan. The separator powders, which had mesh size ranges of -60 to +120, were either hot pressed or vibratorily loaded to form a 2-mm thick layer. The cells were charged at an ∿8-hr rate (30 mA/cm^2) and discharged at a 4.5-hr (60 mA/cm^2) or 5.5-hr (40 mA/cm^2) rate.

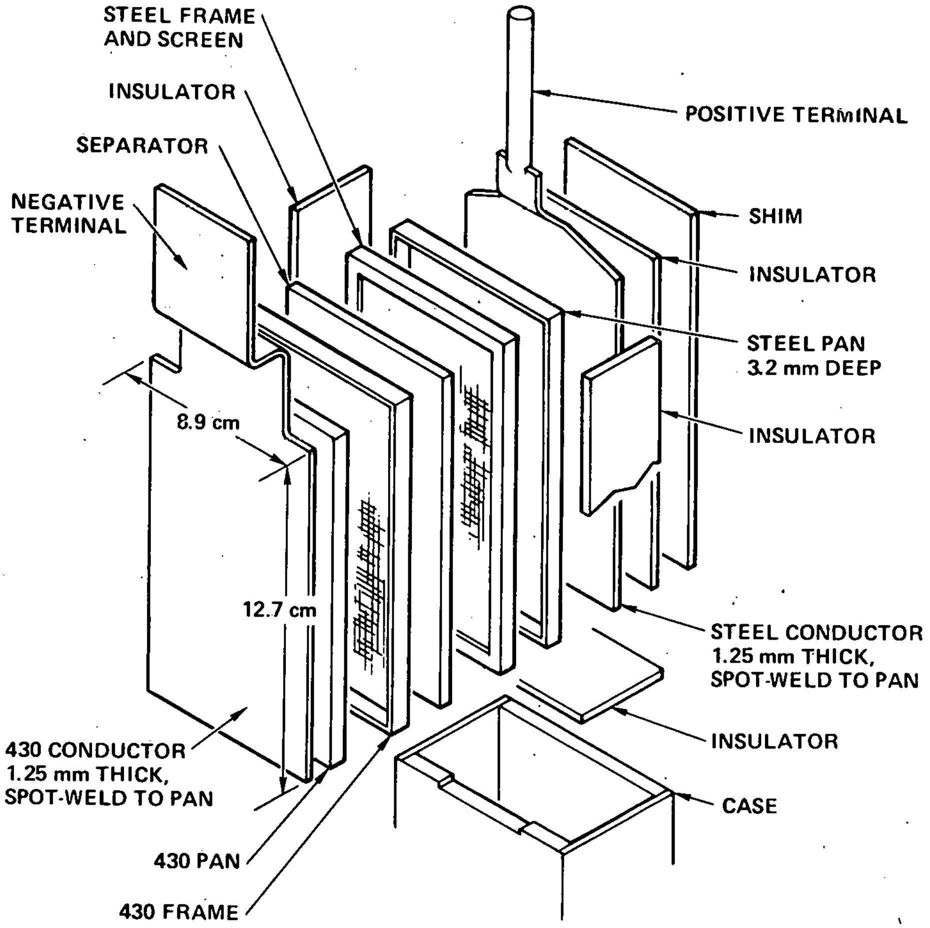

Fig. II-22. Separator Test Cell

Current interruptions were made, and the voltage changes at 0.2 sec and 15 min recorded. These were converted into resistances at various stages of discharge. The resistance at $t \cong 0$ is a fair measure of ohmic losses, while the measurement after 15 min includes much, but not all, of the polarization resistance. No significant reduction in either value was found when the lithium-silicate-phosphate separator was used rather than MgO powder. Typical data illustrating this statement are shown in Figs. II-23 and -24. In addition, no matter which separator material was used, the positive-electrode utilization was in the range of 60 to 65%. Any advantage to the lithium-silicate-phosphate material over MgO must therefore be sought in its lower cost for the required state of purity or in its lower density (2.37 *vs.* 3.58 g/cm^3).

The stability of BN felt toward Li-Si electrodes has been questioned in view of the attack observed on BN fibers in tests involving simultaneous contact with liquid lithium and molten electrolyte. To resolve this matter, a small Li-Si/FeS cell with a BN felt separator was tested. Despite an unpromising start (94% coulombic efficiency), the cell completed over 500 cycles, during which time the efficiency gradually improved and remained in in the range of 97 to 98%. The improvement may have been associated with improved wetting of the separator by electrolyte during cycling.

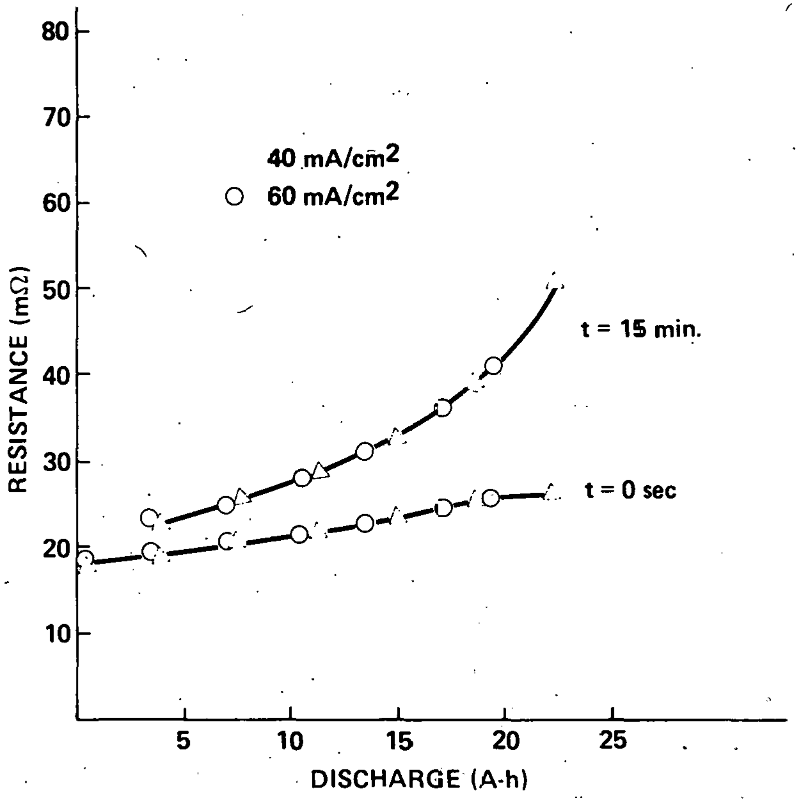

Fig. II-23. Resistance Curves for Test Cell (STC-III) with Lithium Silicate Phosphate Separator

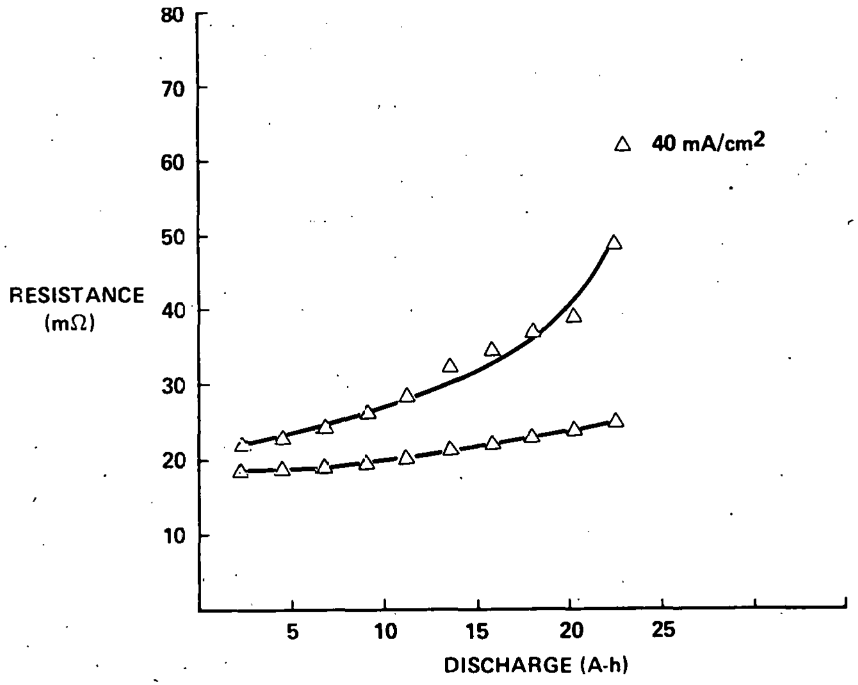

Fig. II-24. Resistance Curves for Test Cell (STC-VI) with MgO Powder Separator

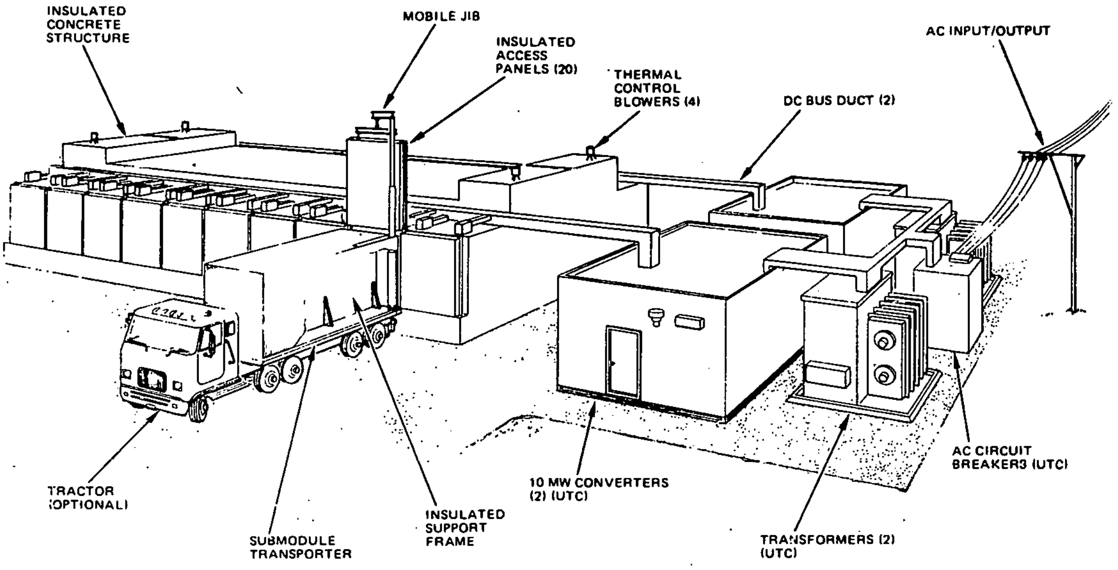

Fig. II- 25. Drawing of Proposed 100 MW-hr Plant

3. Design and Cost Study of 100 MW-hr Plant

(B. L. McFarland, W. R. Grieve)

In ANL-78-94, pp. 116-120, a conceptual design for a 100 MW-hr energy-storage plant having 2.5 kW-hr Li-Si/FeS or Li-Al/FeS cells was proposed. In developing this design, the use of state-of-art technology and conservative design practices was emphasized. However, a study of this design indicated a resultant cost of \$80/kW-hr (exclusive of cells and conversion equipment), which is well above the cost goal of \$20 kW-hr. A breakdown of the various costs for individual components showed that a significant cost reduction could be achieved by modifying the design for the plant. Therefore, both Rockwell and ANL, in separate efforts, made modifications in the reference design to reduce cost.

An overall view of the modified design by Rockwell is shown in Fig. II-25. Basically, the plant consists of twenty 5 MW-hr battery modules connected in parallel, two 10 MW converters, two transformers, and AC circuit breakers. These components are schematically represented in Fig. II-26. The cell chosen for this plant is a 2.5 kW-hr Li/MS multiplate cell with vertically oriented electrodes. As shown in Fig. II-27, twelve of these cells are stacked on top of one another, ceramic (Al_2O_3) insulating spacers being used at the cell corners. Two rows of seventeen cell stacks are connected in series and mounted in a metal support frame, as shown in Fig. II-28, to form a submodule. A submodule weighs a total of 16,150 kg (35,600 lb), is transportable by truck, and is loaded through a panel on the plant side (see Fig. II-25). Five of these submodules are connected in series to yield an operating voltage in the range of 2,040 to 3,264 V and housed in a thermally insulated enclosure to form a module. An open view of a module is shown in Fig. II-29. The twenty modules are contained within a structure consisting

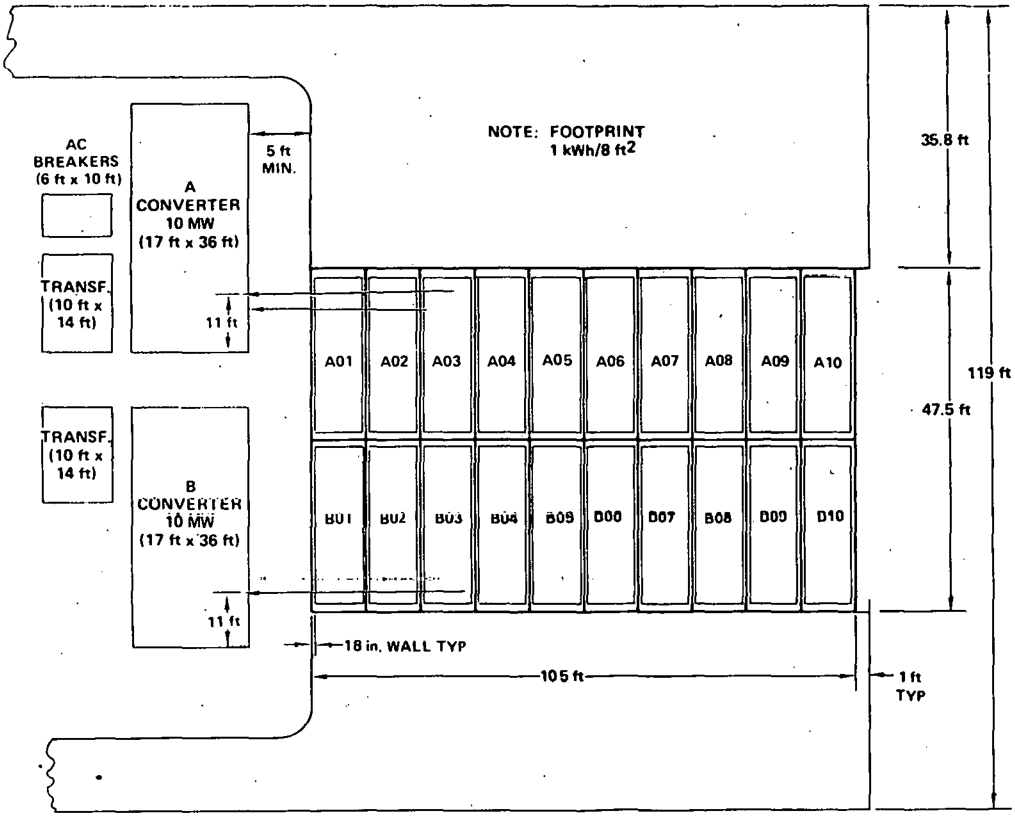

Fig. II-26. Arrangement of Modules and Other Equipment in 100 MW-hr Plant

of heat-resistant concrete and Portland cement. In the earlier design, the external plant structure was sheet metal, which added significantly to the plant cost. The modified plant design has a footprint of 74 kW-hr/m^2 (8 kW-hr/ft^2), not including the area covered by the power processing equipment.

Close vertical stacking of cells requires the development of a very compact, hermetically sealed feedthrough larger than that presently used for electric-vehicle cells. In addition, it has been proposed that the cell terminal in the stack be brazed directly to a socket at the cell bottom to eliminate the need for expensive inter-cell connectors.

In the plant, cell temperatures are maintained within 25°C of one another at all times by a direct air recirculation system that utilizes convective cooling. As the air circulates through the plant, the energy removed from the cells is dissipated through the insulation and the exterior walls to the environment. For this type of cooling system to be successful, the thermal losses through the exterior walls of the plant must be almost as great as the amount of energy emitted from the cells. The cooling air circulates through two main distribution ducts in the center of the plant and is introduced into bays at the base of submodules. Orifices in between each stack of cells, fifty-one per submodule, are used to maintain equal air flow between

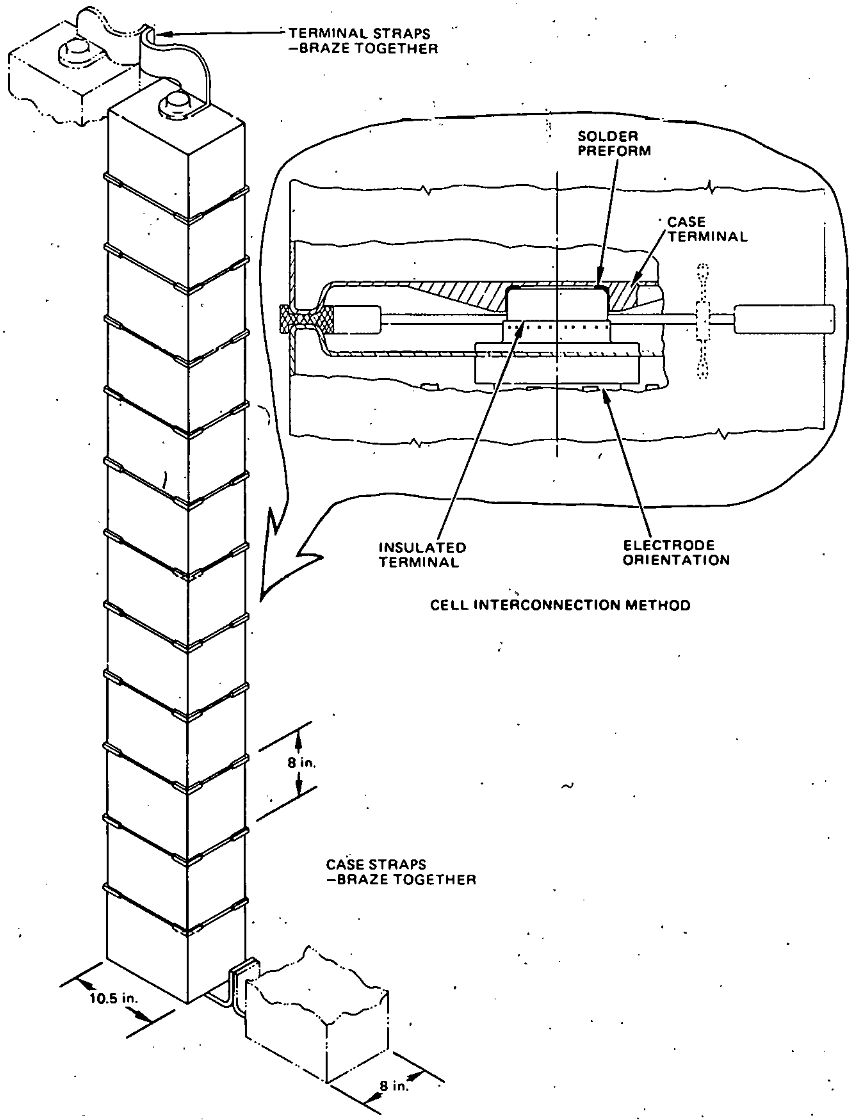

Fig. II-27. Cell Stack for 100 MW-hr Plant

each of the cell stacks to provide good convective heat transfer, and to minimize the differences in air temperature from bottom to top of the stacks. The cooling air is circulated using centrifugal fans of approximately 25 hp that service five bays each. Startup heating and heating during inactive periods are supplied by electrical heaters.

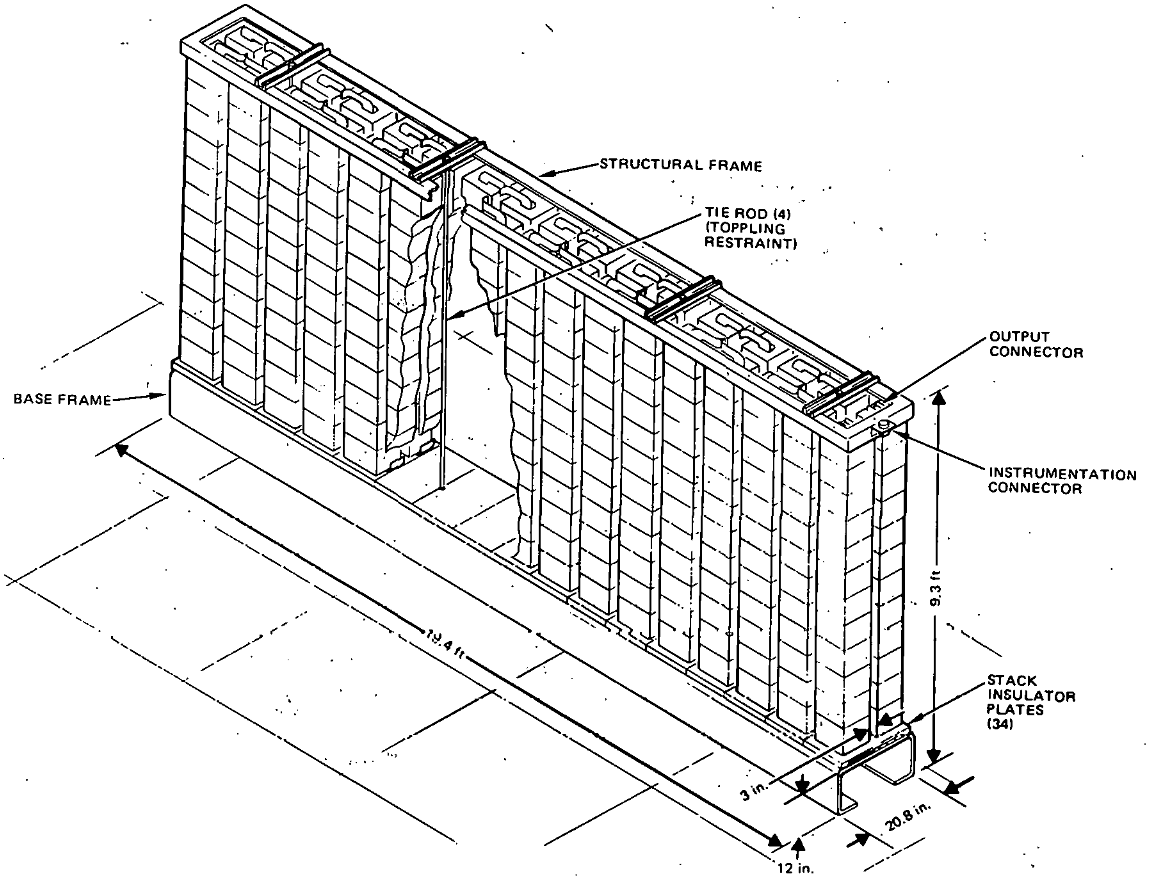

Fig. II-28. Submodule for 100 MW-hr Plant

In the Rockwell plant design, major cost reduction, suggested by S. Zivi of ANL, was brought about by including small shunt resistors across each cell to provide for charge equalization of the battery system. The need for equalization arises from the fact that small differences in the coulombic efficiencies of the cells will, after repeated cycling, result in the system capacity being limited by the cells with low coulombic efficiency on discharge and with high coulombic efficiency on charge. Computer simulations have indicated that shunt resistors of properly chosen sizes can achieve equalization at an acceptably small loss in overall system energy efficiency. This approach replaces the many leads and complex electronic circuitry proposed for equalization in the earlier design.

Computer studies have also been made to determine the voltage monitoring required to prevent overcharge or overdischarge. At present, it appears that fifty series-connected cells can be monitored adequately as a unit by measurements of current and voltage excursions upon completion of charge and discharge without requiring equipment of unusual precision. This finding indicates that a significant amount of the wiring used in the previous system design for voltage monitoring can be eliminated.

A preliminary estimate of the cost for this new design was found to be about \$28/kW-hr. Further studies are required to properly assess the reliability of the cells and other system components, to ensure that the long

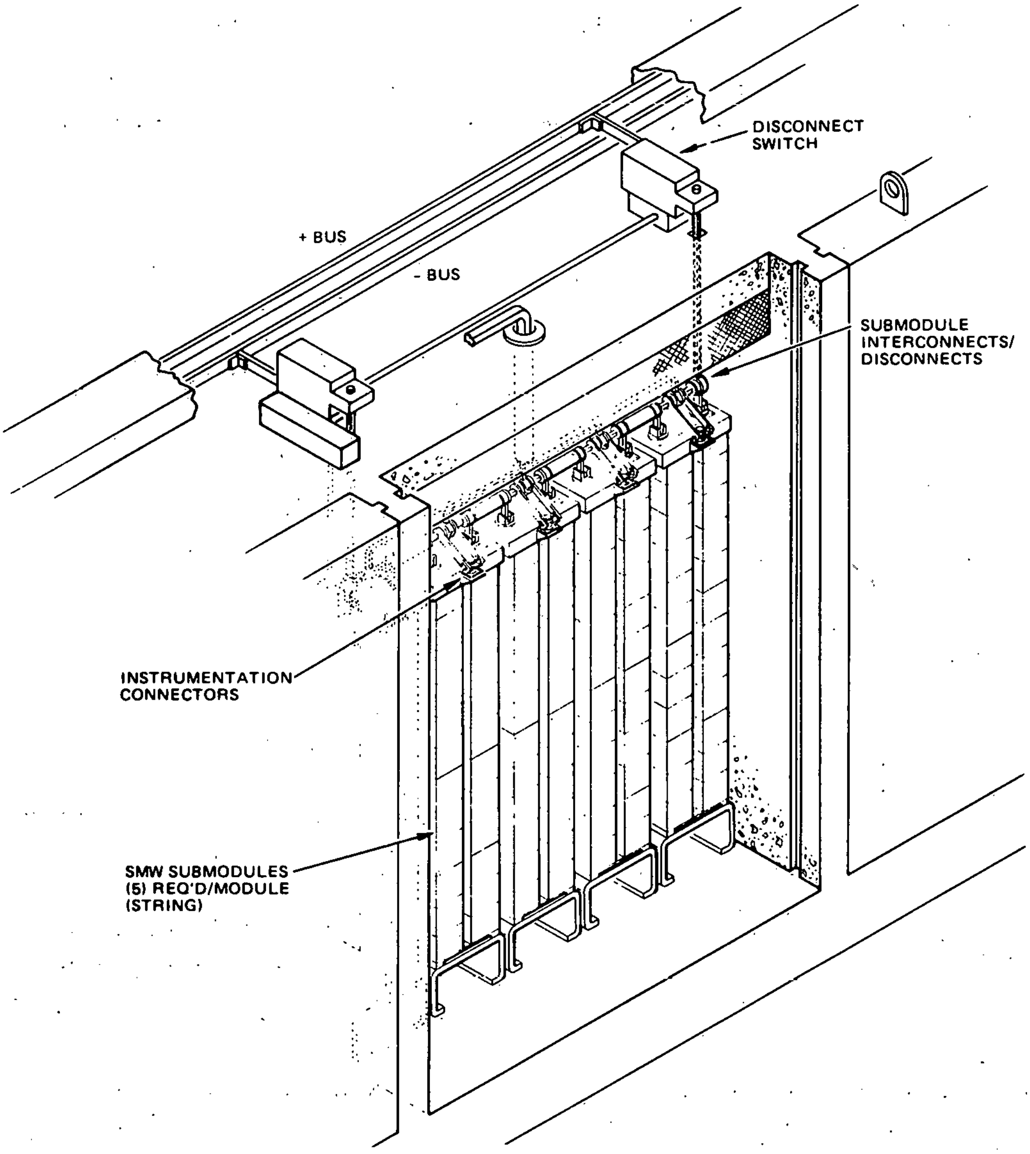

Fig. II-29. Open View of Module for 100 MW-hr Plant

lifetime goals for these large battery systems can be achieved, to minimize shut-down time, and to keep maintenance costs low.

D. General Motors Research Laboratory

(J. S. Dunning)

This program was designed to systematically determine the discharge behavior of the FeS_2 electrode in molten salt electrolytes as it is affected by construction variables such as electrode thickness, porosity, current collection, and electrolyte composition. The experimental results are useful in the development and verification of theoretical models of discharge behavior.

A typical discharge curve for the FeS_2 electrode exhibits two voltage plateaus (Fig. II-30). In general, the upper ($2Li + FeS_2 \rightarrow Li_2S \cdot FeS$) plateau is well behaved, yielding 80% to 90% utilization of the active material, while it is more difficult to utilize the lower ($2Li + Li_2S \cdot FeS \rightarrow 2Li_2S + Fe$) plateau.

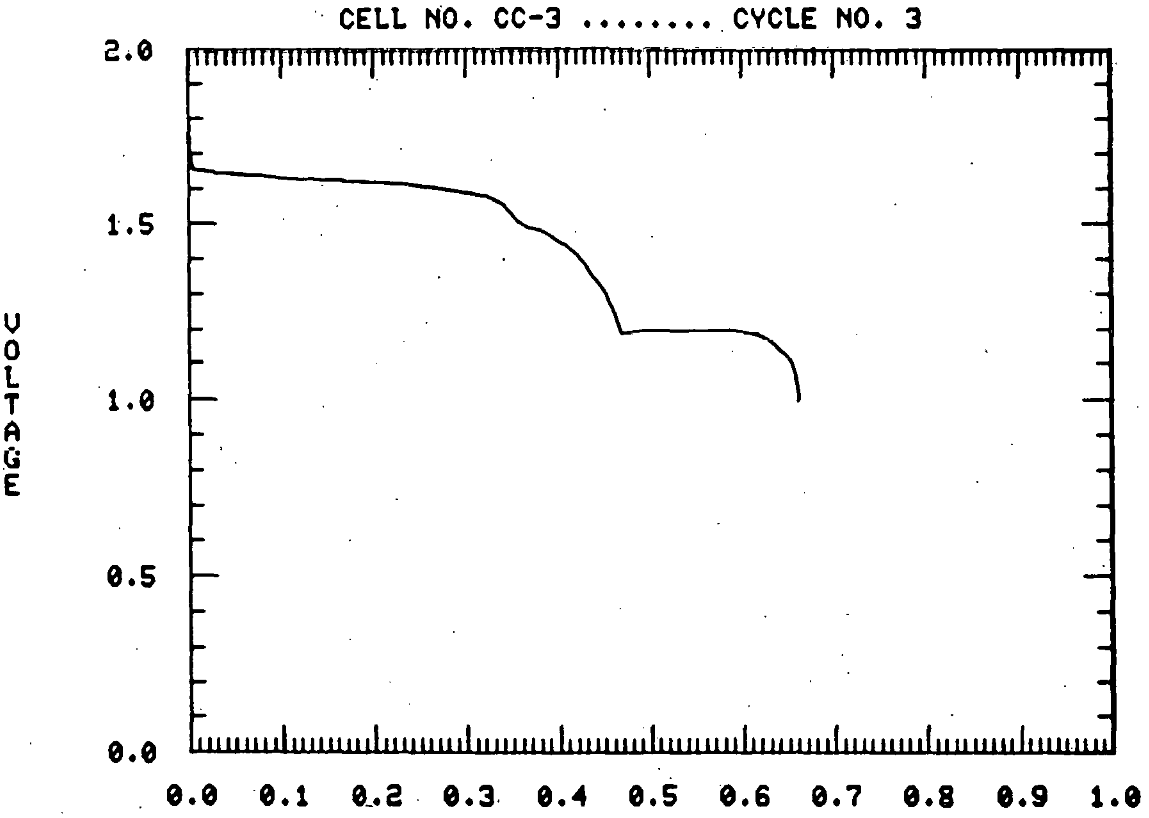

Fig. II-30. A Typical Discharge Curve for an FeS_2 Electrode in LiCl-KCl Eutectic Salt at 400°C (current density = 50 mA/cm^2)

Postive-electrode performance was characterized by observations of the voltage-time behavior of test cells. Small electrodes ($\sim$3 cm^2) of various thicknesses and porosities were prepared by hot-pressing mixtures of Fe, Li_2S, FeS_2, electrolyte and current collector at 27 MPa and 325°C in a graphite die. The resulting pellets were placed in the test assembly shown in Fig. II-31. A schematic diagram of the test cell is shown in Fig. II-32. Tests were performed at constant current during discharge. A current-limited (100 mA/cm^2), constant-voltage (2.0 V) charge was used. Potentials were measured with respect to a Li-Al alloy reference electrode, and the influences of current density and operating temperatures were determined.

Electrode Thickness. These tests were conducted in LiCl-KCl eutectic electrolyte using positive electrodes ranging in thickness from 2 to 5 mm. The electrodes had a theoretical porosity of 30 vol % when fully discharged and contained no added current collector. The testing was carried out at current densities of 50, 100, and 200 mA/cm^2. In addition, cycling was carried out at both 400°C and 450°C.

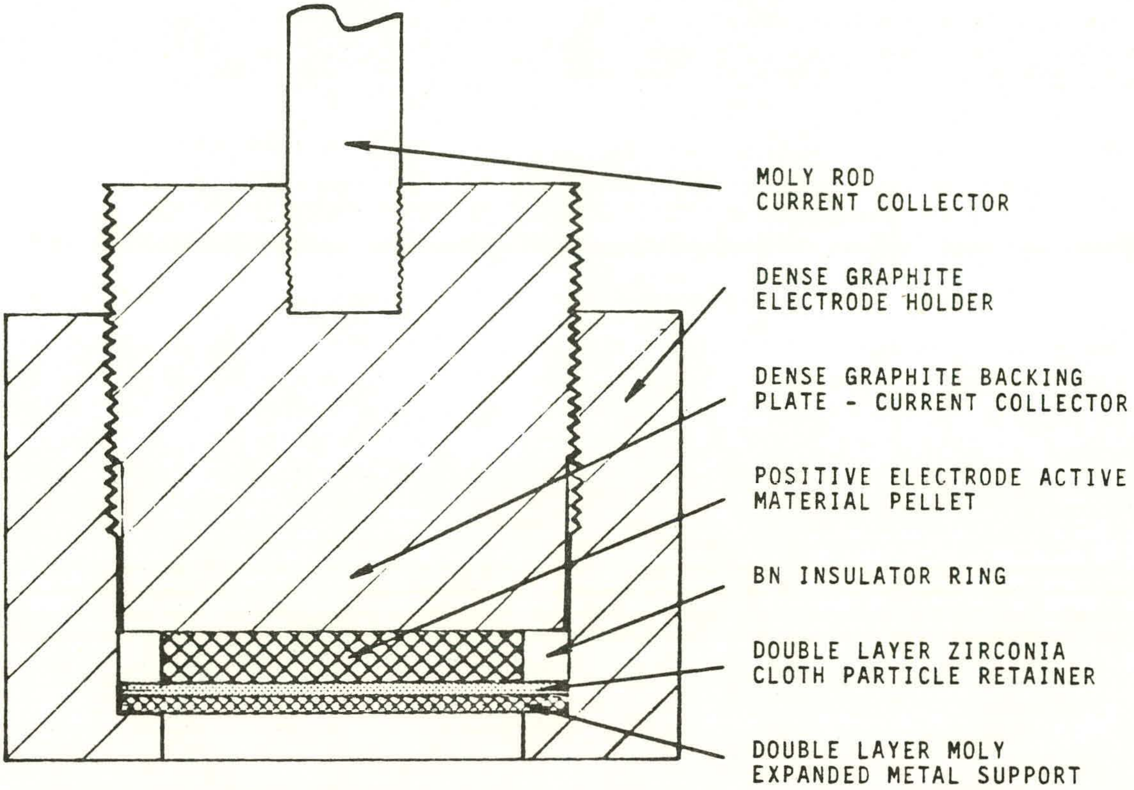

Fig. II-31. Schematic Diagram of the Positive Electrode Assembly

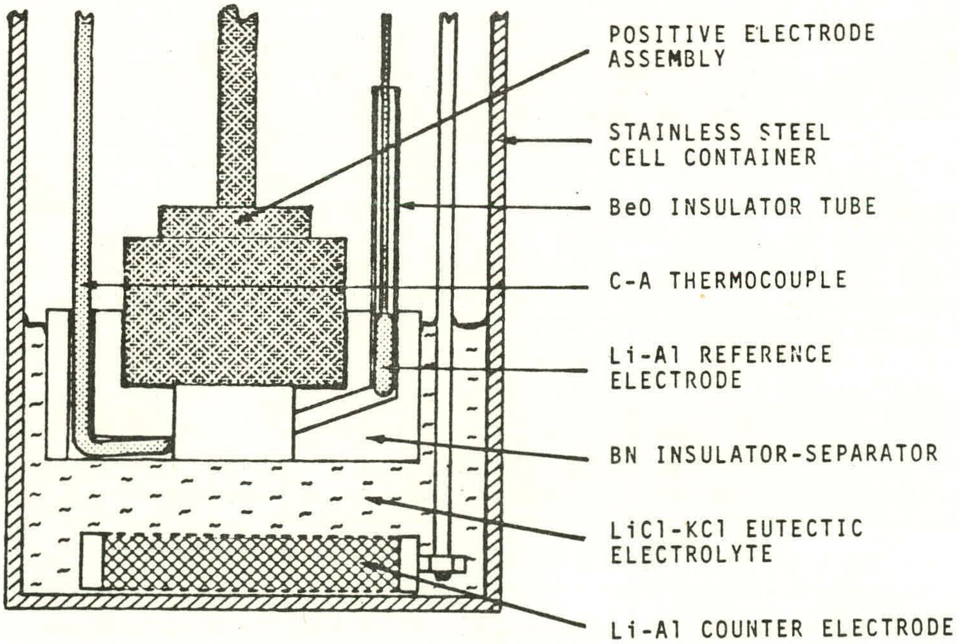

Fig. II-32. Schematic Diagram of the Positive-Electrode Test Cell

The data indicated that electrodes thinner than those tested at 400°C would have higher specific energies, and that a specific energy maximum lies within the thickness range of 2.5 to 3.5 mm for electrodes tested at 450°C.

Electrode Porosity. These tests were conducted in LiCl-KCl eutectic electrolyte using positive electrodes having theoretical porosities of 30 and 50 vol % when fully discharged. The electrodes were both 3-mm thick, had no added current collector, and were examined under the same test regime mentioned above.

The data indicate that raising the electrode porosity from 30 to 50 vol % increases the utilization of both the upper and lower voltage plateaus. With the higher porosity electrodes, the capacity and specific energy increased marginally on the lower plateau, but decreased significantly on the upper plateau, presumably as a result of the decrease in theoretical capacity and energy available.

Current Collection. The conductive diluent was Vulcan carbon XC72R. This highly conductive graphite powder was tested in concentrations ranging between 1.9 and 5.8 vol % of the electrode. These tests were also conducted in LiCl-KCl eutectic electrolyte using five positive electrodes which were 3 mm thick. The theoretical porosity was 50 vol % when fully discharged, and the electrodes were examined under the same test regime mentioned above.

Initially, the behavior of these electrodes at 400°C was similar to that observed in earlier studies: high utilization of the upper plateau but severe truncation of the lower plateau, especially at high current densities. However, a striking improvement in the utilization of the lower plateau was obtained upon testing these electrodes at 450°C. In the optimum case (3.8 vol % current collector), the electrode delivered 90% utilization at a current density of 70 mA/cm^2, and maintained over 85% utilization at 200 mA/cm^2. When the temperature was returned to 400°C, the lower plateau retained good utilization (>80%) at high current densities. During cycling, the upper plateau had a loss in capacity, but was still showing >75% utilization at 200 mA/cm^2.

All five of the electrodes tested responded similarly to thermal cycling and changes in current density. The data indicated that a maximum in electrode performance can be obtained with very little addition of this current collector. Performance peaked when 3 to 4 vol % of current collector was incorporated into the electrode.

Electrolyte Composition. Three different electrolyte compositions were studied: the familiar eutectic composition (58 mol % LiCl-42 mol % KCl), a KCl-rich mixture (53 mol % LiCl-47 mol % KCl), and a LiCl-rich mixture (68 mol % LiCl-32 mol % KCl). All of the electrodes were 3-mm thick and had 3.8 vol % of added current collection. Two porosities were tested--30 and 50 vol % of theoretical at full discharge. The testing of these electrodes followed essentially the same test regime mentioned above. Because of the higher liquidus temperature of the salt in the cells using noneutectic electrolytes (425°C), cycling was initiated at 450°C in these cells.

The effects of electrolyte composition on the capacity density and the electrode specific energy for the 30 vol % porosity electrodes are shown in Figs. II-33 and -34, respectively. The data indicate that the performance of the upper plateau is not a strong function of electrolyte composition; however, this plateau was found to lose capacity with cycling in all three of the electrolytes studied. It was further observed that the rate of capacity loss from this plateau is related to the LiCl concentration of the salt, a higher LiCl concentration resulting in a higher loss rate. The data in these two figures also indicate that the performance of the lower plateau is very dependent on electrolyte composition. In KCl-rich salt, less than 5% utilization of this plateau is achieved, even at very low current densities (25 mA/cm^2). In the eutectic salt, the plateau is severely truncated, especially at higher current densities as only 35% utilization is obtained at 90 mA/cm^2 (4-hr rate). However, in the LiCl-rich salt, utilization of 85% of theoretical capacity can be obtained at 90 mA/cm^2 and 65% utilization at 180 mA/cm^2 (2-hr rate).

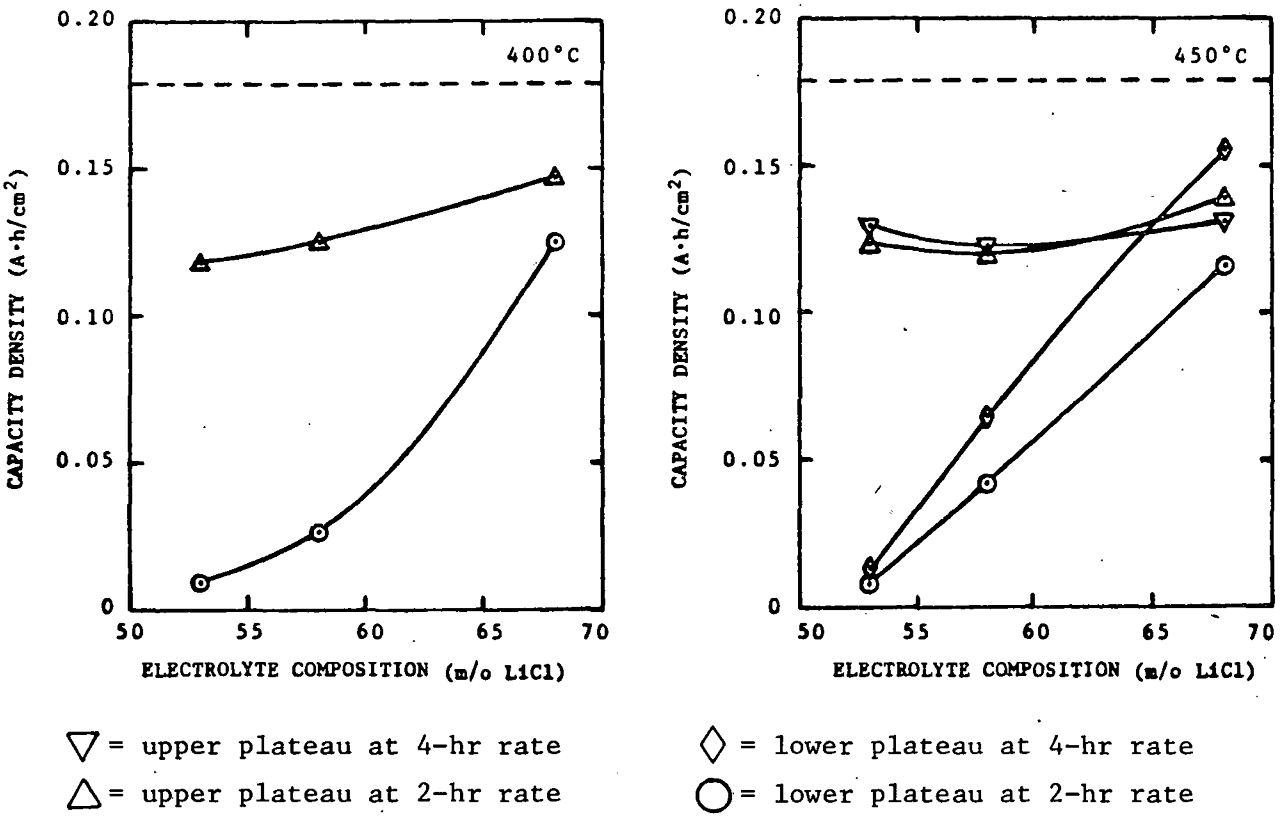

Fig. II-33. Capacity Density *vs.* Electrolyte Composition for FeS_2 Electrode

Similar results were observed for the 50 vol % porosity electrodes. Temperature was not found to affect the performance of these electrodes in noneutectic salts. Even when operating in the slush region at 400°C, the relationships between electrolyte composition and performance persisted.

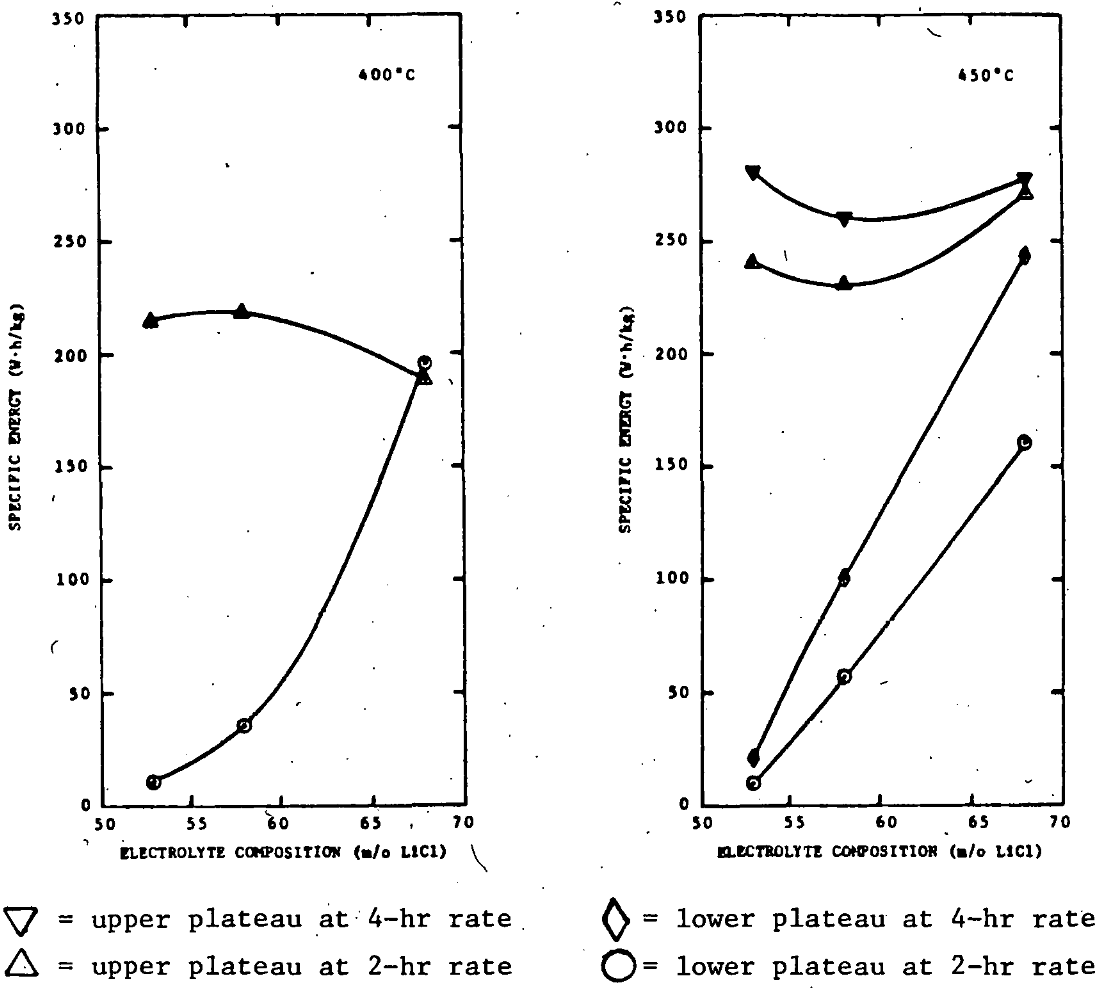

Fig. II-34. Specific Energy *vs.* Electrolyte Composition for FeS_2 Electrodes

E. Institute of Gas Technology (IGT)

Low-cost positive current collectors for the $LiAl/FeS_2$ cells continue to be an obstacle in their development. In this area, IGT is exploring methods of boronizing low-carbon steel structures. It may be possible to form a protective coating of iron boride that could be made self-healing by the addition of a boronizing agent to the active material in the positive electrode.

A simple pack boronization technique using B_4C, KBF_4, and graphite produced FeB and FeB_2 coatings on AISI 1008 or 1018 steel structures. After a few hours of boronizing, coatings with thicknesses of 0.10 to 0.30 mm were obtained; the coating was found to have a dentate structure. A boronized steel sample exhibited corrosion protection in LiCl-KCl eutectic solutions at 425°C up to potentials of 2.13 V *vs.* liquid lithium. Initial experiments on boronized steel samples in Li_2S-saturated LiCl-KCl eutectic also showed adequate corrosion protection, although further work is required for more conclusive results.

The ability of iron borides and elemental boron to incorporate into steel substrates was examined. Ion-microprobe results showed that appreciable boron had incorporated into steel when exposed to iron-borides, but not when exposed to elemental boron. This suggests that iron-boron alloy (elemental iron plus iron borides) in the positive active material has the potential of *in-situ* boronizing of exposed current collector substrate.

REFERENCE

1. Y-W. Hu, I. D. Raistrict, and R. A. Huggins, *Ionic Conductivity of Lithium Orthosilicate-Lithium Phosphate Solid Solutions*, J. Electrochem. Soc. *124*, 1240 (August 1977).

III. CELL AND BATTERY TESTING
(E. C. Gay)

At ANL, cells are being fabricated and tested; these cells have designs that are expected to reduce cost and/or improve performance. Contractor-fabricated cells and batteries are also tested at ANL. These tests are described below.

A. Testing of ANL Cells
(H. Shimotake, F. J. Martino, L. G. Bartholme, G. L. Chapman, J. Thomas)

Over the past year, ANL fabricated and tested 57 engineering-scale cells. A summary of the performance obtained by these cells is given in Appendix B. For most of the cells, the electrodes are pressed mixtures of active materials (charged, uncharged, or semi-charged) and electrolyte, the separators are BN felt, and the electrolyte is LiCl-KCl (eutectic and LiCl rich). These cells have designs or materials that are expected to improve cycle life and performance or to lower the cell cost. When advances in cell technology are demonstrated, they are incorporated into the contractor cells.

1. Negative-to-Positive Capacity Ratio

In the past, Li-Al/FeS bicells fabricated by ANL have generally shown stable capacity during cycling. The negative-to-positive (Li/S) capacity ratio for these cells was usually about 1.3; the excess capacity in the negative electrode was believed to serve as a reservoir to offset losses during cycling. During this period, the capacity stability of a bicell with a Li/S capacity ratio of 1.4* (Cell M-8) was compared with that of a similar bicell with a capacity ratio of 1.0† (Cell M-8-NP). Both of these cells had LiCl-rich electrolyte, pressed electrodes, and BN felt separators. Cell M-8 was operated for 347 cycles and Cell M-8-NP for 184 cycles, and the capacity decline rates were 0.02% and 0.07% per cycle, respectively. Thus, the excess lithium capacity in Cell M-8 appears to have improved the capacity stability. Power-pulse tests were made on both cells during cycling and the power densities were found to be similar (0.45 and 0.32 W/cm^2 at 3% and 50% depth of discharge, respectively). Plans have been made to repeat these tests with more cells.

2. Positive-Electrode Capacity Density

In past tests (ANL-78-94, p. 130), high initial capacity densities‡ (1.4 to 1.6 A-hr/cm^3) in the positive electrode were found to improve the specific energies of Li-Al/FeS bicells, especially at current densities above 74 mA/cm^2. This improved specific energy occurred in cells with Cu_2S added to the positive electrode and eutectic electrolyte as well as cells with no additives and LiCl-rich electrolyte. The high capacity densities in these cells had little or no effect on the power output. However, post-test examination of cells with the Cu_2S additive showed that short circuits were

---

*Negative electrode, 155 A-hr; positive electrode, 113 A-hr.

†Negative and positive electrodes, 120 A-hr.

‡The theoretical capacity divided by the electrode volume.

sometimes caused by migration of the copper from the positive electrode. Consequently, further efforts were concentrated on improving the specific energy of high capacity-density cells with LiCl-rich electrolyte.

In a series of five Li-Al/FeS bicells (assembled in charged state) with LiCl-rich electrolyte, the capacity density of the positive electrode at cell assembly was varied from 1.0 to 1.6 A-hr/cm^3; these cells had pressed electrodes and BN felt separators. Table III-1 shows the initial capacity density and performance for the five cells, and Fig. III-1 shows their

Table III-1. Performance of Charged Cells of Various Capacity Densities

	M-15	M-13	SM8F08	M-14	M-11
Pos. Elect. Capacity Density, A-hr/cm^3	1.0	1.2	1.4	1.5	1.6
Specific Energy,[a] W-hr/kg	60	63	72	63	55
Specific Power, W-kg					
3% depth discharge	96	100	103	102	102
50% depth discharge	73	71	73	74	71
Cycle Life	57	27	>154	28	365

[a] Measured at current density of 75 mA/cm^2.

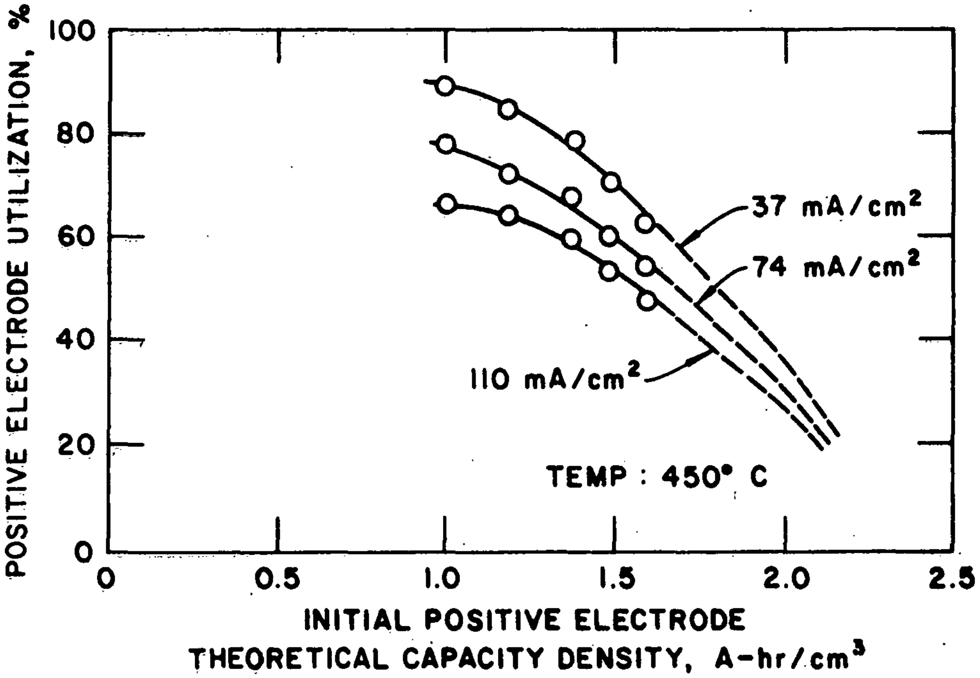

Fig. III-1. Utilization of Positive Electrode Versus Capacity Density utilizations at discharge current densities of 37, 74 and 110 mA/cm^2. As can be seen in this figure, the utilization of the positive electrode was strongly dependent on the capacity density; at each current density measured, the utilization decreased as the positive capacity density was increased. Thus, more active material (or less electrolyte volume) in a given electrode volume decreased the utilization. In each cell tested, the utilization also decreased as the current density was increased, the decline in utilization as a function of discharge current density being less in cells with higher capacity densities. As can be deduced from Table III-1, the highest specific energy was achieved by the cell with a positive capacity density of 1.4 A-hr/cm^3 (SM8F08); higher or lower capacity densities resulted in significantly lower energies. The power output per unit area for the cells increased by almost 30% as the capacity density was increased from 1.0 to 1.6 A-hr/cm^3 (*e.g.*, from 0.40 to 0.53 W/cm^2 at 3% depth of discharge). However, as shown in the table, the specific power (W/kg) was not significantly affected by the capacity, increasing from 96 to 102 W/kg at 3% depth of discharge (a 6% improvement).

3. Design or Material Modifications

Five R-series Li-Al/FeS bicells (pressed electrodes; BN felt separators) were built to test various changes in cell design and materials that were expected to result in improved performance or lower cost.

Cells R-47 and -48 had similar designs except for the material used in the current collectors--nickel and iron, respectively; both cells had 66.7 mol % LiCl-33.3 mol % KCl electrolyte. To date, Cells R-47 and -48 have been operated for more than 400 cycles and achieved about the same performance: a cell resistance of 3.8 mΩ at full charge and an active-material utilization of 60% at a current density of 72 mA/cm^2. Neither cell has lost more than 5% of its initial capacity or coulombic efficiency. Previous in-cell corrosion tests (ANL-78-94, p. 164 and ANL-79-39, p. 86) had indicated that the nickel current collector should outlast the iron one; however, these test results indicate similar electrode compatibility for both current collector materials. Two explanations of this finding have been proposed: (1) a conductive, passive film formed over the metal structure, and (2), even though the metal surface had corroded, the structure provided suitable current collection. After operation of these two cells is terminated, post-test examinations will be conducted to determine the physical state of the current collectors.

The third R-series cell tested, R-53, had a positive current collector fabricated from an iron-based alloy (Fe-5 wt % Mo) developed at ANL (see Section VI.C). This cell has been operated for 245 cycles and shown similar positive utilization and capacity retention to those of the above two cells. However, the resistance of Cell R-53, 4.4 mΩ at full charge, was slightly higher than that of the other two cells. This higher resistance is believed to be due, in part, to the higher specific resistivity at 450°C of the ANL alloy, which is 64 μΩ-cm (as compared with 52 μΩ-cm for low-carbon steel).

Cell optimization studies at ANL (reported in Section V.C) indicated that an electrolyte of 9.1 mol % LiF-62.7 mol % LiCl-28.2 mol % KCl (liquidus, 397°C) might be an acceptable alternative to LiCl-rich electrolyte (liquidus, ∿425°C). Therefore, Cell R-54 was built similar in design and materials to

Cell R-48 but with the LiF-LiCl-KCl electrolyte. So far, Cell R-54 has been operated for 41 cycles at 430°C and shown acceptable performance; testing of this cell is continuing. Other cell optimization studies (Section V.C) indicated that the addition of TiS_2 (10 wt %) to the FeS positive electrode should result in lower cell resistances. Thus, Cell R-55 was built with a design and materials similar to those of R-48 but with this positive-electrode additive. This cell has been operated for 16 cycles and has achieved a lower resistance than that of Cell R-48 (2.5 *vs.* 3.8 mΩ at 10% depth of discharge).

4. Alternative Separator Materials

Earlier work (ANL-77-75, p. 35; ANL-78-21, p. 134) had indicated that MgO powder is a possible low-cost alternative to BN felt as the electrode separator. During the past year, eight cells (PW-9, -12, -13, -17, -18, -19, -20, and -25) were tested with 50% porosity separators of MgO powder obtained from Cerac/Pure, Inc. These cells maintained high coulombic efficiencies for up to 700 cycles of operation; however, the relatively low porosity of the MgO powder restricted ionic transport, thereby resulting in high cell resistances (∿5 to 10 mΩ).

Recently, an MgO powder from Iwatani Co. (Type MJ-30) was obtained. From this powder, described more fully in Section VI.B, a separator could be formed with a porosity of 88%. This material was tested in Cell PW-24, which showed a resistance of 2.8 mΩ at full charge (similar to that obtained in cells with BN felt separators). However, operation of this cell was terminated after only 10 cycles due to short circuits caused by extrusion of the separator material. Future tests of this MgO are planned in cells designed to prevent separator extrusion.

5. Multiplate Cells

The goals for the Mark II battery require that it use materials with the potential for low cost in mass production. Consequently, two multiplate Li-Al/FeS cells with BN felt separator (BN fabric was used in Mark IA cells) were tested. These two cells, K-MP-1 and M-MP-3, had three positive electrodes (1.4 A-hr/cm^3) and four negative electrodes and separators of 2-mm thick BN felt. All of the electrodes for these two cells were formed by cold pressing except for the positive electrodes of K-MP-1, which were carbon-bonded.*

Table III-2 summarizes the performance of Cell K-MP-1 along with that of a similar bicell. As shown, the performance of Cell K-MP-1 was somewhat better than that of KK-15. However, Cell K-MP-1 developed short circuits in the feedthrough, and operation was terminated after 42 cycles.

As shown in Fig. III-2, Cell M-MP-3 operated for over 200 cycles with stable capacity (3% decline from peak). The performance of this multiplate cell and that of a similar bicell (M-8) are shown in Table III-3. Cell M-MP-3 showed significantly better performance than that of the bicell.

---

*This structure is formed by the pyrolysis (450-550°C) of a paste-like mixture of active material, a voltatile pore-forming agent (ammonium carbonate) a binder (furan resin), and a carbonaceous filler.

Table III-2. Performance of Cells K-MP-1 and KK-15

	K-MP-1	KK-15
Specific Energy,[a] W-hr/kg	79	70
Cell Resistance,[b] mΩ	1.1	2.9
Specific Power,[b] W/kg	101	80
Cycle Life	42	245

[a] Measured at a discharge current density of 75 mA/cm^2.

[b] Measured at 50% depth of discharge.

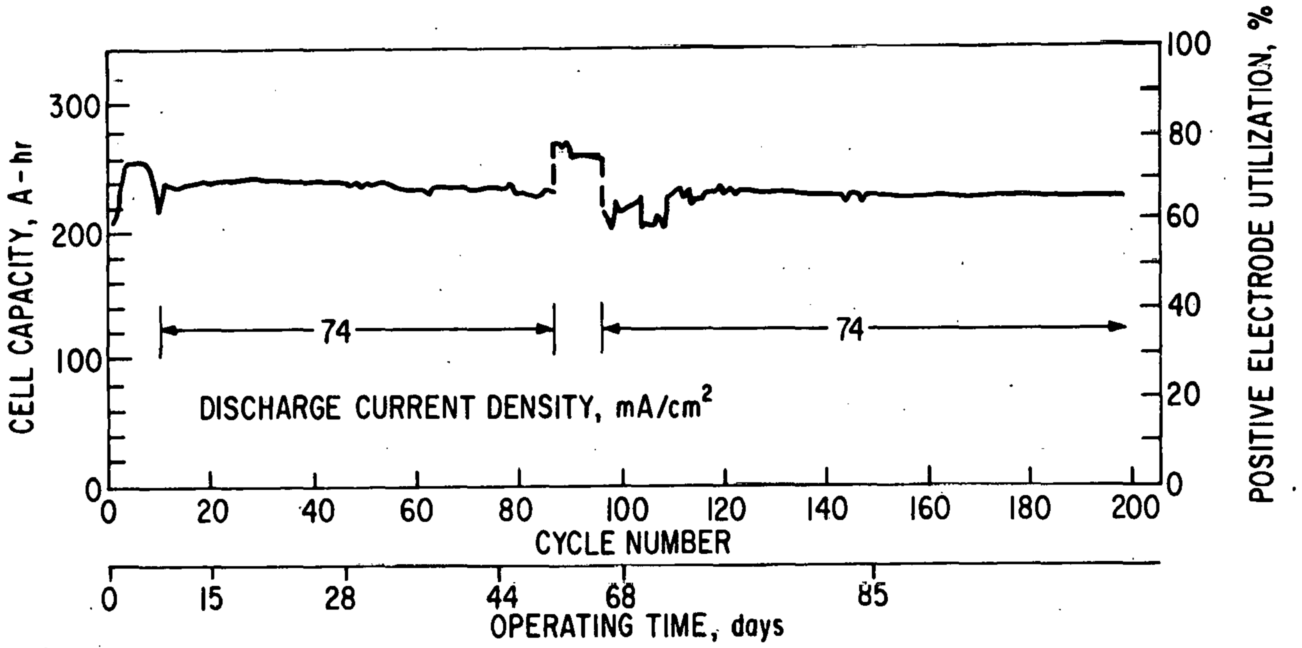

Fig. III-2. Capacity during Cycling of Cell M-MP-3

B. Testing of Gould Cells at ANL

(T. D. Kaun, W. E. Miller, P. F. Eshman, J. D. Arntzen, and W. A. Kremsner)

Over the past year, Gould fabricated about 25 cells for testing at ANL.[*] The first ten of the cells were Li-Al/FeS bicells (theoretical capacity, 165 to 175 A-hr) fabricated in the uncharged state (Gould's X-series cells). The ten cells had BN felt separators and various conductive powder additives to the positive electrode such as iron, molybdenum, carbon, cobalt, etc. Most of these cells had very short lifetimes; short circuits in the electrical feedthroughs and internal hardware problems were responsible for cell failure. Cell X-45 was the longest operating of these cells (113 cycles in 52 days). Subsequent Gould cells were fabricated in the half-charged state and some of the internal hardware was redesigned. These changes resulted in improved performance and lifetimes in the Gould Li-Al/FeS bicells.

---

[*] See Appendix C for cell performance data on contractor cells tested at ANL.

Table III-3. Performances of Cells M-8 and M-MP-3

	M-8	M-MP-3
Electrode Area, cm^2	270	780
Cell Weight, kg	1.5	4.0
Cell Volume, L	0.52	1.52
Pos. Elect. Util., %		
37 mA/cm^2	73	76
74 mA/cm^2	66	69
110 mA/cm^2	62	63
Specific Energy, W-hr/kg		
8-hr rate	71	81
4-hr rate	59	69
2-hr rate	56	60
Cell Resist.,[a] mΩ	4.1	1.14
Specific Power, W/kg		
3% discharge	83	106
50% discharge	62	87
Cycle Life	347	200

[a] Measured at 50% depth of discharge.

One of the X-series cells delivered to ANL had a multiplate (two positive and three negative electrodes) design. Although the lifetime of this cell was short (25 cycles), the performance was excellent--a specific energy of 95 W-hr/kg at the 4-hr rate and a specific power of 85 W/kg at 50% state of charge.

In a series of ten identical Li-Al/FeS bicells (Q-series), the BN felt separator was held in place by a retainer-screen basket which facilitates cell assembly. The unfired BN felt had an area of 450 cm^2, a thickness of 2.2 mm, and a basis weight of 60 mg/cm^2. These Q-series cells were assembled with half-charged active materials and had 10 wt % iron (in excess of stoichiometric iron), 1 vol % molybdenum, and 2 vol % carbon added to the positive electrode. The positive-electrode additives were selected on the basis of previous tests on X-series cells at Gould (see Section II.A). The theoretical capacities were 117 A-hr for the positive electrode and 154 A-hr for the negative electrode; the electrolyte was 52 wt % LiCl-48 wt % KCl. Testing of these cells at ANL showed their performance to be excellent (see Table III-4); the positive-electrode utilization was 60 to 70% at a discharge current density of 75 mA/cm^2. All of these cells are still operating. Initial cycling time of many of these cells was short as capacity gradually accumulated; therefore, the operating time (200 to 1150 hr) is more representative of the testing time than the number of cycles.

In another cell test, four identical Gould Li-Al/FeS bicells except for the current collector material (C-7, C-8, C-9, and C-10A) were tested at ANL. These 171 A-hr cells were assembled uncharged and had BN fabric separators and positive electrode additions of 100 wt % excess iron, 4.6 vol % cobalt powder,

Table III-4. Performance of Q-Series Cells

Cell No.	Capacity, A-hr	Energy, W-hr	Operating Time Cycles	Operating Time Hours
Q-1	72	85	82	700
Q-2	74.5	89	110	1150
Q-3	70	83	144	1150
Q-4	82.5	97	62	500
Q-5	72	84	70	500
Q-6	78	92.5	67	500
Q-7	61	71	106	475
Q-8	66	77	65	400
Q-9	66	77	61	400
Q-10	56	66	44	200

and 3.7 vol % carbon powder. The current collector material was Hastelloy B for Cell C-7, iron for C-8, copper for C-9, and nickel for C-10A. The four cells were operated at a constant charge and discharge current of 15 A. The copper current collector proved unacceptable because of a short circuit that resulted from copper transfer during the initial charge cycle. The effect of conductivity of the positive-electrode current collector was evident in the overall internal cell resistance. Cell resistance as a function of state of charge is given in Fig. III-3 for the other three cells; the rise in

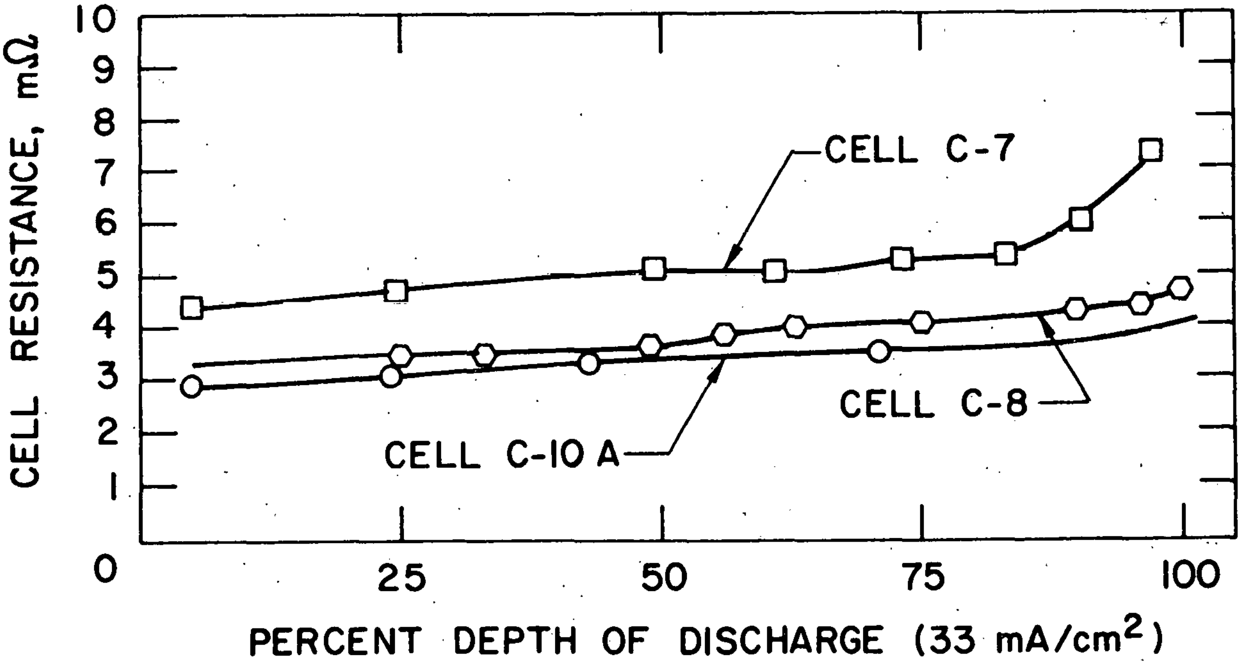

Fig. III-3. Resistances of Gould Cells Testing Current Collector Material resistance during discharge was similar for the three cells. Cell C-7 had substantially higher average internal resistance (5.0 mΩ) in comparison with Cell C-8 (3.6 mΩ) and C-10A (3.3 mΩ). During the course of operation, the resistances of all three cells increased approximately 0.2 mΩ after cycle 50. The peak capacities were 103 A-hr for Cell C-7, 118 A-hr for Cell C-8, and 121 A-hr for Cell C-10A. After 250 cycles, the capacity of Cell C-10A had not declined, whereas that of Cell C-7 had declined by 12% of the peak capacity. The operation of Cells C-7 and C-10A was terminated after 59 cycles and 303 cycles, respectively, due to the development of short circuits. Cell C-7 is still operating after 456 cycles.

Four cells similar in design and materials to C-10A, but without any positive-electrode additives, were then constructed by Gould and tested at ANL. The capacity of these cells was significantly lower than that of C-10A--∿90 A-hr (53% utilization).

C. Testing of Eagle-Picher Cells at ANL

During the cell development stage of the Mark IA program (Section II.A), it was discovered that the Eagle-Picher multiplate cell (EPMP-series) had a lower power output than that required by the Mark IA goals, showed significant capacity decline with cycling, and frequently failed due to swelling of the cell can which allowed extrusion of active material from the positive electrode. Efforts at ANL to resolve these problems as well as other tests of Eagle-Picher's cells are described below.*

1. Cell Swelling

(T. D. Kaun, W. E. Miller, W. A. Kremsner)

A frequent failure mode of the Mark IA developmental cells was a short circuit caused by outward bowing of the edges and bottom of the cell can which allowed extrusion of active material from the positive electrodes.† This effect leads first to a loss of capacity and coulombic efficiency, and finally to a short circuit. The can failure may be attributed to a buildup of internal cell gas pressure.

To achieve the very high goals for specific and volumetric energy density, the Mark IA cells were initially filled with a large volume fraction of active materials, cell hardware, and electrolyte. The electrolyte expands about 20% when it melts, thereby reducing the gas volume available inside the cell. As an example, in Cell EPMP-7-094, 74.2% of the electrolyte plus gas volume was occupied by electrolyte before it was melted; with the electrolyte molten, this volume was 88.1%. The available gas volume decrease from 25.8% to 11.9% causes a factor of 2.2 increase in the gas pressure. When the cell was sealed at room temperature and then heated to 450°C, the pressure was increased by an additional factor of 2.6. Since the feedthrough is not completely gas tight, this pressure is relieved gradually. Because of the time required to heat the cell to operating temperature (several hours), the temperature effect on gas pressure is probably small. However, melting of the electrolyte takes place rather quickly once the eutectic temperature is reached, resulting in a pressure surge. This pressure surge was noted experimentally when a pressure gauge was attached to Cell EPMP-7-094.

---

*Performance data of Eagle-Picher cells tested at ANL are given in Appendix C.

†See Section IV.C for a more detailed description of the cell failure modes of Eagle-Picher's cells.

Figure III-4 shows the effect of electrolyte volume prior to melting on the pressure differential, *i.e.*, the internal cell pressure after electrolyte melting divided by the internal cell pressure prior to electrolyte melting. In the case of Cell EPMP-7-094 (0.74 electrolyte volume prior to melting), the pressure inside the cell prior to melting is about 1 atm (absolute), and after melting the pressure is about 2.2 atm (absolute). Thus, the pressure differential across the can wall after melting is about 1.2 atm, which is sufficient to deform the thin can wall. As illustrated in Fig. III-4, the extent of the pressure increase is largely a function of the available void space after the electrolyte filling operation, which was not closely controlled in most of the Mark IA developmental cells. However, for the cells used in the Mark IA battery, the amount of electrolyte added to the cells was closely regulated.

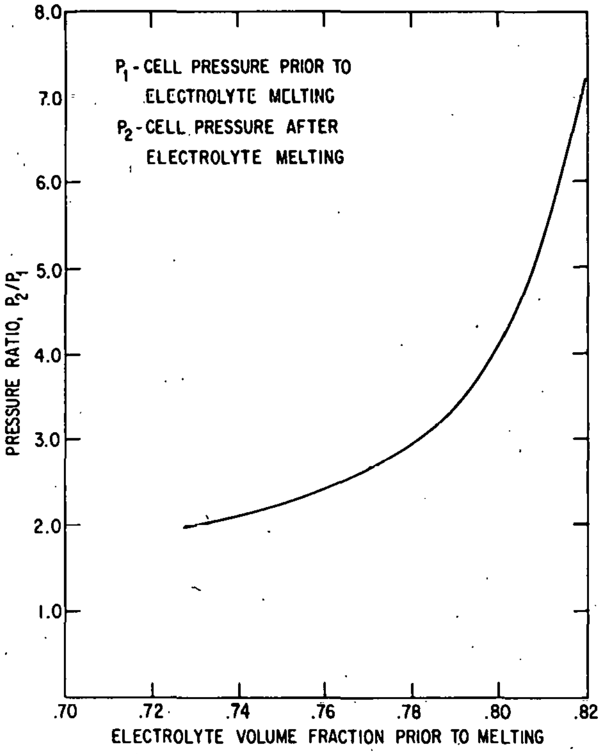

Fig. III-4. Increase in Cell Pressure Related to Electrolyte Melting Operation

2. Capacity Fading

(T. D. Kaun, W. E. Miller, W. A. Kremsner, J. D. Arntzen)

In general, the multiplate cells fabricated by Eagle-Picher showed a significant decline in capacity during cycling. Figure III-5 shows the capacity decay typically exhibited by the Mark IA cell, 1.0 A-hr/cycle, and the Matrix D cell (see Section II.A), 0.6 A-hr/cycle. Both of these types of cells contained FeS electrodes with Cu_2S additive and LiCl-KCl eutectic electrolyte, and they were operated at 465°C. The Li/S capacity ratio was

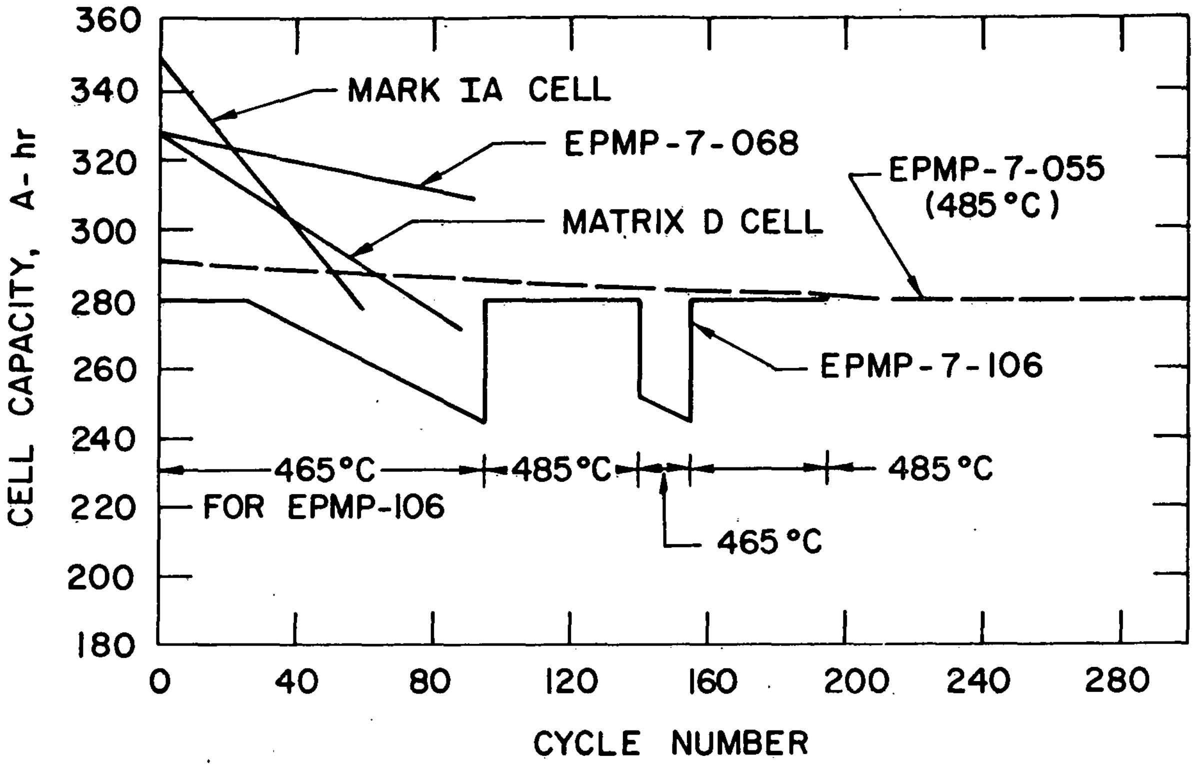

Fig. III-5. Capacity Stability of Eagle-Picher Multiplate Cells (operated at 465°C except as noted)

about 1.1 for the Matrix D cells and 1.0 for the Mark IA cells. Post-test examinations of multiplate cells have identified an agglomeration phenomena in the negative electrode, which appears to be symptomatic of cell capacity fading (Section IV.C).

The two Eagle-Picher cells which exhibited the most stable capacity during cycling were EPMP-7-055 and -106, which had no Cu_2S added to the positive electrode and LiCl-rich electrolyte. These two cells were operated at 465-485°C, and the depth of discharge was limited to less than 75% of the negative-electrode capacity after the initial cycles. The capacity of these two cells is shown in Fig. III-5. Also shown in this figure is the capacity of EPMP-7-068, which had Cu_2S added to the positive electrode and LiCl-rich electrolyte.

The above cell test results suggest that two mechanisms are involved in the capacity fading. The first mechanism could be partial freezing of electrolyte (raising the operating temperature for Cell EPMP-7-106 stabilized the capacity), or possibly negative-electrode poisoning. The other appears to be over-utilization of the negative electrode (>75% of theoretical capacity) either through exclusion of electrolyte or through sintering and resulting agglomeration of the α-LiAl phase. Eagle-Picher multiplate cells operated at temperatures of 485-500°C and with high utilization of the negative electrode have been found to show the rapid capacity decline typical of Mark IA cells.

The effect of the cell hardware upon capacity fade is unclear. Since agglomeration of LiAl was most obvious in the inner negative electrodes of multiplate cells, which are electrochemically cycled from both faces, a multiplate cell containing a centrally partitioned inner negative electrode* and a bicell fabricated from Mark IA cell hardware were tested. The multiplate cell, EPMP-DC-5, containing partitioned negative electrodes lost capacity at a rate of 1.14 A-hr/cycle or 0.34% of peak capacity per cycle. Therefore, dividing a multiplate cell into parallel bicells did not alter the rate of capacity decline. The bicell (EMP-DC-1), which was effectively one-third of the three-positive-plate cell, exhibited capacity decline of 0.56 A-hr/cycle or 0.48% of peak capacity when operated at the same current density (36 mA/cm^2) as the multiplate cell. In conclusion, these two cells had about the same capacity decline rate as the typical Mark IA cell. Two other bicells (EMP-DC-3 and -4) were fabricated with Mark IA hardware and a negative-to-positive capacity ratio of two (same electrode thickness); the capacity decline rate of these cells was similar to that of the Mark IA cell. However, post-test examinations revealed irregularities in the cell fabrication, leaving this result somewhat in doubt.

3. Power Improvement

(T. D. Kaun, W. A. Kremsner)

The power requirement for the Mark IA battery was 30 kW at 50% depth of discharge. At this discharge depth, the cell must attain a power output of at least 250 W at a discharge current of 300 A, which is the motor-controller limit for the Mark IA test van.

As mentioned in Section II.A, Eagle-Picher constructed and tested four cell matrixes (A, B, C, and D) before selecting the final design for the Mark IA cell. Figure III-6 shows the typical power obtained by the final two matrices (C and D). As can be seen in this figure, the power attained by the Matrix D cells, 220 W at a current of 300 A, is below the power goal set for the Mark IA cell. The resistance for these cells was 1.65 and 1.8 mΩ at 5% and 50% depth of discharge, respectively. Therefore, efforts were undertaken at ANL to improve the power attainable by these cells.

To improve the power in Cell EPMP-7-071, the negative terminal resistance was bypassed when the negative voltage connection was made directly to the negative-electrode bus bars. With this modification (design E), somewhat higher power (240 W at a 300-A current) and a lower cell resistance (1.4-1.5 mΩ) was achieved; however, the cell power was still below the Mark IA goal. An earlier experiment revealed that 315 W of power could be attained when voltage connections were made directly to both positive and negative internal bus bars of a multiplate cell (EPMP-7-067).

As a result of the low power attained by earlier Mark IA cells, ANL made resistance measurements on the components of a number of cells. Figure III-7 shows the resistances obtained by various modifications in the components of the Eagle-Picher cells. The current collectors in the Matrix C cells were honeycomb structures (about 1.3-cm honeycomb cell size) woven from 0.0075-cm thick mild-steel (AISI 1010) ribbons. About half of these ribbons were connected to the electrode bus bars. Cell resistance was decreased by

---

*A continuous metal sheet was placed between the two negative half-electrodes.

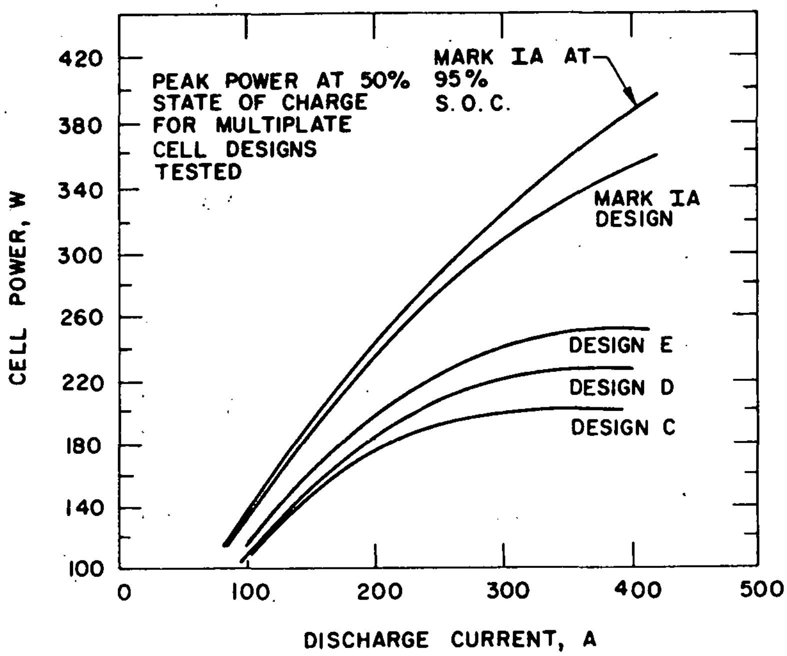

Fig. III-6. Power Obtained in Eagle-Picher Multiplate Cells

about 0.1 mΩ through the following changes in this structure: decreasing the honeycomb-cell size by half, increasing the ribbon thickness to 0.0125 cm, and connecting all the honeycomb ribbons to bus bars. This modification is indicated by symbol R_{EC} in Fig. III-7. A thicker and wider positive bus bar and improved techniques for welding the current collector ribbons to the positive bus bar (R_{PB}) gave a resistance decrease of about 0.05 mΩ. The connection between the positive terminal and the bus bar was improved (components redesigned and welding improved), and this modification (R_{PT}) resulted in a decrease in resistance of about 0.1 mΩ. Changes in the connection between the negative bus bar and lead ribbons resulted in only small resistance improvements (R_{NB}). The largest resistance improvement, 0.2 mΩ, came from adding a copper overlay to the top of the cell to lower the resistance path between the negative bus bar and the intercell connector (R_{NT}). These changes were implemented by Eagle-Picher in the final fabrication of Mark IA cells (see Fig. III-8), and the resistance was in the range of 1.1 to 1.2 mΩ which increased the peak power well above the Mark IA goals.

4. Driving Profile Tests

(T. D. Kaun, W. A. Kremsner)

One of the Mark IA development cells (EPMP-7-071) was operated in the laboratory for 60 cycles under simulated driving conditions (the SAE J227a cycle B). During each discharge, the driving profile, which includes a power pulse, constant-power discharge, and open circuit, was repeated every 72 sec until a cutoff had been reached.* For 35 of the cycles, the driving

---

*The point at which the cell cannot reach the power requirement.

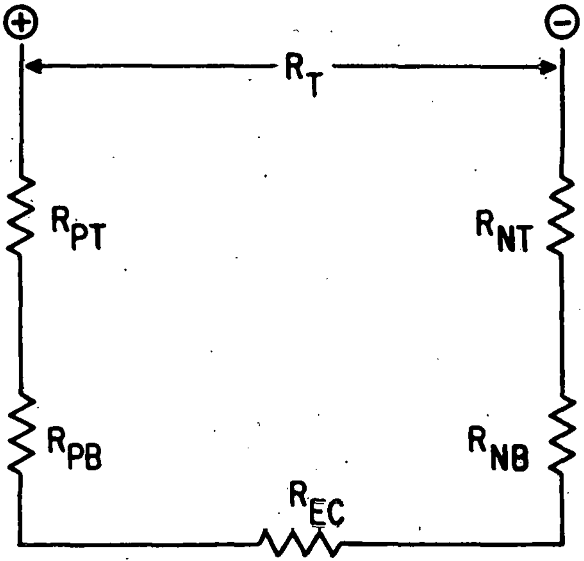

	Symbol	Resistance, mΩ Standard Design	 Modified Design
Electrode couples at full charge state[a]	R_{EC}	0.85-0.95	0.73-0.83
Positive bus bar connection	R_{PB}	0.05-0.1	0.025-0.05
Positive cell terminal	R_{PT}	0.25-0.30	0.15-0.20
Negative bus bar connection	R_{NB}	0.05-0.1	0.05-0.025
Negative cell terminal connections	R_{NT}	0.25-0.30	0.075-0.1
Total Cell	R_T	1.45-1.75	1.0-1.23

[a] Add 0.1 mΩ for 50% depth of discharge.

Fig. III-7. Resistance Mapping for Eagle-Picher Multiplate Cells

profile consisted of a constant power acceleration (140 W). Under these conditions, the cell would discharge about 305 A-hr in each deep cycle, the capacity at a 70-A constant discharge current being 320 A-hr. For the balance of the profile testing, more severe acceleration conditions (240 W) were used. Under these conditions, the cell achieved the full power of 240 W over 65% of its discharge capacity (200 A-hr). This cell failed after 118 deep discharge cycles due to mechanical causes. Post-test examination showed no unusual effects related to the harsh testing. The rate of capacity decline was also typical.

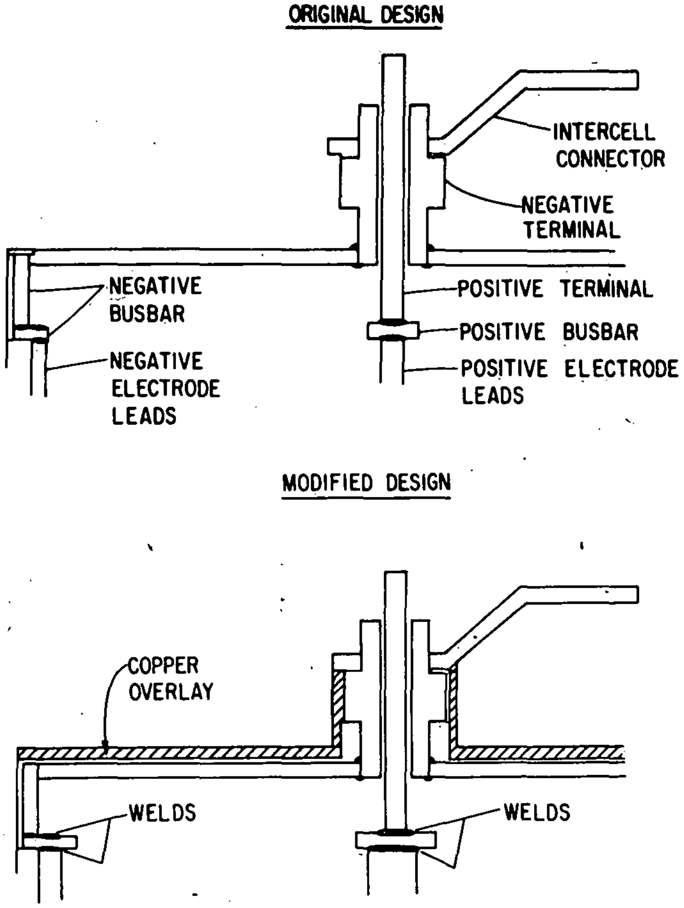

Fig. III-8. Design Changes to Improve Resistance in Multiplate Cells

A prototype Mark IA cell, EPMP-7-224, which had an FeS-Cu_2S positive electrode and LiCl-KCl eutectic electrolyte and incorporated features of the low resistance cell design discussed above, was also tested under the J227a cycle B (140-W power pulsing) and achieved a capacity of 363 A-hr and an energy of 445 W-hr. Using a modified J227a cycle C (187.5-W power requirement) with regenerative braking added, the discharge capacity for the Volkswagen Transporter test van would have been 346 A-hr or 400 W-hr per battery cell. A simulated vehicle range test was performed on another Eagle-Picher cell (Cell EPMP-7-388) by discharging the cell at 58 W constant power (approximately 40 km/hr vehicle speed); a vehicle range of 282 km was estimated.

5. Cell Failure Studies

(V. M. Kolba, J. L. Hamilton, G. W. Redding)

In a full-scale Li-Al/FeS battery, it would be desirable if the battery would continue to operate after some of the cells had developed internal short circuits. Continued operation would be possible only if certain conditions were met: (1) an open circuit or very high resistance did not develop within a cell, and (2) continued operation did not contribute to cell rupture and electrolyte leakage. Two multiplate cells (EPMP-7-029 and -060) have been operated beyond failure, *i.e.,* cycling continued after the coulombic efficiency of the cells had dropped to low values. The cycling mode was to discharge at 70 A for 4 hr and then charge at 40 A for about 7 hr, regardless of the voltage state of the cell. (This would be the manner in which a failed cell would cycle in a series-connected battery.) The peak voltages developed in the two test cells are shown in Table III-4. The main finding was that as cycling continued with the failed cells, a reverse voltage occurred in the discharge cycle. This voltage peaked for each cell: -1.44 V for Cell EPMP-7-029 and -1.64 V for Cell EPMP-7-060. One of the cells was examined after its operation was terminated. This examination showed no signs of excess swelling or stress due to the continued cycling. If cycling were to be continued in a battery after some cells had failed, our conclusion is that the discharge voltage of the battery would be reduced by about 3 V for each cell that failed. No other effect would be noticeable.

Table III-4. Cell Reversal Tests

Cell EPMP-7-029			Cell EPMP-7-060		
Cycle No.	Voltage, V		Cycle No.	Voltage, V	
	Charge	Discharge		Charge	Discharge
143	+0.22	-0.3	114	+1.45	-1.5
150	+0.34	-0.64	115	+1.42	-1.55
155	+0.45	-0.88	120	+1.08	-1.54
160	+0.69	-0.93	125	+0.86	-1.53
165	+0.61	-1.52	130	+1.13	-1.63
170	+0.89	-1.01	134	+1.16	-1.63
175	+0.98	-1.15	140	+1.18	-1.64
180	+1.10	-1.44	155	+1.28	-1.64
185	+1.17	-1.45	160	+1.29	-1.65
190	+1.18	-1.44	165	+1.31	-1.65
195	+1.19	-1.44	170	+1.32	-1.64
200	+1.20	-1.44	172	+1.32	-1.64
205	+1.22	-1.46			
210	+1.22	-1.44			
215	+1.23	-1.45			
220	+1.23	-1.45			
230	+1.23	-1.46			

D. Battery Testing

During this period, Eagle-Picher completed fabrication of two small (6 V) batteries and a full-scale battery for vehicle propulsion. The results of battery testing at ANL are described below.

1. Small Mark IA Battery

(V. M. Kolba, J. L. Hamilton, G. L. Chapman, W. H. DeLuca)

As mentioned in Section II.A, Eagle-Picher fabricated a 6-V battery module containing five Mark IA cells connected in series and multi-foil thermal insulation. The data obtained from testing this module were expected to provide assistance in developing the final design for the Mark IA battery.

Figure III-9 shows the capacity of this module throughout the testing period. The initial 10 cycles were completed at Eagle-Picher and then the module was delivered to ANL. At ANL, this battery was operated at a constant-current 70-A discharge followed by a constant-current 40-A charge for the first 27 cycles. The initial energy output for the module at ANL was 1636 W-hr. It was difficult to equalize the cells in the battery because of the high resistance of the equalization lead wires. (The wires installed were pure nickel wire rather than nickel-plated copper as specified, through an error by the wire supplier.) For 5 cycles, starting at Cycle 27, the battery was tested on the J227b Cycle C driving profile. The energy output for the

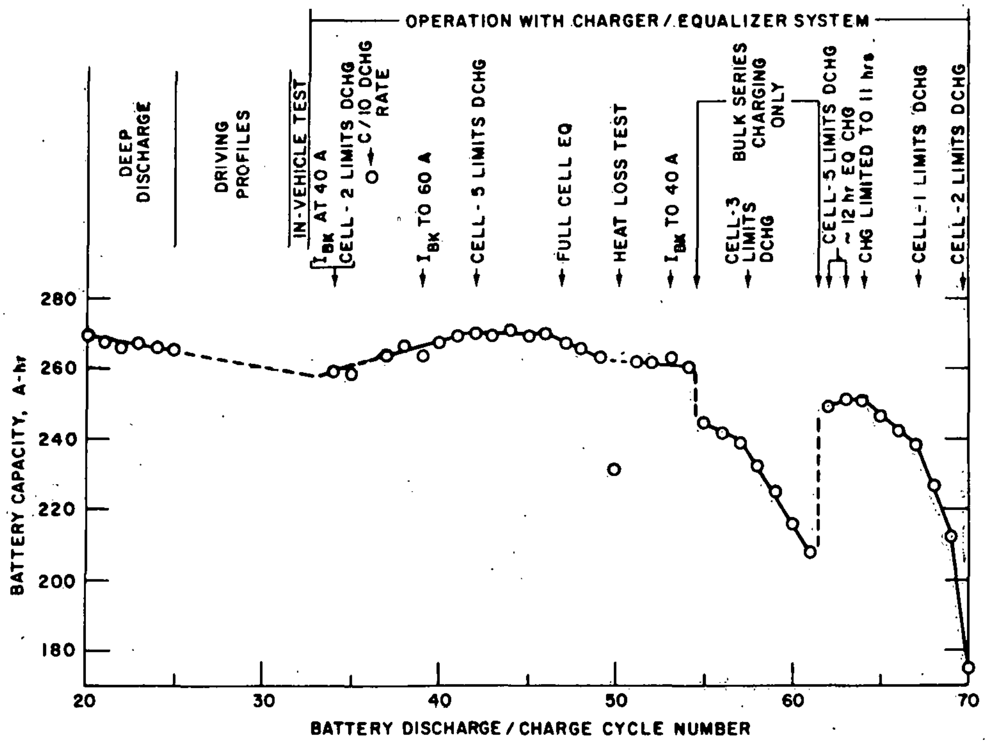

Fig. III-9. Capacity during Cycling of 6-V Mark IA Module peak deep cycle during these tests was 1653 W-hr. At discharge Cycle 32, the module was installed in series with the existing 144-V lead-acid batteries in a Volkswagen Transporter van and was operated on the road for one hour to determine the battery response to chopper frequency and current peaks. On the road, the battery performance was excellent for the 4.85 kW-hr discharge; no serious problems were noted in the interaction of the battery and the drive motor and controller.

At Cycle 33, charging and equalizing of the cells in this module were conducted with the system described in Section VII.D. Equalization charging of 3.5 A was started at Cycle 35, and battery capacity was measured at 260 A-hr (1.49 kW-hr), with Cell #2 limiting the module capacity on discharge. Within the first three charge cycles, three of the battery cells achieved full equalization, 1.60 V. After nine complete cycles, sufficient equalization had been performed so that a different cell (#5) was limiting discharge capacity. At this time, the battery capacity was 270 A-hr (1.54 kW-hr). A total of 15 cycles were required before all five cells achieved full equalization to 1.60 V within the 8-hr maximum charge cycle time. The battery capacity, however, showed a small decline with each charge/discharge cycle, and on the 53rd cycle measured 262 A-hr.

From Cycle 54 to 60, the charging conditions were altered to only constant-current charging until a cell reached the 1.60-V level. The battery capacity declined from 260 to 208 A-hr during these seven cycles. Cell #5 limited the discharge for the first two cycles, with Cell #3 becoming the capacity limiting cell on subsequent cycles; Cell #4 was the limiting cell at 1.60 V for all seven charge cycles.

On the next charge cycle, an extended period of 14 hr was used for cell equalization after constant-current and taper charging. This restored the capacity to about 250 A-hr. The capacity dropped rapidly with further cycling. After 70 cycles, battery operation was terminated, and the cell parts were removed from the battery case. Two of the five cells were found to have short circuits in the feedthrough. The short circuits resulted from electrolyte creep through the BN powder seal in the feedthrough. In tests of approximately 200 single cells that were cycled in the Mark IA cell development program, no similar problem has arisen. In the battery, the intercell connectors, which are not flexible, place a stress on the positive terminal rods of the battery cells. This stress, which probably is somewhat variable during cycling, caused failure to occur during battery operation.

2. MERADCOM* Module Test

(T. D. Kaun, J. L. Hamilton, G. L. Chapman, R. W. Kessie)

Another 6-V module (five Mark IA cell pairs and Min K thermal insulation) was fabricated by Eagle-Picher for testing at ANL. This battery module, described in Section II.A, was tested for MERADCOM to determine the viability of this system for fork-lift applications. As requested by MERADCOM, the module was discharged at the 6-hr rate (106-A constant current). The initial discharge at ANL on Cycle 6 gave 623.8 A-hr or 3.7 kW-hr of energy storage. The normal mode of charging was 8 hr of constant current at 80 A

---

*U. S. Army Mobility Equipment Research and Development Command, Fort Belvoir, NJ.

followed by 2 hr of equalization at 1.55 V per cell pair. However, numerous problems were encountered in getting the computer-controlled testing to operate properly with the equalizer/cell monitoring electronics. Three sources of electronic noise had to be eliminated. After the tenth charge, equalization charging was not done.

Table III-5 shows the average cell voltage, capacity and energy from Cycle 6 to 23. The MERADCOM battery was built from ten Mark IA cells whose individual resistances were about 1.5-1.8 mΩ, which gives a cell pair with a resistance of about 0.8 mΩ. Overall battery resistance was 5.0 mΩ at

Table III-5. Testing of the MERADCOM Module at ANL

Cycle No.	Capacity, A-hr	Energy, W-hr	Avg. Voltage, V
D-6	623.8	3703.5	5.936
C-6	424.16	3024	7.13
D-7	495.75	2879.75	-
C-7	608.13	4404	7.24
D-8	589.37	3391.4	-
C-8	611.88	4445	-
D-9	611.61	3520.2	5.75
C-9	562.16	4086.7	7.27
D-10	568.8	3345	5.88
C-10[a]	548.8	3989.5	7.27
D-11	578.7	3359.5	6.19
C-11	578.3	4210.1	7.28
D-12	570.9	3291.5	5.76
C-12	-	-	-
D-13	572.25	3321.8	5.80
D-14	-307.6	-1762.5	5.8
C-14	611.9	4480.1	7.32
D-15	-576.3	-3368.2	5.84
C-15	-	-	-
D-16	-534.4	-3153.9	5.9
C-16	489.6	3583.3	7.23
D-17	-534.9	3119.4	5.83
C-17	-	-	-
D-18	535	-	-
C-18	540	3960	7.32
D-19	520	3050	5.86
C-19	533	3899.9	7.31
D-20	540	3143	7.32
C-20	539.7	3949	7.31
D-21	530	3097	5.84
C-21	532	3896.5	7.32
D-22	525	3061.6	5.83
C-22	527.3	3860	7.32
D-23	518.97	3020	5.82

[a] Equalization not done after this point.

50% depth of discharge. Power pulse data were taken for this battery, using 15-sec pulses to 1000 A. Peak power was 2.62, 2.02, and 1.87 kW for 4.6, 52.3, and 78.5% states of discharge, respectively. The power test results are shown in Fig. III-10. On the 24th cycle, cycling was stopped and the battery was returned to Eagle-Picher for examination. A short circuit was found in one cell; this was replaced and the battery was subsequently cycled for 11 more cycles by the contractor after which another failure occurred. This failure was of the same type seen in the Mark IA 6-V module, *i.e.*, a feedthrough failure caused by stress of the positive cell terminal transmitted through the rigid intercell connectors.

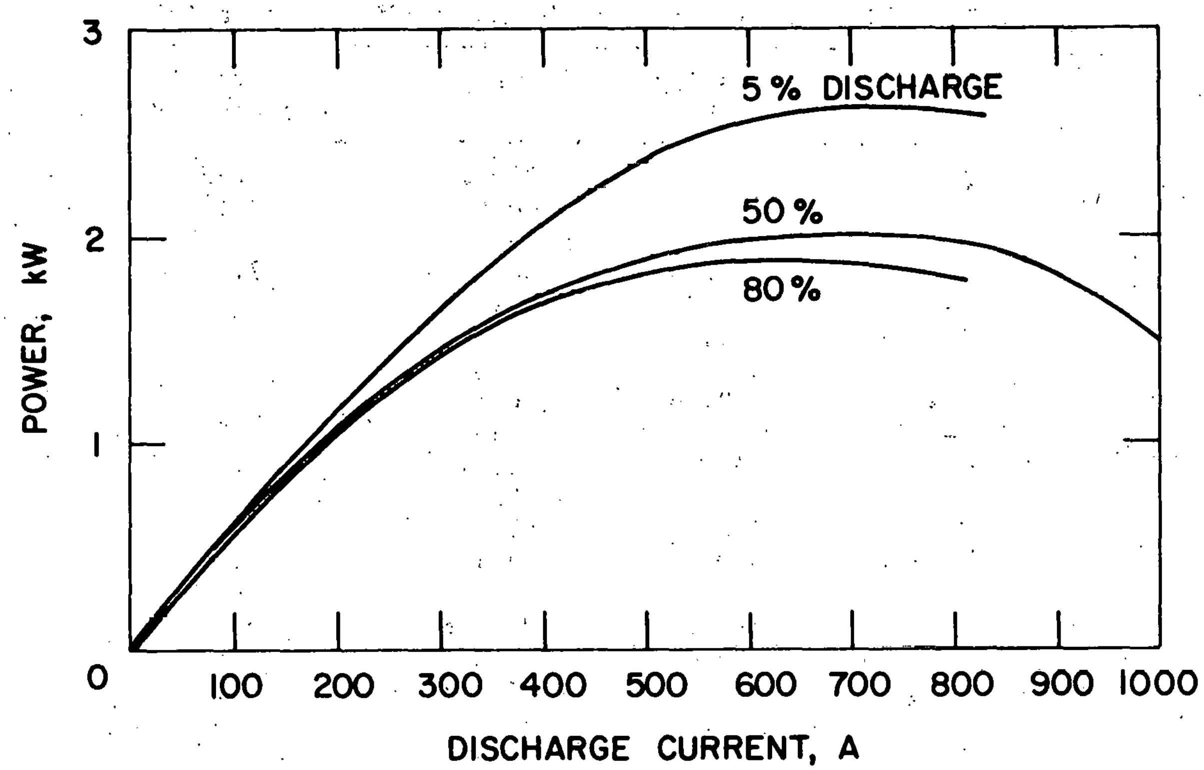

Fig. III-10. Power Tests of MERADCOM Module

3. Mark IA Battery
(V. M. Kolba, G. L. Chapman, J. L. Hamilton, G. W. Redding)

The first module (designated D-002) of the Mark IA battery (Section II.A) was delivered to ANL on May 8, 1979. Upon the receipt of Module D-002, room-temperature resistance measurements were made on the module and the individual cells; no abnormal results were found. The vacuum annulus in the insulated case maintained a satisfactorily low pressure (6×10^{-5} torr) with use of an ion pump. After the delivery of Module D-001 on May 22, room-temperature resistance measurements were made with no abnormal findings, and both units were installed in a Volkswagen Transporter electric van. Figure III-11 shows the two modules in the van. The two modules were connected in

Fig. III-11. Mark IA Modules Installed in Volkswagen Transporter Van. ANL Neg. No. 308-79-319.

series, but left on open circuit. Instrumentation on the battery included a computer data acquisition system (DAS) that recorded battery and individual cell voltages and sixteen (8 for each module) thermocouples (maximum reading = 1040°C) that provided temperature readings every minute.

a. Failure Description

Both modules were heated at a rate of about 10-15°C/hr, using internal resistance heaters limited by Variac transformers and controlled by a thermal management system that included control thermocouples inside the modules.

After the battery had been at the operating temperature (400-450°C) about 12 hr, the voltage of Cell 33 in Module D-002 began a slow decline and, after about 1 1/2 hr, had declined about 50 mV, ∿1.4 V. The voltage then dropped gradually to 0.1 V over a 2-hr period. No thermal effects were evident. About 2 hr later the voltage of Cell 45 began to decrease: the voltage dropped from 1.3 V to zero in about 3 hr. Although no temperature rise was observed during this voltage drop, it was noted that the heaters on Module D-002 had stopped and remained off for about 4 hr. An attempt was made to recharge Cells 33 and 45 using the cell equalization system. Neither cell, however, would accept a charge, and charging efforts were terminated after ∿7 hr.

With a portion of the battery at or near operating temperature, the heating rate was adjusted in preparation for thermal-loss tests. A small decrease (0.1-0.2 V) was noticed in the voltages of Cells 24 through 27 in Module D-001; at the same time, the pressure in the vacuum annulus of D-001 increased from 9×10^{-5} to 1.1×10^{-4} torr. The voltages of Cells 26 through 37 then began to drop significantly, and this effect progressed to the other cells. Figure III-12 shows the rapid voltage drops with time in Cells 22 to 31. Figure III-13 shows the battery voltages and the temperature registered at the eight thermocouple locations over a 20-min period in Module D-001; also shown are the approximate times at which individual cells (numbered 1 to 60 in figure) failed.

Table III-6 shows the time at which the initial voltage decline had occurred and the temperature had reached 630°C. As can be seen in this table, the temperature rise lagged the voltage decay of cells. Representative temperatures registered at four thermocouples during failure are shown in Fig. III-14. Another 45 min after the battery voltage had dropped to 90 V, all of the cells except No. 60 had reached zero voltage; and 20 min later, the temperatures on the various thermocouples had leveled out in the general range of 750-850°C. The thermocouples on the outside of the case indicated 113°C. Seven hours later, Module D-001 had been cooled below the melting point of the electrolyte, and it was allowed to continue to cool to room temperature. The heaters on Module D-002 were turned off, and this module was cooled at a rate of about 10°C/hr until the electrolyte had solidified. Module D-002 was totally unaffected by the failure of D-001. There was no external breach of the D-001 module case.

After the event, a failure analysis team was appointed[*] (1) to

---

[*] Team members V. M. Kolba, J. E. Battles, and J. D. Geller from ANL and K. Gentry from Eagle-Picher.

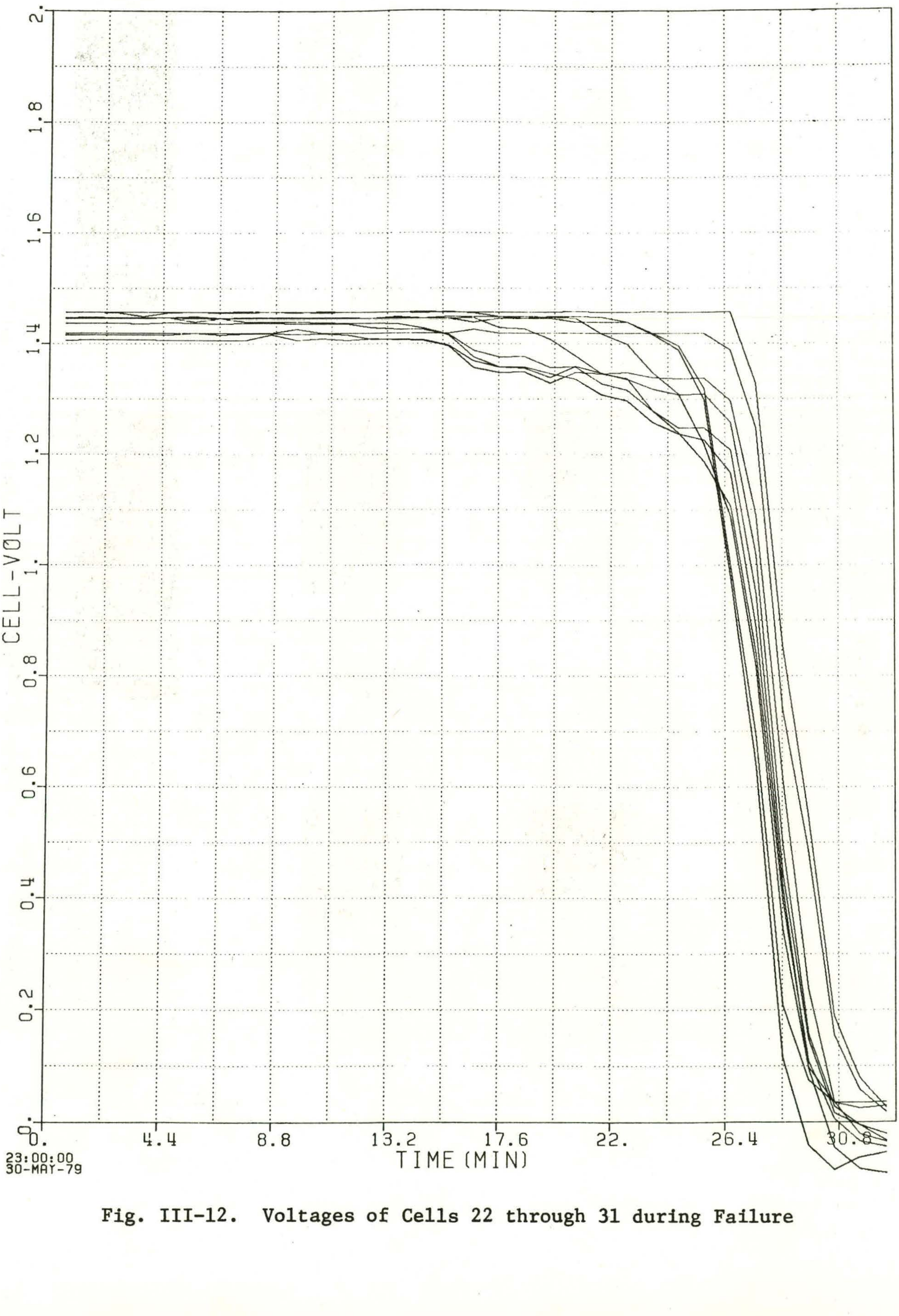

Fig. III-12. Voltages of Cells 22 through 31 during Failure

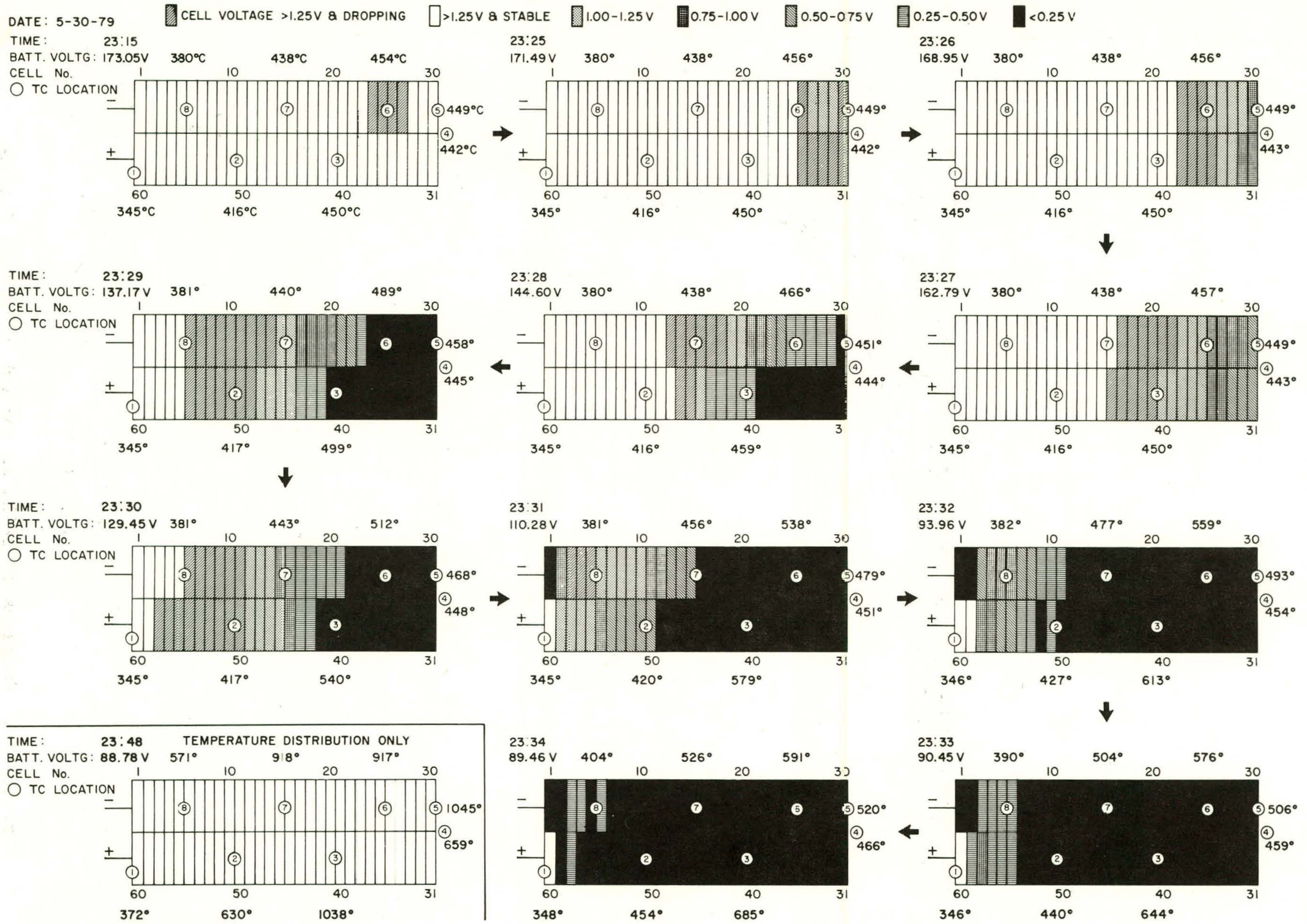

Fig. III-13. Voltages and Temperatures of Module D-001 during Failure

Table III-6. Relationship of Voltage Decline to Temperature Rise during Module Failure

Thermocouple Location	Cell Location	Time of Day: Initial Voltage Drop	Time of Day: Temperature 630°C	Difference, min.
2	50	2328	2348	20
	51	2328	2348	20
12	5	2330	2355	25
	6	2330	2355	25
4	41	2326	2333	7
11	15	2328	2342	14
	16	2327	2342	15
10	25	2316	2337	21
	26	2314	2337	23
9	30	2322	2338	16

investigate the possible mechanisms for failure and the most probable sequence of events involved in the failure, and (2) to make recommendations for corrective actions.

b. Failure Analysis

Upon examination of the outside of Module D-001, there was no evidence of the electrical components or wires having caused the short circuit. The cell-tray assembly could not be pulled out as designed; therefore, the module had to be cut open. Examination of the inside of the module showed that the mica electrical insulation which had been placed on the cell tops was still intact and that no positive terminals were exposed. Lateral expansion of the cell tray was found to have occurred, and electrolyte had spread over the cell tops and throughout the cell tray. These two factors account for the difficulty experienced in disassembling the module. Many of the cells had significantly bulged at the edges or tops, probably as a result of rapid discharge or high temperatures. Displacement of the cells in the tray was responsible for bending of most of the cross-over straps, breakage of two of these straps, and contact of fill tubes or feedthroughs of several cells with the straps; arcing between the straps and feedthrough housings had occurred. In many areas, evidence was present of "electrolyte corrosion" (formation of electrolyte solution containing metallic material) and arcing between cell housings and the cell tray. Melted braze and copper as well as iron had electrochemically reacted to form bridges between cells. Lithium-aluminum alloy had escaped from the negative electrodes of eight cells and contacted the cell tray or tray angle. The position of the intercell connector was found to have shifted on a few cells. The findings of post-test examinations on some of the cells from this module as well as the cell tray are reported in Section IV.C.

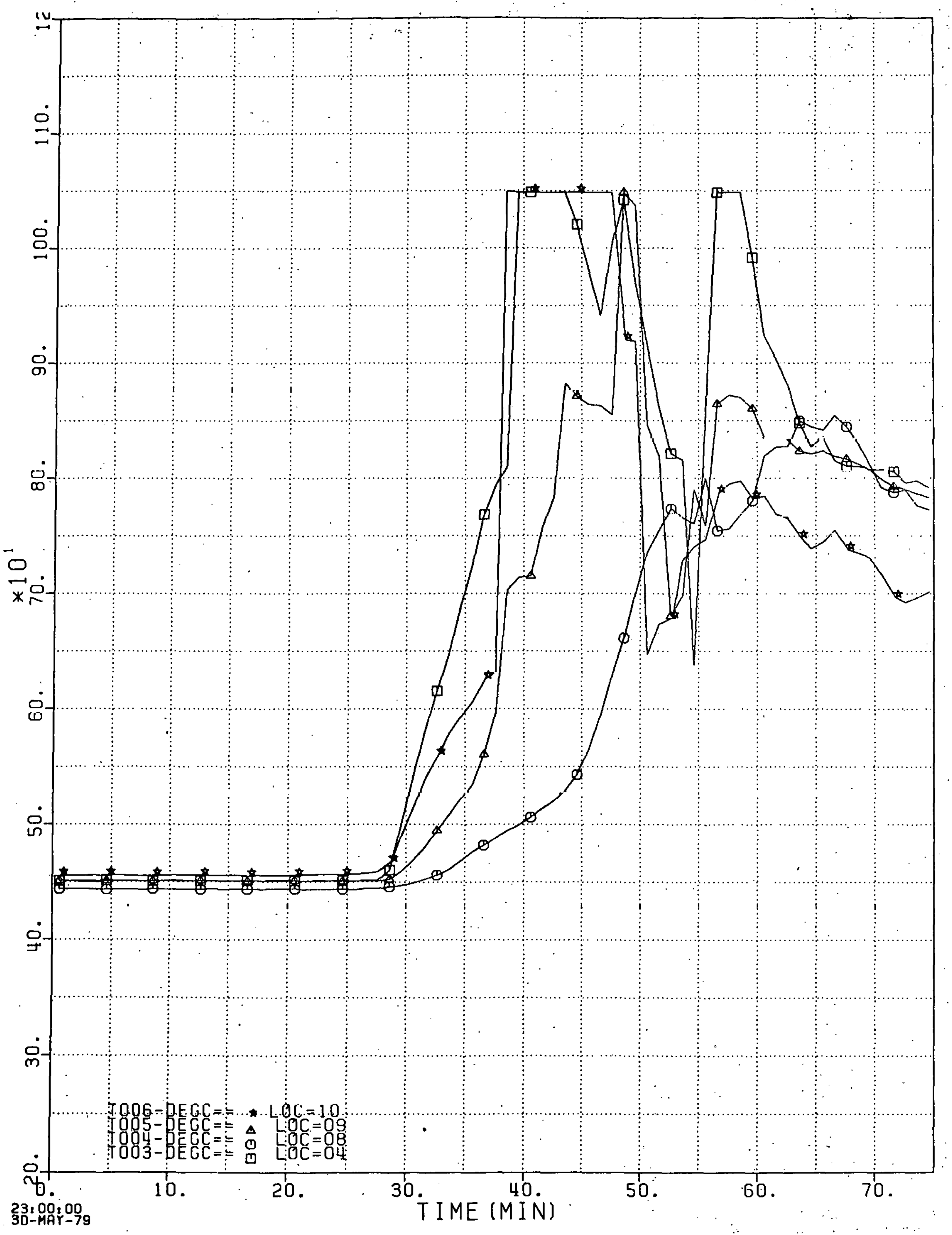

Fig. III-14. Temperatures Registered during Module Failure

To assist in the failure analysis, Module D-002 was sent to Eagle-Picher for analysis. The results of this examination are summarized in Table III-7.

Table III-7. Observations from Examination of Module D-002

Cell tray assembly was difficult to remove because of lateral expansion.
Rear cover mica insulator was slightly displaced exposing parts of positive terminal on Cells 16 and 46 (may have occurred during tray removal).
Displacement of cells relative to cross-over straps was observed.
Dimensional checks confirmed lateral expansion of cell tray.
Braze flux was present on most intercell connectors.
Slight displacement was observed in mica insulators, *e.g.*, bottom rear, center vertical rear, vertical left rear.
Electrolyte was observed on top outside edge of Cell 34 (metallography showed localized intergranular corrosion on the exterior surface only).
Cells 33 and 45 had developed short circuits in the feedthroughs.
Several small foreign objects were found in cell tray.
No physical defects were observed in the mica insulators.
Vertical height of cells was uneven.
Most cells were convex along vertical edges--more severe along outside edge.

Based upon the results from the examinations of both modules and the data obtained during the failure, the Failure Analysis Team has proposed mechanisms for the initiation and propagation of failure. The failure analysis indicated the probable mechanisms for failure initiation were as follows: (1) escaped electrolyte from cells corroded the metal in the nearby region and subsequently formed a metallic bridge between cells and the cell tray, and (2) arcing between cells and the cell tray occurred through butt joints in the electrical insulation. The above two mechanisms were also believed to be responsible for failure propagation; in addition, expansion of cells due to rapid discharge and high temperatures might have propagated the failure. Table III-8 presents a detailed summary of the most probable sequence of events during the failure.

Table III-8. Most Probable Sequence of Events during Failure

Initiation of Failure

- Contact of Cells 24 and 28 with cell tray resulted in discharge of Cells 24 to 27.

Propagation of Failure

1. Contact of fill tube on Cell 29 with cross-over straps (cause for drop-out of Cell 29 not identified).
2. Contact between tray angle and Cells 32 and 33 at top.
3. Failure of Cells 33 and 34: probably via electrolyte corrosion, braze transport, or feedthrough failure.
4. Contact between tray and Cells 23, 24, 37 and 38 via corrosion.
5. Multiple contacts between tray and cells via arcing, corrosion, and braze transport (Cells 39-44 and 22-18).
6. Contact at junction of Cells 45/46 and 15/16 with cell tray via arcing and corrosion.
7. Multiple contacts between cells, cell tray, tray angle, and cross-over strap (Cells 47-52 and 14-19).
8. Propagation of failure (except for Cell 60) by contact of Cells 1, 2 and 59 with cell tray via corrosion caused by electrolyte.

Based upon the failure analysis findings, the following recommendations were made:

CELL

1. consider cell-container materials with a higher strength at the operating temperature and/or increase the thickness of the cell container,
2. obtain low resistance in cells by internal rather than external modifications (*i.e.*, do not use copper strips that require brazing on the outside of the cell),
3. design cells so that they do not leak electrolyte,
4. consider isolation of the cell can from the positive and negative electrodes.

BATTERY

1. modify cell tray assembly to obtain adequate cell restraint,
2. modify intercell connectors to eliminate stresses and braze materials,

3. eliminate or accommodate thermal expansion differences between cells and the tray,
4. utilize improved high-temperature insulating materials,
5. eliminate gaps in electrical insulation (cell to cell and cell to tray),
6. modify cell arrangement in the module to minimize voltage differences between cells,
7. provide external circuit breaker between modules during testing.

As a result of the Mark IA experience, the strategy for the Mark II battery development has been revised somewhat. The first phase of the Mark II battery program will stress the development of high-reliability cells and will involve the fabrication and testing of ten-cell modules; this phase will conclude with qualification tests of these modules. The second phase will then consist of the development of inter-connected modules and full-scale batteries.

c. Failure Analysis Experiments

(J. D. Arntzen, W. E. Miller, Z. Tomczuk, V. M. Kolba, J. E. Battles, N. C. Otto)

As a follow-up to the failure analysis, a number of experiments were conducted at ANL.

Strips of Vitrabond mica insulation (7.6-mm thick) contacted with electrolyte at ~435°C for about 100 hr increased slightly (~0.05 mm) in thickness. Wetting of the insulator above the liquid electrolyte level was evident, indicating wicking of the electrolyte. Lithium-aluminum powder was added to the above electrolyte and the exposure continued for an additional 100 hr at 435°C with no visible change in the specimens. A new insulation strip was added to the above test strips and the temperature was increased to 520°C. After 16 hr, its thickness had increased by ~0.25 mm; laminar separation of the material was evident and the specimens had darkened.

A "T"-shaped piece of insulation was clamped between two carbon-steel plates, and the exposed bottom of the mica immersed in electrolyte saturated with lithium. Prior to immersion, the resistance between the plates (at ~450°C) was 2×10^6 Ω. After one hour of immersion, the resistance was ~800 Ω, indicating that electrolyte had wicked up the mica between the steel plates. After about 24 hr at 455°C, up to a 10-V potential difference was applied between the plates and showed a linear increase in current with voltage; at 10 V, the current was ~100 μA. After ~115 hr at 450°C, a maximum current of 2.4 mA was obtained at a 40-V potential. About 21 hr after the temperature had been increased to 520°C, the resistance between plates had declined to about 15 Ω. When testing was resumed, at a potential of 6 V, the current rose from 1.25 A to 2.5 A and then erratically to ~4 A, with peaks of >6 A. A series of voltage tests indicated a peak current of >4.5 A at ~20 V. These tests indicate that, at ~450°C, there is a very low leakage current through the electrolyte-saturated mica. However, when the temperature was increased to ∿520°C, relatively large currents can be supported through the mica sheet at relatively low voltages.

In another experiment, two sheets of mica insulation were sandwiched between two steel plates which contained a reservoir for supplying electrolyte saturated with Li-Al to the mica sheets. The two sheets of mica were brought together at one edge to form a butt joint, just as joints were made in the Mark IA battery. For about the same area of contact between the mica sheet and the plates as in the previous test, a current of about 6 A was produced with only 0.1-V potential difference between the plates at 450°C. After the test, examination of the plates showed evidence of iron transport at the butt joint in the mica. The above experiments suggest that short circuits can be initiated through joints in mica insulation and boundaries of the sheets of mica used to insulate the cells from each other and from the other battery hardware. After a brief period of short circuiting, the temperature of the battery increases, and the temperature rise causes breakdown of the mica insulation with additional short circuiting.

Experiments were also performed to investigate the corrosion of iron by molten aluminum. A strip of 0.06-mm thick AISI-1008 low-carbon steel was ground clean and washed, and the thickness carefully measured. Seven samples from this strip were placed in Al_2O_3 crucibles, and an aluminum plus LiCl-KCl mixture was added to four of the crucibles and only aluminum to the remaining three. The approximate mole ratio of aluminum to iron was 9 to 1. The samples were loaded into a furnace well in a helium glove box and held at 800°C ± 10°C for times ranging from 15 minutes to three hours. Metallographic examination showed that both sets of samples had the same parabolic rate of corrosion, indicating that the reaction was diffusion controlled and that the presence of salt had little or no effect on the corrosion process. The corrosion product was $FeAl_3$, which penetrated the low-carbon steel in needle-like crystals rather than along a uniform front. Complete penetration of the 0.06-cm thick steel occurred after approximately one hour, with 50% penetration occurring after 15 min.

IV. CELL PERFORMANCE AND LIFETIME SUMMARY

The purposes of this effort are (1) to estimate the typical performance of cells tested during the past year, (2) to obtain performance and lifetime data on at least six cells with the same design, and (3) to determine the failure mechanisms for previously operated cells.

A. Status Cell Tests

(E. C. Gay)

Tests are being conducted on Li-Al/FeS bicells with BN felt separators and Li-Al/FeS multiplate cells with BN fabric separators to obtain performance and lifetime data on at least six similar cells of each type. The results from these tests will be used to establish the status of the development of various cell designs and to aid in the selection of the optimal cell design for the Mark II battery.

1. Bicell Tests

(H. Shimotake, F. J. Martino, T. W. Olszanski, C. Ruiz,*
M. Fitzgibbons,† W. Moore‡)

The lifetime goal for the status bicells is more than 200 cycles. These cells will be cycled under the same operating mode: operating temperature, 460°C; charge and discharge cutoff voltages, 0.90 V and 1.62 V, respectively; and discharge current density, 74 mA/cm^2.

The design chosen for the felt-separator status cells was similar to that of Cell M-8, which had previously shown excellent performance characteristics (ANL-78-94, pp. 122-125). In addition to the BN felt separator, Cell M-8 had LiCl-rich electrolyte (67 mol % LiCl) and an initial positive capacity density of 1.4 A-hr/cm^3 at full charge. The BN felt used for the status cells was treated with a wetting agent, $LiAlCl_4$ (ANL-78-94, p. 158), and loaded into the cell through the side. The felt could not be loaded at the top, as is normally done, because of its fragility (initial porosity, 96%). The porosity of this BN felt has been found to reduce during cycling to about 85% owing to electrode swelling. During this report period, seven of these felt-separator status cells were placed in operation. Of these, two are now approaching 125 cycles with no decline in capacity and are maintaining a coulombic efficiency of over 99%. The specific energy of these cells is 63 to 68 W-hr/kg at a current density of 74 mA/cm^2 (4-hr rate), which is about 8% higher than the specific energy achieved by Cell M-8. This higher specific energy has been attributed to improved assembly techniques.

2. Multiplate Cell Tests

(W. E. Miller, T. D. Kaun, V. M. Kolba)

For these status cell tests, Eagle-Picher Mark IA cells will be tested at ANL.

---

*Student from the University of Puerto Rico.

†Student from Northwestern University.

‡Student from Illinois Institute of Technology.

B. Electrical Performance
(E. C. Gay)

A statistical analysis has been carried out on the performance of the Li/MS cells tested during this fiscal year. In the period, 297 cells were tested--60% by ANL, 22% by Eagle-Picher, 14% by Gould, and 4% by Rockwell. Of the cells tested, Eagle-Picher fabricated 36%, Gould, 33%, ANL, 26%, and Rockwell, 5%. The design for these cells was multiplate for 38% and bicell for the rest. Most of the cells had FeS positive electrodes (86%), and the separator was BN felt for 27%, MgO powder for 11%, and BN fabric for the rest.

Table IV-1 presents the average performance of four series of bicells tested during the fiscal year. The design within each series (*i.e.*, capacity loading, electrode thickness, electrode additives, electrolyte composition, etc.) varied somewhat. The R- and M-series cells had BN felt separators, and the PW-series cells had MgO powder separators. The G-series cells, which were fabricated by Gould Inc., had BN fabric separators. As shown in the table, the average performance for each cell series did not vary significantly. Table IV-2 shows the performance for the four series of Li-Al/FeS multiplate cells fabricated by Eagle-Picher for the Mark IA battery program. Each series was built to test variations in the multiplate cell design (see Section II.A). As can be deduced by comparing Tables IV-1 and -2, the average specific energy for the multiplate cells was considerably higher than that for the bicells (52.4 *vs* 99.2 W-hr/kg), but the average decline in specific energy per cycle for the multiplate cells was over four times higher than that for the bicells (0.25% *vs* 0.06%). The performance of six multiplate cells that operated for >190 cycles (the lifetime goal for the Mark IA was 200 cycles) is shown in Table IV-3. For these six cells, the average specific energy was higher but the average specific power lower than stipulated by the Mark IA goals (specific energy, 90 W-hr/kg at the 4-hr rate; specific power, 80 W/kg at 50% discharge).

Table IV-1. Performance of Li-Al/FeS Bicells

Cell Designation	No. of Cells	Average Specific Energy,[a] W-hr/kg	Average Discharge Rate, hr	Average No. of Cycles Operated[b]	Percent Decline in Specific Energy	Percent Decline in Specific Energy Per Cycle
M-series[c]	6	54.3	3.5	252	24	0.09
R-series[c]	14	52.9	4.0	235	12	0.05
PW-series[c]	8	47.2	7.0	328	18	0.05
G-series[d]	7	55.8	7.6	107	5	0.05
Total	35	54.2	5.3	250	14	0.06

[a] Typical value determined within the first 20 cycles.

[b] Reasons for termination include cell failure (short circuit or declining coulombic efficiency) as well as the end of scheduled testing.

[c] Fabricated at ANL.

[d] Fabricated at Gould Inc.

Table IV-2. Performance Summary for Li-Al/FeS Multiplate Cells (Mark IA)

Cell Designation	No. of Cells	Average Specific Energy,[a] W-hr/kg	Average Discharge Rate, hr	Average No. of Cycles Operated[b]	Percent Decline in Specific Energy	Percent Decline in Specific Energy Per Cycle
A-series	7	95.4	5	97	20	0.21
B-series	18	100.5	4	100	23	0.23
C-series	13	102.4	4	111	36	0.32
D-series	24	97.2	4	119	28	0.24
Mark IA Production Cells	21	100.7	4	122	26	0.24
Total	83[c]	99.2	4	110	27	0.25

[a] Typical value within the first 25 cycles; 4-hr rate.

[b] Reasons for termination include cell failure (short circuit or declining coulombic efficiency) as well as the end of scheduled testing.

[c] 65 cells tested at Eagle-Picher; 18 at ANL.

Table IV-3. Performance of Six Multiplate Li-Al/FeS Cells (Mark IA)

	Six-Cell Average	EPMP-7 -062	EPMP-7 -096	EPMP-7 -089	EPMP-7 -046	EPMP-7 -055	EPMP-7 -095
Specific Energy,[a] W-hr/kg	101.3	106.8	104.6	106.8	100.8	100.8	87.8
Specific Power,[b] W/kg	54.4	58	-	58	52	46	58
Percent Decline in Energy	30	32	40	38	25	12	21
Percent Decline in Energy per Cycle	0.12	0.17[c]	0.14[d]	0.12[d]	0.13[c]	0.04[e]	0.10[c]
Cycle Life	258	190	289	330	200	320	218

[a] Measured at the 4-hr rate.

[b] Measured at 50% depth of discharge.

[c] Cell still operating as of the end of September 1979.

[d] Cell operation voluntarily terminated.

[e] Cell failure due to short circuit.

Table IV-4 summarizes the reasons that operation was terminated for the cells tested at ANL and Eagle-Picher during the past year. Most of the cells tested at ANL had BN felt separators, whereas the cells tested at Eagle-Picher had BN fabric separators. At present, the BN felt has weaker physical properties than the BN fabric. Thus, it is not surprising that the cells tested at ANL should have a higher percentage of short circuits than the cells tested at Eagle-Picher. Carborundum Co. is undertaking an intensive development effort to improve the BN felt quality.

Table IV-4. Reasons for Cell Termination

	Percentage of Cells Terminated	
	Eagle-Picher[a]	ANL[b]
End of Test Period	70	25
Electrical Short Circuits	18	38
Equipment Malfunction	9	3
Electrolyte Leak	3	2

[a] A total of 68 cells terminated.

[b] A total of 172 cells terminated.

C. Failure Mechanisms

(J. E. Battles)

Post-test examinations are conducted on engineering-scale cells (fabricated by industrial contractors and by ANL) to determine cell failure mechanisms, in-cell corrosion reactions, and electrode morphology (*i.e.*, microstructure, active material distribution and utilization, reaction uniformity, impurities, and cross-contamination of electrodes). These results are evaluated, and appropriate recommendations are made for improving cell performance and lifetime.

1. Post-Test Examinations

Post-test examinations have been completed on 30 multiplate cells fabricated by Eagle-Picher for the Mark IA battery program and 30 bicells fabricated by ANL and industrial contractors.

a. Multiplate Cells

(F. C. Mrazek, N. C. Otto)

Of the 30 multiplate cells* examined, operation was terminated because of electrical short circuits in 19 cells and declining coulombic efficiency in eight cells. Three cells had completed the scheduled testing without failure. A short circuit (or partial short circuit) was identified

---

*All but two of these cells were fabricated by Eagle-Picher as part of the Mark IA battery program.

in each of the cells whose operation was terminated due to declining coulombic efficiency; one of the cells that had reached the end of testing was also found to have developed short circuits. Therefore, 28 of the multiplate cells had developed short circuits.

A summary of the failure mechanisms of the multiplate cells is presented in Table IV-5. The major cause of short circuits was extrusion of active material from the positive electrode (through a rupture in the retainer screen and the overlapping BN fabric cups), and subsequent contact of this material with the cell can or the negative electrode. This rupture is apparently caused by the pressure exerted by expansion of the negative electrodes and inadequate electrode restraint (this effect was discussed more fully in Section III.C). The second major cause of cell failure was short circuits in the electrical feedthrough. In five feedthroughs, the short circuits consisted of metallic bridges across the top of the upper insulator caused by corrosion due to the presence of electrolyte in this area. The electrolyte was apparently from a source outside the feedthrough in three cases since there was no evidence of electrolyte migration through the BN powder feedthrough seal. In two feedthroughs, the electrolyte migrated through the BN powder seal, apparently the result of broken seals caused by mechanical stresses on the feedthrough terminals. These cells were from the 6-V Mark IA module (described in Section II.A), which had rigid intercell connectors. In the sixth feedthrough, the short circuit occurred because the lower insulator had broken, apparently during feedthrough assembly.

Table IV-5. Cell Failure Mechanisms for Multiplate Cells

	No. of Cells
Extrusion of active material from positive electrode	10
Short circuit in electrical feedthrough	6
Metallic deposits in separator	4
Equipment malfunction	4
Difficulty in cell assembly	2
Rupture in separator	2
End of test[a]	3

[a] One of these cells was found to have a short circuit which was caused by a metallic deposit in the separator.

A summary of the post-test examination for each of the multiplate cells is given in Appendix D. The following general observations were made from the post-test examinations: the typical negative electrodes expanded in thickness by 20-25%, the separators and negative electrodes were deficient in electrolyte, and varying degrees of Li-Al agglomeration occurred in the negative electrodes. Electrolyte deficiency and Li-Al agglomeration are believed to be important factors in the sharp capacity decline with cycling observed in these cells.

Previous metallographic and chemical analyses (ANL-77-17, p. 40) as well as ion microprobe mass (IMM) analysis (ANL-78-94, p. 160) indicated a significant lithium concentration gradient in thick (0.6 to 1.2 mm) Li-Al electrodes from bicells. These analyses have been extended to the thinner (0.5 to 0.6 mm) electrodes used in the multiplate Mark IA cells; in this cell design, the inner negative electrodes react from both faces rather than from one face, as with the bicell design. The results of IMM analysis of the electrodes from Mark IA cells showed a steeper lithium gradient than that found with the bicells. This result is consistent with the finding of Li-Al agglomeration of the negative electrodes of multiplate cells but not bicells. Further study of the lithium gradient in Li-Al/FeS cells is needed.

b. Bicells

(F. C. Mrazek, N. C. Otto)

A summary of the failure mechanisms for the 30 bicells examined is presented in Table IV-6; this table also includes all engineering-scale bicells examined to date. Cell operation was terminated mainly because of short circuits, although in a few cases the causes of cell failure were loss of capacity, broken conductor, or declining coulombic efficiency. A detailed description of the results of the post-test examination of each bicell is presented in Appendix E.

Copper sulfide has been added to the positive electrode of Li-Al/FeS cells to improve performance. However, post-test examinations have shown that copper deposits across the electrode separator produce short circuits in some cells. Therefore, seven Eagle-Picher bicells[*] were examined to determine the depth of copper penetration into the electrode separator as a function of time (see ANL-79-39, p. 49). The results showed that a 1.6-mm thick BN separator would be completely penetrated[†] in about 20,000 hr (833 days) and that a 1.0-mm thick BN separator would be penetrated in about 10,000 hr (420 days). The depth of copper penetration is generally fairly uniform; however, in cells with long operating times, the copper particles are generally larger and the depth of penetration more rapid in localized areas. Because of this behavior, copper sulfide should probably not be used as an additive to FeS electrodes.

2. Failure Analysis of Mark IA Module D-001

(N. O. Otto, J. A. Smaga, and J. E. Battles)

As reported in Section III.C, Module D-001 of Mark IA failed as a result of a series of short circuits. Post-test examinations of cells and the cell tray were conducted to assist the Failure Analysis Team in determining the mechanisms for the initiation and propagation of failure. The results of these examinations are presented below.

---

[*] These are Li-Al/FeS-Cu_2S bicells with BN fabric separators.

[†] Complete penetration results in a short circuit.

Table IV-6. Failure Mechanisms of Bicells

	Number of Cases		
	FY 79	FY 78	Total[a]
Extrusion of active materials (inadequate confinement)	7	5	29
Metallic copper deposits in separator[b]	1	3	13
Separator cut by honeycomb current collector	2	11	22
Equipment malfunction[c]	0	2	10
Short circuit in feedthrough	2	4	9
Cell assembly difficulties	0	10	12
Broken positive-electrode conductor	0	0	2
Declining coulombic efficiency	3	1	12
Unidentified short circuits	0	3	5
Loss of capacity and poor utilization	2	3	5
Metallic[d] and/or sulfide deposits across separator	2	4	9
End of test	9	6	17
Ruptured BN felt separator and non-uniform expansion of electrodes	2	0	2
Total	30	52	147

[a] All cells that have undergone post-test examinations to date.

[b] FeS cells with Cu_2S additive; one cell used a copper current collector.

[c] Overcharge, temperature excursion, or accidental polarity reversal.

[d] Other than copper.

a. Examination of Cell Tray

The cells in Module D-001 rested on a stainless steel tray lined with mica insulation. Upon disassembly of the module, certain locations of this tray showed evidence of reaction. The predominant feature noted for the module tray was two nearly continuous reaction bands. One band bisected the tray along almost the entire length and corresponded to the gap between the two rows of cells. The second band bisected the tray along its width (extending down one side of the tray wall, across the tray bottom, and up the tray wall on the other side). This reaction band corresponded to the gap between the mica sheets which lined the tray. Both reaction bands had a width of 7 mm, except for some spreading in low spots present in the tray bottom. In some areas, the reaction bands were actually two fine parallel lines, but, in most areas, these twin lines had merged into single broader lines. Also, evidence of reaction was observed at the junction of the vertical sides of the tray with the bottom. The most severe reaction (and possibly arcing) occurred at cell positions 8-10, 15-16, and 24.

Microscopic examination of the reaction bands in several locations revealed very irregular surfaces. Part of the unevenness was due to particle layers which covered or were still attached to the surface in these depressions. These particle layers were composed of fine Type 304 SS particles. Intergranular penetration, ranging from minor to moderate, was also noted for the areas in or adjacent to the reaction zone. Grain-boundary penetration was apparent by the presence of a grey phase (presently unidentified) which delineated the individual grains. Grain-size measurements near the depressions indicated that some grain growth had occurred due to localized heating. However, the sequence in which grain growth and intergranular attack had occurred could not be established.

Pinholes due to severe arcing were observed at two locations on the cell tray bottom. The larger pinhole was located near the center of the tray, between Cells 15 and 16. The hole was ringed by a microstructure which closely resembled an overheated weld zone. Grain growth in the area adjacent to this zone produced grains with diameters three to six times greater than those found in unaffected regions. The smaller pinhole was located at the intersection of the reaction bands. In the area surrounding this hole, the grains had diameters up to four times greater than those for unaffected grains. A metal deposit located near the small hole was also observed on the bottom side of this sample. This deposit consisted of chromium-depleted stainless steel grains in a network of phosphorus-rich P-Fe-Cr-Ni alloy. Another metal deposit was found welded to the bottom bend in the tray near Cell 24. The head of this deposit was once a molten ball of low carbon steel. The neck of this deposit showed evidence of alloying with the stainless steel tray and grain growth was in the direction of heat flow.

b. Examination of Cells

Extensive examinations were conducted on cells from the failed module to determine cell resistance (cold), weight loss, appearance of cells, and condition of feedthroughs. In addition, four cells were subjected to a complete post-test examination, *i.e.*, metallography, scanning electron microscopy, and x-ray diffraction analysis.

A total of 15 feedthroughs from the Mark IA battery were examined; two from short-circuited cells in Module D-002 and the remainder from Module D-001. Examination of the feedthroughs from Module D-002 showed that both short circuits were located in the feedthroughs and were caused by the formation of a metallic bridge across the upper insulator between the conductor rod and the metal retaining ring. Electrolyte had leaked into this location and corroded the conductor rod, subsequently resulting in metal deposition across the insulator gap. The BN powder seal in one feedthrough appeared to be free of electrolyte. In the second feedthrough, the terminal was bent and electrolyte appeared to have leaked through the BN seal. In all of the examined feedthroughs from Module D-001, the loose BN powder (above upper insulator) was discolored to various shades of brown and contained considerable electrolyte. However, the BN powder seal was very near the normal white color and free or nearly free of electrolyte. Removal of the loose BN powder generally improved the resistance across the feedthrough. The lower BeO insulators were fractured in at least one area, and five conductor rods were completely melted at locations near the lower end of the feedthrough assembly.

Sections from Cells 26, 27, 35 and 36 of Module D-001 were examined. These cells were selected as representative of the cells in the failed module; they were completely discharged and only the negative electrodes showed any radical change in appearance. The observations are summarized below:

Positive Electrodes

1. Some areas showed 100% dense packing of the Li_2S, particularly at the electrode faces. Typically, however, the positive electrodes had 80 to 90% active material.

2. Substantial porosity was present, indicating loss of electrolyte.

3. The copper additive appeared to have been molten after discharge since some Li_2S and iron particles were surrounded by copper.

4. The positive current collectors showed only very minor corrosive attack.

5. The stainless steel retainer screens were substantially corroded.

6. No aluminum was detected.

Negative Electrodes

1. The Li-Al alloy had been molten.

2. The current collectors (low-carbon steel) had completely alloyed with Al in most areas.

3. Corrosion of the negative retainer screen was non-uniform (100% reacted in some areas).

4. Two major phases were present: $FeAl_3$ and Fe_2Al_5.

5. Very minor quantities of Li_2S were observed, generally near the electrode face.

6. The electrode did not contain much electrolyte; the electrolyte that was present contained some primary crystals of LiCl.

Separators

1. The positive-electrode Y_2O_3 retainer was nearly 100% reacted. The individual Y_2O_3 fibers had been replaced by small rounded particles which outlined the original fiber shape. Energy dispersive X-ray analysis (EDX) showed only yttrium to be present; however, one or more of the following elements must have been present: Li, B, O, and N.

2. Some Li_2S and iron was found a slight distance into the BN fabric separator.

3. Some areas of the separator, up to 200 μm from the positive Y_2O_3 retainer, were dark under polarized light. EDX analysis indicated that this darkening of the separator was due to the deposition of submicroscopic particles of iron and copper.

4. Generally, the copper and iron deposits penetrated no more than 200 μm into the separator. However, a few scattered areas showed complete penetration of the separator by copper.

5. Most of the separator appeared unaffected by the failure; EDX analysis showed no aluminum in the separator.

Mica Insulation

1. The mica insulation had undergone some reaction caused by the presence of electrolyte and the high temperatures. The microstructure had changed and EDX analysis detected very large amounts of chlorine.

2. Minute spheres of a silicate material were found in several areas and also just inside the cell housings of two cells near a burned through area of the cell housing. These spheres are characteristic of the deterioration of mica under an electric arc. These spheres and other areas of mica insulation had lost most of their metallic cations (aluminum and potassium) which also occurs under the action of electrical discharges.

Cell Housings

1. Most of the cell housings were penetrated by the iron-aluminum reaction in one or more areas along the edges of the cells.

2. In several areas where large holes had been opened in the cell housings, there was extensive evidence of creep. Considerable porosity was detected both within metal grains and in the grain boundaries. This would indicate the presence of high temperatures and appreciable stress levels.

The resistance of each cell was checked during the macroscopic examination and 56 of the 60 cells had cold resistances below 25 Ω. Some of these low resistances were caused by short-circuited feedthroughs brought about by electrolyte being deposited on the outside surfaces of the feedthrough. Most of the remainder of the short circuits were caused by extrusion of positive active material. All but two of the cells showed loss of electrolyte in the range of 50-500 g. Thirteen cells had weight losses equivalent to more than 50% of the total electrolyte. The average weight loss was slightly less than 300 g of salt.

V. CELL DEVELOPMENT

Developmental efforts are in progress to improve the performance of the Li-Al/FeS cell for electric-vehicle applications. These efforts include the following: development of a cell model that relates specific energy and lifetime to design characteristics and mode of operation, development of reference electrodes for polarization measurements in cells and other electrochemical data, and tests of small-scale cells to determine the optimal cell design.

A. Cell Modeling Studies

1. Macro-Modeling Studies

(E. C. Gay, W. E. Miller, F. J. Martino)

During the first half of this report period, engineering cell modeling studies were conducted with the objective of developing empirical equations that relate cell performance to the design characteristics of the cell and the mode of cell operation. For this model, very general empirical equations were developed to fit performance data from FeS and FeS_2 bicells and multiplate cells, the coefficients in the equations being determined by multiple regression analysis. The equation derived to predict the initial (*i.e.*, within 25 cycles) specific energy of a cell was

$$\begin{aligned} \mathrm{SPE} = {} & 2.0710 - 0.37414\ \mathrm{FSUBL} + 14.408\ \mathrm{TSUBLR} \\ & - 1.2149\ \mathrm{VOLT1R} - 1.0586\ \mathrm{VOLT2R} \\ & + 1.4718\ \mathrm{F/LMUL} - 20.790\ \mathrm{LTLV1R} \\ & + 47.968\ \mathrm{LOGV1R} \end{aligned} \tag{1}$$

where

FSUBL = F/L = percent utilization of the limiting electrode*
TSUBLR = TL = limiting electrode thickness/separator-retainer thickness
VOLT1R = V1R = $(\mathrm{OCV} - \mathrm{DCO})/A_e i_D \bar{R}_c$ †
VOLT2R = $(\mathrm{CCO} - A_e i_D \bar{R}_c - \mathrm{DOC})/A_e i_c \bar{R}_c$ ‡
MUL** = 0.01 (theor. cell capacity) (OCV - DCO)/cell weight
F/LMUL = product of F/L and MUL
LTLV1R = natural logarithm of product TL and V1R
LOGV1R = natural logarithm of V1R

---

[*] The electrode that limits cell capacity.

[†] OCV is the open-circuit voltage (V); DCO is the discharge cutoff voltage (V); A_e is the limiting electrode area (cm^2); i_D is the discharge current density (A/cm^2); and R_c is the average cell resistance (Ω).

[‡] CCO is the charge cutoff voltage (V), and i_c is the charge current density (A/cm^2).

[**] This is the only parameter that is not dimensionless (W-hr/kg).

For the specific power (W/kg), the multiple regression analysis produced the following equation:

$$\text{LOG (SP)} = 0.28259 + 0.86170\ \text{LOG (PF)} + 0.12012\ \text{LOG (CF)} + 0.31889\ \text{FCCF} \qquad (2)$$

where

PF = $(\text{OCV})^2/(4\bar{R}_c W)$[*]
CF = charge factor[†]
FCCF = full charged correction factor[‡]

As a check of the model, the calculated and measured performance of sixteen cells was determined and found to be in good agreement; statistical analyses of the error gave favorable results. Further discussion of these equations can be found in ANL-79-39, pp. 55-59.

During the second half of this report period, the same method was used to derive equations for the specific energy of a cell at a given cycle. For development of these equations, data were collected on the design, operating mode, and performance (including lifetime) of 33 previously operated Li/MS cells. The design and performance variables noted for these cells included number of positive plates, active material composition in the positive electrode, LiCl content of the electrolyte, electrolyte volume in the electrodes, negative-to-positive capacity ratio, electrode thickness, separator and retainer thickness, cell resistance, electrode utilization and coulombic efficiency. The operation mode included the number of cycles, discharge rate and current density, cutoff voltages, and cell operating temperature. The cells for which these data were gathered included the following: six Li-Al/FeS bicells fabricated by Eagle-Picher (1A6, I-3B-2, I-3B-1, I-3C-2, 1B4, 1B6) and three by ANL (M-6, M-8, KK-15); five Li-Al/FeS_2 bicells fabricated by Eagle-Picher (2A5, 2B6, 2B8, I-8-040, I-8F-17), three by ANL (M-2, M-4, M-7), and one by Gould (G-04-003); and fourteen Li-Al/FeS multiplate cells fabricated by Eagle-Picher (EPMP-5-017, EPMP-7-031, -032, -033, -036, -046, -055, -056, -057, -062, -063, -071, -075, -086) and one by ANL (M-MP-3).

From the multiple regression analysis, the following equation for the specific energy of a cell at a given cycle number was obtained:

$$\begin{aligned}\text{SPECYC} = {} & 25.210 + 0.442\ \text{SPEBAS} + 0.411\ \text{FSLMUL} \\ & + 0.271\ \text{FSUBL} + 47.442\ \text{VFSNEG} \\ & - 59.373\ \text{VFSPOS} - 0.009\ \text{PPXCYC} \qquad (3)\end{aligned}$$

where SPEBAS and FSLMUL are given by the equations described below; FSUBL is the percent utilization of the limiting electrode; VFSNEG and VFSPOS are the

---

[*] OCV is the open-circuit voltage (V); $\bar{R}_c$ is the average cell resistance (Ω); and W is the cell weight (kg). PF is in dimensions of W/kg.

[†] This factor is assumed to be 1.0 at full charge, 0.5 at 50% discharge, and 0.01 at full discharge, *i.e.*, discharged to the cutoff voltage which is normally 0.9-1.0 V.

[‡] This factor is assumed to be 1.0 at full charge and 0.05 at any state of discharge.

volume fraction of electrolyte salt in the negative and positive electrodes, respectively, and PPXCYC is the product of the number of positive plates and the number of cycles. In Eq. 3, FSLMUL is equivalent to the product of FSUBL and MUL and is defined by

$$\begin{aligned}\mathrm{FSLMUL} = {} & 51.146 + 0.316\ \mathrm{VOLT2R} + 0.665\ \mathrm{VOLT1R} + 0.137\ \mathrm{AHREFF} \\ & + 24.287\ \mathrm{VFSPOS} + 56.418\ \mathrm{TEMPR} - 17.590\ \mathrm{POSPIN} \\ & - 0.359\ \mathrm{OFFEUT} - 91.757\ \mathrm{VFSNEG} - 14.057\ \mathrm{NSPTHC} \qquad (4)\end{aligned}$$

where

VOLT1R = $(\mathrm{OCV} - \mathrm{DCO})/A_e i_D \bar{R}_c$
VOLT2R = $(\mathrm{CCO} - A_e i_D \bar{R}_c - \mathrm{DCO})/A_e i_c \bar{R}_c$
AHREFF = percent coulombic efficiency
TEMPR = (cell operating temp. - 450°C)/450°C
POSPIN = reciprocal of the no. of positive electrode plates
OFFEUT = LiCl composition in electrolyte - 44.2 wt % LiCl
NSPTHC = negative-to-positive capacity ratio

The variable SPEBAS is the specific energy of the cells during the initial cycles (<25 cycles) and is defined by

$$\begin{aligned}\mathrm{SPEBAS} = {} & 141.350 + 0.631\ \mathrm{FSLMUL} - 2.722\ \mathrm{TSUBCR} - 48.032\ \mathrm{VFSPOS} \\ & - 0.052\ \mathrm{FSUBL} - 37.453\ \mathrm{NSPTHC} - 29.754\ \mathrm{TEMPR} \\ & - 11.744\ \mathrm{POSPIN} \qquad (5)\end{aligned}$$

where TSUBCR = counter electrode half-thickness/separator-retainer thickness.

As can be seen in Figs. V-1 and -2, the calculated and measured specific energies at a given cycle for the cells used in the multiple regression analysis are in good agreement (±10%). The correlation coefficient (R^2) was determined from the experimentally determined values and those calculated from Eqs. 3-5. The values of R^2 were found to be 0.90 for Eq. 3, 0.79 for Eq. 4, and 0.75 for Eq. 5, which indicate good correlation. In addition, the standard deviation of the residuals (the difference between the calculated and measured values) was found to be 5.75 for Eq. 3, 4.79 for Eq. 4, and 8.77 for Eq. 5, which also indicate good correlation. The measured and calculated specific energies as a function of cycle number are shown for Cell EPMP-7-055 in Fig. V-3, for Cell M-8 in Fig. V-4, and for Cell I-3B-1 in Fig. V-5. These figures show that the predictive capability of Eq. 3 is very good.

2. Micro-Modeling Studies

(J. Newman and R. Pollard)*

The scale-up of cells depends critically on the current-collector grid transmitting current to the electrode terminals from the location where it is generated electrochemically. This must be accomplished with a minimum of ohmic potential drop and at a minimal collector weight. These conflicting parameters can be used to determine the maximum practical dimensions of an electrode plate. Computer programs for evaluating the ohmic drop in current

---

*Consultants from University of California at Berkeley.

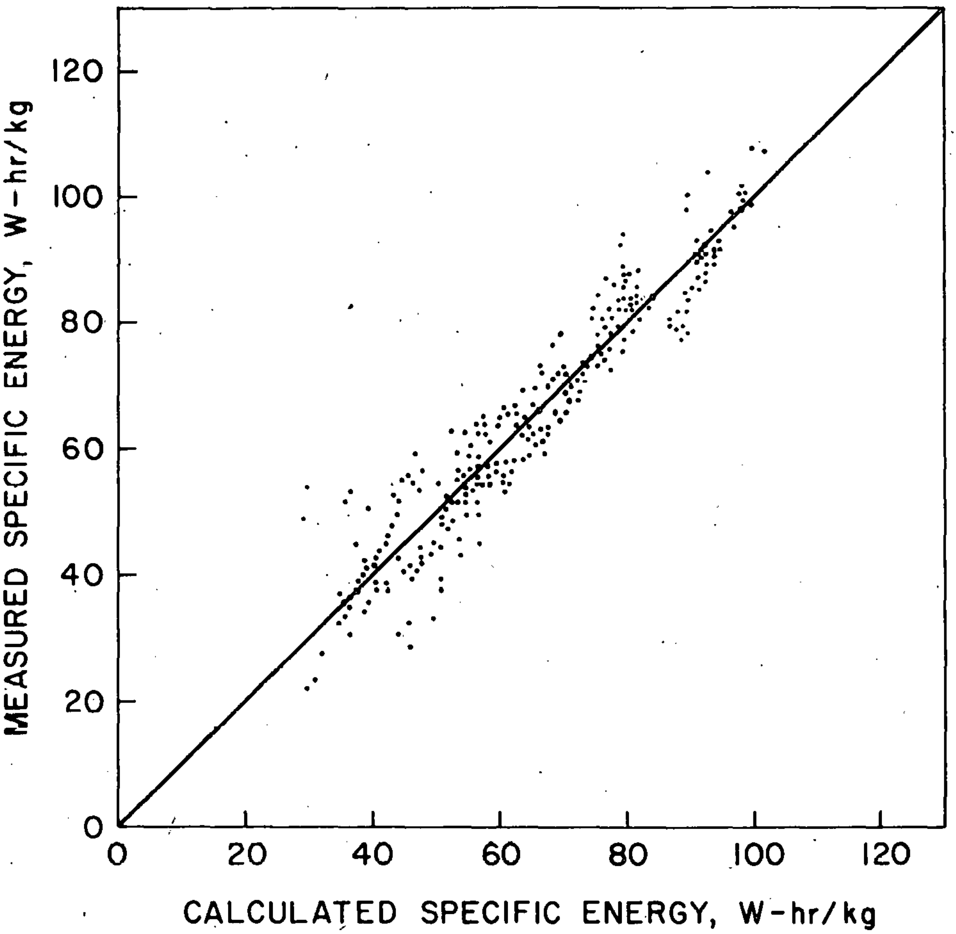

Fig. V-1. Calculated and Measured Specific Energy at the Same Cycle for 19 Li/MS Cells. (Cell Nos.: M-4, M-8, 1A6, M-MP-3, I3B1, I3C2, 1B4, 1B6, 2A5, 2B8, I-8-H-040, G-04-003, and EPMP-7-17, -33, -46, -55, -56, -62, and -63)

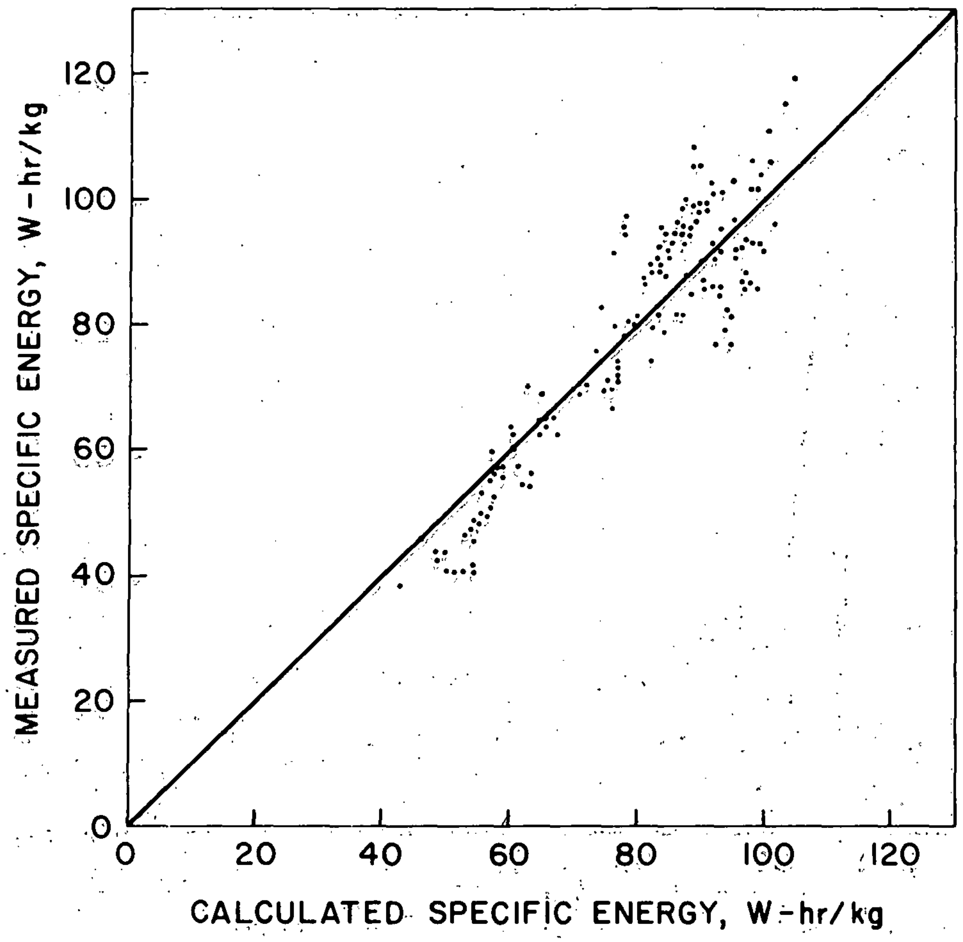

Fig. V-2. Calculated and Measured Specific Energy at a Given Cycle for 14 Li/MS Cells. (Cell Nos.: M-2, M-6, M-7, KK-5, I3B2, I3C1, 2B6, I-8-F17, EPMP-7-31, -32, -57, -71, -75, -86)

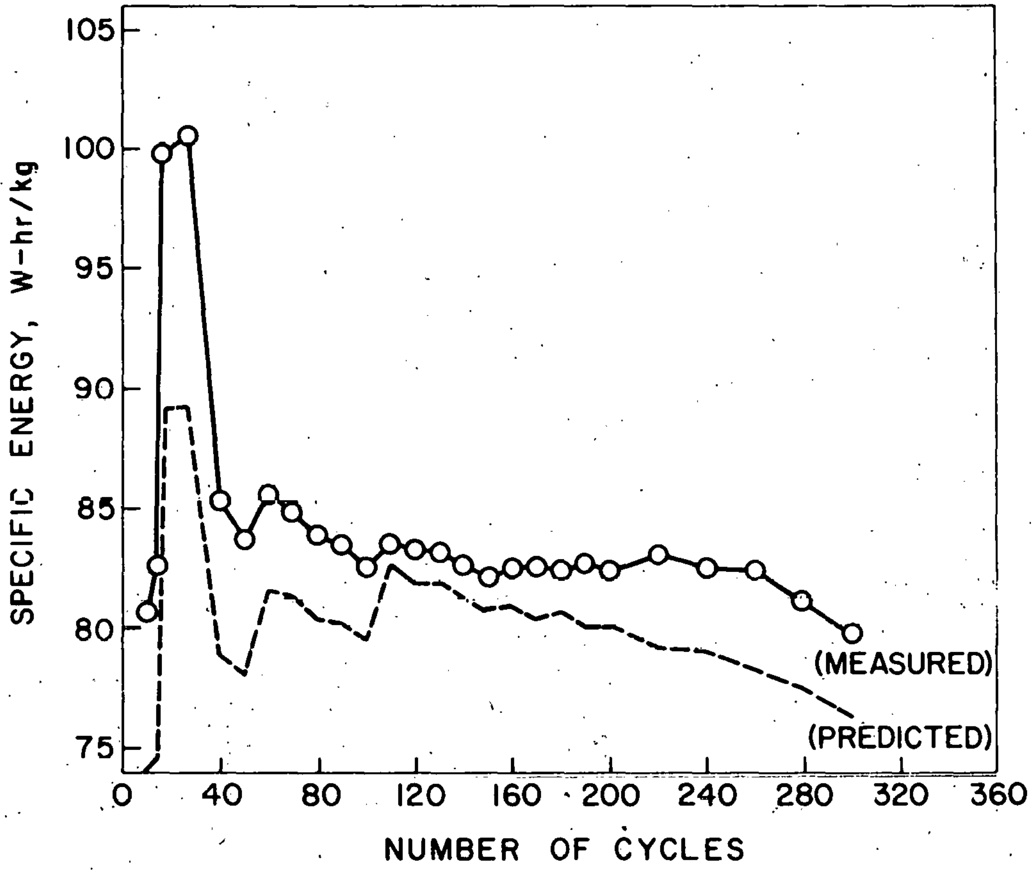

Fig. V-3. Measured and Predicted Specific Energy as a Function of Cycles for Cell EPMP-7-055.

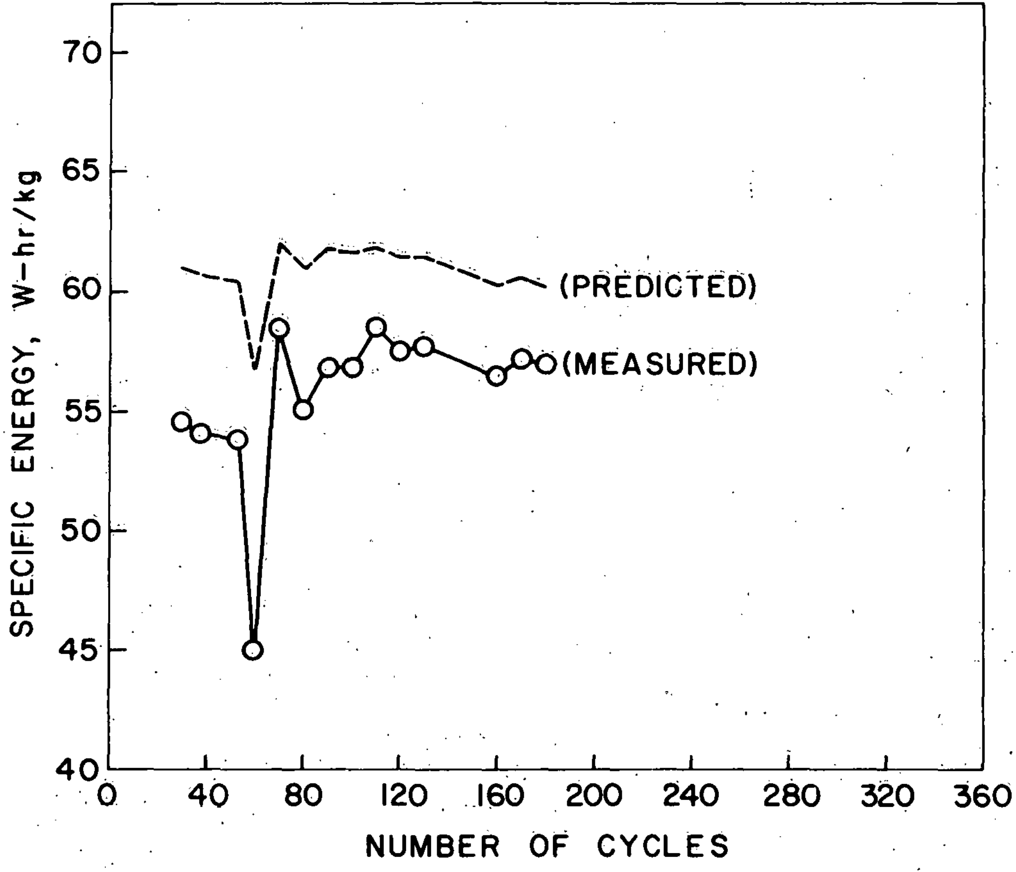

Fig. V-4. The Measured and Predicted Specific Energy as a Function of Cycles for Cell M-8.

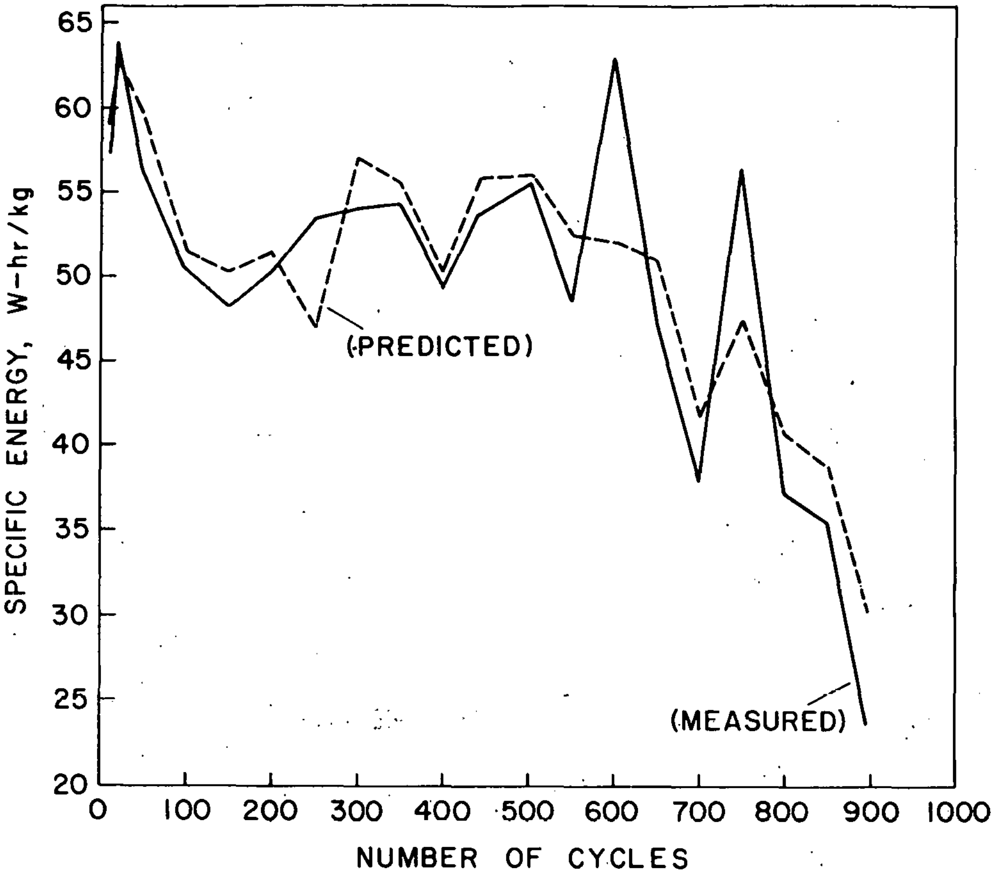

Fig. V-5. Measured and Predicted Specific Energy as a Function of Cycles for Cell I-3B-1.

collecters have been developed at Globe Union, Inc.,[1] and these have been applied to the Li/MS system to determine the optimal current collector weight with respect to specific power without significantly decreasing the specific energy. For these calculations, it was assumed that the positive electrode had dimensions of 17.8 x 17.8 x 0.48 cm and an active-material density of 1.4 A-hr/cm^3, and that its current collector had a conductivity of 1.9 x 10^4/Ω-cm, a weight of 94.3 g, and a density of 7.86 g/cm^3; in addition, it was assumed that the center collector tab was one seventh as wide as the plate.

Figure V-6 shows the current distribution over the face of this positive plate at the beginning of discharge and ∿50% discharge. As can be seen in this figure, the current distribution is highly nonuniform at the beginning of discharge, and more uniform toward the middle of discharge. Late in the discharge, the top of the plate will be completely exhausted, and the total current will need to be produced toward the bottom. An increase in the mass of the current collector will lead to more uniform distributions through most of the discharge. Figure V-7 shows the effect of collector weight on the maximum specific power at the beginning of discharge, at a 1 V cutoff potential, and at a time halfway to the 1 V cutoff (assumed cell weight, 3.5 kg). Resistances external to the plates, such as the bus and feedthrough, have not been included in this analysis. This figure shows that the maximum specific

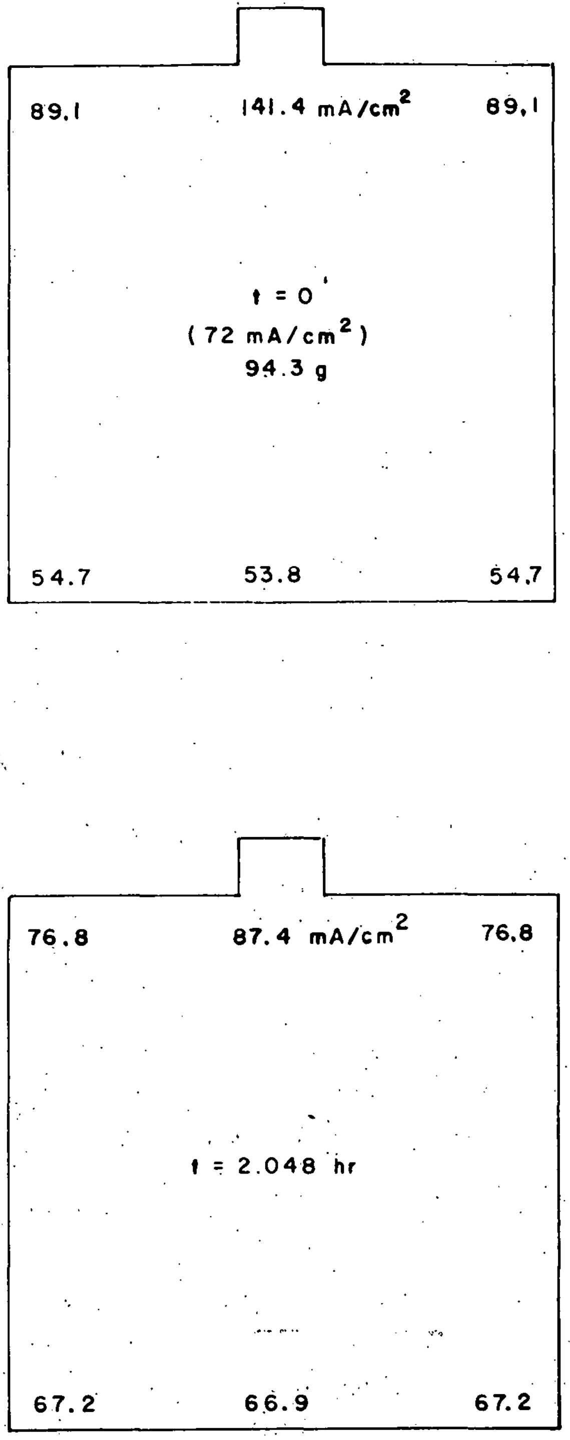

Fig. V-6. Variation of Current Density Over the Face of a Positive Plate at an Average Current Density of 72 mA/cm^2.

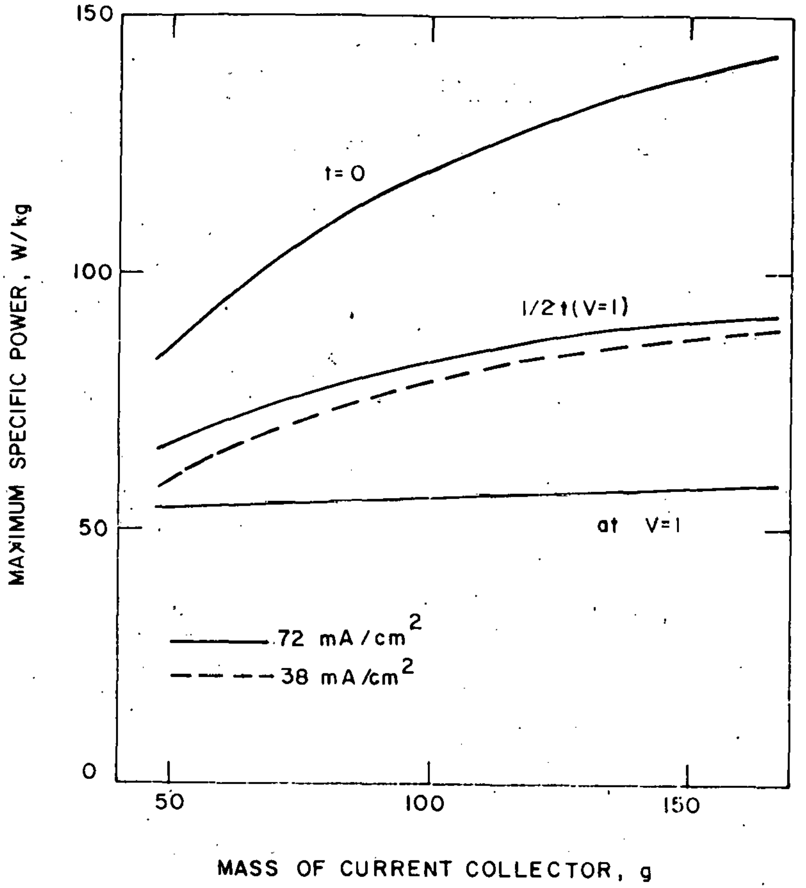

Fig. V-7. Maximum Specific Power as a Function of the Weight of the Current Collector

power increases when the current collector weight is increased between 50 and 150 g; whether a discharge current density of 38 or 72 mA/cm^2 was applied did not appear to have much of an effect on the specific power. Figure V-8 shows the specific energy (the voltage times the current integrated to a 1-V cutoff potential) as a function of current collector weight. This graph shows that the specific energy at a discharge current density of 72 mA/cm^2 is a maximum at a current collector weight of 150 g. For a current density of 38 mA/cm^2, the specific energy is maximized at a much lower collector weight--∿70 g.

The adiabatic temperature rise can be computed on the basis of the equation,

$$\Delta T = \frac{U_o - V - T_o \frac{dU_o}{dT}}{C_p} I\Delta t$$

Here I is the current per positive plate, U_o is the open cell potential, V is the actual cell voltage, and C_p is the heat capacity per positive plate. To calculate the adiabatic temperature rise, the following assumptions were made: C_p = 0.245 cal/g-K or 1.025 J/g-K (Ref. 2), U_o = 1.34 V, and $dU_o/dT = -1.55 \times 10^{-4}$ V/K (ANL-77-17, p. 47). Figure V-9 shows that an increase in the grid weight will decrease the internal heat losses of the cell. This figure does not apply directly to the Mark IA cell, which has different electrode

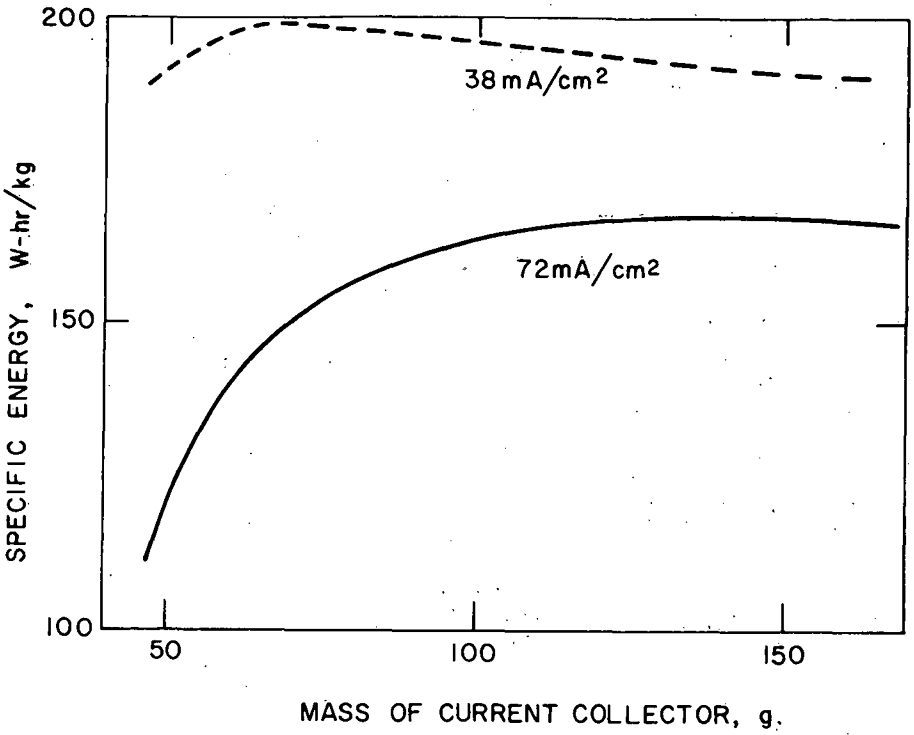

Fig. V-8. Specific Energy as a Function of the Weight of the Current Collector

characteristics from those used for the model calculations. Thus, a separate calculation was made to determine the adiabatic temperature rise for a complete short circuit of the Mark IA cell (weight, 3.9 kg; positive-electrode charge, 136.7 A-hr per positive plate). The equation used for this calculation,

$$T_f = T_o + \frac{(U_o - T_o \frac{dU_o}{dt})Q}{C_p}$$

yielded a temperature rise to 986°C.

Future work will include refinement of the basic electrochemical characteristics of the system by comparison with new experimental data. By including the weight of the can and terminals as well as the terminal resistance, it will be possible to predict the plate thicknesses and plate areas, as well as current collector weights, which will yield desired values of specific energy and specific power.

In a related program (direct Department of Energy funding through the Division of Solar, Geothermal, Electric and Storage Systems), reaction distributions within the porous electrodes of the LiAl/FeS cell were calculated.[3] A one-dimensional model has been developed for a prismatic cell consisting of a negative electrode, separator, electrolyte reservoir, and positive electrode.

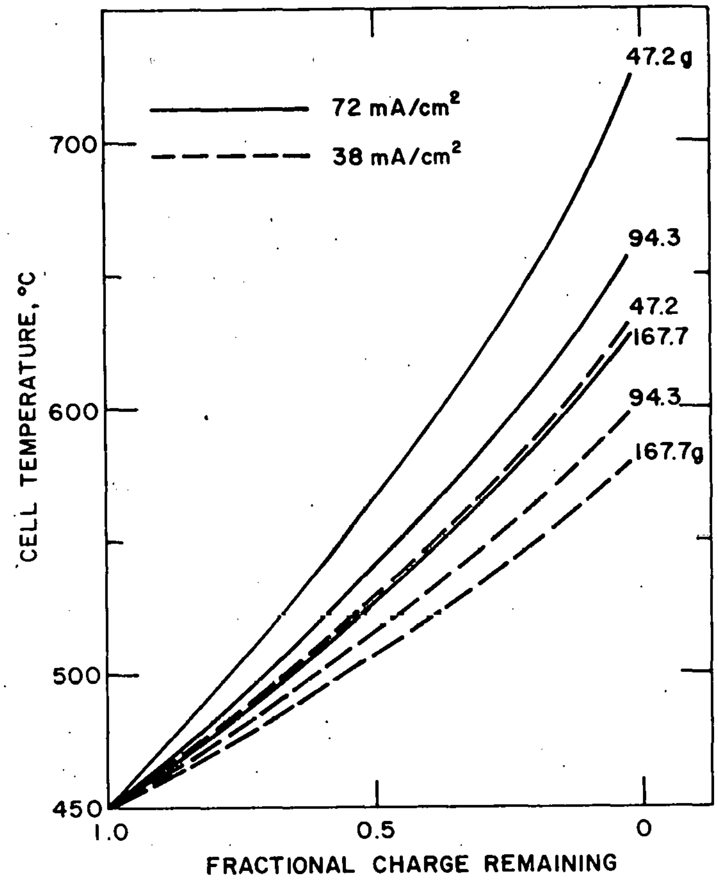

Fig. V-9. Adiabatic Temperature Rise

In this model, five coupled, non-linear, partial differential equations are solved simultaneously in a direction normal to the separator, and a description of the whole system is obtained at each time step; the possibility of consecutive reactions, or specific simultaneous reactions, is incorporated in this analysis. Physical phenomena described by this model include ohmic potential drop and diffusion potential within the electrolyte; changes in porosity and electrolyte composition due to electrochemical reactions; local reaction rates and their dependence on local composition and potential; and diffusion, convection, and migration of electrolyte.

Figure V-10 shows the electrolyte composition in the cell at several times during a constant-current discharge. The dashed horizontal line indicates the solubility limit for LiCl at the initial temperature of 450°C; the solid horizontal line indicates the initial LiCl composition of the electrolyte. The initial composition (67 mol % LiCl) is LiCl-rich compared with the eutectic composition (58 mol % LiCl). Consequently, precipitation of KCl in the positive electrode is delayed until about 3 hr of discharge. However, LiCl would have had a tendency to precipitate in the negative electrode if the temperature of the cell had not risen from 450°C to 477°C after 2.5 hr of discharge.

The nonuniform concentration during discharge results because lithium ions are removed from the electrolyte at the positive electrode according to one of the reactions,

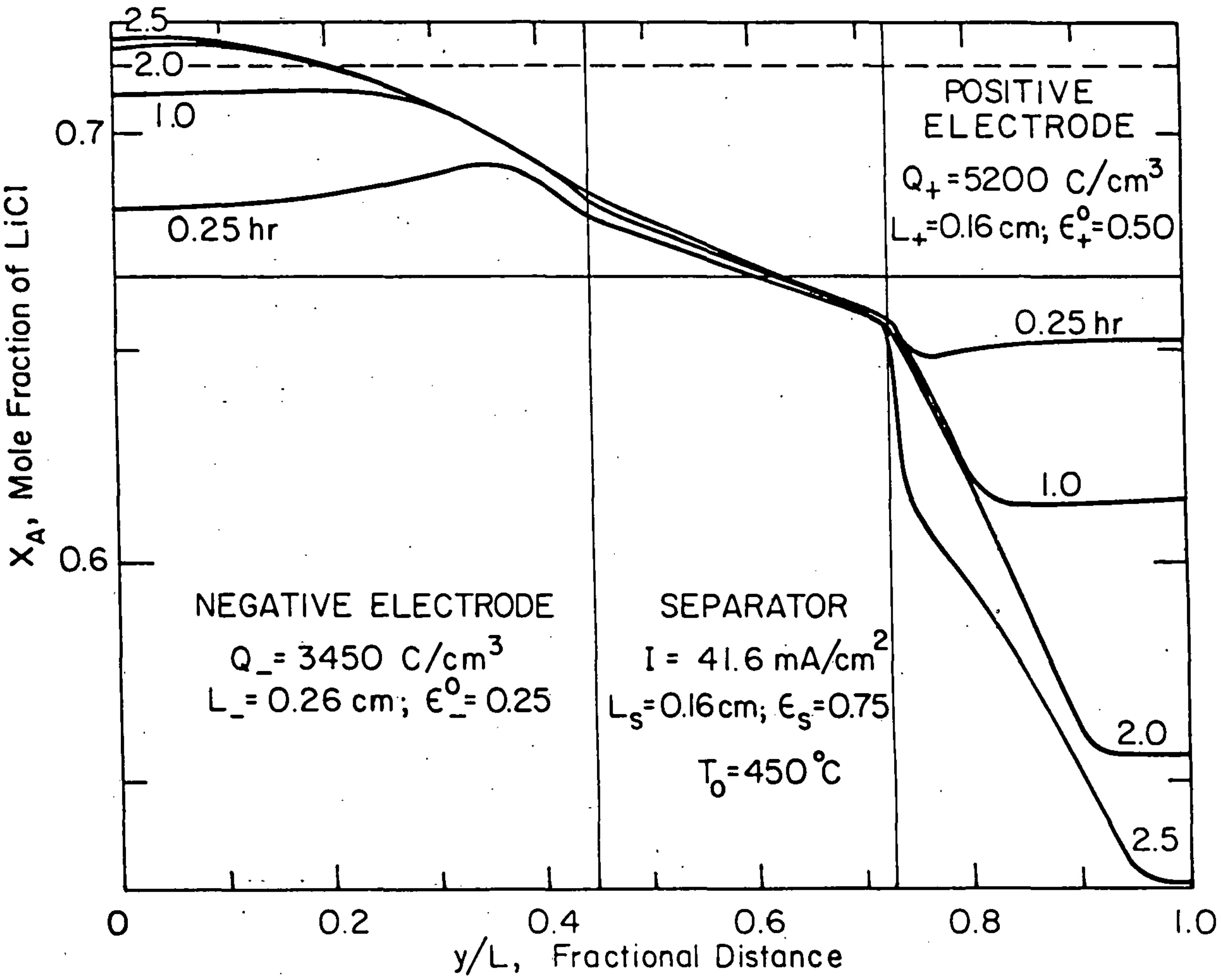

Fig. V-10. Position Dependence of Mole Fraction LiCl at Different Discharge Times at 450°C.
Current Density = 41.6 mA/cm^2
Capacities: Q_- = 3450 C/cm^3; Q_+ = 5200 C/cm^3
Initial Porosities: $\varepsilon_{-}^{o} = 0.25$; $\varepsilon_{s}^{+} = 0.75$; $\varepsilon_{+}^{o} = 0.50$
Thickness: L_- = 0.26 cm; L_s = 0.16 cm; L_+ = 0.16 cm

$$2\ FeS + 2e^- + 2Li^+ \rightarrow Li_2FeS_2 + Fe \qquad (1)$$

or

$$Li_2FeS_2 + 2e^- + 2Li^+ \rightarrow Fe + 2\ Li_2S \qquad (2)$$

and introduced into the electrolyte at the negative according to the reaction

$$Li \rightarrow Li^+ + e^- \qquad (3)$$

Since the transference number of Li^+ is not unity, a nonuniform concentration develops, and diffusion aids migration in the transport of lithium ions.

The negative electrode starts with a small initial porosity (0.25), which increases as the reaction proceeds. The reaction zone also penetrates somewhat into the negative electrode as lithium is partially consumed and the potential required for reaction (3) becomes more positive. At the positive electrode, reaction (1) proceeds first; and, after 2 hr, this reaction front has proceeded about two-thirds of the way through the positive electrode (see Fig. V-10). The FeS is fully converted to Li_2FeS_2 behind this reaction front, which is itself relatively narrow. Subsequently, a reaction front for reaction (2) begins to move through the positive electrode; its effect on the electrolyte composition can be seen in Fig. V-10 at 2.5 hr. The electrode porosity becomes smaller in the positive electrode as reactions (1) and (2) proceed, and this results in steeper concentration gradients. Any precipitation of KCl (or LiCl in the negative electrode) which might occur further aggravates the problem of ohmic potential drop in the electrolyte.

Figure V-11 shows the volume fraction of the active materials in the positive electrode shortly after reaction (2) has begun to occur (same cell variables as given for Fig. V-10). Here the initial electrolyte composition is that of the eutectic, and precipitation of KCl can occur. This is responsible for the extremely small volume fraction of electrolyte at a distance of about 0.075 cm. This effectively blocks the back portion of the electrode. Within the electrode, reaction (1) has occurred to some extent, producing a certain volume fraction of Li_2FeS_2 and decreasing the electrode porosity somewhat from its initial value of 0.5. Near to the separator (<0.07 cm), there is a plateau for the volume fractions of Li_2FeS_2, Fe, and electrolyte, corresponding to completion of reaction (1). At distances <0.01 cm, the consequence of reaction (2) can be seen: Li_2FeS_2 is consumed, Li_2S is produced, and the electrolyte volume fraction is small. (This effect may be compensated for in the real system by appreciable swelling of the positive electrode.)

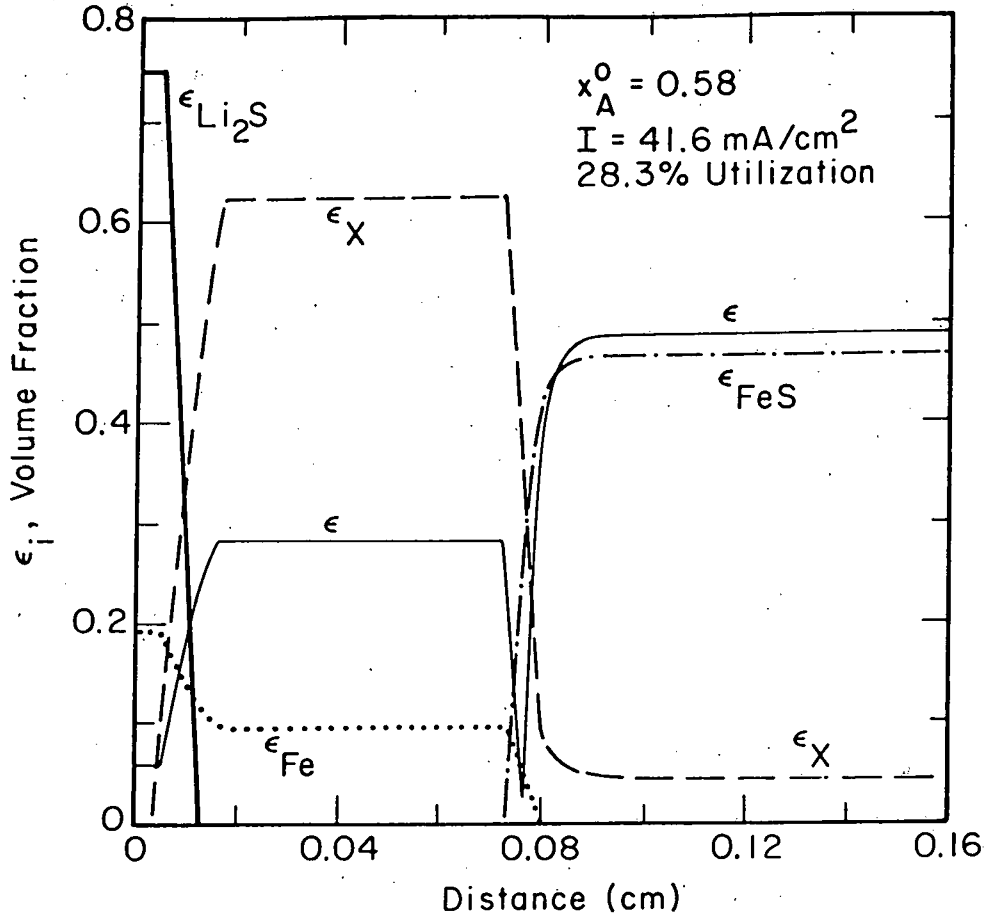

Fig. V-11. Volume Fraction of Active Materials in the Positive Electrode

B. Reference Electrode System

(D. R. Vissers)

Micro-reference electrodes are being developed to investigate the polarization characteristics of electrodes in Li/MS engineering cells and to carry out other electrochemical studies in these cell systems.

1. Development

(L. Redey)[*]

The reference electrodes used in engineering-scale cells must possess a well-defined potential, be electrochemically stable for long periods (months), and be rugged and adaptable to miniaturization. The high lithium and sulfur activities present in the Li/MS cell system place stringent limitations on the suitable materials for the reference electrode.

Five cell couples were investigated as potential reference electrode systems: $Ag/AgCl/Cl^-$, $Ag/Ag_2S/S^=$, $Ni/Ni_3S_2/S^=$, Fe/Li-Al (α and β phase)[†]/Li^+,

---

[*] Technical University of Budapest, Hungary.

[†] The Li-Al alloy used for these tests contained 43 at. % Li.

and Al/Li-Al (α and β phase)/Li^+. (Some of these couples had been investigated in earlier studies.)[4-7] The stabilities of these cell couples were evaluated against a Li-Al alloy electrode with a capacity of 3 to 5 A-hr; consequently, all emf values presented are given *vs.* the two-phase Li-Al alloy electrode. The Li-Al electrode has a very stable potential in LiCl-KCl melts; but, because of its large size, it is impractical as a reference electrode in engineering cells.

The reference electrodes tested had a BeO tube, 17.8 cm in length and 3.2 mm in diameter, as the insulator housing, and a Y_2O_3 plug on top of a short section of Al_2O_3 tube to form a diffusion barrier (which develops a resistance of 7 kΩ/cm). A drawing of one of the reference electrode couples is shown in Fig. V-12. All the electrochemical couples, with the exception of the Fe/Li-Al (α and β phase)/Li^+ couple (fabricated using particulate Li-Al), were formed electrochemically by pulse charging.

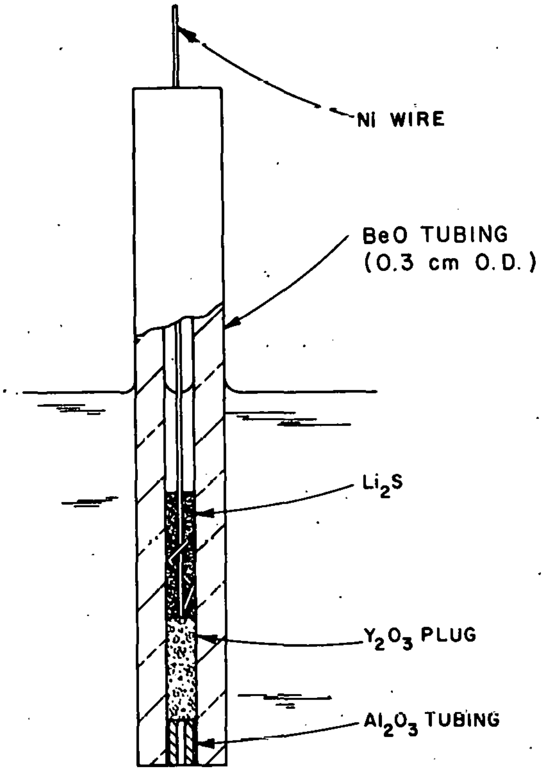

Fig. V-12. Reference Electrode Design

The stabilities of the five electrode couples are presented in Table V-1. The data indicate that the $Ni/Ni_3S_2/S^=$ couple possesses the best long-term stability, and also that the Al/Li-Al/Li^+ electrode couple has excellent short-term (∿30 min) stability. Therefore, $Ni/Ni_3S_2/S^=$ is the most suitable reference electrode, and Al/Li-Al/Li^+ has potential as an *in situ* reference electrode calibration standard for the $Ni/Ni_3S_2/S^=$ electrode. For the latter purpose, an aluminum wire will be intermittently charged with lithium, thereby resulting in a well-defined potential. One can characterize this charging technique by the potential recorded during the procedure (see Fig. V-13). The constant potential value indicated by the consecutive steady-state, open-circuit values corresponds to the well-defined potential of the two-phase (α and β phase) Li-Al alloy. This series of potential values can be obtained with a reproducibility of ±1 mV on new aluminum wires or on the same wire with the consecutive charging procedures. After a period of time, depending on the quantity of lithium deposited, the steady-state potential of this alloy electrode shifts up toward positive values, but a repeat of the intermittent charging technique can again achieve the well defined value. After a few repetitions of this charging technique, the same aluminum wire can no longer be used; but replacement of this monitoring electrode is very simple.

Table V-1. Summary of Data on Reference Electrode Couples

Couple	Observed Potential, V *vs* Li-Al	Observed Stability *vs* Li-Al
$Fe/Li\text{-}Al/Li^+$	0.001 ± 0.001	±0.0015 V/day[a]
$Al/Li\text{-}Al/Li^+$	0.001 ± 0.001	±0.0005 V/hr
$Ag/Ag_2S/S^=$	1.610 ± 0.003	±0.010 V/day
$Ag/AgCl/Cl^-$	2.3 ± 0.1	±0.100 V/day
$Ni/Ni_3S_2/S^=$	1.361 ± 0.0015	±0.0005 V/day

[a] The potential of this couple tended to drift upward with time.

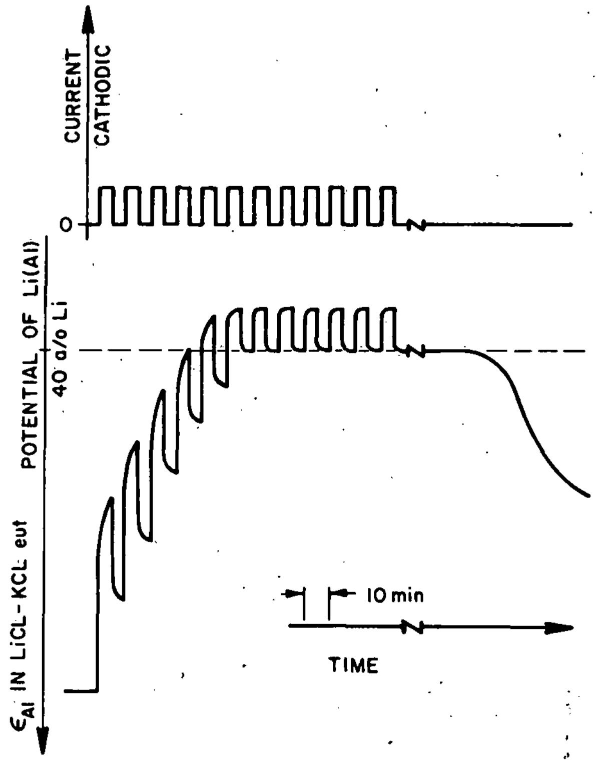

Fig. V-13. Formation of $Al/Li\text{-}Al(\alpha+\beta)/Li^+$ Reference Electrode (Primary Standard)

A $Ni/Ni_3S_2/S^=$ reference electrode inserted in an engineering cell is schematically shown in Fig. V-14. As shown in the figure, the reference electrode is encased in a stainless steel tube. A saw-toothed loop at the bottom of the nickel wire is used to hold the BeO tubing firmly in place, thereby avoiding the need for a rigid connection between the reference electrode and the stainless steel tubing. With this design, the reference can be raised or lowered quite easily; however, recent studies indicate that electrolyte has a tendency to creep up the BeO tube and/or stainless steel tube and create a short circuit in the reference electrode. Therefore, to prevent this problem and to simplify the use of reference electrodes in engineering-cell applications, attempts are being made to shorten the reference electrode enclosure external to the cell; at present, the enclosure is 50 cm long. A Conax thermocouple feedthrough (∿10 cm in length) is being considered as an alternative to the present enclosure design.

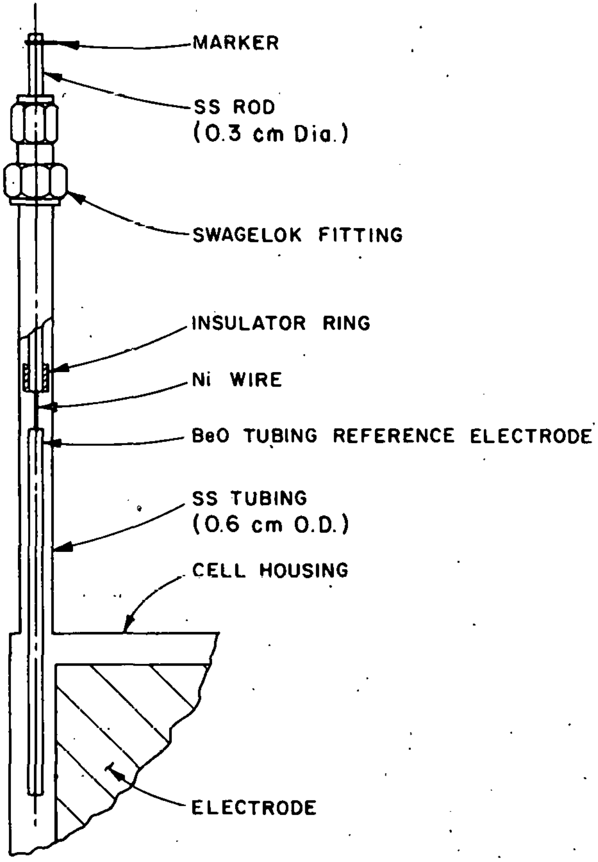

Fig. V-14. Reference Electrode Enclosure and Placement.

2. Electrode Potential Measuring Techniques
(L. Redey, F. J. Martino)

The basic principles of Luggin capillary tip placement to avoid error in electrode potential measurements for simple laboratory cells are well known.[8-11] Such cells are usually designed for the special purpose of the measurement. However, the electrodes used in engineering cells have large areas (∿300 cm^2) on each face, and are placed in cells of fixed geometry.

Consequently, the potential gradients which will develop over these large electrode surfaces and the limited locations available for reference electrode placement make it difficult to determine the proper placement of the Luggin capillary.

To investigate the potential distribution, an engineering-scale (122 A-hr) Li-Al/FeS bicell (M-8-RE),* was equipped with reference electrodes in six locations, as shown in Fig. V-15. A computerized eight-channel data acquisition system was used to monitor the potential of the working electrodes with respect to the reference electrodes. Measurements of the electrode potentials were obtained during a steady state (constant-current discharge) and after current interruption. For the relaxation measurements, a fast switch was used to interrupt the current, and a magnetic disc was used to record the potential decay curves. The accuracy of the relaxation measurements was about ±1 mV. The usual time interval of recording was 5 min (plus a short period prior to the current interruption), with a 1 to 500 msec sampling time.

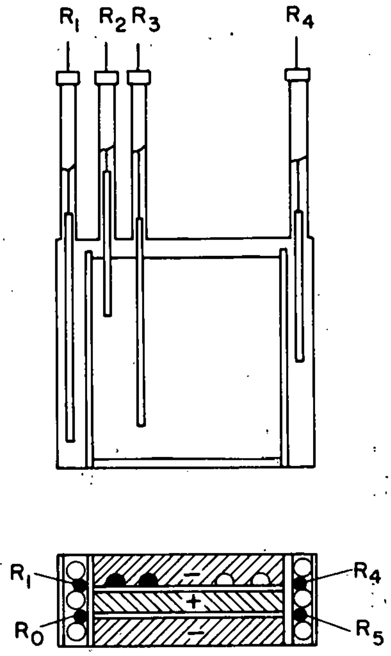

Fig. V-15. LiAl/FeS Bicell with Six Reference Electrodes

Figures V-16 and 17 show the effect on polarization of a current interruption during a 10-A discharge with a 20-A and a 50-A pulse, respectively. As can be seen by comparing Figs. V-16 and V-17, the positive electrode is limiting the power of the cell. In addition, the reference electrodes indicate large differences in potentials for both the positive and negative electrodes, both during steady state and current interruption. Therefore,

---

*This cell has a design similar to that of Cell M-8, reported in ANL-79-84, p. 125.

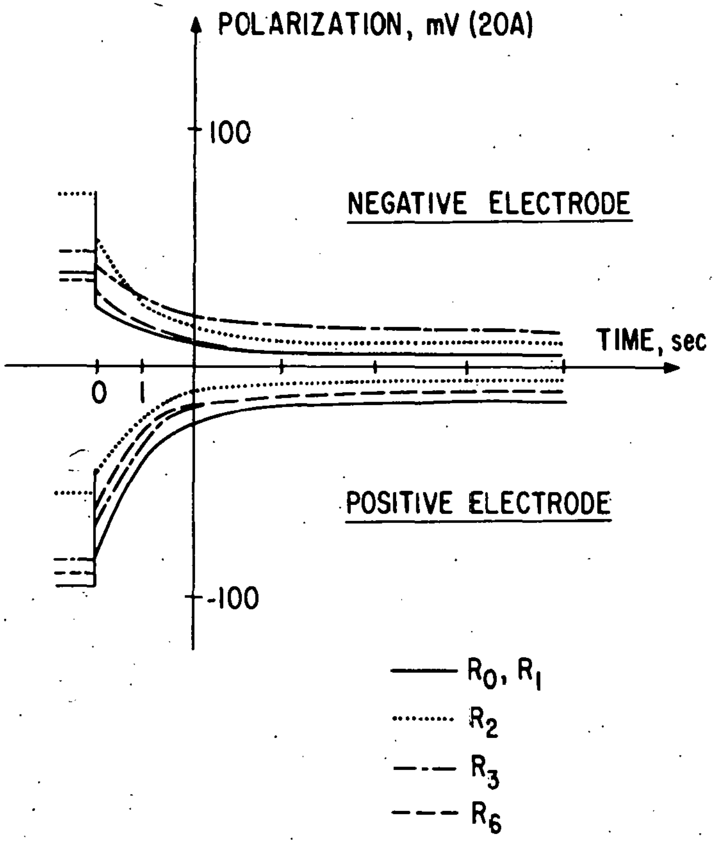

Fig. V-16. Potentical Decay Curves Recorded after 20-A Discharge Pulse (10-A discharge cycle).

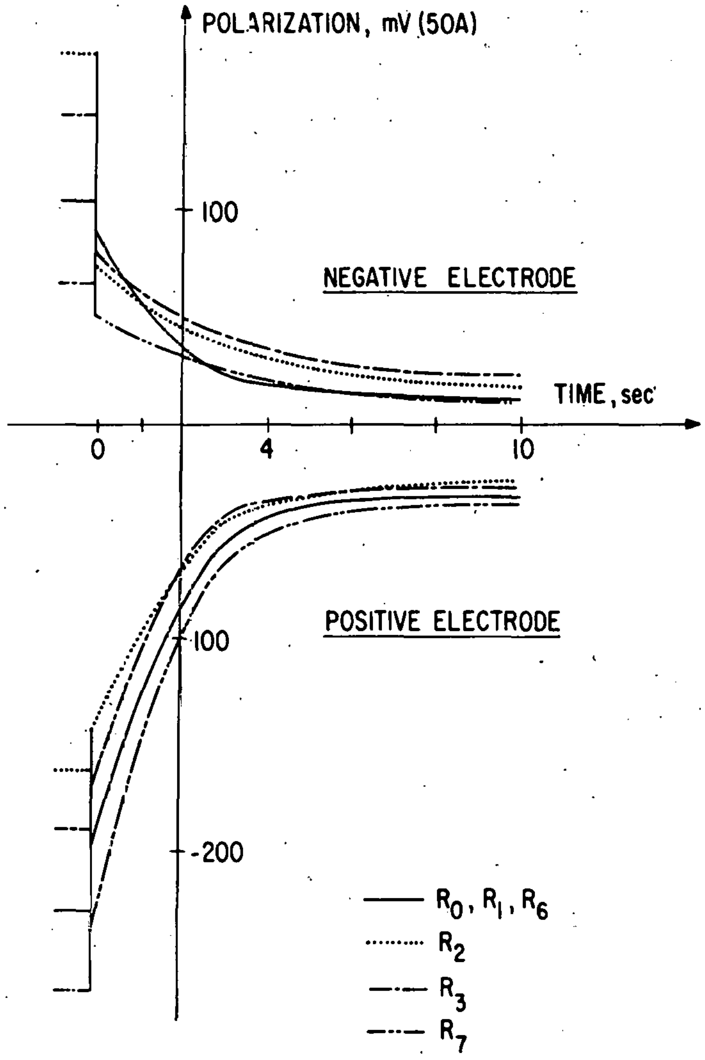

Fig. V-17. Potential Decay Curves after a 50-A Discharge Pulse (during a 10-A discharge cycle).

there are large potential gradients present across the surfaces of the working electrodes, probably caused by non-uniform current distributions on the electrode surface developed during operation. These non-uniform current distributions create activity gradients, which cause local currents to develop within the working electrodes. The presence of these local currents complicate the electrochemistry of the cell, and analyses of the local currents using reference electrodes will probably be necessary to successfully characterize the engineering cell and its working electrodes.

Of the reference-electrode positions tested, R_2 and R_3 were found to be the most reliable for measurements of electrode potentials; however, the installation of reference electrodes at these two positions is very difficult. Further work on the optimal position for the reference electrode will be continued in the next report period.

3. Applications

(L. Redey, F. J. Martino, K. E. Anderson, T. D. Kaun, J. D. Arntzen, P. F. Eshman)

Measurements are being made with reference electrodes in three different size cells: large prismatic cells (∿100 A-hr), intermediate-scale (5-15 A-hr) cylindrical cells, and small tubular cells. To evaluate the polarization of the electrodes in large engineering cells, an automatic data acquisition system has been built. This system can be programmed to obtain either IR-free or IR-included data, as well as the relaxation characteristics of the electrodes as a function of current, state of charge, and cycle number.

A reference electrode was inserted into position R_2 in an engineering prismatic bicell (EP-RE-1) with Mark IA-type electrodes. The capacities of the 12.7 x 17.8 cm FeS-Cu_2S and Li-Al electrodes were 97 and 108 A-hr, respectively. The cell was charged at a 10-A current and discharged with a 17.5-A current. After 10 cycles of operation, this cell attained its peak capacity, 90 A-hr, which declined by 0.22% (0.2 A-hr) per cycle thereafter. After 230 cycles, the rate of capacity decline had decreased to 0.04% per cycle. At this stage of cycling, the capacity was 69 A-hr, but the coulombic efficiency remained at 99%.

Figure IV-18 shows the electrode potential as a function of utilization for both electrodes at charge cycles 18 and 37 and discharge cycles 19 and 38. The following observations were made from the test results of this cell:

a. The power of the cell is limited by the positive electrode at all states of charge.

b. The capacity of the cell is limited by the negative electrode during discharge and by the positive electrode during charge.

c. For evaluations of the performance characteristics of electrodes in engineering cells, the end of the charge and the discharge cycles should be determined by the potential of either the positive or negative electrode rather than by the cell potential itself.

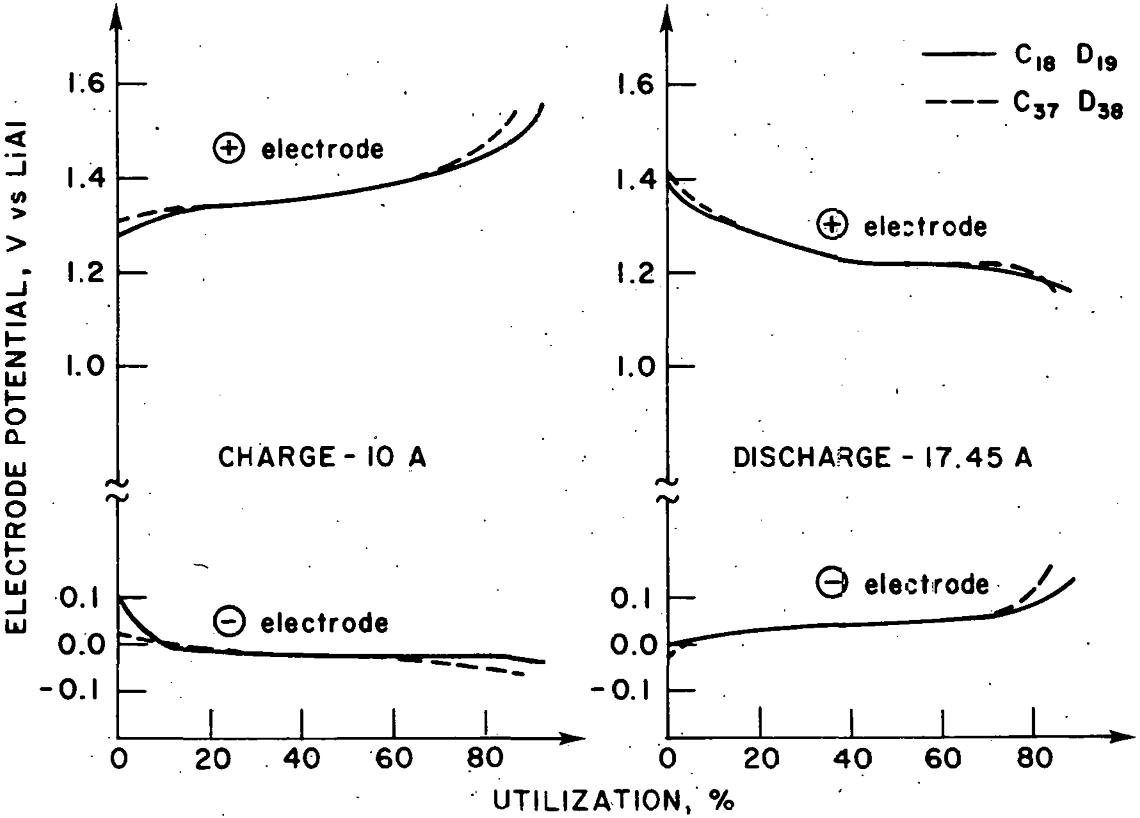

Fig. V-18. Electrode Potential as a Function of Utilization for Cell EP-RE-1

d. An examination of the potential curves of the negative electrode obtained for Cell EP-RE-1 suggest that Li-Al alloys of higher lithium content (perhaps ~50 at. % Li) should be used.

e. Insufficient information is available at present to determine which electrode in Cell EP-RE-1 limits lifetime.

A reference electrode has also been placed at the interface of the electrodes in an intermediate-scale LiAl(12 A-hr)/FeS_2(10 A-hr) cylindrical cell with horizontally mounted electrodes. The cutoff potentials were 1.9 V for charge and 1.0 V for discharge. Measurements made with this reference electrode are being used to investigate the performance and capacity retention characteristics of the Li-Al/FeS_2 system. Preliminary results indicate the following: (1) when the cell was operated at 25 mA/cm^2, the capacity was limited by the positive electrode, and (2) the capacity decline of the cell appears to result from an increase in the internal resistance of the positive electrode. The reference electrode systems seems to be working perfectly.

Small (0.6-cm dia), tubular cells which contain reference electrodes are being developed to obtain electrochemical cell data, *e.g.*, electrode polarization and current distribution for the one-dimensional cell model described earlier in this section. Data obtained from the model will be used to help optimize large-scale engineering cells.

C. Cell Optimization Studies

(E. C. Gay)

In this effort, means of improving the performance of Li/MS cells were investigated through tests with small-scale cells; those changes found to be promising were then tested in engineering-scale cells (Section III-A).

1. Electrolyte Alternative

(H. Shimotake, H. Ohno,* K. E. Anderson)

Past studies (ANL-78-94, p. 126) had indicated that utilization in the FeS electrode is improved when the LiCl-KCl electrolyte contains 66.7 mol % LiCl (liquidus temperature, 425°C). This departure from the eutectic composition, however, raises the liquidus temperature close to the normal operating temperature of the cell (450°C), which may result in solidification of part of the electrolyte. Therefore, addition of a third compound to the LiCl-KCl electrolyte as a means of increasing the lithium ion concentration without significantly raising the liquidus temperature of the eutectic was investigated.

In a preliminary study, LiF, LiBr or NaCl (less than 10 mol %) was added to 68 mol % LiCl-32 mol % KCl electrolyte, and the liquidus temperature determined by differential thermal analysis. Typical results are shown in Table V-2 together with those of the LiCl-rich and eutectic electrolytes. As can be seen in this table, the ternary salt systems containing the LiF, LiBr, and LiI additives all have lower liquidus temperatures than those of the LiCl-rich system. The LiCl-KCl-LiF system was particularly attractive because of its low liquidus temperature and relatively low cost.

---

*Research Associate from Japan Atomic Energy Research Institute.

Table V-2. Liquidus Temperatures of Electrolytes

Electrolyte	Composition, mol %	Liquidus Temperature, °C
LiCl-KCl	58.8-41.2	352
LiCl-KCl	66.7-33.3	425
LiCl-KCl-LiF	62.7-28.2-9.1	397
LiCl-KCl-LiBr	57.0-33.9-10.0	416
LiCl-KCl-NaCl	61.2-29.7-9.1	429

In a subsequent test, four small-scale cells were cycled with the following electrolytes: Cell 1, LiCl-KCl-LiBr; Cell 2, LiCl-KCl-LiF; Cell 3, LiCl-rich, Cell 4, LiCl-KCl eutectic. The compositions of these electrolytes are given in Table V-2. The positive electrodes for these cells had a theoretical capacity of about 6 A-hr, and the negative electrodes contained approximately 3 A-hr of Li-Al powder and 9 A-hr of aluminum powder. These cells were operated at temperatures of 425-500°C and were cycled at a charge current density of 50 mA/cm^2 and discharge current densities of 25 to 200 mA/cm^2; the cutoff potentials (IR excluded) were 1.6 and 1.0 V for charge and discharge, respectively.

Figure V-19 shows the positive-electrode utilization of the test cells as a function of temperature at charge and discharge current densities of 50 mA/cm^2. At 450 and 500°C, Cells 1 and 3 have about the same utilization (90-93%). At 435°C, the utilization of Cells 1 and 2 is greater than 85%. In addition, at 425°C, Cell 2 has a utilization that is slightly lower than that at 450°C; however, the cell capacity remained stable. At 425°C, Cell 3 has very little capacity because the operating temperature is very close to the electrolyte liquidus temperature. On the basis of these tests, it was decided to test the LiCl-KCl-LiF electrolyte in an engineering-scale cell (reported in Section III.A).

2. Ionic Conductance of Ceramic Separators

(H. Ohno, Y. Iwadate,* H. Shimotake)

The ionic conductances of the porous ceramic separators used in Li/MS cells are important to know for cell design and cell modeling studies. Therefore, an experimental apparatus was constructed to measure the ionic conductances of BN felt and MgO powder at different porosities.

The experimental apparatus developed for these measurements is shown in Fig. V-20. Prior to testing, the BN felt was treated with a $LiAlCl_4$ wetting agent (ANL-78-94, p. 158), and the MgO powder was mixed with a known amount of LiCl-KCl powder, heated to the melting point of the salt, cooled to room temperature, and ground up. The test materials were then packed into a conductance cell (Fig. V-20b) made of BN to a desired porosity and retained in the cell

---

*Student from Tokyo Institute of Technology.

with 300-mesh stainless steel screen. The loaded cell was lowered into a glove-box furnace well containing molten LiCl-KCl. The furnace was evacuated and pressurized with helium to fill the conductance cell with molten salt. A current was passed between this cell and a counter electrode (iron) by means of a frequency generator, and the conductances at different frequency levels (0.6 to 15 kHz) were measured with an AC impedance bridge. To obtain the polarization-free resistance, the curve for the measured resistance versus the inverse of the frequency was extrapolated to infinity.

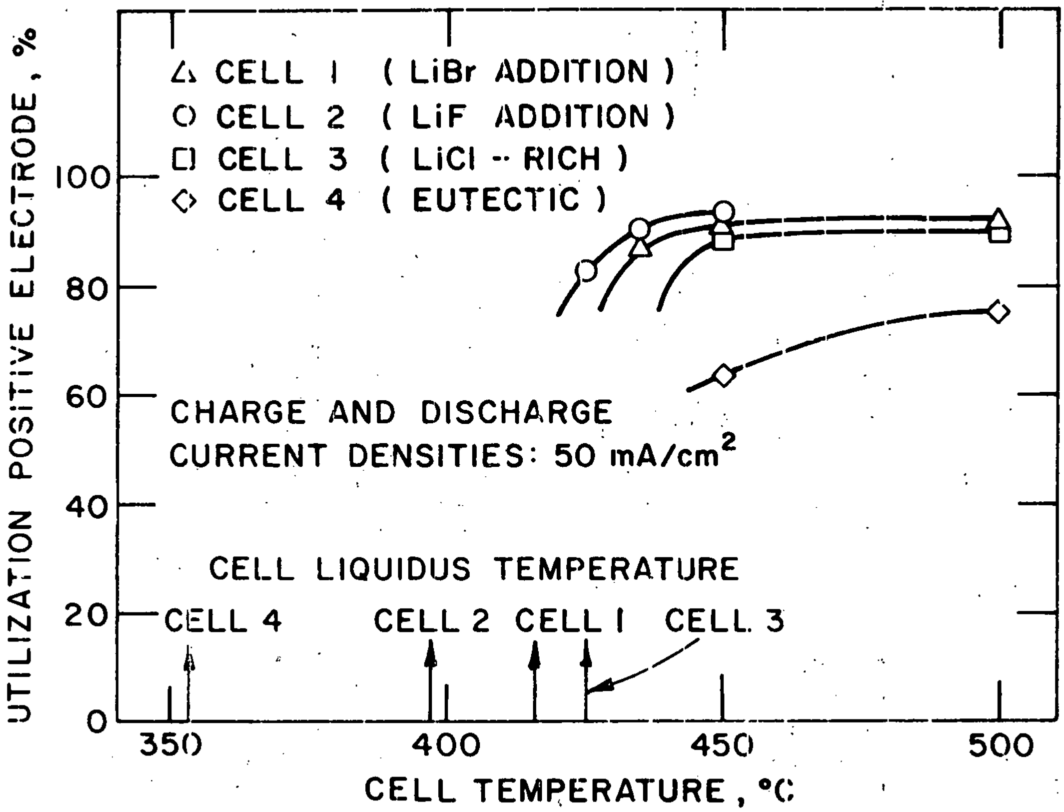

Fig. V-19. Positive-Electrode Utilization for Four Test Cells as a Function of Temperature.

With the above apparatus, the specific conductances (or resistivities) were measured for BN felt (porosity, 88% and 94%) and MgO powder (porosity, 41.8% and 85%) in LiCl-KCl electrolyte at 400°C and 450°C. These measurements are shown in Table V-3

The specific conductivity of separator material impregnated with electrolyte (K) and that of pure electrolyte (K_O) has been correlated to the separator porosity (ϕ) as follows:

$$K/K_o = \phi^{n}$$

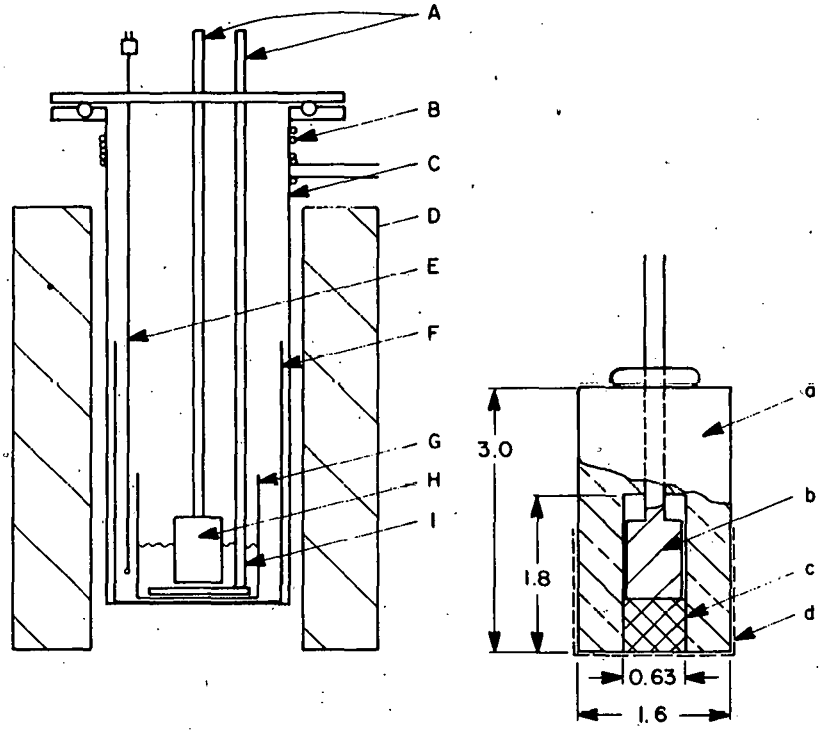

(a) (b)

FURNACE ASSEMBLY:
A ELECTRODE
B COOLING COILS
C VACUUM LINE
D FURNACE
E THERMOCOUPLE
F Al_2O_3 CRUCIBLE
G Mo CRUCIBLE
H BN CONDUCTANCE CELL
I ELECTROLYTE

BN CONDUCTANCE CELL:
a BN (1.6 cm x 3.0 cm)
b ELECTRODE
(0.63 cm OD x 1.0 cm)
c BN FELT OR MgO
POWDER WITH
ELECTROLYTE
(0.63 cm x 0.6 cm)
d STAINLESS STEEL
SCREEN

Fig. V-20. Apparatus for Measuring Separator Conductance

Table V-3. Observed Specific Conductances and Specific Resistances of BN Felt and MgO Powder Containing Molten LiCl-KCl Eutectic

Material	Fractional Porosity	400°C K, (mho-cm)$^{-1}$	400°C R, ohm-cm	450°C K, (mho-cm)$^{-1}$	450°C R, ohm-cm
--	1.00	1.439	0.695	1.547	0.646
BN felt	0.94	1.022	0.978	1.264	0.791
BN felt	0.88	1.030	0.971	1.199	0.834
MgO Powder	0.85	1.923	1.084	1.057	0.946
MgO Powder	0.418	1.672	1.487	0.829	1.207

Figure V-21 shows the curve obtained for K/K_0 from the conductance data given in Table V-3. The dashed line in this figure was calculated from the above equation for $\eta=1.5$ (commonly used for this type of equation). The calculated and measured values were in reasonable agreement for porosities of 80 to 100%, but a significant deviation occurred below 45% porosity.

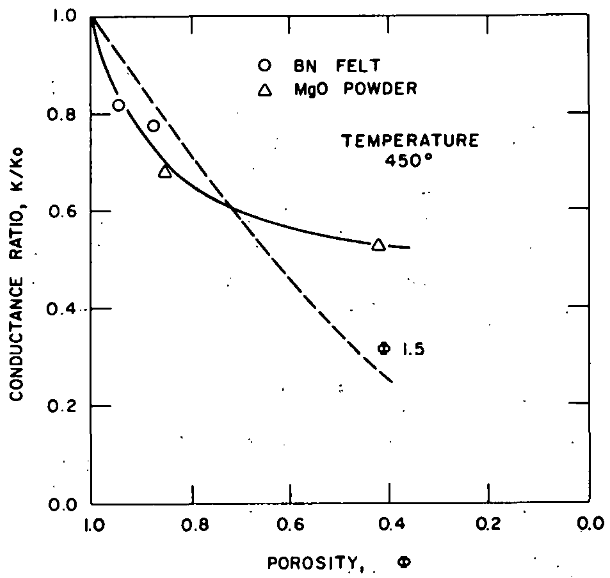

Fig. V-21. Conductance Ratio of Ceramic Separators

The resistance of a cell, r, can be estimated from the specific resistivity at a given porosity as follows:

$$r = R(\phi)t/A$$

where t and A are the separator thickness and area, respectively. Thus, the internal cell resistance for BN felt (88% porosity) and MgO powder (85% porosity) having a thickness of 2.3 mm and an area of 278 cm^2 is 0.70 and 0.78 mΩ, respectively.

3. Alternative Positive-Electrode Additive

(H. Shimotake, K. E. Anderson)

The product, Li_xTiS_2, is an intercalation compound which is ionically and electronically conductive;[12] therefore, TiS_2 additions to the positive electrodes of Li-Al/FeS cells were expected to lower cell resistance. Three small-scale Li-Al/FeS cells (∿16 A-hr capacity, 15.6 cm^2 electrode area) had 5, 10 and 30 wt % of TiS_2 added to the positive electrode; a similar cell with no TiS_2 was also tested for comparison purposes. These cells were operated at 450°C and cycled at a discharge current density of 50 mA/cm^2. Table V-4 shows the cell resistances measured at 0 to 50% depth of discharge. The test results indicated that 10 and 30 wt % of TiS_2 added to the positive electrode resulted in significant improvements in cell resistance. On the basis of these tests, it was decided to test the 10 wt % TiS_2 in the positive electrode of an engineering-scale cell (reported in Section III.A).

Table V-4. Resistances of Small Cells with TiS_2 Additives

Depth of Discharge, %	Cell Resistance, Ω			
	a	b	c	d
0	0.244	0.244	0.231	0.179
5	-	0.110	0.110	0.122
10	-	0.105	0.109	0.115
15	-	0.110	0.113	0.108
20	-	0.118	0.115	0.115
25	0.154	-	-	-
30	-	0.131	0.123	-
40	-	0.155	0.131	0.127
50	0.167	0.283	0.140	-

[a] Cell with no positive additive.

[b] Cell with 5 wt % TiS_2 added to positive electrode.

[c] Cell with 9.6 wt % TiS_2 added to positive electrode.

[d] Cell with 30 wt % TiS_2 added to positive electrode.

4. Electrode Discharge Processes

(H. Shimotake, M. Fitzgibbons*)

Four identical Li-Al/FeS cells (MF-series) having a very small electrode area (0.32 cm^2) were tested to investigate the discharge processes in the positive electrode. These cells were constructed small enough to be frozen instantaneously after termination of operation; this prevents diffusion and chemical reactions from occurring after the electrochemical reaction has stopped. The data obtained from these cell tests may be helpful in the development of a mathematical model to predict cell performance.

---

* Northwestern University, Evanston, IL.

The electrodes for the MF-series cells were 1.2-cm dia. pressed pellets. The thickness of these pellets was similar to that of engineering-scale electrodes: 0.3 cm for the positive electrode (capacity density, 1.4 A-hr/cm^3) and 0.6 cm for the negative electrode. The pellets were electrically separated by two layers of 2-mm thick BN felt and retained by a stainless steel screen. A weight breakdown of the cell components is given in Table V-5.

Table V-5. Weight Breakdown of MF-Series Cells

Components	Weight, g
Positive Mix[a]	1.20
Negative Mix[a]	1.23
BN Tube[b]	2.7
BN Felt Separator	0.16
Retaining Screens	0.50
Glass Feedthrough	5.9
Negative Current Collector	4.0
Positive Current Collector and Outerhousing	22.5
Salt	3.0
TOTAL	41.19

[a] Including electrolyte.

[b] Used to insulate the sides of the pellets from the outer housing.

The small electrode area and heavy current collectors of these test cells produce a negligible ohmic resistance in the current collector. This should result in uniform cell voltage across the collector, thereby eliminating the effect of mixed potential in the cell. Thus, the measured voltage of the cell at a given state of charge should be a good approximation of the equilibrium voltage of the cell at a given state of charge.

The four cells were operated at 450°C and a discharge current density of ∿74 mA/cm^2 for 3 to 6 cycles. Operation was terminated at various states of charge or discharge: fully discharged for MF-1, 80% charged for MF-2, 25% discharged for MF-3, and fully discharged for MF-4.

The positive-electrode utilization for the cells, ∿70%, was similar to that of engineering-scale cells. Figure V-22 shows the ohmic resistances of Cell MF-4 and that of an engineering-scale, R-48 (reported in Section III.A), at various depths of charge and discharge. The large differences in the ohmic resistances of these two cells can be attributed to the method of resistance measurement. An instantaneous open circuit was used to measure the resistance of Cell MF-4, whereas a one-second open circuit was used to obtain the resistance of Cell R-48. As can be seen in the figure, the resistances obtained for Cell MF-4 were close to the resistance calculated from the ionic conductivity data previously presented.

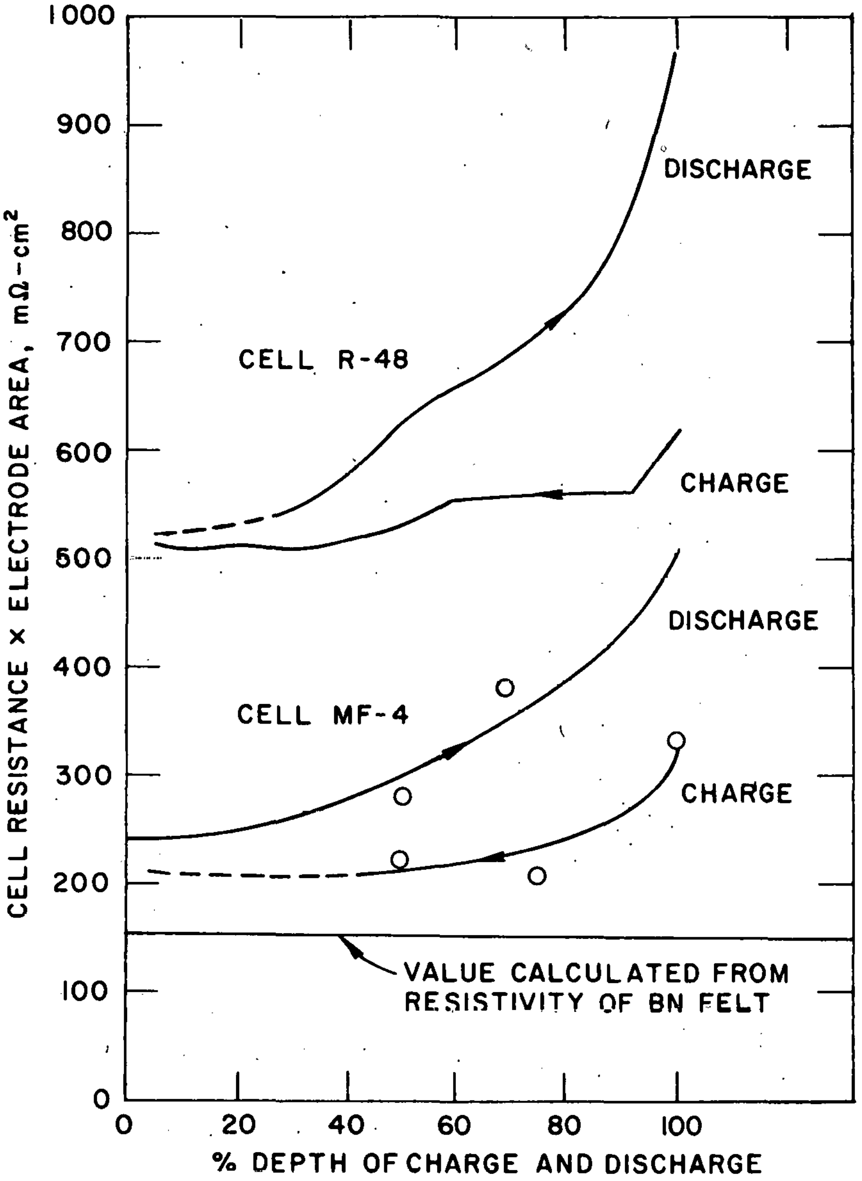

Fig. V-22. Ohmic Resistances of Cells MF-4 and R-48

Post-test analysis of these cells did not show a phase gradient from the face to the back of the electrode. Thus, the diffusion processes in the positive electrode appear to be sufficiently rapid (the cells were quenched in a few minutes) to eliminate large concentration gradients.

In conclusion, this test-cell design appears to be useful for evaluating electrodes in cells.

REFERENCES

1. W. H. Tiedmann and J. Newman, *Current and Potential Distribution in Lead-Acid Battery Plates*, Proc. of Symp. on Bat. Design and Opt., ed., S. Gross, The Electrochemical Society, Inc., pp. 39-49 (1979).
2. M. M. Farahat, J. A. E. Graae, A. A. Chilenskas, and D. L. Barney, SAE Technical Paper No. 790161, Detroit, MI (Feb. 1979).
3. R. Pollard, dissertation for University of California, in preparation.
4. N. P. Yao, L. A. Heredy, and R. C. Saunders, Electrochem. Soc. *118*, 1039 (1971).
5. C. H. Liu, A. J. Zielen, and D. M. Gruen, J. Electrochem. Soc. *120*, 67 (1973).
6. M. L. Saboungi, J. Marr, and M. Blander, J. Chem. Phys. *68*, 1375 (1978).
7. M. L. Saboungi, J. Marr, and M. Blander, J. Electrochem. Soc. *125*, 1567 (1978).
8. R. Piontelli and G. Bianchi, Gass. Chim. Ital. *80*, 581 (1950).
9. R. Piontelli, G. Bianchi and R. Aletti, Z. Electrochem. *56*, 86 (1952).
10. B. R. Sundheim, J. Electrochem. Soc. *115*, 158 (1968).
11. B. D. Cahan, Z. Nagy and M. A. Genshaw, J. Electrochem. Soc. *119*, 64 (1972).
12. M. S. Whittingham, J. Electrochem. Soc. *123*, 315 (1976).

VI. MATERIALS AND COMPONENTS DEVELOPMENT

The objectives of this part of the program are (1) to provide solutions to chemical and electrochemical problems that arise in the development of cells and batteries, (2) to develop improved compositions for electrodes and electrolytes, (3) to acquire a basic understanding of the chemistry and electrochemistry of cells, and (4) to improve the performance of various cell components (*e.g.*, separators, current collectors, and other cell hardware).

A. Electrode Development

(D. R. Vissers)

The chemical, electrochemical, and physical properties of various electrode materials are being investigated. The studies performed during this period are reported below.

1. Li-Al Electrode Studies

The Li-Al alloy electrodes have shown great promise for meeting the performance requirements (specific energy and specific power) of negative electrodes in Li/MS batteries. However, the capacity retention characteristics of the electrode need to be significantly improved for this system to achieve the lifetime goal for the stationary energy-storage battery of 3,000 deep discharges. Therefore, our recent efforts have been concentrated on improving the capacity retention with cycling of the cell.

a. Mechanism of Agglomeration in Negative Electrodes

(A. K. Fischer)

Past testing of the Mark IA multiplate cells has indicated a significant capacity decline with cycling (0.24 %/cycle), and post-test examinations indicated that the capacity decline may be partly due to metallic agglomeration in the center of the negative electrode (see Section IV.C). A fairly simple model has been hypothesized to explain the formation of agglomerated regions and its correlation to capacity decline. In this hypothesis, termed the blocked pore model, the consequences of KCl precipitation in the LiAl electrode on charging are considered. In a given pair of adjacent pores in the porous electrode during charge, it is unlikely that the electrochemical process proceeds equally in each pore, so that precipitation of KCl will occur in one before the other. Since a multitude of pores comprises the electrode, there would be many adjacent pairs of which one member becomes plugged with KCl before the other during charge. In the subsequent discharge, the blocked pore would probably not become unblocked and, therefore, remains blocked during the next charge. At this point, ingress of lithium in the wall of the adjacent, unblocked pore results in the formation of relatively voluminous LiAl, which exerts pressure on the remaining aluminum-rich, relatively plastic material between the pores and compresses it into an agglomerated condition. Lithium held in the agglomerated material is believed to be relatively unable to function electrochemically, and would therefore contribute to capacity decline.

A number of implications attend this rather simple model: (1) A LiCl-rich electrolyte or high cell operating temperature (>450°C) should hinder KCl precipitation and hence retard agglomeration. Indeed, a lowering of the capacity decline rate has been observed in cells operated at high temperatures (ANL-78-94, p. 104) and in cells with LiCl-rich electrolyte (ANL-78-94, pp. 122-125). (2) Modeling calculations by Pollard and Newman[1] have shown that a maximum in the KCl concentration in the electrolyte, and hence eventual KCl precipitation, occurs in an interior zone of the negative electrode on charging. In terms of the blocked pore hypothesis, this would establish conditions leading to agglomeration in an interior zone of the electrode. Experimentally, agglomerated regions are usually found in the interior of electrodes and not at the surface. (3) A high electrolyte volume in the negative electrode should help to buffer against KCl build-up, thereby reducing agglomeration. In cell tests, when the electrolyte volume in the negative electrode was decreased, the capacity decline rate of the cell increased; post-test examination of the negative electrode showed agglomeration. Addition of electrolyte during cell operation was followed by capacity recovery. (4) A relatively low depth of discharge should prevent or retard the onset of agglomeration because the interior of the negative electrode would contain relatively more hard, brittle β-LiAl (lithium-rich) and less soft α-LiAl (aluminum-rich) and aluminum. (5) A low charge current density should minimize agglomeration because there would be more time for diffusion in the electrolyte to counteract the increasing KCl concentration. (6) The inter-pore compressive forces proposed in the model may not cease at the instant charging ends; they are generated by volume changes in solids between pores and could thus persist into an open-circuit period or into a discharge period. This situation could lead to "limiting behavior" in the negative electrode during both charging and discharging. (7) The agglomeration mechanism described by the blocked-pore model should be especially appropriate for cells operated at high current densities; local differences in agglomeration would be expected because of different current distribution patterns.

Other agglomeration mechanisms might exist. However, at the present time, the blocked-pore model provides a plausible explanation for several aspects of the agglomeration and capacity fading problem observed in multiplate cells.

b. Morphological Changes in Negative Electrodes

(A. K. Fischer)

To investigate the morphological properties of the negative electrode, we partially cycled small solid aluminum-block electrodes and then examined them. This block has a small screened circular area (0.63-cm diameter) on the block surface as the electrochemically active zone. A large counter electrode of porous Li-Al was used to eliminate any effects from metal sulfide. The polarization of the test electrode was also measured. Solid rather than porous electrodes were selected as the working electrode because (1) a solid structure is a more reproducible starting point than a porous one, (2) the pressure changes that are suspected to cause agglomeration are better confined in a reaction zone having a solid rather than a porous matrix, and (3) new surfaces generated within the block by formation and break-up of LiAl will be oxide-free and therefore unimpeded by a surface film from participating in particle growth, a coalescence process.

After numerous cycles of the block electrode, microscopic examination showed that tentacular growth containing considerable β-LiAl had formed at the surface of the reaction zone. This localized zone of high lithium content was found with the electrode supposedly in the discharged state. Apparently, such tentacular growth leaves considerable lithium unavailable for electrochemical discharge. Voids were disposed in an arcing zone near the bases of the protrusions; these voids might be significant in reducing electrical contact with the protrusions containing β-LiAl and contribute to the isolation of these lithium-rich regions. Under the microscope, the areas at the bases of the protrusions and surrounding the voids had the same metallic appearance as the bulk aluminum, although it seemed highly probable that lithium had penetrated to the region of the voids or else they would not have formed. It was desirable, therefore, to develop a convenient technique to reveal the extent of lithium penetration under the microscope. Various etching procedures were tried. Ultimately, etching with iodine vapor at room temperature was found to be effective. A scan with the ion microprobe mass analyzer confirmed that the etch line reveals a sharp change in lithium content from a lithium-penetrated region to bulk aluminum. In the block electrode, this technique revealed that lithium had penetrated slightly beyond the voids into the bulk aluminum.

In another experiment, a block electrode was cycled to a discharge-cutoff potential of 1 V (*vs* LiAl). Upon the first discharge after the first charge, which implanted 0.0523 A-hr, 63% of the charged lithium was recovered. With open circuit periods of 5 min between subsequent discharges (no further charging), seventeen incremental discharges were conducted until a discharge lasted for only a few seconds; the final total recovery of lithium capacity was 89% of that charged. Since the aluminum block electrode at this point would have developed some pore structure, it was of interest to see if the charge-discharge characteristics were different in the more porous substrate. Therefore, a second charge was given to the electrode, equalling 0.0108 A-hr of lithium.

In the first discharge after this charge, 80% of this 0.0108 A-hr was recovered; however, this recovered lithium is equal to only 52% of the total lithium capacity present in the electrode (*i.e.*, the 0.0057 A-hr present after the first charge plus the 0.0108 A-hr added upon the second charge). After another seventeen incremental discharges, the additional capacity recovered brought the total to 90% of that introduced by the second charge, or only 58% of the total lithium capacity present in the electrode. Therefore, the greater porosity developed during and after the second charge increased the recoverable lithium in the first discharge following charge (from 63% to 80%) and in the protracted discharges (from 89% to 90%). However, a considerable portion of the total lithium inventory remained locked up.

The state of the material in the reaction zone of this blocked electrode was found to be similar to that in agglomerated regions of Li-Al electrodes: a lithium-containing, extended metallic system. If it is assumed that the electrochemical behavior in the two situations is similar, then the evidence presented here strongly supports the view that agglomeration in the Li-Al electrode, once developed, by whatever means, leads to capacity loss. Up to now, agglomeration had been found only in engineering-sized

Li-Al/FeS cells and the capacity loss in these cells could not be ascribed to a particular electrode, or to implicate, unambiguously, a certain process. It appears reasonable to state that, while other causes of capacity decline might exist, agglomeration in the negative electrode, if it is mimicked by the block electrode, produces capacity decline. Further work to uncover the process by which agglomeration develops is being pursued along lines suggested by the blocked pore model.

c. Additive Studies

(K. E. Anderson)

Studies are continuing on additives to the porous Li-Al electrode that may result in sustained high capacities during extended cycling. As mentioned previously, the decreasing capacity presently observed in Li-Al electrodes may be due, in part, to morphological changes of the active material during cycling. The present study is focused on the use of zinc additive (15 wt %) to the Li-Al alloy as a means of controlling or modifying these morphological changes. Preliminary studies had indicated that the morphology of the Li-Al-Zn electrode was much different from that observed for a Li-Al electrode. The particles of this zinc containing alloy electrode were coarser and appeared to have a three-dimensional structure that had better and more uniform electronic conduction pathways than those observed in the binary Li-Al alloy electrode.

The electrochemical performance (capacity density) of a LiAl-15 wt % Zn electrode was determined, and its capacity retention evaluated through 200 cycles. The cell design (see ANL-78-94, p. 182) utilized horizontally mounted electrodes, a LiAl-15 wt % Zn electrode with a theoretical capacity of 10 A-hr, and a liquid-lithium counter electrode with a theoretical capacity of 16 A-hr. In general, the cutoff potentials were 0.15 V during charge and 0.70 V during discharge (all cutoff potentials cited are IR-free voltage *vs* lithium). The capacity density of the electrode at constant current was used as a measure of electrochemical performance. The effect of the additive on the capacity retention of the electrode was assessed by measuring the rate of capacity-density decline at a current density of 0.05 A/cm^2 during cycling.

Performance data from this study, along with performance data from the first 50 cycles of a baseline binary LiAl alloy electrode which was investigated earlier (ANL-78-94, p. 183), are presented in Table VI-1. The lithium utilization of the Li-Al-Zn electrode dropped to a mere 28% of theoretical, whereas the Li-Al electrode had a utilization of 81% of theoretical at 200 cycles. These results clearly indicate that the 15 wt % zinc additive does not improve the performance of the Li-Al electrode. The poor performance of the Li-Al-Zn electrode is very probably related to its coarse particle structure which creates a low particle surface area for lithium transport. This conclusion is in agreement with the performance improvements for the Li-Al electrode observed earlier with indium additives (ANL-78-94, p. 183), which tended to increase the surface area of the structure of the Li-Al electrode material. Future studies in this area will be directed toward the evaluation of the indium additive.

Table VI-1. Utilization of LiAl and Li-Al-Zn Alloy Electrodes During the First Fifty Cycles of Operation

Charge Rate, A/cm^2	Discharge Rate, A/cm^2	Capacity Density, A-hr/cm^2		Lithium Utilization, % of Theoretical	
		Li-Al	Li-Al-Zn	Li-Al	Li-Al-Zn
0.050	0.050	0.60	0.51	92.3	75.8
0.050	0.100	0.58	0.50	89.2	74.8
0.050	0.200	0.55	0.49	84.6	71.8
0.050	0.300	0.53	0.44	81.9	65.4
0.100	0.050	0.52	0.39	80.2	58.0
0.100	0.100	0.50	0.37	76.6	55.0
0.100	0.200	0.50	0.35	76.6	51.7
0.100	0.300	0.43	0.33	65.6	48.0

2. FeS Electrode Studies

(Z. Tomczuk, M. F. Roche)

The discharge of FeS electrodes in an electrolyte of LiCl-KCl eutectic leads to the formation of Li_2S and iron at full discharge, but intermediate compounds of $LiK_6Fe_{24}S_{26}Cl$ (J phase) and Li_2FeS_2 (X phase) have been found to form in electrodes that are only partially discharged (ANL-78-94, p. 178). Earlier metallographic examination of the FeS electrodes at various states of discharge (ANL-77-17, p. 45) revealed that the surface of the FeS particle follows a different discharge path than its interior. Initially in the discharge of FeS, the surface of the FeS particle is discharged to J phase. The interior of the particle then discharges to X phase, and finally to Li_2S and iron. At this point, the J phase of the surface discharges to Li_2S and iron. However, we could not determine if X or J phase formed first on charge, since both phases formed when electrodes containing Fe and Li_2S were charged. Nevertheless, the likely charge sequence was thought to be:

$$Li_2S + Fe \rightarrow X \rightarrow J \rightarrow FeS \rightarrow Fe_{(1-x)}S \qquad (1)$$

The phase of $Fe_{1-x}S$ was found only in cells which were overcharged (>1.6 V).

Although this early work established the phases found in FeS electrodes, the reaction sequence was not firmly established, and the emf of each electrode reaction as a function of temperature and electrolyte composition was not measured. Thus, our efforts in the past year were directed toward determining the reaction sequence and the emf for each reaction.

a. Cell Studies

In previous Li/FeS cell studies (ANL-75-1, p. 103), two plateaus were observed on the time *vs* current curves during charge, corresponding to the formation of J phase and FeS, respectively. For a cell at 438°C and a current density of 21 mA/cm^2, the transition from J phase to FeS was reported to be 1.87 V *vs* Li or 1.57 V *vs* Li-Al. During discharge, only one plateau was observed on the time *vs* voltage curves for these cells; thus the potential of the FeS to J phase transition could not be measured. In studies performed in this report period, two 2 A-hr Li-Al/1 A-hr FeS cells (eutectic electrolyte) were operated at current densities of 6 to 12 mA/cm^2 and 444°C, and two plateaus were again observed on the time *vs* voltage curves during charge. The J phase to FeS transition was found to occur at 1.62 V, which is only slightly above that observed earlier. During discharge of the cell, two plateaus were seen in the time *vs* voltage curves; one of these plateaus was very short (∿7% of total capacity) and occurred at approximately 1.4 V. The short plateau is believed to be associated with the FeS to J phase transition, but the reason that it was not observed in the earlier studies is uncertain. It has been suggested that the higher current density used in earlier cells produced this discrepancy between the curves. The present results also suggest that there is a large overpotential associated with the J and FeS transition during charge.

A third cell utilizing a LiCl-LiBr-LiF electrolyte was tested to elucidate the phases formed in the FeS electode when J phase is not present. When the LiAl/LiCl-LiBr-LiF/FeS cell was operated at 490°C and cycled at a current density of 12 mA/cm^2 between 1.0 and 1.6 V, two distinct plateaus were observed. Operation of the cell was terminated during a 12 mA/cm^2 charge at approximately the 50% charge point, and the positive electrode was rapidly removed. Metallographic examination of the electrode revealed only the presence of X phase. The results of these studies are consistent with the Li-Fe-S phase diagram (ANL-78-94, p. 16), and suggest that the discharge reactions are simply:

$$\mathrm{FeS} \rightarrow \mathrm{X} \tag{2}$$

$$\mathrm{X} \rightarrow \mathrm{Li_2S} + \mathrm{Fe} \tag{3}$$

b. Cyclic Voltammetry

Cyclic voltammetry studies were conducted to determine the effects of electrolyte composition and temperature on the electrochemistry of the FeS electrode.

The voltammetry cell consisted of an FeS working electrode, a Li-Al counter-electrode, and a Li-Al (42 at. % lithium) reference electrode. In these experiments, the LiCl content of the LiCl-KCl electrolyte and cell operating temperature were varied as follows: 52.8 mol % LiCl at 389, 425, and 451°C; 63.8 mol % LiCl at 435°C; 66.6 mol % LiCl at 433, 440, and 451°C; and 74.4 mol % LiCl at 478 and 495°C. In addition, a voltammetry cell was operated with an electrolyte of LiF-LiCl-LiBr eutectic at temperatures of 484, 492, and 495°C. The voltage range examined was 0.98 to 1.606 V for all systems, except the 66.8 mol % LiCl electrolyte one which had a range of

1.00 to 1.70 V. The FeS electrodes were cycled at a slow scan rate (15-20 μV/sec) to insure high resolution of the current peaks associated with each of the electrode reactions.

The voltammograms obtained with the LiF-LiCl-LiBr eutectic indicated that three reactions occurred on cycling, which are believed to correspond to:

$$\mathrm{FeS} \rightleftarrows \mathrm{X} \qquad (4)$$

$$\mathrm{FeS} \rightleftarrows \mathrm{Li_2S + Fe} \qquad (5)$$

$$\mathrm{X} \rightleftarrows \mathrm{Li_2S + Fe} \qquad (6)$$

Reactions (4) and (6) appeared to be reversible on the voltammograms. Upon continuous cycling, only one discharge-charge peak could be observed, indicating that the reaction was simply:

$$\mathrm{FeS} \rightleftarrows \mathrm{Li_2S + Fe} \qquad (7)$$

The latter condition was achieved only after considerable operating time, when some Li_2S from the electrode was probably lost by dissolution into the bulk electrolyte.

Typical voltammograms* obtained for the FeS electrode (20 μV/sec) are shown in Figs. VI-1 (eutectic electrolyte) and VI-2 (66.6 mol % LiCl); both electrolytes were maintained at 451°C. As can be seen in

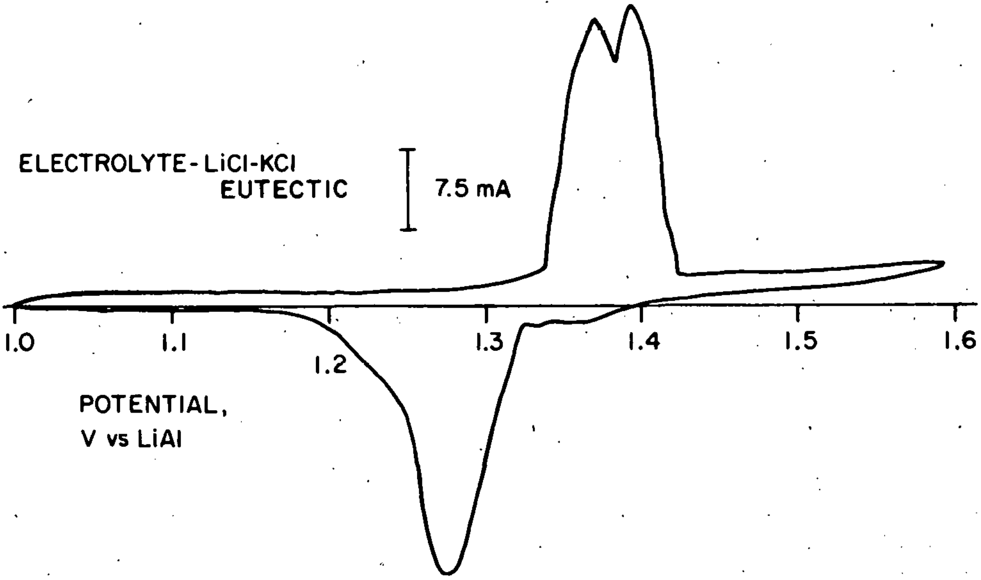

Fig. VI-1. Voltammogram of FeS Electrode in Eutectic Electrolyte at 451°C

---

[*] Charge reactions are shown above the horizontal lines and discharge reactions below.

Fig. VI-1, a doublet is obtained on charge and a large peak and two much smaller ones on discharge. The start potential of the doublet was found to be temperature dependent and electrolyte-composition independent (compare Figs. VI-1 and -2). Since the electrochemical reactions involving J phase have been shown to be dependent upon the electrolyte composition (ANL-78-94, p. 178), it was concluded that J phase was not being formed electrochemically during charge. This doublet also appeared in the voltammogram for the LiF-LiCl-LiBr electrolyte, and was believed to correspond to reactions (4) and (6). At higher scan rates (100 μV/sec), the voltammograms for LiCl-KCl electrolyte showed a third charge peak, which is believed to correspond to reaction (5). For the discharge peaks of the voltammograms for LiCl-KCl electrolyte, their number and shape were found to be strongly dependent on temperature and electrolyte composition. Therefore, the discharge reactions associated with the peaks were assigned to:

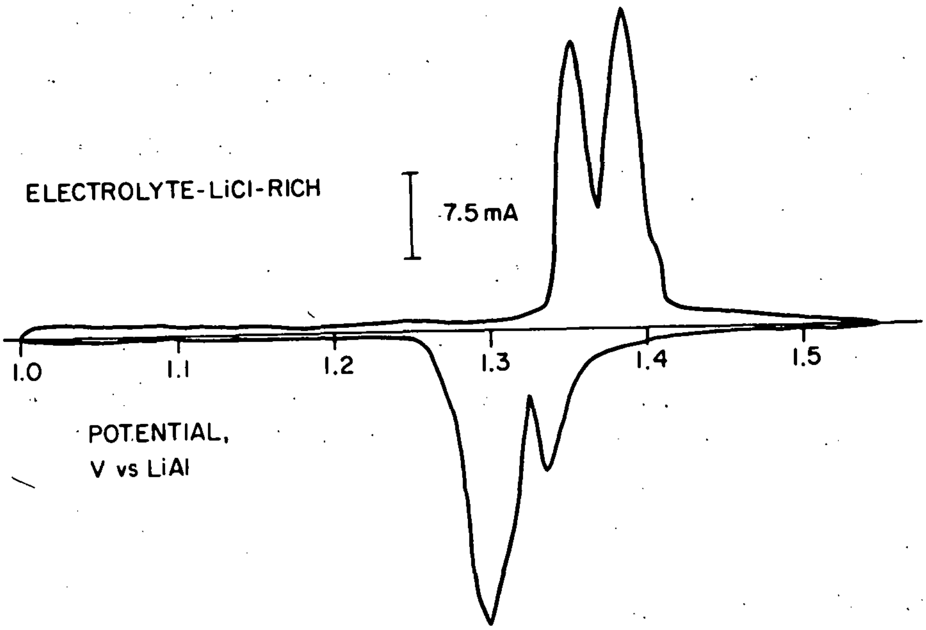

Fig. VI-2. Voltammogram of FeS Electrode in LiCl-Rich Electrolyte at 451°C

$$\mathrm{FeS} \rightarrow \mathrm{J} \tag{8}$$

$$\mathrm{J} \rightarrow \mathrm{X} \tag{9}$$

$$\mathrm{J} \rightarrow \mathrm{Li_2S} + \mathrm{Fe} \tag{10}$$

Overall, the voltammetry studies indicated that the discharge reaction kinetics of the FeS electrode is improved by increasing the LiCl content of the electrolyte above that of the eutectic or by increasing the operating temperature of the cell above 450°C.

c. Emf Measurements and Thermodynamic Calculations

Metallographic examinations of the FeS electrode (ANL-77-17, p. 45) indicated that five phases (FeS, J, X, Li_2S and Fe) may be formed in the electrode during cycling. These phases were thought to electrochemically form in the LiAl/FeS cell as follows:

$$26FeS + 6KCl + 6LiAl \rightarrow 2Fe + LiK_6Fe_{24}S_{26}Cl + 5LiCl + 6Al \tag{11}$$

$$LiK_6Fe_{24}S_{26}Cl + 5LiCl + 20LiAl \rightarrow 13Li_2FeS + 11Fe + 6KCl + 20Al \tag{12}$$

$$LiK_6Fe_{24}S_{26}Cl + 5LiCl + 46LiAl \rightarrow 26Li_2S + 24Fe + 6KCl + 46Al \tag{13}$$

$$2FeS + 2LiAl \rightarrow Li_2FeS_2 + Fe + 2Al \tag{14}$$

$$FeS + 2LiAl \rightarrow Li_2S + Fe + 2Al \tag{15}$$

$$Li_2FeS_2 + 2LiAl \rightarrow 2Li_2S + Fe + 2Al \tag{16}$$

The emf's for the above six reactions were assigned the symbols E_1 through E_6, respectively. By suitably combining these reactions, we obtained the following four equations:

$$E_4 - E_5 = (E_5 - E_6) \tag{17}$$

$$E_1 - E_4 = 3.33\ (E_4 - E_2) \tag{18}$$

$$E_1 - E_5 = 7.667\ (E_5 - E_3) \tag{19}$$

$$E_2 - E_3 = 1.300\ (E_5 - E_6) \tag{20}$$

The emf's of E_2, E_3 and E_6 as a function of temperature were measured experimentally on small-scale cells. (From these measurements, the emf's of the other three reactions can be easily determined from Eqs. 17-20.) The small-scale cells had working electrodes of 1 A-hr FeS, counter electrodes of 8 A-hr Li-Al, reference electrodes of Li-Al (42 at. % Li), and eutectic LiCl-KCl electrolyte. These cells were cycled until reproducible performance was obtained and then discharged or charged to a preselected value. The E_6 values were obtained on an FeS electrode which had been fully discharged and then partially charged (∿30%), and the E_2 and E_3 values were obtained with the FeS electrodes partially discharged (∿30%). The voltages were obtained after the cells had been placed on open circuit and their voltages had become constant. The measured voltages were plotted as a function of temperature, and then the following equations were obtained from a least squares fit of the data:

$$E_6 = 1.4055 - 0.0001776\ T \tag{21}$$

$$E_2 = 1.2123 + 0.0002289\ T \tag{22}$$

$$E_3 = 1.34575 - 0.0000519\ T \tag{23}$$

where T is in degrees centigrade. On the voltage *vs* temperature curves, these voltages intersect at 475°C (1.321 V). This result agrees with a previous finding[2] that above 455°C the reaction of Li_2S and J phase forms X phase in the eutectic electrolyte.

Combining Eqs. 21-23, we obtain

$$(E_2 - E_3) = 2.232\ (E_3 - E_6) \tag{24}$$

which is different from Eq. 20. Thus, the electrochemical reactions of the FeS electrode probably do not entirely conform to reactions (11) through (16), but instead involve complications that have not yet been resolved. However, the lack of reversibility of the FeS electrode reactions in LiCl-KCl electrolyte, which was observed in the FeS cyclic voltammograms, may have distorted the emf data used to obtain Eq. 24.

The transition potentials at which reaction (11) through (16) occur can also be calculated from the following thermodynamic data: the Gibb's free energy data reported for Li_2S,[3] LiAl,[4] and FeS,[5] the J → FeS and J → X transition temperatures, and the X → Li_2S transition potential (ANL-77-17, p. 43). The transition potentials for these six reactions as a function of temperature are plotted in Fig. VI-3. The dashed lines illustrate regions where a reactant or product for the respective transition is thermodynamically unstable.

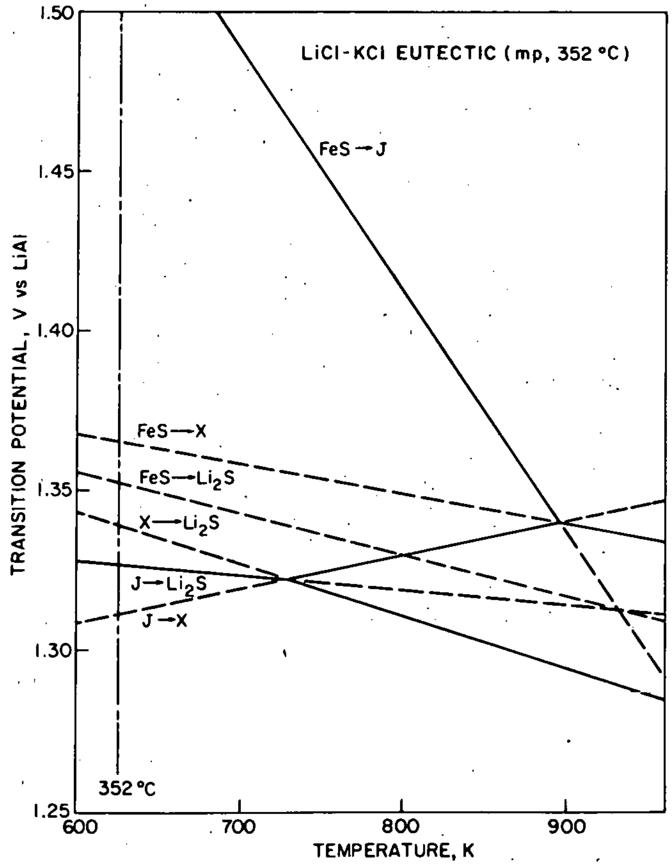

Fig. VI-3. Transition Potentials as a Function of Temperature for FeS Electrode Reactions

3. FeS_2 Electrode Studies

(A. E. Martin, Z. Tomczuk)

During the operation of an Li-Al/FeS_2 cell, the composition of the FeS_2 electrode traverses the Li_2S-FeS-FeS_2 triangle and the Li_2S-Fe-Li_2FeS_2 triangle in the Li-Fe-S phase diagram (see ANL-78-94, p. 167). The phase relations in the latter triangle are simple and have been known for some time. The phase relations in the former triangle are more complicated and have been the subject of considerable study at ANL.

Powders of Li_2S, Li_2FeS_2, FeS and FeS_2 were equilibrated with LiCl-KCl molten salt at 450°C in graphite crucibles in an inert-atmosphere glovebox. The salt, which was present in an amount approximately equal in weight to the powders, served as an inert vehicle to facilitate equilibration. Corrections were made to overall powder compositions for minor weight losses which were assumed to be sulfur. The products were examined metallographically and by X-ray diffraction* to identify the phases that were present. The phase diagram for the Li_2S-FeS-FeS_2 triangle, with appropriate phase designations, is presented in Fig. VI-4; composition fields have been drawn from the data defining two-phase and three-phase fields; the single phases are essentially the same as previously reported. The points C, D, E, and F

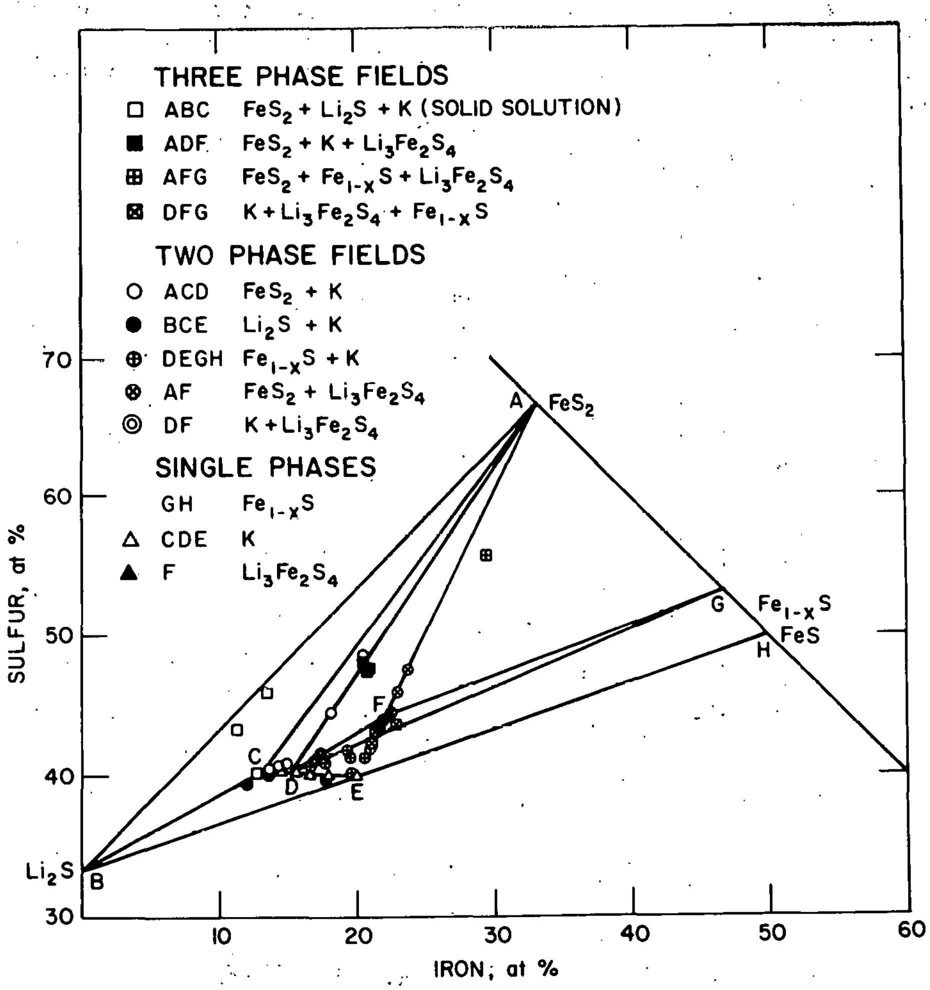

Fig. VI-4. The Li_2S-FeS-FeS_2 Triangle of the Li-Fe-S Phase Diagram

---

*X-ray diffraction analysis reported in this section was performed by B. S. Tani, Analytical Chemistry Laboratory at ANL.

correspond to Y phase ($Li_7Fe_2S_6$), W phase ($Li_{12}Fe_4S_{11}$), X phase (Li_2FeS_2) and Z phase ($Li_3Fe_2S_4$), respectively. The line CDE appears to correspond to a solid solution; no abrupt change in metallographic appearance occurs in this composition region. Room-temperature X-ray diffraction data on samples in the CDE region were not useful in confirming whether this solid solution exists. It is possible that future X-ray diffraction data obtained with special equipment will resolve this question.

Previous cyclic voltammetry studies (ANL-77-68, p. 48) indicated poor electrochemical reversibility of the FeS_2 electrode in the voltage range of 1.5 to 2.0 V. In the FeS_2 voltammogram (LiCl-KCl eutectic; ∿450°C), the major discharge peak begins at 1.74 V, which is the potential observed on the upper voltage plateau of $LiAl/FeS_2$ cells; however, the major charge peak begins at 1.86 V, which is close to the potential required for oxidation of Li_2S to sulfur. Thus, cell tests and further voltammetry studies were carried out to further investigate the phases formed during cycling of the FeS_2 electrode.

In a continuing effort to understand the electrochemistry of the FeS_2 electrode during charge, we potentiostatically charged three small cells (Z-7, -8, and -9) to preselected cutoff voltages, then examined the FeS_2 electrode. The test cells had LiAl negative electrodes (4 A-hr), FeS_2 positive electrodes (1 A-hr), and the LiCl-KCl eutectic electrolyte. These cells were cycled at constant current densities of 25 to 30 mA/cm^2 between voltage limits of 1 V (discharge) and 2 V (charge) for at least ten cycles. The cell temperatures varied between 407-419°C. Cell operation was terminated after a normal charge followed by a trickle charge at current densities of <2 mA/cm^2 at a selected voltage for at least 18 hours. Finally, the positive-electrode product was examined metallographically and by X-ray diffraction. The selected charge voltages for cells Z-7, -8, and -9 were 1.786, 1.85, and 1.64 V, respectively.

The results of these tests and others in this series, summarized in Table VI-2, indicate that, under these conditions, FeS_2 does not form at the reversible potential of 1.76 V, which is obtained when FeS_2 discharges to Z. Moreover, these results indicate that $Fe_{1-x}S$ is formed in the transition region between Z phase, $Li_3Fe_2S_4$, and FeS_2. The metallographic examination of the electrode products revealed that at 1.85 V the FeS_2 formed on $Fe_{1-x}S$ particles rather than Z phase particles, as would be expected from the phase diagram. These results suggest, therefore, that there is a barrier to the formation of FeS_2 from Z. Perhaps Z converts to some other phase which is readily soluble in the electrolyte and which transports the sulfur necessary to react with the $Fe_{1-x}S$ particles.

Ancillary studies were carried out during the cycling of cell Z-7 to determine the effect of discharge cutoff voltage on the reversibility of the upper voltage plateau (∿1.6 V). At the voltage plateau, the phase transition is believed to involve $FeS_2 \rightarrow Z$ on discharge, but not necessarily $Z \rightarrow FeS_2$ on charge (see previous section on cell results). When this cell was discharged at a current density of 2 mA/cm^2, the lowest value yet used in laboratory cells, five distinct breaks in the time *vs* voltage curves were observed; thus five distinct cell reactions were taking place on discharge (four were predicted from the phase diagram).[2] The voltages and the reaction

Table VI-2. Summary of LiAl/FeS_2 Cell Results

Cell Designation	Charge Potential *vs* LiAl, V	X-ray Findings		Metallographic Findings
		Major Phase	Minor Phase	
Z-1	1.53	X	J	X + trace of J
Z-9	1.64	$Fe_{1-x}S$	Y and X	X + $Fe_{1-x}S$
Z-2	1.72	Z	None Detected	Z
Z-7	1.786	Z	None Detected	Z + 5% $Fe_{(1-x)}S$
Z-3	1.82	Z	FeS_2 + $Fe_{(1-x)}S$	-
Z-8	1.85	FeS_2	$Fe_{1-x}S$	$Fe_{1-x}S$ and Z

assignments for these breaks are given in Table VI-3. When this cell was charged from the fully discharged condition, the normal irreversible plateau at ∿1.86 V was observed. However, when the cell was discharged to a 1.60-V cutoff, two plateaus of equal length were observed upon the subsequent charge: one occurring at the reversible emf (1.74 V) and the other at the normal irreversible emf (∿1.86 V). The results of this ancillary study indicate that further work is necessary on the Li-Fe-S phase diagram before the phase

Table VI-3. Voltage Observed During Discharge of Cell Z-7

Reaction Assignment	Emf *vs* LiAl
$FeS_2 \rightarrow Li_3Fe_2S_4$	1.74
$Li_3Fe_2S_4 \rightarrow W + Fe_{1-x}S$	1.64
$W + Fe_{1-x}S \rightarrow T$[a]	1.56[b]
$T \rightarrow Li_2FeS_2$	1.54 to 1.32
$Li_2FeS_2 \rightarrow Fe + Li_2S$	1.32

[a] The product is designated as T because the composition is not known.

[b] The total observed capacity for this reaction was ∿2% of the total.

relationships in the Li-Fe-S system are completely resolved. These results are, however, in accord with previous cyclic voltammetry and cell tests (ANL-78-94, pp. 169 and 175).

In cyclic voltammetry studies, voltammograms at low scan rates (<1 mV/sec) were obtained for FeS_2 electrodes in electrolytes of LiCl-KCl eutectic and 55 mol % LiCl-45 mol % KCl over a temperature range of 400-450°C. Initially, the working electrodes were ∿100 mg of powdered FeS_2 (sometimes mixed with graphite powder, ∿0.1 g) contained in a PG-60 graphite cup (∿5 cm^2); later the housing was changed to molybdenum. The counter and reference electrodes were both LiAl (∿42 at. % Li). The working electrodes were repeatedly cycled over a potential region of 1.0 to 2.0 V *vs* LiAl.

The voltammograms for the FeS_2 electrode in eutectic electrolyte were similar to those obtained previously (see ANL-78-94, p. 169). The peak resolution, however, depended on the addition of current collector material to the working electrode. Without the graphite powder additions, the discharge reactions were well resolved, but the charge reactions were not. This finding suggests that the current collector improves the kinetics of the FeS_2 electrode reaction during charge.

The voltammograms with 55 mol % LiCl-45 mol % KCl indicated more discharge and charge reactions than those observed previously (ANL-78-21, p. 53). Figure VI-5 is a voltammogram of the FeS_2 electrode in this electrolyte at 407°C. This voltammogram has a very broad cathodic peak at ∿1.3 V, which is normally associated with the discharge of X phase; this finding suggests that large amounts of J phase, which possesses poor discharge kinetics, are probably present in the electrode at this point. Above 1.45 V, this voltammogram indicates the presence of at least seven reactions on charge and five on discharge. At a higher operating temperature (455°C), the FeS_2 voltammogram in the 55 mol % LiCl electrolyte, shown in Fig. VI-6, has a much narrower discharge peak at 1.3 V than that shown in Fig. VI-5; this finding suggests that little or no J phase is present. Above 1.45 V, Fig. VI-6 has a doublet on discharge. In the voltammogram for eutectic electrolyte, this reaction was found to correspond to the discharge of FeS_2 to Z phase; therefore, the discharge reaction on the upper plateau is much more complex in the FeS_2 electrode with eutectic electrolyte than with 55 mol % LiCl. Earlier work (ANL-78-21, p. 57) had indicated that $KFeS_2$ is being formed in the FeS_2 electrode with 55 mol % LiCl at this discharge stage.

4. Physical Properties of Electrode Materials

(A. K. Fischer)

Investigations of the physical properties of the electrode materials are being conducted to supply the information needed for cell and battery development and optimization. Mathematical modeling of the cell is especially dependent on such data. Therefore, electronic conductivity and entropy data were gathered for different electrode materials.

a. Electronic Conductivity

Pridmore *et al.*[6] reported that the n-type conductivity at room temperature of pyrite, FeS_2, covers five orders of magnitude, from 0.0037 to 530/Ω-cm. The variation arises from deviations from stoichiometry

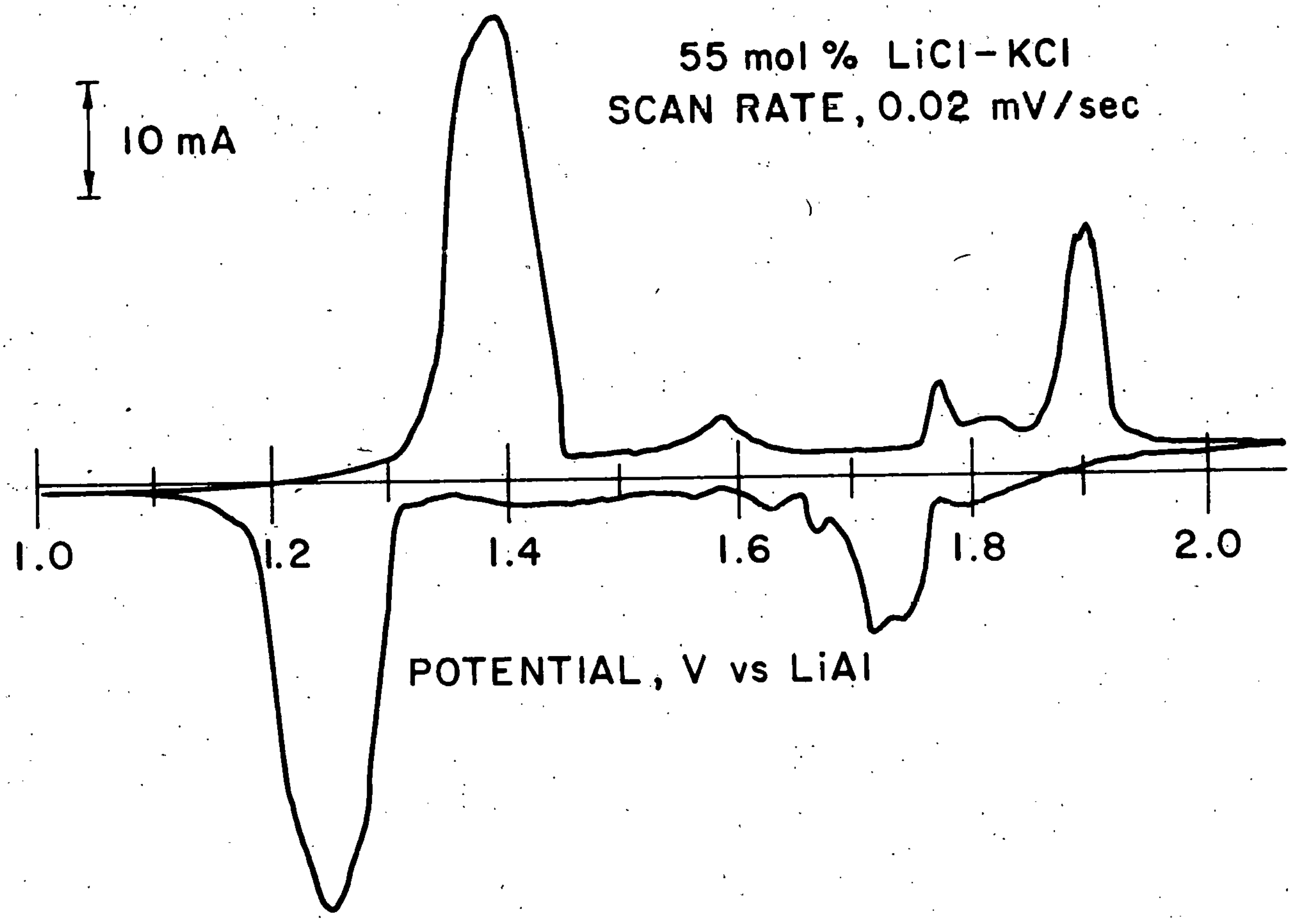

Fig. IV-5. Voltammogram of the FeS_2 Electrode in 55 mol % LiCl-45 mol % KCl at 407°C.

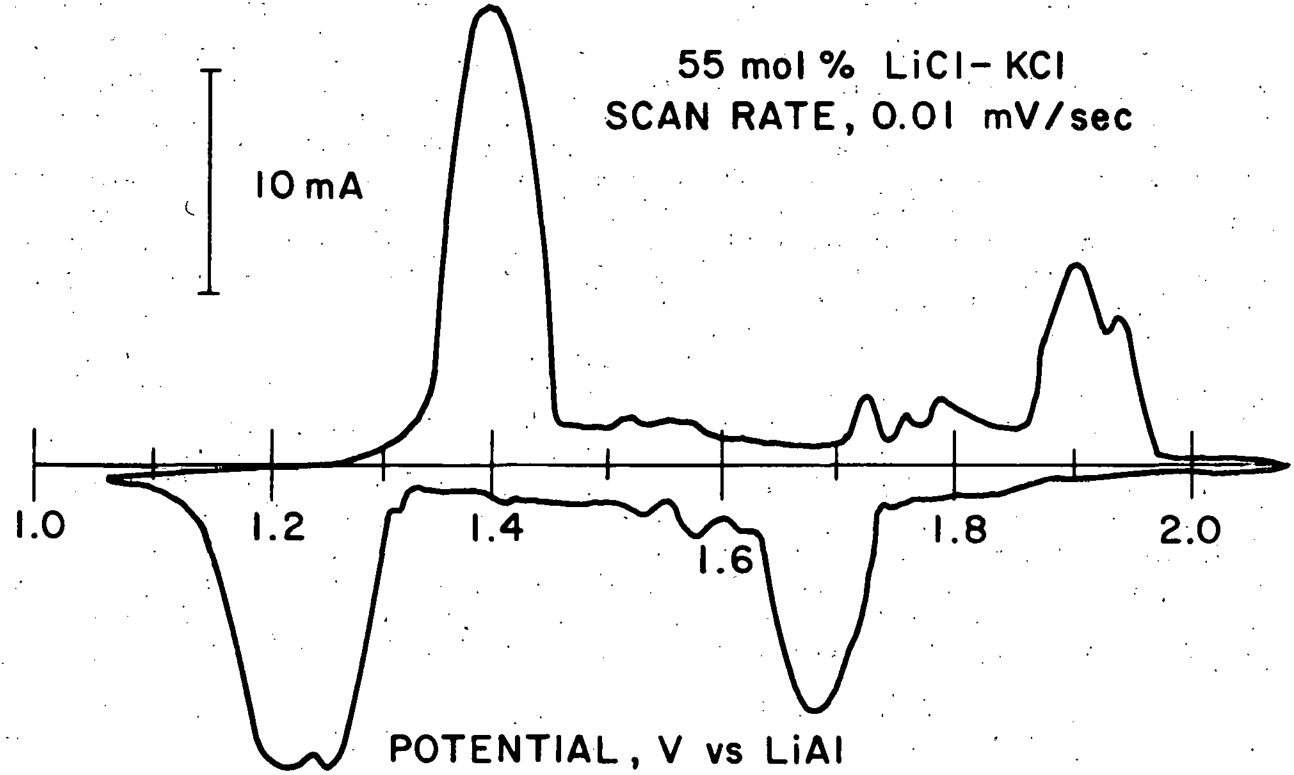

Fig. VI-6. Voltammograms of FeS_2 Electrode in 55 mol % LiCl-45 mol % KCl at 455°C.

and from impurities. The range of conductivity of FeS_2 was estimated to be about 0.04 to 5000/Ω-cm, with the peak of the distribution curve corresponding to about 100/Ω-cm. For FeS (or $Fe_{1-x}S$), published data[7] show that the conduction can be n-type with excess iron or p-type with excess sulfur, and that the magnitude of the conductivity is variable. Below 150°C, single crystals of $Fe_{1-x}S$ show anisotopic conductivity. However, the curves for the conductivities at 450°C parallel to and perpendicular to the c-axis appear to merge and show values[8] of about 1100 and 2700/Ω-cm, respectively. For a polycrystalline sample, such as might occur in an electrode, some intermediate value might be expected.

The existing data for the conductivities of the iron sulfides appear to support the assumption of Heus and Egan[9] that the ratio of their electronic conductivities to that of the electrolyte is large. Such an assumption is involved in some of the modeling of the cell that is being done by Newman and Pollard.[1]

b. Entropy and Entropic Heat in Cell Processes

Entropic heat effects in an operating cell have a strong bearing on the thermal management of the system. Some of the data needed to evaluate the effects are not in the literature, such as the absolute entropies of X phase, J phase, Z phase, and some copper-containing cell products. Estimates of the entropies of these species were made by the Latimer method.[10] For LiAl, the entropy was derived from the data of Yao *et al.*[4] For some other species of interest, entropies at room temperature were available, and it was necessary only to extrapolate the data to 723 K. The resulting entropy values are listed in Table VI-4.

From the entropies reported in Table VI-4, the slopes of the emf *vs* temperature curves were determined for several electrochemical reactions of the Li/MS system. For the upper-plateau reaction of the FeS_2 cell, $3LiAl + 2FeS_2 \rightarrow Li_3Fe_2S_4 + 3Al$, the calculated value of dE/dT was 0.34 mV/deg, which is in excellent agreement with the experimentally determined value of 0.33 mV/deg (ANL-77-17, p. 47). For the lower plateau reaction, $2LiAl + Li_2FeS_2 \rightarrow 2Li_2S + Fe + 2Al$, the calculated dE/dT was -0.092 mV/deg, which is in only fair agreement with the experimentally determined value of -0.16 mV/deg (ANL-77-17, p. 47). This difference of 0.068 mV/deg is probably attributable to the entropy estimated for Li_2FeS_2.

B. Separator Development

(J. E. Battles)

The electrode separator is a key component of the cell, and must meet several requirements, including compatibility with the electrode materials and electrolyte, adequate mechanical strength, acceptable cost, suitable porosity and thickness, and lack of electronic conductivity. Because the BN cloth separators* currently used are expensive, efforts have been directed toward the development of felt, ceramic powder, and sintered ceramic separators.

---

*Boron nitride cloth separators have been successfully used in cells of approximately 2.5 years life.

Table VI-4. Entropies of Species Involved in Lithium/Iron Sulfide Cells

Substance	S_{298}, cal/mol deg	S_{723}, cal/mol deg	Source
Fe(s)	6.5	12.7	Ref. 11[a]
Al(s)	6.8	12.4	Ref. 11[a]
Li(ℓ)	8.113	14	Ref. 11[a]
Li(s)	6.9	13.0	Ref. 11[a]
S(ℓ)	8.4	15.8	Ref. 11[a]
S(s)	7.6	13.8	Ref. 11[a]
LiCl(s)	14.2	25.3	Ref. 11[a]
KCl(s)	19.7	31.2	Ref. 11[a]
Li_2FeS_2(s)	31.6	62.1	Estimated[b]
Li_2S(s)	14	32	Estimated[b]
FeS_2(s)	12.6	31.1	Ref. 12[a]
Cu_2S	28.9	46.0	Ref. 12[a]
FeS(s)	-	32.2	Ref. 13[a]
$Li_3Fe_2S_4$(s)	59.0	114.0	Estimated[b]
$LiK_6Fe_{24}S_{26}Cl$(s)	466.0	824.9	Estimated[b]
$KFeS_2$(s)	29.6	54.8	Estimated[b]
$CuFe_{1.83}S_{8.33}$[c]	136.8	241.6	Estimated[b]
$FeCl_2$(s)	19.8	35.4	Estimated[b]
LiAl(s)	-	21.8	Refs. 4, 11

[a] Interpolated for 723 K.

[b] Estimates for S_{298} for the solid compounds were made by the Latimer method.[10] This step was regarded as accounting for the entropy effects associated with compound formation from the elements. Values of S_{723} were obtained by adding to S_{298} the entropy changes for the constituent solid elements between 298 K and 723 K as given by the JANAF tables.[11]

[c] Corresponds to 94 mol % FeS-Cu_2S (Ref. 14).

1. Boron Nitride Felt Separators

(R. B. Swaroop)

Boron nitride felt separators produced by the Carborundum Co. were characterized for thickness, basic weight, porosity, burst strength and compressibility. These felt separators were hand-made at Carborundum, using a 12-inch square Williams sheet mold, into nominal thicknesses of 1.4, 1.9 and 3.1 mm. The porosity was between 92 and 94%. Some of the felt sheets were heated at 1750°C in flowing nitrogen for 8 hr to remove the residual B_2O_3 remaining from the incomplete conversion of the B_2O_3 bonds to BN. As shown by the data in Table VI-5, this treatment causes a reduction in the basic weight and burst strength of the felts. The amount of decline in these two properties appears dependent on the time of exposure of the felt to ambient environment before stabilization, *i.e.*, moisture reacting with the B-O-N complex results in the B_2O_3 being incompletely converted to BN during stabilization.

Table VI-5. Average Properties of BN Felt (obtained from Carborundum Co.) before and after Stabilization

Felt Thickness, mm	Basic Weight, mg/cm^2 Before	Basic Weight, mg/cm^2 After	Burst Strength, kPa/mm Before	Burst Strength, kPa/mm After	Porosity, % Before	Porosity, % After
1.37 ± .13	21.86	20.26	5.05	5.56	92.20	92.40
1.91 ± .13	34.44	29.81	4.47	1.84	92.10	93.13
3.12 ± .15	42.86	40.97	3.78	1.67	93.37	93.65

The Carborundum felts were reduced to half thickness at compressive stresses of about 150 kPa; at stresses above 175 kPa, the felts underwent plastic deformation. Also, compressive stresses of 690 to 1035 kPa reduced the felt to a powder. The compressibility of the felts was independent of whether they were stabilized.

The wettability of BN felts (stabilized and unstabilized) by the LiCl-KCl electrolyte has been shown to be very poor (ANL-78-94, p. 157). Studies were conducted that showed improved wetting was on the addition of $LiAlCl_4$ powder to the surface of the BN felts (ANL-78-94, p. 158). Additional studies have shown that good wetting of the BN felt by electrolyte can be obtained by using $\sim$10 mg of $LiAlCl_4$ per square centimeter of separator ($\sim$5 mg/cm^2 surface area). Excessive use of this wetting agent should be avoided to prevent metallic aluminum deposition from the lithium reduction of the $LiAlCl_4$.

2. Porous, Sintered Ceramic Separators
(G. Bandyopadhyay, J. T. Dusek, T. M. Galvin)*

Procedures have been developed for the fabrication of porous, sintered ceramics of Y_2O_3 and MgO for separator applications (ANL-78-94, p. 150). Separator plates were prepared with porosities up to ∿60% and good mechanical properties. Higher porosities resulted in weak and non-uniform structures that were not suitable for separator applications. Separators of MgO and Y_2O_3 have been subjected to in-cell testing (ANL-79-39, p. 79), and the results have confirmed that the sintered plates are a viable separator concept.

3. Magnesium Oxide Powder Separators
(H. Shimotake, T. W. Olszanski, F. J. Martino, C. Ruiz, C. Wyrick†)

Earlier tests (ANL-78-94, pp. 134-135) had shown that the separator layer of MgO formed in engineering-scale cells had a relatively low porosity, ∿45%, which resulted in high ohmic resistances. Typical resistances for cells with MgO powder separators were 6.8 mΩ at 50% discharge, which is about twice that obtained in similar cells with BN felt separators. Microscopic examination of the MgO powder used in these cells showed glass-like particles with sharp edges and a very low surface area (5 to 10 m^2/g); the bulk density of this material was also found to be very high (2.0 g/cm^3).

During this period, a new MgO powder, produced by a plasma-discharge method, was found. This powder consists of amorphous particles and has a lower bulk density (0.45 g/cm^3) and a higher surface area (70 m^2/g) than those of the previously used powder. With this new powder, the MgO powder separator in engineering-scale cells should have a much higher porosity (∿80 to 90%) and lower weight (∿50 to 60 g). It is expected that cells with this new powder should attain similar performance to that of cells with BN felt separators. Therefore, such cells are being constructed for testing.

4. Corrosion Rates of Candidate Ceramics for Cell Components
(J. A. Smaga)

A one-year corrosion study was conducted for several candidate ceramics identified by previous screening tests of 1000 hr or less. For these static corrosion tests, an equal-volume mixture of β-LiAl and LiCl-KCl eutectic at 450°C was used to simulate the negative electrode. The evaluated ceramics included the following materials: heat-treated BN rod‡ from Union Carbide Corp., BN fabric** from Carborundum Co., BeO‡ from the National Beryllia Corp. (grade K-151) and the 3M Company (grade AlSi Mag-794), Y_2O_3 insulators‡ from Coors Porcelain Co. (grade 933-HPY), and Y_2O_3 felt** from Zircar Products Inc. Upon completion of the testing period, the samples were cleaned in water followed by alcohol to remove adhering particulate, dried, and then examined.

---

*Materials Science Division, ANL.

†Student from North Carolina State University.

‡Used as electrical feedthrough components.

**Used as separator material.

The BN fabric and rod showed a slight weight gain, corresponding to an average corrosion rate of +1.3 μm/yr. Duplicate samples of BN rod remained intact and nonconductive; the BN fabric also remained intact, nonconductive, and showed only mild discoloration. Weight change measurements of the fabric were impractical, but the individual fibers appeared to be in excellent condition.

The yttria samples proved to be much less resistant to the test environment. Two Y_2O_3 insulators were tested and both fractured, one during testing and the other during the washing procedure. The thin-walled sleeves of both insulators fractured further with continued washing. A very adherent metallic film was also present on the outer surfaces of the insulators. Resistance measurements were often less than 20 Ω for these areas. Accurate weight measurements could not be made on these samples because of their fragmented condition. The Y_2O_3 felt tested was supported in a folded stainless steel screen throughout the testing, cleaning, and drying procedures. In spite of this precaution, the tested felt deteriorated, discolored, and lacked mechanical strength. These findings indicate that Y_2O_3 is not suitable for cell applications.

The corrosion behavior of the BeO samples was dependent on the source of the material. The AlSiMag 794 samples (3M-Company) demonstrated excellent compatibility with the negative electrode environment, showing virtually no evidence of attack. The average corrosion rate for this BeO was less than 0.4 μm/yr based on minor weight losses. The samples of K-151 BeO (National Beryllia Corp.) showed severe discoloration and had mosaic crack patterns covering the entire surface. These samples readily fragmented during handling. The widely differing results for the two BeO materials had to be attributable to their relative impurity levels. Spark-source mass spectrometry tests were conducted on both types of BeO in the as-received and tested conditions; the results of this analysis are shown in Table VI-6. The AlSiMag 794 BeO has significantly higher concentrations of aluminum (400 ppm) and magnesium (200 ppm), but these levels are not detrimental. The high concentrations of sulfur (200 ppm) and silicon (300 ppm) in the K-151 BeO are an order of magnitude higher than those in AlSiMag 794, and appear to be responsibile for the intergranular cracking. Therefore, future orders of BeO components should specify 30 ppm as the maximum allowable concentration for silicon and sulfur impurities.

Table VI-6. Impurities in BeO Ceramics

BeO Characteristics	Impurity Concentration,[a] ppm				
	Mg	Al	Si	S	Cl
Tested AlSiMag 794	200	400	30	20	4
As-received K-151	70	60	300	200	2
Tested K-151	50	10	300	80	70

[a] Analysis performed at Oak Ridge National Laboratory.

C. Current-Collector Development

(J. E. Battles)

The corrosiveness of the active materials in the positive electrodes (FeS and FeS_2) and the molten electrolyte places severe restrictions on the materials that can be used for current collectors. Iron has been found to be a satisfactory current-collector material in Li-Al electrodes, and can be used for a limited period (<1 yr) in FeS electrodes; nickel, iron-based alloys, and several other materials are under investigation for longer-term use in FeS electrodes. The only current-collector material that has been used successfully in FeS_2 electrodes is molybdenum, which is expensive and difficult to fabricate; alternatives such as protective coatings for inexpensive metals are under investigation.

1. Current-Collector Materials for FeS Electrodes

(J. A. Smaga)

The development of iron-base alloys at ANL has been one approach in the overall effort to obtain corrosion-resistant and economically priced replacements for the low-carbon steel components presently used in FeS electrodes. Two of these alloys, ANL-5-0 (Fe-4.5 wt % Mo) and ANL-10-20 (Fe-10 wt % Mo-20 wt % Ni), merited preliminary testing in small-scale (∿50 A-hr) FeS cells (ANL-79-39, p. 83). All of these test cells had a 50 A-hr theoretical capacity and the cell design illustrated in Fig. VI-7. Different cell-operation durations were used for these cells to provide information on the time dependence of any observed corrosion effects. Similarly, the initial state of charge was varied from fully charged to uncharged to determine the influence of this parameter on the corrosiveness of the alloy components.

The final cells in the ANL alloy test matrix have completed operation and their performance is summarized in Table VI-7. Two previous cells (reported in ANL-79-39, p. 86), 3C-10 with ANL-5-0 components and 3C-11 with ANL-10-20 components, were assembled in the charged state and operated for one month.

Table VI-7. Performance Summary for Five Cells with ANL Alloy Current Collector Materials

Cell No.	Collector Material	Assembled State	Operating Time Days	Operating Time Cycles	Mean Percent Util. of Pos. Elect.[a]	Final A-hr Eff.
3C-12	ANL-5-0	uncharged	31	52	44.9	25.1
3C-13	ANL-10-20	uncharged	90	167	45.6	99.3
3C-14	ANL-5-0	semicharged	150	259	41.2	99.8
3C-15	ANL-10-20	semicharged	154	277	40.8	99.8
3C-16	ANL-5-0	uncharged	92	179	44.3	99.3

[a] Based on a discharge rate of 50 mA/cm^2.

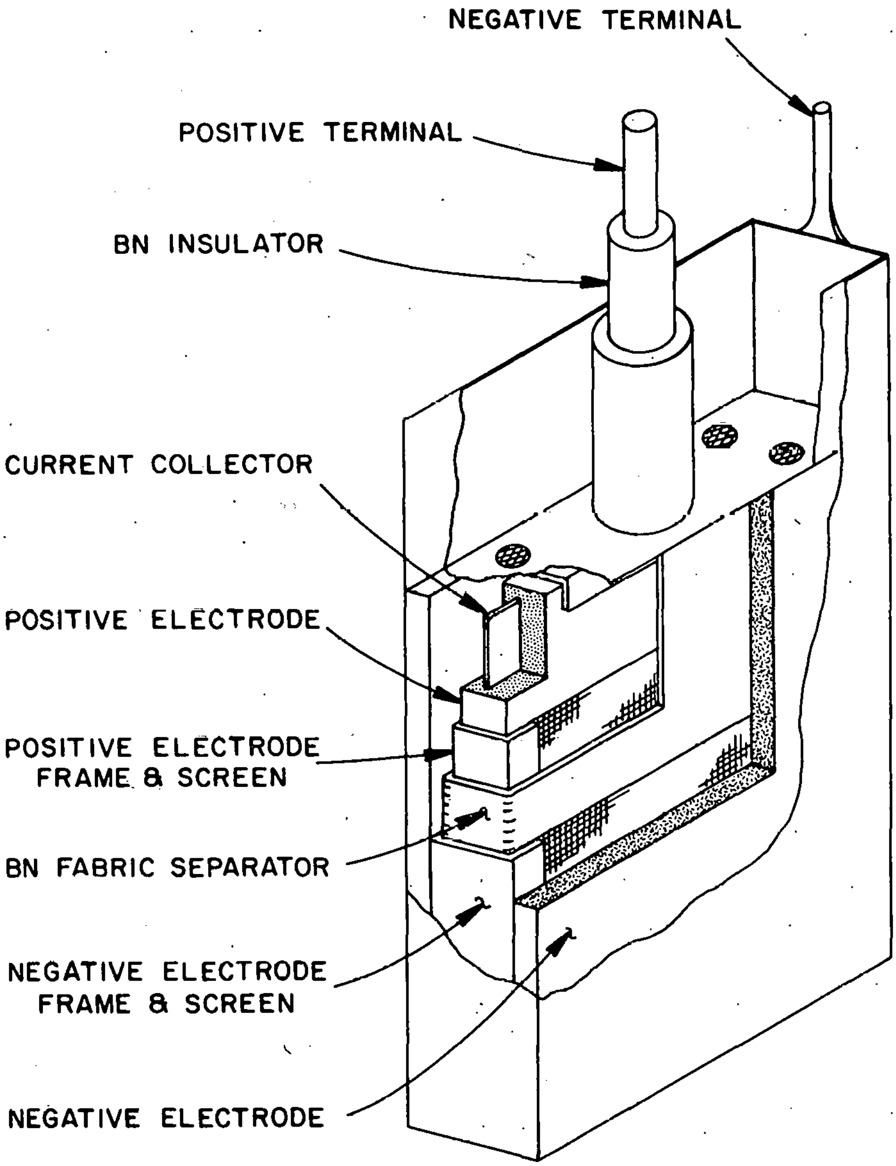

Fig. VI-7. Schematic of the Test Cell Used for the Evaluation of ANL Alloys

Cell 3C-12 was the only cell that failed before completion of the planned period of operation. Over the first 44 cycles, the coulombic efficiency was very stable at 99%. However, a ground loop then developed within the furnace well, and a one-day period of unregulated operation ensued. After the ground loop was repaired, a severe short-circuit was discovered, and operation was terminated at 52 cycles. Post-test examination showed that the short circuit was due to a high concentration of metallic particles throughout the separator. The particulate material was traced to severe attack of the stainless steel particle retainer screens, the positive current collector, and the electrode frames. The latter two components were made from ANL-5-0 and had average corrosion rates of 670 and 350 μm/yr, respectively. These corrosion rates are much higher than the 15 μm/yr rate obtained in the ANL-5-0 components of Cell 3C-10. The severe attack is believed to be primarily attributable to the period of unregulated cell operation because of the rapid development of the particulate short-circuit and certain characteristics of the corrosive attack itself. Cell 3C-16 was assembled as a replacement cell for a more valid test of corrosion in ANL-5-0 alloy.

Cell 3C-13 was operated for 167 cycles and then examined. The ANL-10-20 alloy components showed mild attack from two competing processes. Portions of the collector, primarily the central regions, showed net gains in thickness due to the deposition of a semi-adherent layer of iron particles. The iron deposition layer served to protect the alloy substrate, which therefore exhibited very minor corrosion. Other regions of the collector showed a slight reduction in thickness, ranging from 30 μm near some edge locations to a more typical value of 8 μm. The mean corrosion rate for the ANL-10-20 collector was 27 μm/yr (the thickness change was positive). Near the collector edges, where alloy dissolution was observed, the maximum corrosion rate was 60 μm/yr; the iron deposition rate reached a maximum of +40 μm/yr in some areas. The positive electrode frames also showed alloy dissolution and iron deposition. The degree of reaction was roughly equivalent to the amount noted for the collector, with the deposition reaction more predominant. The mean corrosion rate for Cell 3C-13, which was assembled uncharged, is somewhat higher than the 15 μm/yr deposition rate found for the components of Cell 3C-11, which was assembled charged. This discrepancy in the corrosion rate has been attributed to the state of charge in which the cell was assembled. The better positive-electrode utilization obtained by Cell 3C-13 (46% *vs.* 39%) may also be a factor in the slightly higher corrosion rate. For test cells with nickel collectors, the degree and nature of the attack has been previously (ANL-78-94, pp. 142-143) found to be very sensitive to the original state of charge: 20 to 30 μm/yr iron deposition rate if assembled charged and a 110 to 280 μm/yr corrosion rate if assembled semicharged. The use of finer iron particles (-150, +200 mesh) in the positive electrode mix of Cell 3C-13 instead of the coarser powder (-50 +150 mesh) used in the semicharged nickel-collector cells apparently alleviates accelerated attack on the structural components.

Completion of the post-test examinations for the three remaining cells will provide additional information on the corrosion resistance of these alloys and on the factors that influence the corrosion behavior.

2. Resistivity Measurements of Candidate Collector Materials (J. A. Smaga)

The ohmic losses of the current collectors are contributing factors to the total internal resistance of a cell. Therefore, resistivity values were determined for the ANL alloys and commercial alloys of interest at both 450°C and ambient temperature.

Test samples with a known geometry were prepared from sheet stock. A series of resistance readings was taken at measured intervals along a sample with a four-probe, low-resistance ohmmeter. The resistivity of the test material was then deduced from the slope of the best-fit line through the resistance data points, as determined by linear regression analysis. The measurements at 450°C were conducted in the furnace well of a dry box using extender probes for electrical contact and ceramic blocks to maintain the desired spacing.

The measured resistivity values of seven candidate materials are listed in Table VI-8. The measured values for the commercial materials and their reported values (listed in parentheses in the table) show good agreement; thus, the experimental technique is reasonably reliable. As can be seen in this table, the resistivity of ANL-5-0 at 450°C is 23% higher than that of low-carbon steel; and the resistivities of ANL-10-20 and ANL-15-30 at 450°C are somewhat greater than that of Type 304 stainless steel.

Table VI-8. Experimentally Determined Resistivities

	Resistivity,[a] μΩ-cm	
Material	25°C	450°C
"A" Nickel	9.7 (9.5)	38
AISI 1008	13.7 (12)	52 (52)
ANL-5-0[b]	24.3 (25.4)	64
Type 304 SS	73.9 (72)	105 (103)
ANL-10-20[c]	79.5 (78.0)	109
ANL-15-30[d]	94.4 (92.4)	115
Hastelloy B	135 (135)	138

[a] Values enclosed in parenthesis are reported values for commercial materials or the previously determined values for the ANL alloys.

[b] Alloy composition: Fe-4.5 wt % Mo.

[c] Alloy composition: Fe-10 wt % Mo-20 wt % Ni.

[d] Alloy composition: Fe-15 wt % Mo-30 wt % Ni.

3. Ceramics for Current Collectors in FeS_2 Electrodes

(G. Bandyopadhyay, T. M. Galvin, J. T. Dusek)*

Electrically conductive ceramic coatings on inexpensive metallic substrates are being investigated as substitutes for the high-cost molybdenum current collectors now being used in the positive electrode of FeS_2 cells. The requirements of such a current collector system include (1) sufficient electronic conductivity to provide current collection efficiency, (2) corrosion resistance in the FeS_2 and molten LiCl-KCl environment at 450°C,

---

*Material Science Division, ANL.

(3) resistance to damage under mechanical and thermal stresses that are generated in the cell environment, and (4) significantly less expensive than molybdenum.

Static corrosion tests were conducted on candidate coatings in equal-volume mixtures of FeS_2 and LiCl-KCl eutectic at 500°C for up to 1000 hr. The candidate coatings include seven ceramics--TiC, TiN, TiCN, TiB_2, FeB/Fe_2B, MoS_2, and $MoSi_2$--and two metals--molybdenum and chromium. These coatings were applied by chemical vapor deposition* (CVD) and rf-sputtering† (RFS) techniques on a low carbon steel (AISI 1008) substrate; in some cases, two different coatings were applied to the substrates. Also, monolithic ceramics of TiC, TiN, and TiB_2 were tested. Some of the preliminary test data were presented in the earlier report (ANL-79-39, p. 87). Table VI-9 summarizes the performance of various materials that have been tested in FeS_2 plus LiCl-KCl. Monolithic TiN and TiC showed no evidence of attack by the FeS_2-electrolyte mixture, demonstrating the inherent stability of these materials. The TiC, TiN (with a 1-μm underlayer of TiC)‡, and TiCN coatings which were chemically vapor deposited on substrates showed some attack from the edges and corners of the specimens, whereas all of the rf-sputtered coatings and coating combinations failed in the static tests.

Table VI-9. Summary of Static Corrosion Tests on Ceramic and Metallic Protective Coatings

Materials	Performance[a]
Hot-pressed TiN, TiC	No evidence of corrosive attack.
Hot-pressed TiB_2	Some attack after 300 hr.
CVD coatings:[b] TiC, TiN (with thin underlayer of TiC), TiCN	Some attack after 300 hr.
CVD coating:[b] TiB_2	Severe attack or complete reaction in <300 hr.
RFS coating:[b] Cr, Mo, MoS_2, $MoSi_2$, Cr + TiN, Mo + TiN, TiC + TiN, TiN + TiC	Severe attack or complete reaction in <300 hr.

[a] Tested in FeS_2 plus LiCl-KCl eutectic (equal volume mixture) for up to 1000 hr at 500°C.

[b] Coated on AISI 1008 steel substrates.

---

* Specimens supplied by Materials Technology Corp., Dallas, TX.

† Specimens supplied by Hohman Plating and Manufacturing Inc., Dayton, OH.

‡ Subsequently referred to as TiN coating.

After completion of the above tests, further investigations were carried out on the TiC and TiN coatings. In one experiment, the thickness of the CVD coatings was varied from 8 to 13 µm for the TiC coating and 10 to 23 µm for the TiN coating; these samples were tested at 500°C for 300 hr in FeS_2 plus LiCl-KCl (equal volume), FeS_2 alone, and electrolyte alone. The results from these static tests on TiC- and TiN-coated specimens are summarized in Fig. VI-8, in which the percent of the sample weight loss is plotted as a function of coating thickness. The data show that the bath of FeS_2 plus LiCl-KCl was much more corrosive than either the FeS_2 or LiCl-KCl alone. In addition, increasing the coating thickness beyond 10-12 µm resulted in greatly decreased corrosion resistance of the specimens tested in the bath of FeS_2 and electrolyte.

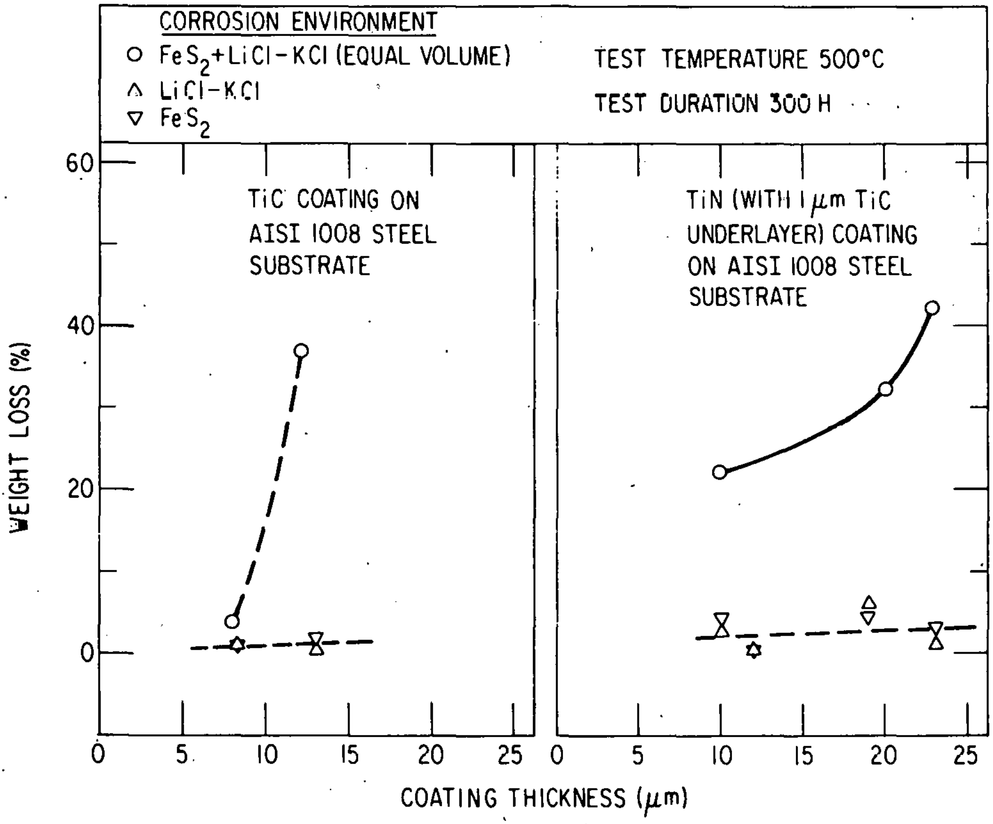

Fig. VI-8. Weight Loss of TiC- and TiN-Coated Samples after Testing as a Function of Coating Thickness

Although the weight loss of the test samples was <5% in the LiCl-KCl environment, examination of these samples indicated that the coating had often spalled off from the edges (see Fig. VI-9). Figure VI-10 shows a high-magnification photograph of this spalling as well as some pitting-type attack by the salt on the coating. The samples tested in the FeS_2 alone also showed some attack at their edges (Fig. VI-11); however, the spalling of coatings was insignificant as compared to that observed on samples in the

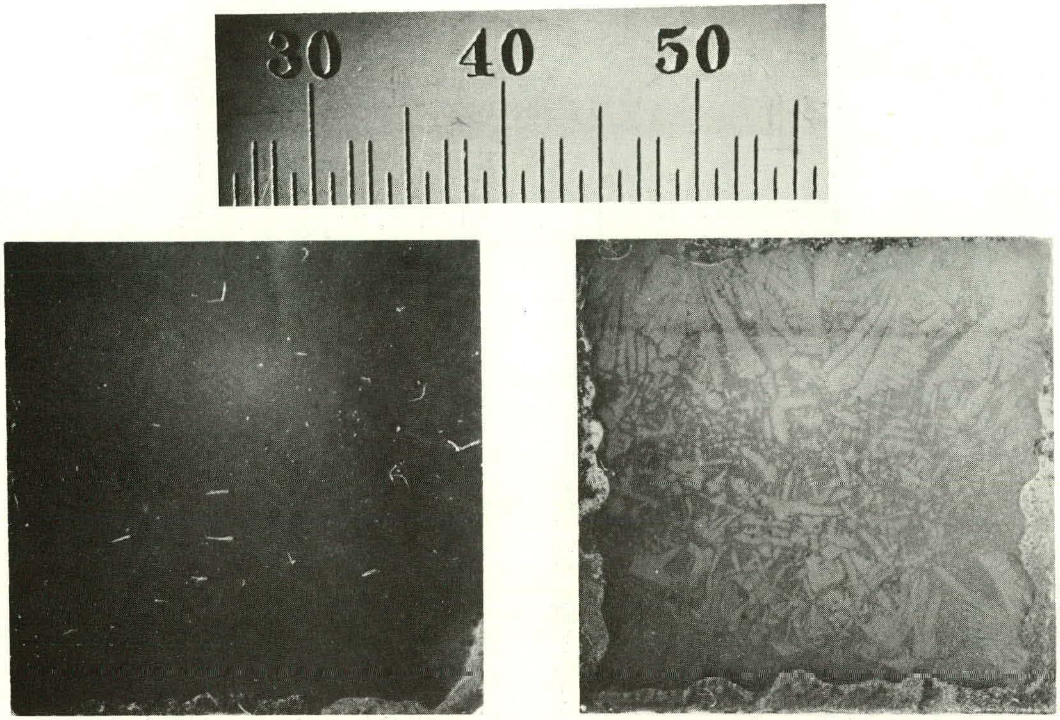

Fig. VI-9. Photographs of TiC-Coated (10 μm thick) and TiN-Coated (10 μm thick) Samples after Testing in an LiCl-KCl Bath for 300 hr at 500°C

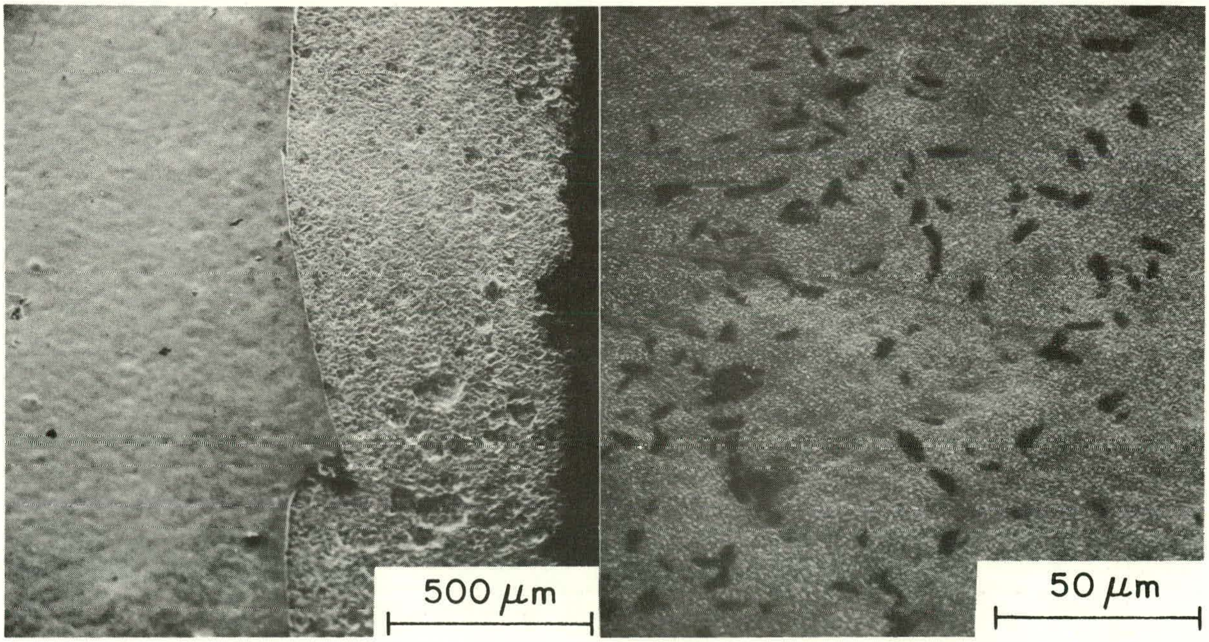

Fig. VI-10. Scanning Electron Micrographs of TiN-Coated Samples after Testing in an LiCl-KCl Bath for 300 hr at 500°C

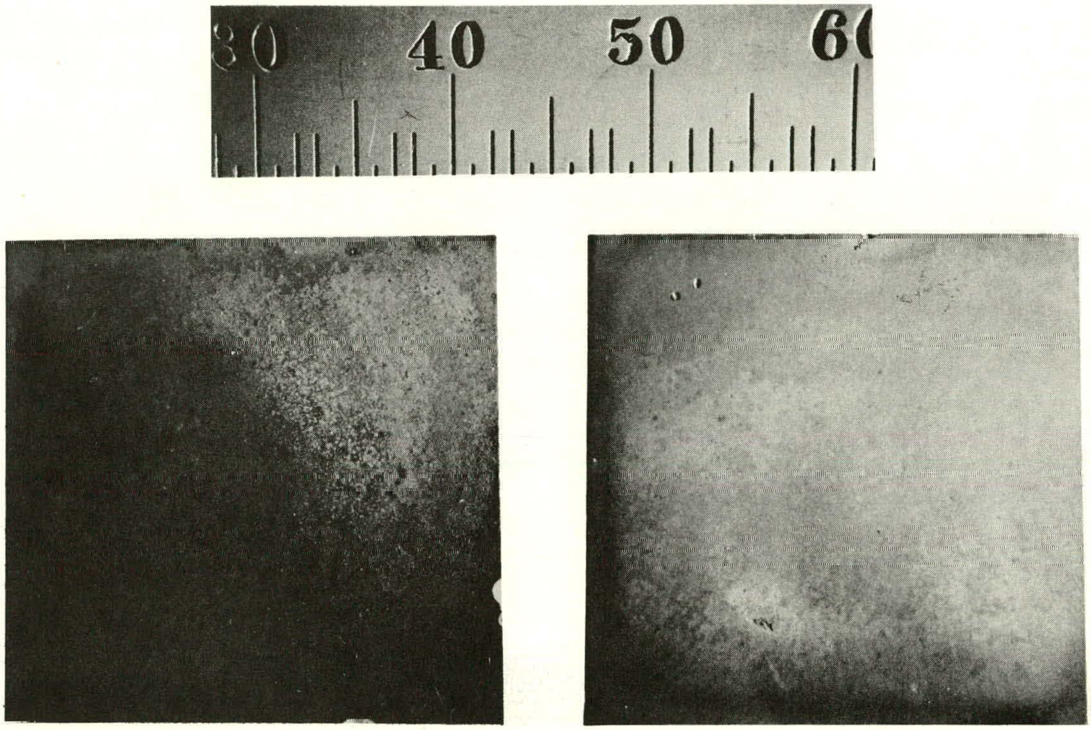

Fig. VI-11. Photographs of TiC (10 μm-thick) Coated and TiN (10 μm-thick) Coated Samples after Testing in an FeS_2 Bath for 300 hr at 500°C

molten electrolyte bath. The above results indicate that the exaggerated corrosion in the FeS_2 plus LiCl-KCl environment is caused by the chloride in the corrosion bath and the residual stresses in the coated test specimens. This resulted in coating failures at the specimen edges and corners, where the residual stresses are expected to be high, by a stress-corrosion mechanism. Once the coating was breached, the substrate was exposed to catastrophic corrosion attack by the sulfide. Figure VI-12 shows the edges of a sample coated with 5-μm TiC and 10-μm TiN which had been immersed in a bath of FeS_2 and electrolyte for 300 hr. Note that most of the coating spalled off from the edge, thus allowing severe corrosion of the substrate by the sulfide. Polishing the edge of a similar specimen tested in FeS_2 plus LiCl-KCl revealed that the substrate was severely damaged from exposure through the edge of the specimen, even in areas where the coating was intact after the test (Fig. VI-13).

To determine the effect of sulfur activity on coatings, samples with the TiC plus TiN coating were immersed for 300 hr in baths having Fe:S mole ratio of 0.9 to 2.0 and eutectic electrolyte at 500°C. In Fig. VI-14, the percent of sample lost during the corrosion tests is shown as a function of Fe:S mole ratio. A sharp drop in corrosion rate was observed as the bath composition shifted slightly to the iron-rich side from FeS_2. This drop in corrosion rate corresponds to a rapid drop of sulfur activity.

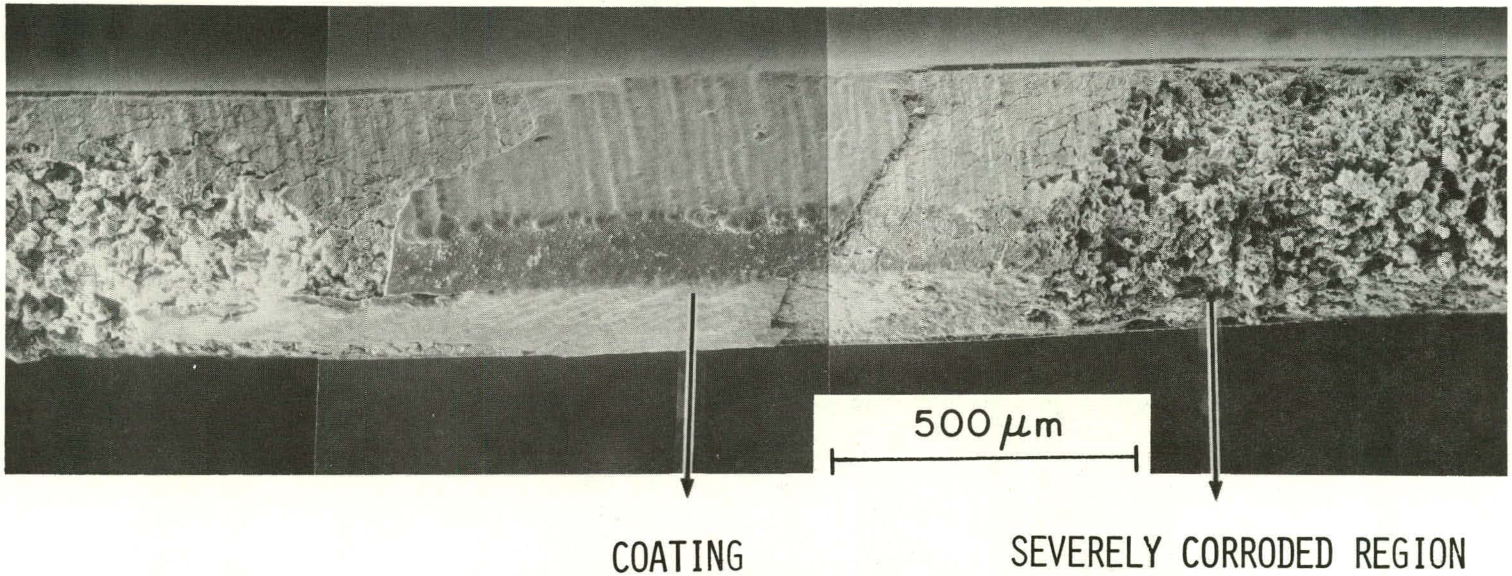

Fig. VI-12. Scanning Electron Micrograph of TiC plus TiN-Coated Samples After Testing in FeS_2 plus LiCl-KCl for 300 hr at 500°C

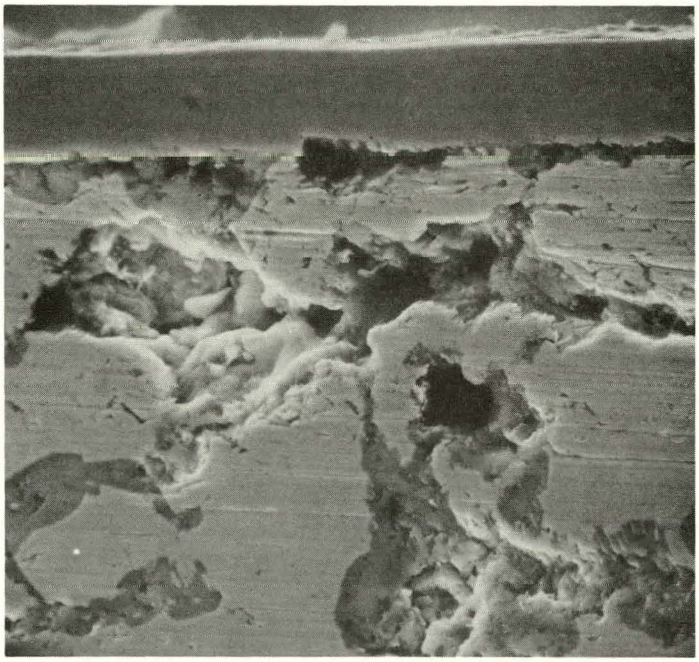

Fig. VI-13. Scanning Electron Micrograph of Corrosion Under Unaffected Coating.

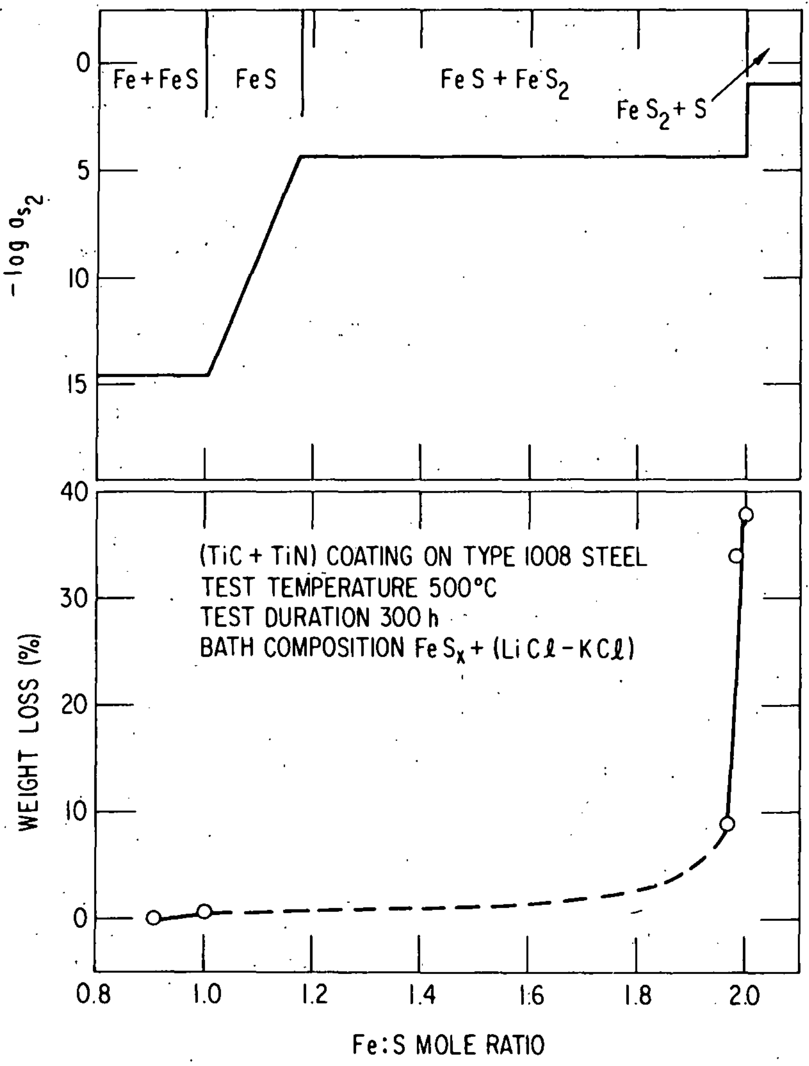

Fig. VI-14. Weight Loss as a Function of Iron-to-Sulfur Mole Ratio of Substrates Coated with TiC and TiN

The coating was vulnerable to corrosiveness, although to a much smaller extent, even in an FeS plus LiCl-KCl environment. This is probably because the molten salt initiated the coating failure. The sulfur activity in the corrosion bath essentially determined the corrosion rates of the coated substrate.

Several samples were obtained with TiN coatings (5 to 22 µm thick) on ANL-5-0 alloys, and they were tested in FeS_2 plus electrolyte baths. The static test data on these specimens are shown in Table VI-10. The ANL-5-0 alloy samples coated with a 10-12 µm thick coating had significantly less weight loss than that of samples coated with 5-7 or 20-22 µm coatings. Also, the corrosion resistance of ANL-5-0 alloy with a 10-12 µm TiN coating was far superior to that of the coated low-carbon steel specimens (*e.g.*, see Fig. VI-8). The improved performance of coated ANL-5-0 alloy can be attributed to better inherent stability of ANL-5-0 alloy in the sulfide environment as compared to that of the low carbon steel.

Table VI-10. Static Corrosion Tests of TiN-Coated ANL-5-0 Alloy Substrate

TiN Coating Thickness, µm	Weight Loss %[a]	
	100 hr	300 hr
5-7	39.00	100.00
10-12	0.64	2.08
20-22	100.00	100.00

[a] Tested in FeS_2 plus LiCl-KCl eutectic at 500°C

The above static corrosion tests indicate that, although some of the coatings provided considerable protection against the corrosive polysulfide environment, additional improvement will be required in their stability for long-term applications. Based on the above results, several modifications can be recommended for improved performance of the coatings: (a) design the current collectors and frames without sharp corners and edges; (b) maintain slightly iron-rich FeS_2 as the positive electrode (*i.e.*, avoid the fully charged state); (c) use a substrate with some inherent corrosion resistance to sulfide (*e.g.*, ANL-5-0); (d) optimize the quality and the thickness of the coating.

The test conditions in cycled cells are considerably milder (lower temperature and lower sulfur activity) than those of the static tests. Therefore, two laboratory-scale cells were tested with TiN-coated positive current collector plates, frames, and screens. Another cell was tested with a monolithic TiN plate as a positive current-collector plate. These cells were operated for approximately 24 cycles (30 days of operation) at a current density of 50 mA/cm^2. Upon post-test examination, neither the monolithic ceramic nor the coated components showed any corrosion. Detailed post-test examinations of these cells are continuing. Additional in-cell tests with coated components will be performed to study the long-time stability of coatings in the cell environment.

REFERENCES

1. J. Newman and Richard Pollard, Extended Abstracts Electrochem. Soc. Meeting, Los Angeles, CA, October 14-19, 1979, Vol. 79-2, Abstract No. *182* (1979).

2. M. L. Saboungi and A. E. Martin, Extended Abstracts of the Electrochem. Soc. Meeting, Pittsburgh, PA, October 15-20, 1978, Vol. 78-2, p. 919 (1978).

3. R. D. Freeman, *Thermochemical Properties of Binary Sulfides,* Okla. State Res. Found., Report No. 60, Jan. 1962.

4. N. P. Yao, L. Heredy, and R. C. Saunders, J. Electrochem. Soc. *118,* 1039 (1971).

5. K. C. Mills, *Thermodynamic Data for Inorganic Sulfides, Selenides and Tellurides,* Butterworths, London (1974).

6. D. F. Pridmore and R. T. Shuey, American Mineralogist *61*, 248 (1976).

7. D. Argyriades, G. Derge, G. M. Pound, Trans. Met. Sco. AIME *215,* 909 (1959).

8. J. P. Suchet, *Crystal Chemistry and Semiconduction in Transition Metal Binary Compounds,* Academic Press, NY, p. 208 (1971).

9. R. J. Heus and J. J. Egan, J. Phys. Chem. *77*, 1989 (1973).

10. W. M. Latimer, J. Am. Chem. Soc. *73*, 1480 (1951).

11. *JANAF Thermochemical Tables,* Dow Chemical Co., Midland, Michigan (1965).

12. K. C. Mills, *Thermodynamic Data for Inorganic Sulfides, Selenides and Tellurides,* Butterworths, London (1974).

13. J. F. Elliott and M. Gleiser, *Thermochemistry for Steelmaking,* Vol. 1 Addison-Wesley Publishing Co., Reading, Mass., 1960-1963.

14. A. H. Clark, Econ. Geol. *65*, 590 (1970).

VII. SYSTEMS DESIGN AND COST ANALYSIS
(A. A. Chilenskas)

The approaches taken in designs of systems for the electric-vehicle (EV) and stationary energy-storage (SES) batteries are discussed below.

A. Conceptual Designs of SES Batteries*
(S. M. Zivi, I. Pollack,† H. Kacinskas†)

The design criteria for an SES battery to be used for daily load leveling are as follows:

(1) 100 MW-hr of electrical energy must be stored in about 7 hr, which can be then discharged over a 5-hr period at times of peak load (this cycle must be repeated five consecutive days per week).

(2) The plant lifetime must exceed 20 years, although the cells can be replaced after 10 years.

(3) The cost per kilowatt hour should be in the range of \$45 to \$55.

In 1978, the first conceptual design of a 100 MW-hr SES battery having Li/MS cells was developed as a result of a joint effort between ANL and Rockwell International (ANL-78-94, pp. 116-120). In this design, the submodule, which is the basic replaceable unit for the battery, consisted of ninety-six 2.5 kW-hr cells. However, the cost for this battery was found to be too high, \$60-80/kW-hr excluding the cells and converters. Therefore, other possible conceptual designs were investigated. Rockwell International proposed a design, described in Section II.C, in which the submodule consists of four-hundred and eight 2.5 kW-hr cells. The other two proposed designs were developed at ANL; the submodule consists of one-hundred 1.2 kW-hr cells in one of them and one 30 kW-hr cell in the other. The above designs will be described more fully in a forthcoming report.[1] The cell technology assumed for these designs was that projected for the mid 1980's as a result of the successful completion of the EV battery program. (Under a separate contract, United Technologies Corp. conducted a study[2] of the interface between the SES battery and the converter. The major conclusion of this study was that the terminal voltage at the converter should be 2000 V.)

The four conceptual designs represent a very broad range of engineering approaches, ranging from designs based on present-day hardware to designs which require significant advances in technology. Table VII-1 presents the costs projected for the four designs in the order of increasing technical advancement required. Of the four, the SCS and LCS systems appear to be the most technically practical and have acceptable costs.

For the 1978 RD, the electronic equalization was the same as that used for electric-vehicle batteries, and contributed to a relatively large portion

---

*This effort was funded by the Electrical Energy Systems Division of the Department of Energy.

†Engineering Division, ANL.

Table VII-1. Cost of Proposed SES Batteries

Designation	Capacity, kW-hr		Battery Hardware Cost,[a] \$/kW-hr	Energy Footprint,[b] kW-hr/ft^2
	Cell	Submodule		
1978 RD	2.5	240	60-88	11
SCS	1.2	120	30-60	10
LCS	2.5	1020	22-37	8
LFSC	30	30	22-25	9

[a] Cell cost not included.

[b] Converters excluded from this value.

of the overall battery cost. For the SCS and LCS designs, a new equalization scheme was proposed which consists of a fixed resistance shunt of appropriate resistance for each cell. This equalization scheme adds very little equipment cost to the battery; the sacrifice in coulombic and energy efficiency is about 4%.

The cell reliability required for an SES battery was assessed since there are no data on the mean time before failure (MTBF) of the cells that would be used in such a battery. The approach taken was to determine what MTBF would be required for a low maintenance battery. It appears that a MTBF of about 200 years[*] will be required over the cell's useful life of ten years. This may be difficult to achieve, although the cell reliability that will probably be required for the EV application is of the same order. This long MTBF favors smaller cells than might otherwise be optimum for this application.

B. Cost Analysis for Li/MS Cells

(A. A. Chilenskas, J. C. Schaeffer,[†] W. L. Towle[‡])

In an earlier report[3] (1976), the cost was estimated for an Li-Al/FeS cell for SES applications (theoretical capacity, 1000 A-hr). For the present cost analysis,[**] these costs have been updated and revised to also include Li-Al/FeS and Li-Al/FeS$_2$ cells for EV applications (theoretical capacity, 400 A-hr). Based on experience with the Mark IA cell, the weights of the components for the EV and SES cells were estimated and are given in Table VII-2. Since these cells can be assembled with the active material in the charged or uncharged state, the component weights for both of these assembly conditions are included in the table. The cost in mass production for the

---

[*] A MTBF of 200 years can be considered as a failure rate of 0.5% of the total cells per year or 5% of the total cells in 10 years.

[†] Industrial Participant, ESB/RAY-O-VAC Corp.

[‡] Private Consultant.

[**] This cost analysis will be described more fully in another report (see Ref. 4).

Table VII-2. Material Weights for Li/MS Cells

	Weight, lb/kW-hr					
	SES		EV (FeS)		EV (FeS_2)	
Component	Disch.	Charged	Disch.	Charged	Disch.	Charged
Electrodes						
Lithium	0	0.67	0	0.67	0.06	0.57
Aluminum	2.52	2.52	2.52	2.52	2.17	2.17
Li_2S	2.22	0	2.22	0	1.69	0
FeS	0	3.75	0	3.75	0	0
FeS_2	0	0	0	0	0	2.12
Fe	2.20	0	2.20	0	0.94	0
Electrolyte						
LiCl	2.19	2.19	2.19	2.19	2.08	2.08
KCl	2.79	2.79	2.79	2.79	1.92	1.92
Separator						
BN	0	0	0.33	0.33	0.33	0.33
MgO	1.95	1.95	0	0	0	0
Current Collector						
Neg.	1.05	1.05	1.05	1.05	1.05	1.05
Pos.	1.05	1.05	1.05	1.05	0.33-0.50	0.33-0.50
Cell Can	3.50	3.50	1.70	1.70	1.70	1.70
Feedthrough	0	0	0	0	0	0
Miscellaneous	2.53	2.53	1.88	1.88	1.47	1.47
Total Cell Wt.	22.0	22.0	17.93	17.93	14.08	14.08
Lithium Content	1.03	1.03	1.03	1.03	0.91	0.91

materials listed in this table were then determined from commodity prices obtained from market publications; when these prices were not available, other sources were used to obtain reasonable estimates. Table VII-3 shows the cost of the five most expensive materials for the Li/MS cell. The most expensive material, lithium, has a cost range of \$4.61/kW-hr for an uncharged cell to \$14.62 for a charged cell. Other costs for cell production, including production equipment and labor, were then estimated from the costs given in the previous report (ANL-76-12) for cell production in a second-generation manufacturing plant of 1.1 MW-hr/yr capacity; these costs were scaled up to account for inflation, production rate, cell size, and fabrication complexity. Combining these other costs with the materials costs, the manufacturing cost for each of the three proposed cell designs was calculated. Figure VII-1

Table VII-3. Most Expensive Materials in a Li-Al/MS_x Cell

Material	Cost Range, $/kW-hr (1979 Dollars)
1. Lithium or Lithium Compounds	4.61-14.26
2. Boron Nitride Felt[a]	4.00-8.50
3. Feedthrough Parts	2.40
4. Molybdenum Powder for Current Collector (FeS_2 Cells only)	1.45-2.20
5. Aluminum	1.43-1.66

[a] For this cost projection, it was assumed that 4-5 ft^2/kW-hr of felt is required for a Li/MS cell.

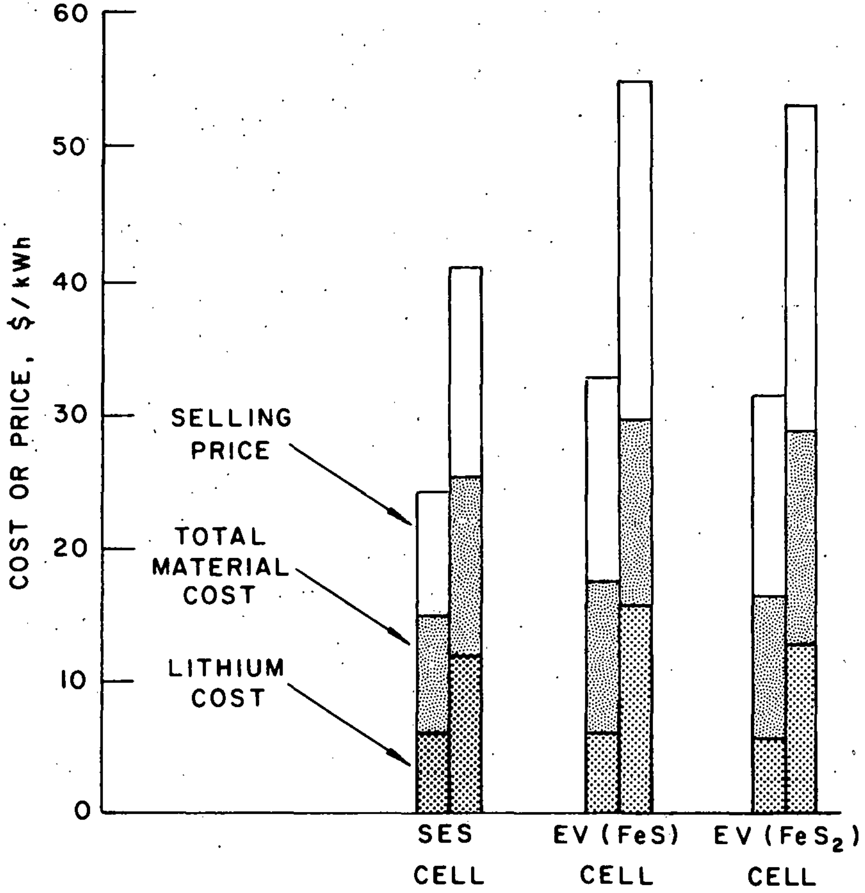

Fig. VII-1. Selling Price for Li/MS Cells shows the final selling price determined for the three cell designs; for each design, high and low estimates were made for each component contributing to the cell manufacturing cost. In summary, the selling prices were estimated to be \$24 to 41/kW-hr for the SES cell and \$31 to 55/kW-hr for the EV cell.

C. Design and Development of In-Vehicle Testing Equipment

After fabrication of Li/MS batteries, they will be tested in the laboratory under a variety of modes, including computer-simulated road conditions. Once this testing is completed, the battery will be road tested at ANL in a vehicle; the instrumentation developed to carry out this testing is described below. This testing will then be followed by vehicle testing of Li/MS batteries by outside contractors and vehicle manufacturers.

1. Instrumentation for In-Vehicle Testing*

(W. H. DeLuca, C. Nelson†)

An instrumentation package was developed at ANL to acquire performance measurements for a vehicle powered by an Li/MS battery under road-load conditions. Technical operational information from various manufacturers and users of in-vehicle test equipment was used to assist in the formulation of both system and component specification. A general block diagram of the ANL testing instrumentation is given in Fig. VII-2. The on-board package includes a microprocessor-controlled data acquisition and recording system, a parameter-signal integrator/display unit, a signal-level monitor/alarm unit, and an operator visual/audible driving schedule meter. This equipment logs measurements of battery and vehicle parameters on magnetic tape, while electromechanical displays furnish an immediate visual indication of battery charge and energy transfer as well as vehicle speed and range. The off-board support system provides a graphical display of recorded road-test data as a function of battery operating time on a cathode ray tube (CRT) terminal. The off-board support system also contains an editor and assembler software package and a programmable-read-only memory (PROM) which may be used to modify, expand, or improve the operating program for the microprocessor of the on-board data-acquisition system.

The on-board data-acquisition system and off-board support system were procured from the Omnibyte Corporation (Oak Brook, IL) with sufficient software to initiate preliminary in-vehicle testing with lead-acid batteries. Transducer interface electronics and display/alarm equipment were designed and fabricated at ANL to satisfy the unique requirements of the electric test vehicle and the parameters to be monitored. A power supply package, to furnish all of the voltage levels necessary to operate the on-board instrumentation electronics, was also developed at ANL.

---

*Funded by the Department of Energy, Division of Transportation Energy Conservation.

†ANL Electronics Division.

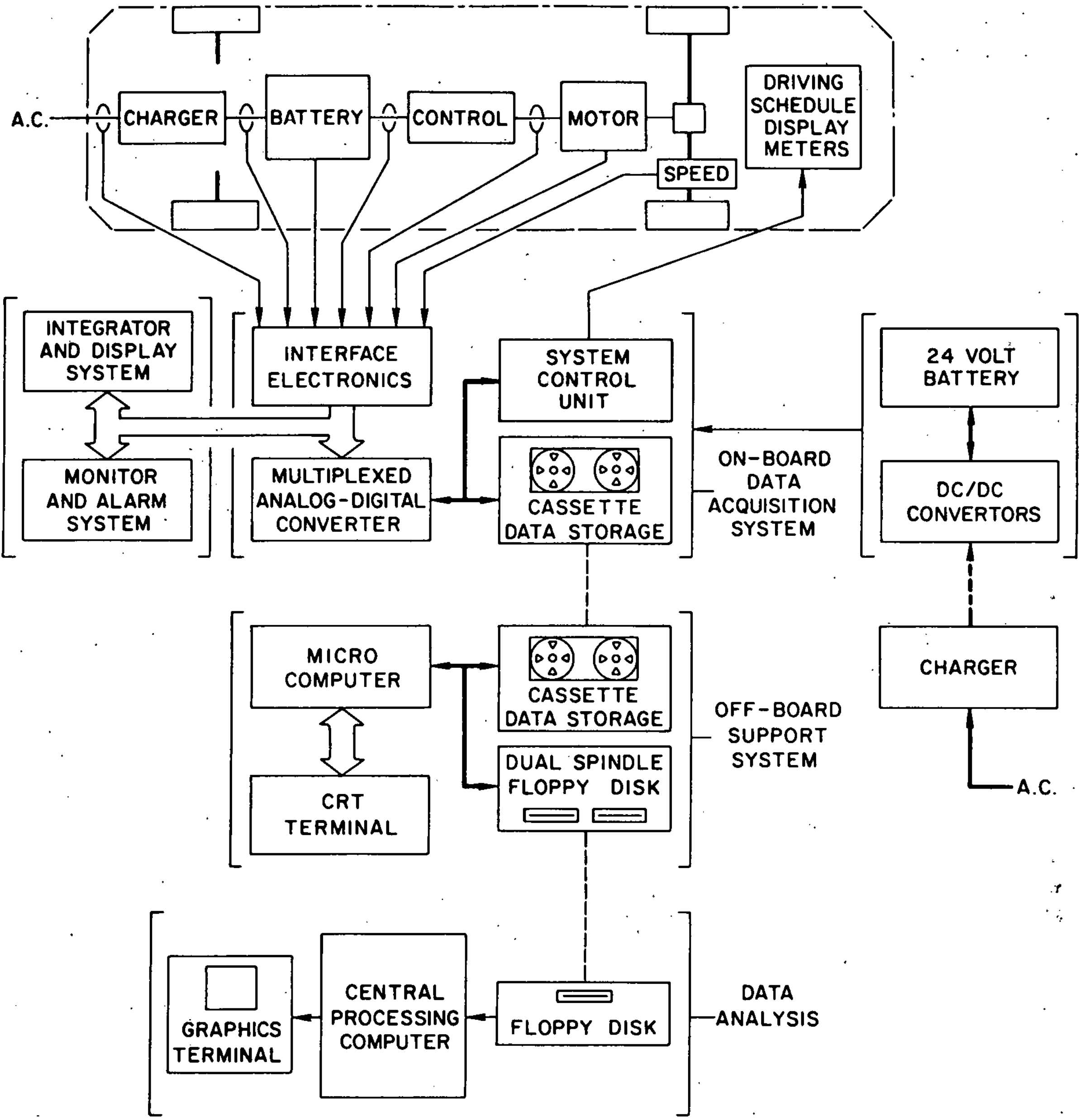

Fig. VII-2. Block Diagram of Data-Acquisition and Processing System for In-Vehicle Battery Tests

The major factor in the overall accuracy of the on-board instrumentation package is the operation and calibration of the interface electronics. The interface electronics (including transducers) is used to electrically isolate parameter detection points, minimize noise interference, and scale transducer signal levels for maximum measurement resolution. To establish battery load and operating conditions, the interface electronics signal the average current, voltage and power, root-mean-square (RMS) current (to assist evaluation of battery temperature fluctuations), and temperature. A simplified block diagram is given in Fig. VII-3 to illustrate the technique employed in establishing these battery operating parameters. A Hall-effect current transducer is used to detect instantaneous battery current. This transducer provides electrical isolation between the instrumentation system and vehicle propulsion components and is easy to install. An average power signal is obtained using a four-quadrant analog multiplier which provides the product of the detected instantaneous current and voltage signals. The RMS value of the detected current waveform is obtained using a "true" (*i.e.*, independent of wave shape) RMS-to-DC conversion module. A second set of electronics with similar circuitry is used to obtain average current, voltage, and power for the vehicle motor. The propulsion battery is divided into two equal modules, and an additional set of electronics is used to detect the average voltage and power of each module. The interface electronics permits battery performance measurement under both charge and discharge conditions. Type K thermocouples with appropriate signal amplification are used to monitor battery temperature. To relate battery parameters to vehicle operation, a speed signal was obtained using a Ford Motorcraft speed sensor (Type DY-114, D4AZ-9E731-A) installed on the speedometer cable. A total of sixteen battery and vehicle performance measurements can be made with the interface electronics.

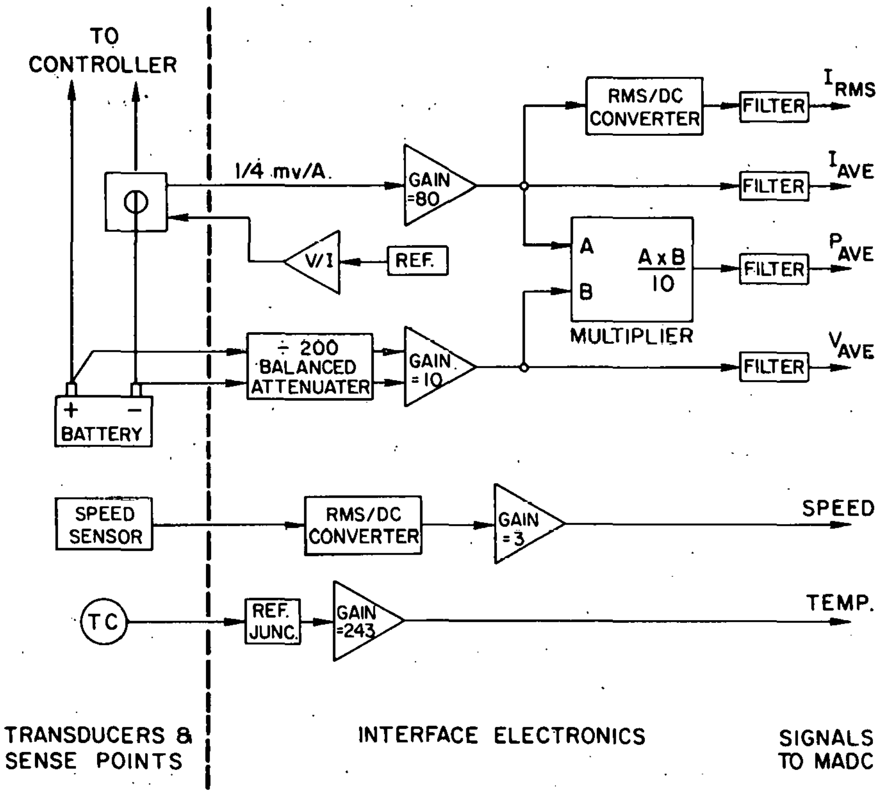

Fig. VII-3. Interface Electronics for On-Board Instrumentation (X and Y are input signals, TC is a thermocouple, and MADC is the multiplexed analog-to-digital converter)

These sixteen parameters were calibrated to particular scaling factors selected to provide a maximum dynamic signal variation within the voltage limits of the analog-to-digital converter (±10 V) for maximum resolution (5 mV). Table VII-4 gives a listing of the range and resolution achievable for the scaling factors selected. To accommodate parameter ranges of alternative vehicles and/or battery configurations, only the scaling factors (amplification/attenuation factors) of the interface electronics require adjustment.

Table VII-4. Battery/Vehicle Parameters

Parameter	Range	Resolution	Scale Factor
Battery			
Average Voltage	0-200 V	0.1 V	20 V/V
Average Current	0-500 A	0.25 A	50 A/V
RMS Current	0-500 A	0.25 A	50 A/V
Average Power	0-100 kW	50 W	10 kW/V
Battery Module[a]			
Average Voltage	0-100 V	0.05 V	10 V/V
Average Power	0-50 kW	25 W	5 kW/V
Temperature	0-1000°C	0.5°C	100°C/V
Motor/Vehicle			
Average Voltage	0-200 V	0.1 V	20 V/V
Average Current	0-500 A	0.25 A	50 A/V
Average Power	0-100 kW	50 W	10 kW/V
Speed	0-100 mph	0.025 mph	10 mph/V

[a] The battery consists of two modules.

The parameter signals from the interface electronics are measured and recorded by the on-board data acquisition system. The rate at which data are acquired is manually selected by the operator. A microprocessor-controlled analog-to-digital converter (ADC) with 16 addressable input channels is used to perform these periodic measurements. The ADC microprocessor is preprogrammed to sequentially address each analog input channel and to obtain the converted digital values in a period of less than 1 msec. The digital values are transferred to the data recorder when the sampling period is completed. The total data sample periods executed from the start of a test are recorded to indicate elapsed test time. This time value is also transferred to the recording unit with the performance measurements to establish the test time at which the data were obtained. The time interval between data sample periods is established by the operator, who manually selects one of the four possible sampling rates (3, 1, 0.5 or 0.1 Hz) on a front panel switch and then initiates the system by pressing the reset button. When initiated, the ADC microprocessor presets an internal interval timer with an appropriate time value (0.333, 1.0, 2.0, or 10 sec) to generate microprocessor interrupt pulses that initiate data sampling at the selected rate.

The data recorder consists of a high-speed cassette, magnetic-tape transport unit controlled by a second microprocessor. To minimize the tape footage wasted by performing repeated start/stop operations, the recorder microprocessor accumulates a record of values from 60 data sample periods (1020 values) before recording the information on magnetic tape. After each record is placed on magnetic tape, the data are read back by the microprocessor to ensure recording accuracy. If the microprocessor detects an error, it will record the data a second time and perform another test. If the second attempt fails to test successfully, a visual and audible alarm is given to indicate the recording error, and data acceptance from the ADC microprocessor is resumed. The operator is provided with a switch to temporarily halt data acquisition and recording if testing is interrupted. In this mode, the elapsed test-time counter (sample period number) continues to operate so that a record of the halt period is obtained when testing is resumed.

Table VII-5 lists the operational specifications for the on-board data acquisition system. When a cassette tape has been completely filled with data (210 records), a visual and audible indication is given to inform the operator that another cassette tape is required. If the installation of a new cassette should exceed the time used to obtain sixty data samples, data acquisition will be halted. The elapsed test-time counter continues to operate during this period so that the true data acquisition time is recorded when operation is resumed after the new cassette is installed. A maximum of 65,000 data samples can be obtained during any given testing period. All of the data can be recorded, provided that additional cassette tapes are installed as each one becomes filled with data.

Table VII-5. Data-Acquisition-System Specifications

1. Analog-to-Digital Converter	
Number of Inputs	16
Input Signal Range	±10 V
Input Resolution (12 Bits)	5 mV
Conversion Time Each Input	∿33 μsec
2. Data Acquisition	
Data Per Sample Period	17
Sample Period Acquisition Time	1 msec
Data Samples Per Record	60
Data Records Per Cassette Tape	210
3. Data Sampling Rates[a]	
3 Samples per sec	1.2 hr
1 Sample per sec	3.5 hr
1 Sample per 2 sec	7.0 hr
1 Sample per 10 sec	35 hr

[a] Numbers on the right indicate the time required before cassette is filled.

To furnish an immediate and continuous indication of certain performance parameters, a multi-channel signal integrator and electromechanical display unit was developed as part of the on-board instrumentation. The operation and function of this unit is illustrated in Fig. VII-4. The input signal is converted to a series of pulses whose frequency is directly proportional to the voltage level of the input signal, using a standard voltage-to-frequency converter module. An electromechanical counter is then used to integrate the signals of battery current, battery power, and vehicle speed from the transducer interface electronics; from these data, battery charge (A-hr), energy (W-hr) and vehicle range (miles), respectively, are determined and displayed. Electromechanical counters are used to ensure that the integrated values are not lost as a result of a power-source interruption. Six integrator/display channels are available for use. Integration is only performed when the input signal has a positive polarity. Thus, if the battery current and power signals are properly connected to two integrating channels each, the capacity and energy during discharge and charge (including regenerative braking) can be accumulated separately. The electromechanical counter values for energy transfer and vehicle range were found to compare within 1% of the values obtained by the vehicle energy meter* and odometer.

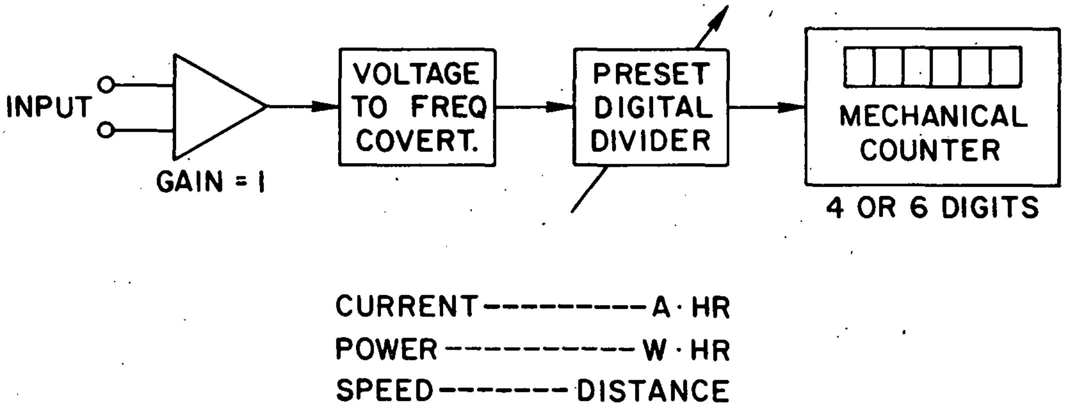

Fig. VII-4. Integrator/Display System
(Six Channels)

A signal monitoring and alarm unit was also developed for the on-board instrumentation. This unit monitors and compares up to six input signals against manually preset (high and low) voltage limits, setting off a visual and audible alarm when any limit is exceeded. Figure VII-5 gives a block diagram of one of these monitor/alarm channels. This unit was intended for monitoring selected individual cells of a LiAl/FeS battery during in-vehicle operation, but may be used to monitor any vehicle or battery parameter.

---

*Manufactured by DAUG, Germany.

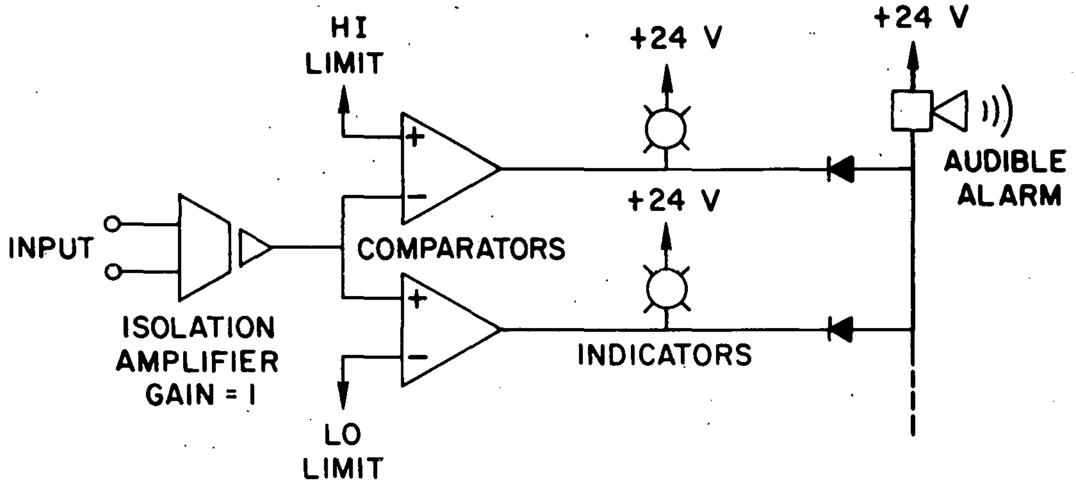

Fig. VII-5. Monitor/Alarm System
(Six Channels)

To assist the vehicle operator in adhering to the driving schedule outlined for a given test, the instrumentation package includes a visual/audible driving aid unit. A display module containing three analog meters is mounted in front of the operator on the vehicle's dash panel. One meter continuously displays vehicle operating speed in miles per hour as detected by the interface electronics package, and a second meter displays the preset driving schedule outlined for the test. The third meter is used to indicate the difference between the two speeds as indicated on the other meters. The operator thus attempts to maintain a null position on the third meter. If the preset driving schedule requires an action from the operator to alter vehicle speed, an audible alarm is sounded one second prior to the start of the required change. To generate the preset driving schedule signal, PROM integrated circuit is preprogrammed with digital values that represent the vehicle speeds to be used during operation. The off-board support system is used to perform this task. During vehicle operation, the values are sequentially outputted to a digital-to-analog converter module at the data sampling rate. An analog driving profile signal results. The memory unit is also programmed to sound the audible alarm to indicate pending speed changes. This unit has proven to be an effective means of achieving driving uniformity to obtain reproducible data for any given testing period.

The power required to operate the electronics and the on-board instrumentation is obtained from a 24-V battery pack. A DC-to-DC switching power supply from Three Etatech Inc. (Plasentia, CA) furnishes ±5, ±12, and ±15 V voltage levels needed for equipment operation. The total power consumption for the instrumentation package is ∿84 W as measured at the battery pack. Two battery packs with different rated capacities were fabricated to accommodate a range of anticipated in-vehicle testing periods. The first unit contains two 32 A-hr, 12-V Titan (9200 LT) lead-acid batteries and weighs a total of

18.6 kg. This unit provides ∿8 hr of equipment operation. The second unit contains two 84 A-hr, 12-V Exide (M-84) batteries that weigh 42.3 kg, and provides ∿20 hr of equipment operation. A current-limited (12 A), constant-voltage (28 V) battery charger was fabricated to power the instrumentation package and recharge its battery pack when the vehicle was not in operation.

Figure VII-6 is a photograph showing the on-board instrumentation equipment. The upper right-hand chassis contains the integrator/display and monitor/alarm units described above. The Omnibyte Corporation unit contains the data acquisition system and transducer interface electronics. All transducer and voltage sensing signals input to the interface electronics via rear panel connectors. The battery and power packs are located on the left side of the photograph. Figure VII-7 shows the off-board support system. A plot of battery current and voltage data recorded during a laboratory test of the 6-V LiAl/FeS Mark IA module fabricated by Eagle-Picher (see Section II.A) is displayed on the CRT terminal. A dual-spindle floppy-disk storage system is contained in the lower right chassis, and the microcomputer chassis is located in the upper right. The cassette tapes containing recorded test data are placed in the off-board support system, and the information is transferred to floppy disk storage. The data on the floppy disk can then be graphically displayed for examination and study. The socket used to program the driving profile data into the memory elements for the operator's driving assistance system is located on the microprocessor chassis front panel.

The data analysis system is presently programmed to accept the test data that are stored on the floppy disks. The parameters can be plotted with respect to elapsed test time. Additional computer programs have yet to be written to utilize the data to characterize testing conditions and obtain battery operational performance information.

2. In-Vehicle Testing

(W. H. DeLuca, E. R. Hayes, J. Brown,* A. Jackson†)

To obtain preliminary test data on vehicle operating characteristics and test procedures, the Volkswagen Transporter Van was operated on a circular test tract at ANL (3.74 km per cycle) when powered by lead-acid batteries. This vehicle has a gross weight of 3080 kg (6780 lb) and a 16 kW shunt-wound DC motor which weighs 87 kg (192 lb) and has a peak power output of 32 kW. The vehicle speed is controlled by the use of a DC chopper in the armature circuit of the motor that regulates the power delivered to the motor up to vehicle speeds of 25 km/hr (14 mph). Motor-field weakening control is used to regulate the vehicle speed from 25 km/hr to 77 km/hr (vehicle top speed). The DC chopper is rated at a voltage of 114 V and capacity of 321 A and weighs 50 kg (110 lb). The electric energy and power is supplied by a battery pack, weighing 687 kg (1512 lb), of 246-V lead-acid batteries (EV-106) manufactured by the ESB/Ray-O-Vac Corp. Vehicle test procedures employed were based upon the manual, published in 1976 by the Energy Research and Development Administration, *Electric Vehicle Test Procedure-SAE J227a*.

---

*Co-op student, North Carolina State University.

†Co-op student, Illinois Institute of Technology.

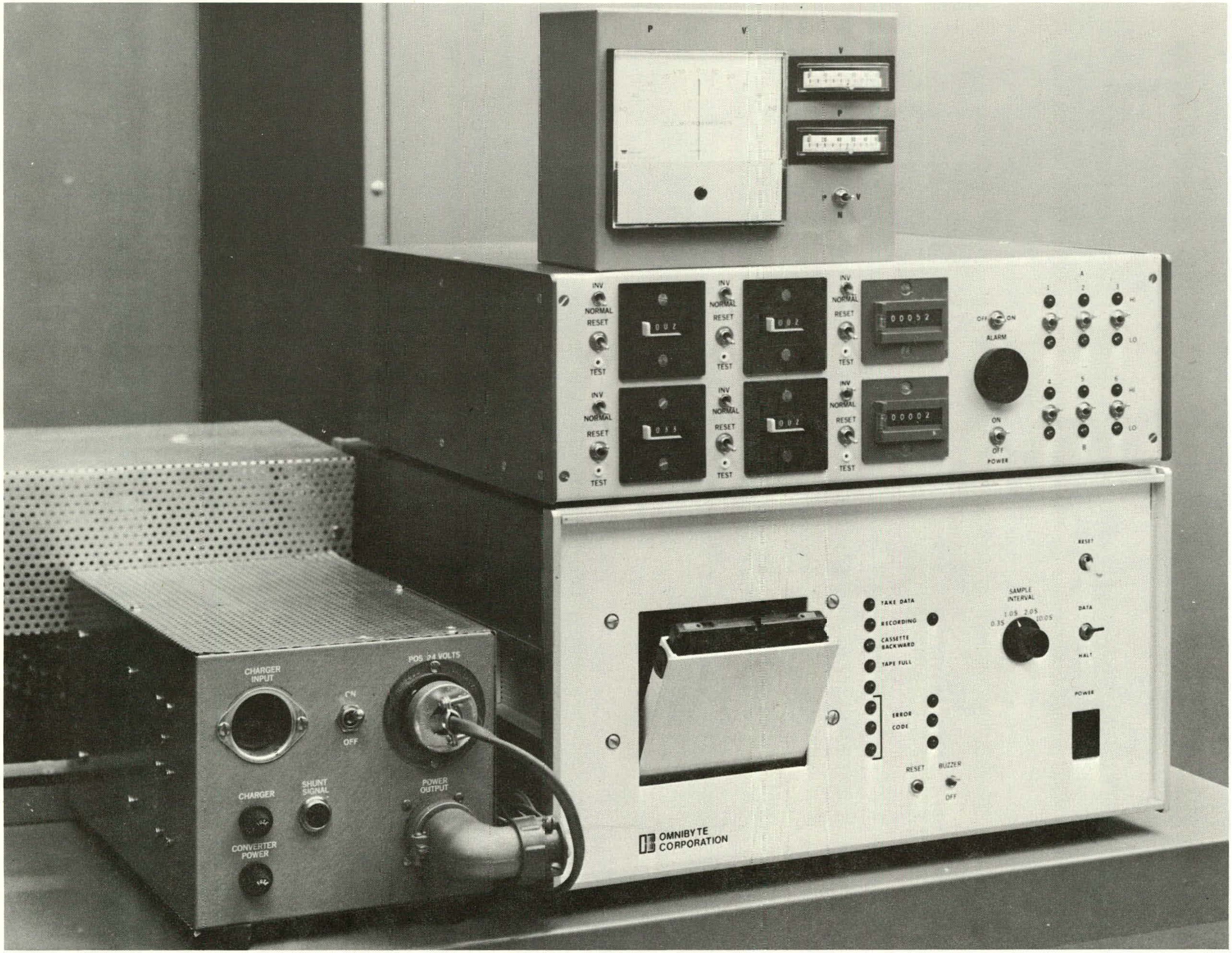

Fig. VII-6. In-Vehicle Instrumentation Package.
ANL Neg. No. 308-80-5.

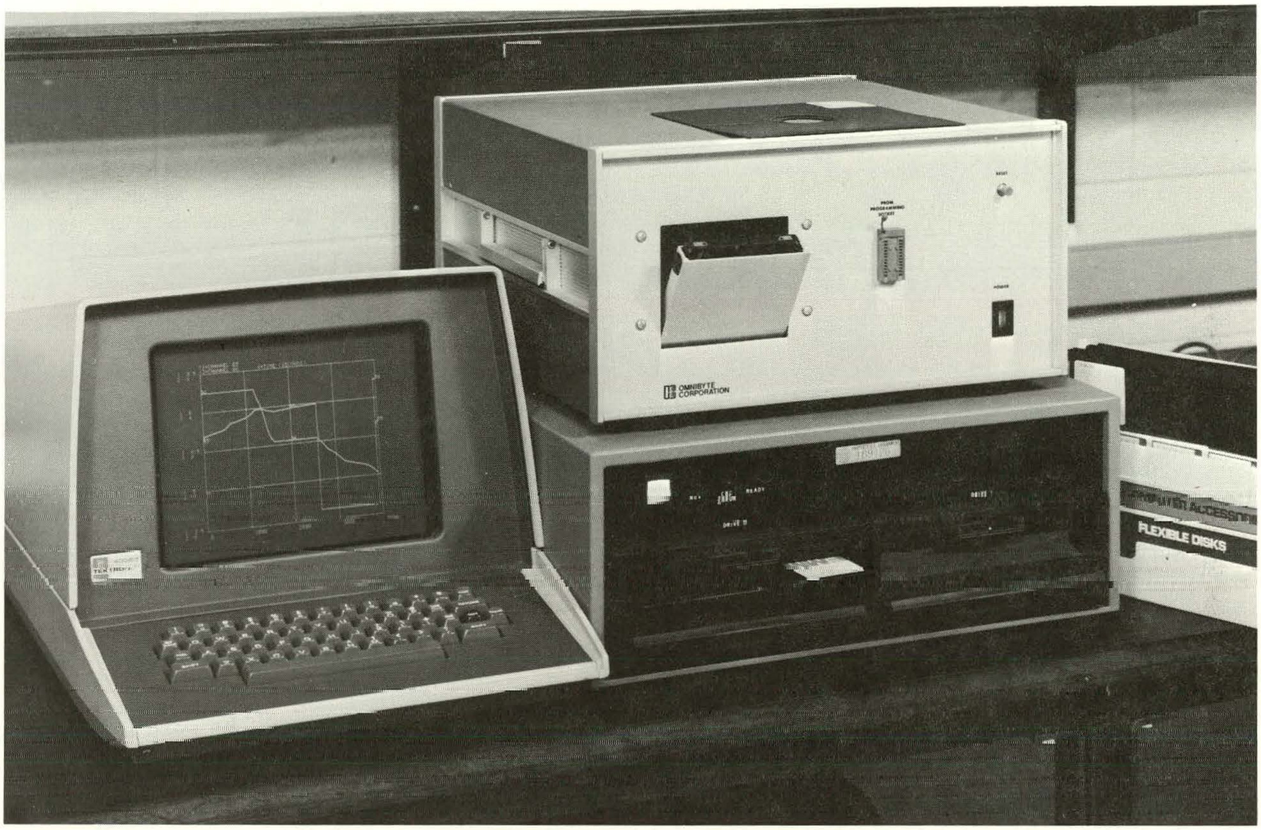

Fig. VII-7. Off-Board Support System.
ANL Neg. No. 308-80-2.

Figure VII-8 shows the acceleration demonstrated by the vehicle. These measured values were used to calculate the maximum vehicle speed as a function of road grade; these calculations are shown in Fig. VII-9. Figure VII-10 shows the power measured to maintain a constant speed. In another test, the vehicle was driven at a constant speed of 39.9 km/hr (24.8 mph). The distance traveled by the vehicle and the battery output are provided in Table VII-6.

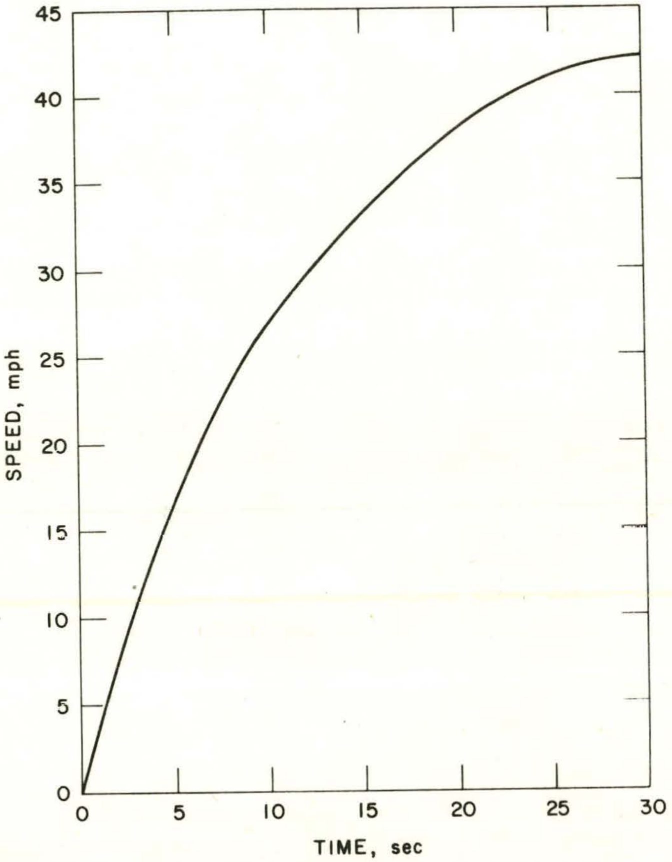

Fig. VII-8. Acceleration of VW Electric Van

Table VII-6. Range Test of Van Driven at Constant Speed of 40 km/hr

Distance Driven, km	100.0 (62.1 miles)
Battery Output[a]	
Capacity, A-hr	131.5
Energy, kW-hr	16.8

[a] Average of two runs.

During the range tests, the road load imposed upon the battery was measured by a vertical axis accelerometer (Entram, EG-500-DS-10) centered on the rear channel of the battery case. The maximum load of 0.25 g was measured at two locations on the track; the average load ranged from 0.05-0.1 g, with a frequency of 10-20 cycles/min.

The operation of the propulsion system controller for the Volkswagen test van was studied to ascertain battery discharge loads for speeds under 27 km/hr (15 mph). During vehicle operation at low speeds, the armature

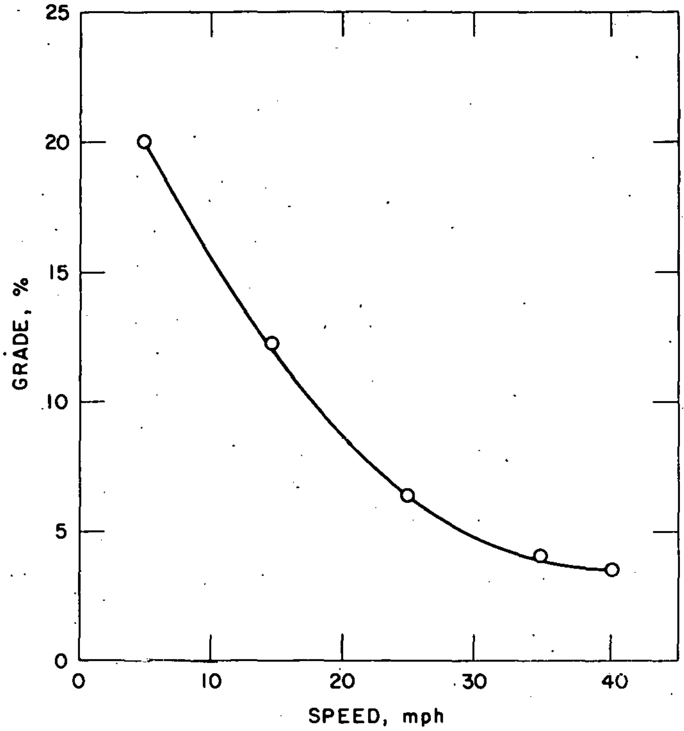

Fig. VII-9. Maximum Speed Achievable as a Function of Road Grade for VW Van

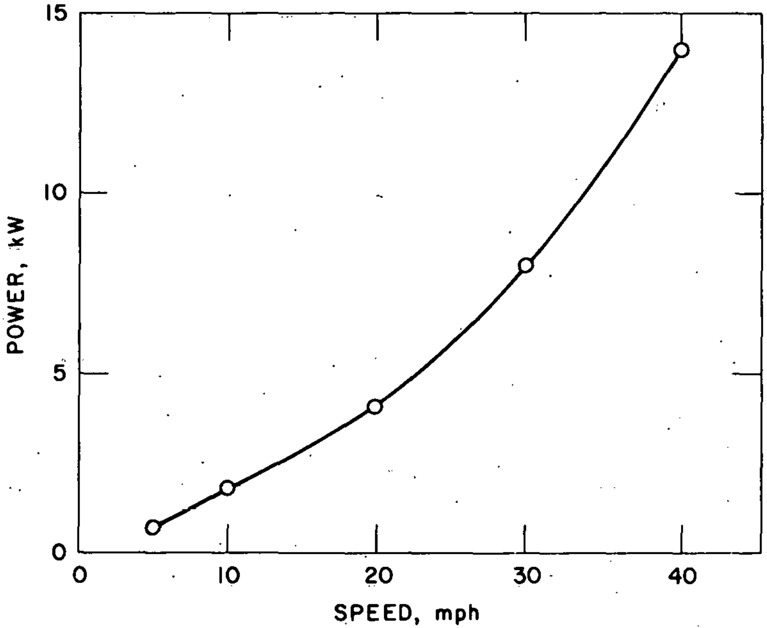

Fig. VII-10. Power Required to Maintain a Constant Speed for VW Van current chopper regulates motor current level. To achieve regulation, a single control unit thyristor is used to intermittently connect the battery to the drive motor. The current is regulated to within ±20% of the demand level established by the positioning of the accelerator pedal. The thyristor is energized to conduct current for the time necessary to bring the motor current to the demand level plus 20% and is then de-energized until the motor current decays to the demand level minus 20%. A minimum thyristor "on" or "off" time of 1 msec is used to allow the commutation circuits to reset. Test measurements with lead-acid batteries in the vehicle showed that, when the thyristor turns on, a step change in the battery output current from 0 to 250 A occurs in less than 0.1 msec during van acceleration at low speeds. After this initial step increase in battery current, the current increased linearly to a peak level of about 400 A in 1.0 msec before thyristor conduction was halted and the current returned to zero. The thyristor is also used to provide regenerative braking at low speeds, which results in pulsed battery charging currents. A transient current spike of ∿50 μsec in width and 300 A peak level was measured at the start of the charge current pulse; the level dropped to 100 A after the initial transient spike.

To determine battery/controller interaction of the Li/MS system, the 6-V Mark IA module was placed in series with the original lead-acid propulsion battery of the VW Transporter and tested. In general, there were no measurable changes in response time of the chopper current waveforms mentioned above. With the current regulation scheme outlined above and at low vehicle speeds, current was regulated even when the battery exhibited an inductive impedance at high frequencies. In the Li/MS cells of the battery, voltages of 0.6 V were measured at high current levels (300 A), and pulsed voltage lows of 0.4 V were observed during rapid acceleration with chopped current operation. The high internal ohmic resistance reported for the 6-V module* accounts for the low cell voltage levels obtained. During regenerative braking, peak transient cell voltage levels of 2.2 V were measured.

D. Design and Development of Battery Sub-Systems

The systems developed to provide thermal management and charging of the Li/MS battery are described below.

1. Thermal Management

(M. Farahat)

Thermal management of the Li/MS battery requires a case that employs high-efficiency thermal insulation to maintain the cells at the operating temperature (450°C) without an excessive energy penalty. Other requirements of thermal management include heating, cooling, and temperature monitoring systems which must be lightweight, energy efficient, and potentially inexpensive to manufacture. The application of two types of thermal insulation is under study. The first type employs a blanket of many layers of a thin reflective metal foil separated by the use of a refractory powder or paper; this material is not efficient under an applied load and requires a pressure-resistant vacuum housing. A second type, under development by the Linde Division of the Union Carbide Corp., is a load-bearing laminated foil.

---

*The cells that were used in the assembly of the module were an early version fo the Mark IA cell with a high resistance (>2 mΩ).

a. Vaccuum-Foil Heat Loss Measurements

The heat loss measurements for the cases of the 6-V Mark IA battery and the 40 kW-hr Mark IA battery (Module D-001 and D-002) are given in Table VII-7; all three battery cases had vacuum-foil insulation. The total heat loss of each battery module was determined by measuring the electrical energy input to heaters inside the battery case, the battery-case inner wall being held at a constant temperature of about 450°C and the vacuum annulus pressure at less than 2.6 x 10^{-2} Pa (2 x 10^{-4} torr). The heat loss at the front plugs was calculated from the difference between the measured total heat loss and the calculated heat loss through the foil. The latter value was based upon a previous measurement using a heat-flux meter, and calculated to be 2 W per square foot of foil area. The heat loss measurements made on the two Mark IA modules (153 and 177 W) suggest that a heat loss of 75-125 W is achievable for a 25-30 kW-hr electric vehicle battery.

Table VII-7. Heat Loss Measurements for Vacuum-Foil Insulated Battery Cases

	Heat Loss, W		
Identification[a]	Foil	Plug Loss	Total
6-V Module	b	b	160
Module D-001 of Mark IA	140	37	177
Module D-002 of Mark IA	116	37	153

[a] See Section II. A for a more complete description of these batteries.

[b] Data not available.

b. Operating Experience with Vacuum-Foil Insulation

The 6-V Mark IA module had a double-walled corrugated case containing vacuum multifoil* insulation. When the 6-V module was delivered to ANL in February, it had a pressure of 100 microns in the vacuum space. This was reduced to $\sim 10^{-2}$ Pa ($\sim 10^{-4}$ torr) prior to heating the module to 450°C. During stationary cycling of this module, small amounts of hydrogen were found in the vacuum annulus. This hydrogen was thought to diffuse through the inside compartment of the module, resulting in an increase of internal pressure and subsequent increased heat loss. The main source of hydrogen was later identified to be the slow decomposition of the electric insulation material in contact with the cells. The hydrogen evolution was eventually controlled by periodic purging of the battery with argon and pumping of the vacuum annulus.

---

* Trade name of Thermo Electron Corp., Waltham, Massachusetts.

In this module, three 500-W heating elements were attached to the cell tray at the front and on both sides. Five Type-K thermocouples were placed inside the module and monitored manually and with a data acquisition system. A temperature-control/fail safe unit was used in conjunction with a Variac transformer to control the heating rate of the module. The heat loss from the module was measured to be 160 W at an inside case temperature of 465°C and a pressure of $\sim10^{-2}$ Pa ($\sim10^{-4}$ torr) in the vacuum annulus. The temperature distribution under these conditions is shown in Fig. VII-11 for the inside and outside of the 6-V module. As mentioned previously, this 6-V module was connected in series with lead-acid batteries in a van and road tested. The test was initiated with the inside battery case temperature at 475°C. After one hour of testing the temperature had dropped about 5°C. In a full-scale battery under these conditions, the battery temperature would be expected to rise 5-10°C.

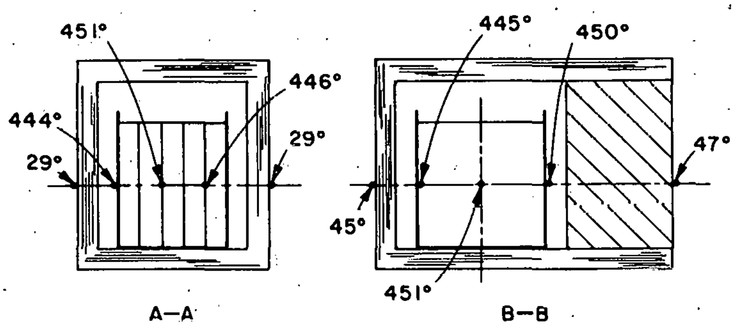

6-VOLT MODULE INSIDE TEMPERATURE DISTRIBUTION

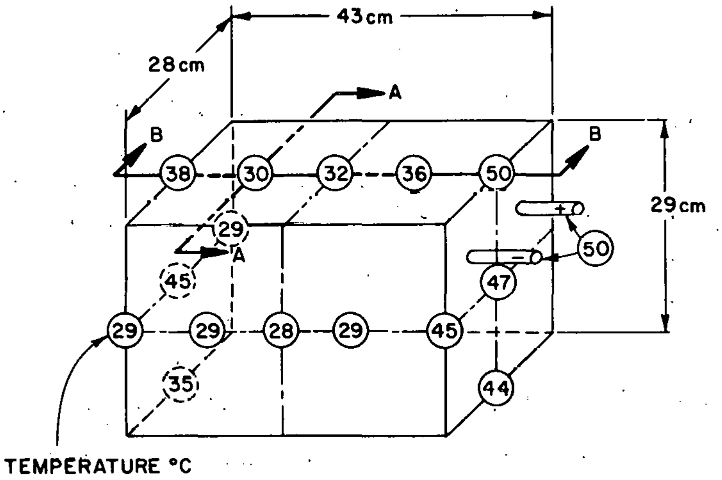

6-VOLT MODULE OUTSIDE TEMPERATURE DISTRIBUTION

Fig. VII-11. Temperatures Measured on Inside (top) and Outside (bottom) of the 6-V Mark IA Module

Thermal measurements were also made on the Mark IA battery. The two module cases were constructed of Inconel 718 with a double wall to provide a vacuum space for the 100 layers of 0.13-mm (0.5-mil) aluminum-foil insulation. The insulation, manufactured by Thermo-Electron Corp., uses a low-density layer of zirconia powder to provide thermal isolation of the aluminum foils. The cavity of the module is sealed with a nine-inch plug of Min-K* insulation through which the bus and instrument wire penetrations are made. Each module was instrumented with thirteen type-K thermocouples placed between cell groups and at various locations inside the cavity where temperature measurements were judged necessary. The module enclosure was heated at the two sides of the cell tray using Calrod-type heaters with a 5-kW capacity. Cooling was provided by blowing air through tubes placed above the cell tray using a 90-W AC blower. The installed blower capacity was 0.37 m^3/min (13 cfm), and the cooling capability was ∿1.1 kW per module. A temperature controller/fail safe unit maintained the battery temperature at 450°C during the thermal measurements. A schematic of the thermal management system for one of the Mark IA modules is shown in Fig. VII-12 (the numbers listed on the module indicate the thirteen thermocouple locations and the sixty cell positions). Table VII-8 shows the thermal performance measured for the Mark IA battery (both modules).

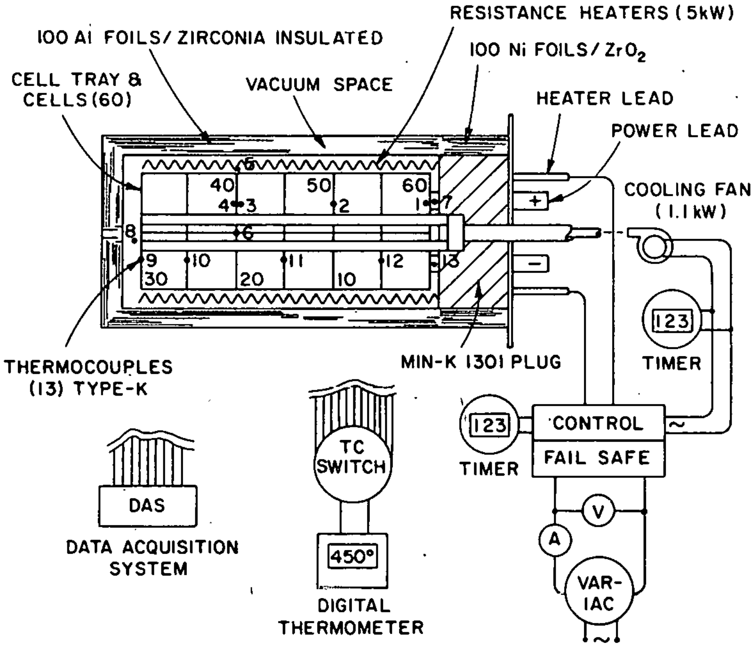

Fig. VII-12. Thermal Management of 20 kW-hr Mark IA Module

Calculations were made to estimate the temperature rise that might result from rapid cell discharge due to cell short circuits. A Mark IA cell initially at 450°C was calculated to reach a maximum temperature of 890°C if it is discharged adiabatically through a dead short circuit. It is assumed for this calculation that all the electrical energy initially present in the fully charged cell is absorbed uniformly by the cell mass. Another calcula-

---

*Registered trade mark of the Johns Manville Co.

Table VII-8. Thermal Performance of Mark IA Battery (both modules)

Heatup (25 to 450°C)	
Power input, kW	2.25
Heat-up time, hr	48
Energy input, kW-hr	108
Ave. heating rate, °C/hr	9
Ave. specific heat, kcal/kg-°C	0.26
Standby Conditions	
Heat loss, W	330
Temperature drop, °C/hr	1.5
Forced Cooling	
Heat removed, kW	2.5
Temperature drop, °C/hr	11.4

tion indicated that the maximum internal temperature for the 20 kW-hr Mark IA module would be 728°C for the simultaneous short circuiting of all 60 cells (assuming adiabatic conditions). The lower value for the battery compared to that of the cell results from the increased mass and heat capacity of the battery. A single cell discharged in 19 minutes within a sixty-cell module would read a maximum temperature of 721°C. The 19-min period was selected because it was the observed discharge period for the failed Mark IA module.

2. Charger

(W. H. DeLuca)

An important sub-system needed for the successful application of LiAl/FeS_x batteries for vehicle propulsion is the charger. The charging system must be efficient and low-cost, and ensure that all the cells in the battery system are charged to their rated capacity. Because present LiAl/FeS cells lack a built-in mechanism to prevent overcharge, there is no inherent cell process to balance cell capacity over a long period of battery operation. Due to small differences in cell self-discharge rates, battery capacity could be reduced to a fraction of its nominal level if the battery is cycled between electrochemically safe cell voltage limits with only bulk charging. This charging system must, therefore, not only replace the bulk charge to the battery, but also electronically equalize the charge of the individual cells without exceeding a predetermined cell voltage limit.

TRW Defense and Space Systems (DSSG) performed a design and cost study for a mass-producible charging system in FY 1978. The study[5] showed that controlled charge-current bypassing about each cell was a cost-effective approach to cell equalization; this system included individual cell-voltage monitoring and current-shunting circuitry suitable for hybrid or monolithic integrated circuit packaging. The cost of a charging system for a full-scale (120-cell) battery was estimated to be $600 (1978 dollars) in large quantities.

Based on the concepts outlined for the TRW system, ANL designed and fabricated a prototype charging system for batteries containing up to six cells[6]. The system has been successfully tested on both LiAl/FeS and lead-acid batteries under a variety of operating conditions. It regulates the battery charge rate to perform bulk and taper charging, and the charge current of individual cells to perform equalization charging. A block diagram of the ANL charger/equalizer system is given in Fig. VII-13. The system consists of three basic parts: the main charger, individual cell monitor/shunt (M/S) electronic circuit modules, and the system control unit.

FUNCTION DIAGRAM OF ANL CHARGER/EQUALIZER SYSTEM

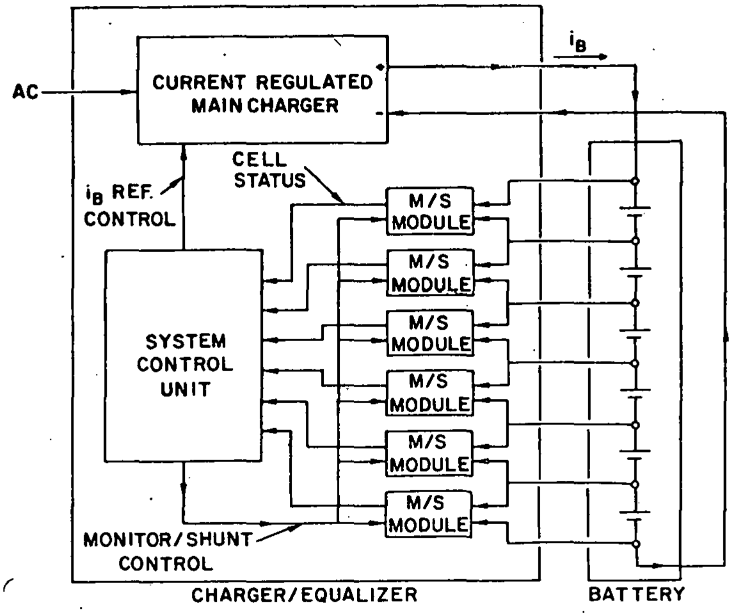

Fig. VII-13. Block Diagram of ANL Six-Cell Charger/Equalizer System

The main charger supplies a regulated constant current to the battery, the amplitude of which is directly proportional to the reference input signal from the system control unit. The M/S modules contain circuitry to detect cell voltage and signal the system control unit if a preset voltage is reached. Each module also contains a current bypass circuit to shunt a preset regulated level of charge current around a cell when the given voltage limit is reached during the equalization period of the charging cycle. A given M/S module acquires its operating power from the battery being charged by using the equalization lead voltages from neighboring cells and operates at a "common mode" voltage level (*i.e.*, the voltage level at which the M/S module is floating with respect to the battery positive and negative terminals) corresponding to the monitored cell's location in the battery system. Optical isolators are used to electrically insulate the M/S modules from the system control unit, which determines overall charge operation. This control unit utilizes the continuous monitoring of cell voltage status to regulate the charge current at a maximum level and to maintain all of the cell voltages at or below a safe level. It regulates the battery charger rate to perform bulk and taper charging, and the charge current of individual cells to perform equalization charging.

In early March of 1979, testing of the charger/equalizer with the 6-V Mark IA battery was started. Figure VII-14 is a photograph showing the battery and cycling apparatus. On the top of the battery is an auxiliary pump which ensures a vacuum in the thermally insulated case. The leads for the power, heater, equalization, cell voltage sensing, and thermocouples are located on the battery front. The cycling apparatus is housed within a relay rack and consists of (from top to bottom in Fig. VII-14) a computer interface module, charger/equalizer, chart recorder, main charger, discharge controller, and discharge power supply. The interface module allows the computer to initiate and terminate both charge and discharge cycles.

Figure VII-15 is a computer-generated plot of the data recorded during a discharge/charge cycle of the Mark IA 6-V module after all five cells had achieved equalization. These data were obtained using the data-acquisition system from the in-vehicle instrumentation described previously. The figure shows battery voltage, battery current, and individual cell voltages. As shown in the figure, a constant discharge current of 70 A was applied until a cell (#5) reached 1.00 V, at which point discharge was terminated. After an open-circuit period of one minute, the charge cycle was initiated: a bulk charge current of 60 A until the leading cell (#4) reached the voltage limit of 1.60 V. Once the voltage limit was reached by a cell, a taper charge was initiated. Three different cells in this battery required reductions in charge current to maintain their voltages below the preset limit during a single taper charge period. Equalization was started when the battery charge current had been reduced to 3.5 A. To achieve equalization, the charge current was shunted around those cells that had reached the voltage limit, those cells below the limit still receiving the full 3.5-A charge current. Cells 1, 4, and 5 reached the limit after only minutes of equalization, while Cells 2 and 3 required about 1.3 and 2.4 hr, respectively. When the last cell (#3) reached the limit level, the charge cycle was automatically terminated by the charger/equalizer. After an open-circuit period of one minute, the discharge cycle was again initiated.

As shown in Fig. III-9, the charger/equalizer apparatus was used on the 6-V Mark IA module between cycles 33 and 70. This testing confirmed that the ANL charger/equalizer is capable of automatically equalizing a string of series-connnected cells without exceeding a predetermined (safe) cell voltage limit. The use of neighboring cells as a voltage supply source for the M/S module provided stable and accurate operation. A shunt current-interrupt technique was used to share battery tap wires for both cell voltage monitoring and current shunting; the testing showed that this technique is an accurate and effective way to minimize the total number of battery wires required for electronic cell equalization.

A charger/equalizer system capable of charging 40 LiAl/FeS cells connected in series (48 V, 26 kW-hr) is being developed for testing. Overall system operation will be similar to that outlined above; but, to accommodate the increased number of cells, the system control unit will be a microprocessor. This will reduce the number of components used and provide additional monitor and interlock functions. The main charger will be capable of providing a battery bulk charge current of 100 A, and equalization will be performed at a

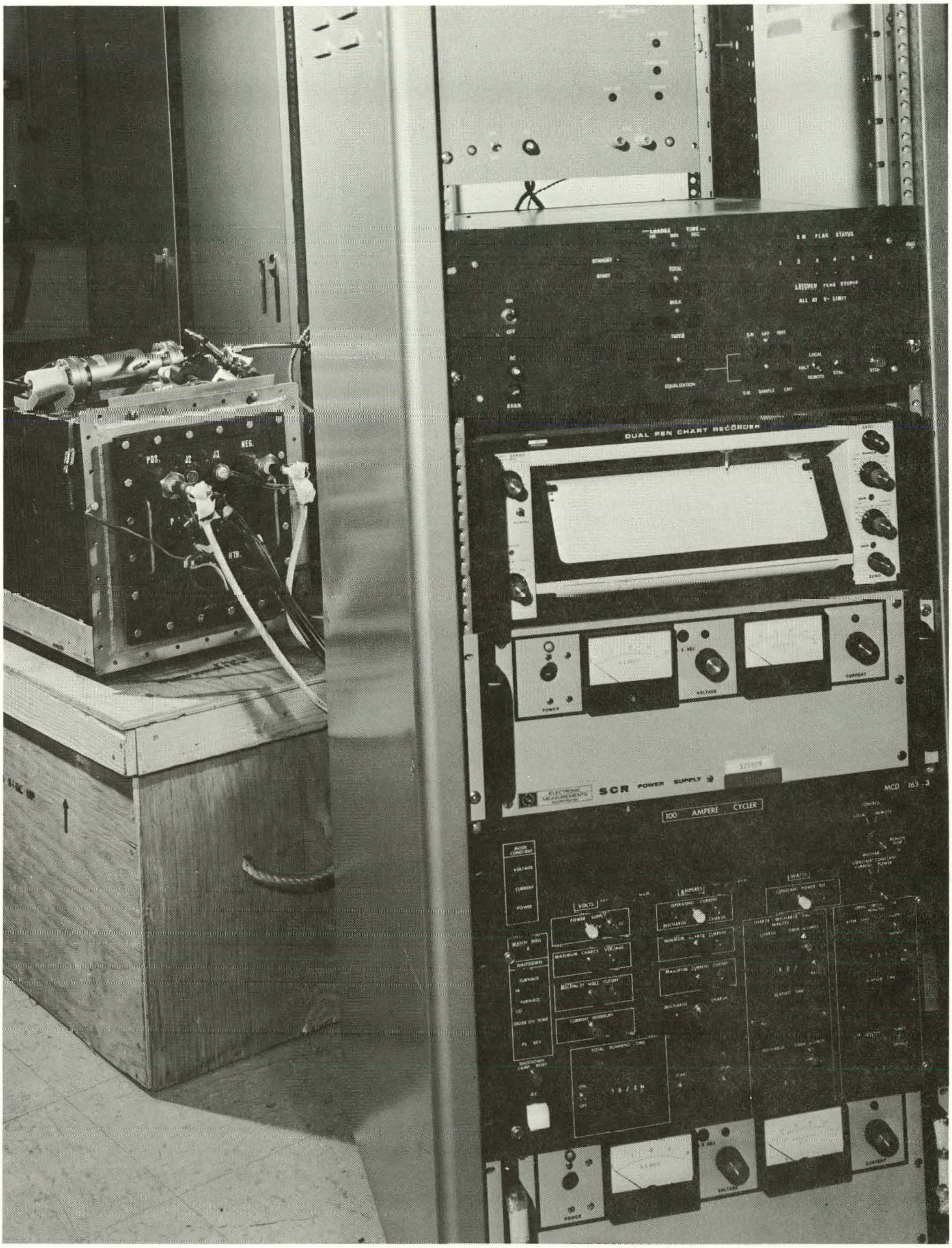

Fig. VII-14. Charger/Equalizer Apparatus Being Used on 6-V Mark IA Module. ANL Neg. No. 308-79-148.

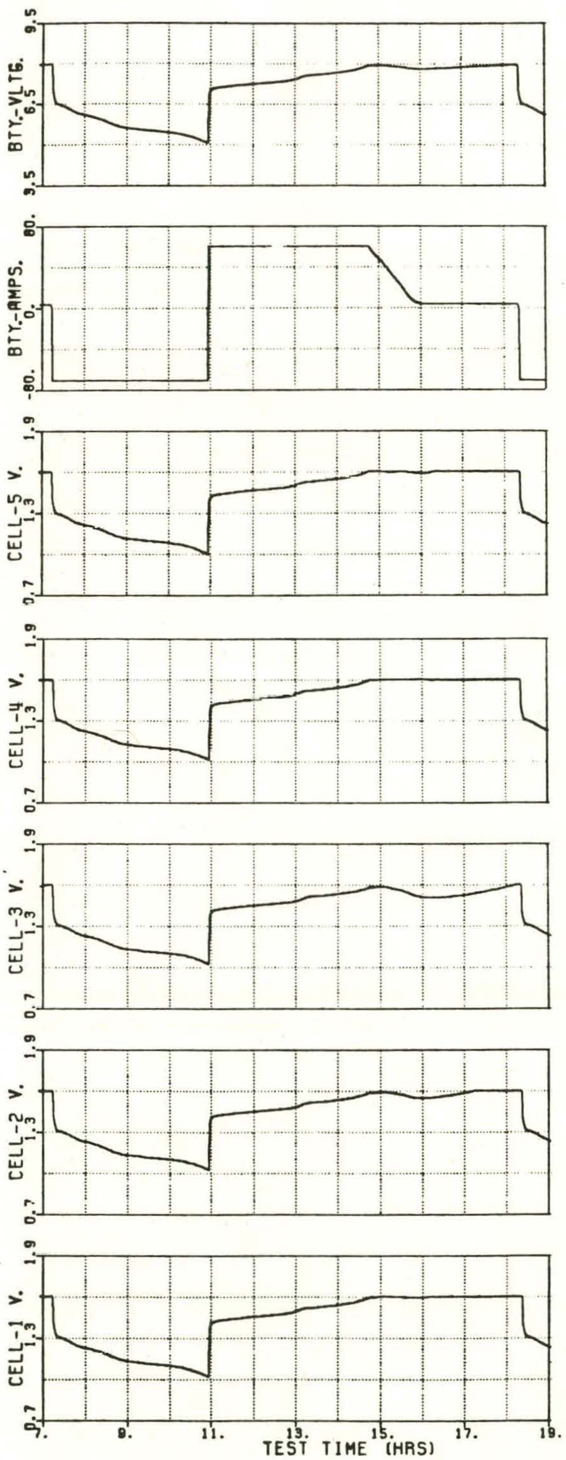

Plot of 6-Volt, 5-Cell LiAl/FeS Battery Parameters During Discharge/Charge Cycle

Parameters

- Battery Voltage (Volts)
- Battery Current (Amperes)
- Five Cell Voltages (Volts)

Discharge Cycle

- 70 A Constant Current
- 262 A·HR/1.49 kW·HR From Battery
- Terminator: Cell-5 At 1.00 V Limit Level

Charge Cycle

- Bulk Charging at 60 A (228 A·HR)
- Taper Charge to 3.7 A (35.8 A·HR)
- Equalization Charging At 3.7 A (8.6 A·HR)
- 272 A·HR/2.04 kW·HR To Battery
- Terminator: All Cells At 1.60 V Limit Level

Fig. VII-15. Data Generated during Cycling of 6-V Mark IA Module current of 8.0 A. The current-regulation requirements of the main charger will be reduced for economic reasons, and voltage monitoring of cells will be synchronized with the AC-line voltage frequency to insure peak cell voltage sensing. In this manner, the increase in charge-current ripple (120 Hz) caused by reduced regulation and filtering will not affect the accuracy of cell-voltage limiting.

With the modifications and additions mentioned above, the cost for the charging system in mass-produced quantities is expected to be similar to that quoted previously for the TRW study.

REFERENCES

1. A. A. Chilenskas *et al.*, *Conceptual Designs for a Utility Load-Leveling Battery Utilizing Li/FeS Cells*, Argonne National Laboratory Report No. ANL-80-20, in preparation.
2. J. M. King *et al.*, *Conceptual Design of Electrical Balance of Plant for Advanced Battery Energy Storage Facility*, FCR-1367, United Technologies Power Systems Division (March 1979).
3. W. L. Towle, J. E. A. Graae, A. A. Chilenskas, and R. O. Ivins, *Cost Estimate for the Commerical Manufacture of Lithium/Iron Sulfide Cells for Load Leveling*, Argonne National Laboratory Report No. ANL-76-12 (March 1976).
4. A. A. Chilenskas *et al.*, *A Preliminary Estimate of the Manufacturing Cost for Lithium/Metal Sulfide Cells for Stationary and Mobile Applications*, Argonne National Laboratory Report No. ANL-79-59, in preparation.
5. G. H. Gelb *et al.*, *Design and Cost Study for LiAl/FeS$_x$ Vehicle Battery Charging System, Final Report*, TRW Report No. 31268-0001-RV-00 (May 1978).
6. W. H. DeLuca *et al.*, *A Charging System for the LiAl/FeS Electric Vehicle Battery*, Proceedings of the 14th Intersociety Engineering Conversion and Engineering Conference, Boston, MA (August 1979).

VIII. CALCIUM/METAL SULFIDE BATTERY DEVELOPMENT

The objective of this program is to develop high-performance cells that use inexpensive, abundant materials while maintaining the performance levels required for electric vehicles or load leveling. These cells are expected to follow the lithium/iron sulfide cells into commercial production. The present goals for the cells are a specific energy of 160 W-hr/kg (same as Mark III goals listed in Table I-1) and a materials cost in mass production of $15/kW-hr (1979 dollars).

A. Electrolyte Development

(C. C. Sy, L. E. Ross, M. F. Roche)

In previous studies (ANL-78-94, p. 187-188), 29 mol % LiCl-20 mol % NaCl-35 mol % $CaCl_2$-16 mol % $BaCl_2$ (mp, 390°C) was operated successfully as the electrolyte in calcium cells with FeS_2 and NiS_2 positive electrodes.[1] This electrolyte is one of three known eutectics in this quaternary system. Table VIII-1 presents the compositions and melting points of these eutectics. The melting points of twenty mixtures of LiF (0-4 mol %), LiCl (3-33 mol %), NaCl (12-38 mol %), $CaCl_2$ (35-47 mol %), and $BaCl_2$ (7-20 mol %) were measured to find electrolytes with a lower lithium content and/or melting point than the eutectics, but none of these electrolytes had a melting point below that of E_2 or E_3. Consequently, the electrolyte development effort for the calcium cell has been concentrated on E_2 and E_3.

1. Solubility Studies

The CaS solubility in E_3 was determined by chemical analysis. For this analysis, the electrolyte was saturated with CaS at various temperatures in a helium-atmosphere furnace, and the sulfide concentrations were measured by gas-chromatographic assay of the H_2S evolved on dissolving the samples in 6M HCl.* Standard curves for this analysis were established by assays of known volumes of H_2S; air oxidation of the samples and standards was avoided by employing a helium carrier gas.

Table VIII-1. Eutectics in Quaternary System

	Eutectic Composition, mol %		
	E_1	E_2	E_3
LiCl	47	33	29
NaCl	3	12	20
$CaCl_2$	30	37	35
$BaCl_2$	20	18	16
Melting pt.,[a] °C	(395)	383(385)	390(378)

[a] The numbers in parenthesis are the melting points for these eutectics reported in Ref. 1.

---

*Assays conducted by M. Bouchard, A. Essling, and M. Homa, Analytical Chemistry Laboratory, ANL.

Two methods of sampling the CaS-saturated molten electrolyte were tried. In the first method, quartz sampler tubes with 40-micron quartz frits were used to draw samples from a CaS suspension in the molten electrolyte. This method led to poor results: the calcium sulfide concentrations at 430°C varied from ∿150 to ∿6000 ppm. The poor results were thought to be due to CaS particulate contamination of the samples. In the second method, a small amount (5 g) of CaS was placed in a sintered stainless-steel packet (25 cm^2) with 15-20 μm-dia holes, which was then immersed in an Al_2O_3 crucible (250 cm^3) containing 295 g molten electrolyte. The packet was flooded with electrolyte by alternate helium evacuations and repressurizations. Samples were obtained at various temperatures by immersing a small (5 cm^3) Al_2O_3 crucible in the electrolyte surrounding the packet and equilibrating for 4-5 days before withdrawing the filled crucible. A calibrated chromel-alumel thermocouple was used to monitor the temperature of the electrolyte.

The solubility of CaS in the quaternary electrolyte as a function of temperature is shown in Fig. VIII-1; these data were determined by the second method described above. Also included in this figure for comparison purposes is the solubility of Li_2S in LiCl-KCl.[2] M.-L. Saboungi-Blander[†] computed the solubility product of CaS at 723 K in LiCl-KCl electrolyte from thermodynamic data; the solubility product divided by the ion fraction of Ca^{++} in E_3 (0.35) is also plotted in this figure for comparison with the linear regression curve of the CaS data.

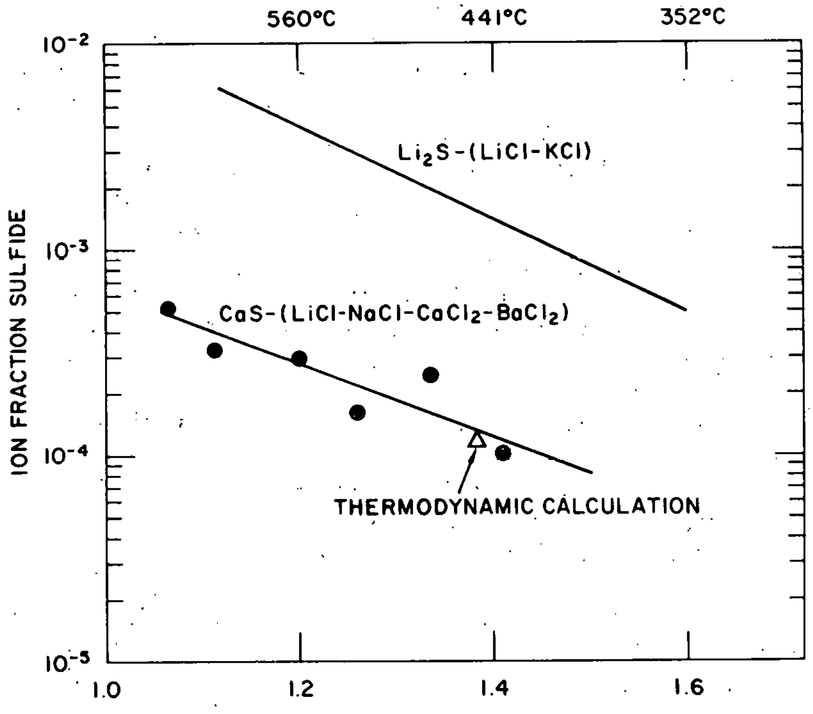

Fig. VIII-1. Solubility of Li_2S in LiCl-KCl and CaS in LiCl-NaCl-$CaCl_2$-$BaCl_2$

[†] Chemical Engineering Division, ANL.

It is apparent that the solubility product of CaS is similar in the two electrolytes and is lower than that of Li_2S in LiCl-KCl. The heat of solution was calculated from the slope of the solubility curves and found to be 7.97 kcal/mol for CaS in E_3 (M. L. Saboungi *et al.*[2] found this value to be 10.22 kcal/mol for Li_2S in LiCl-KCl.)

The above data are expected to be of use for thermodynamic and kinetic comparisons of calcium and lithium cells. For example, emf differences between the positive electrodes in calcium and lithium cells can be derived from the ratio of the CaS-to-Li_2S solubility. This ratio indicates that, at 441°C, an Fe-FeS-CaS electrode would be 78.5 mV more cathodic than an Fe-FeS-Li_2S electrode.

2. Vaporization of Sulfur

In an earlier study (ANL-77-75, p. 50), it was shown that suspensions of Li_2S and either FeS_2 or NiS_2 in LiCl-KCl electrolyte at 525°C lost sulfur through vaporization at a much higher rate than that of similar mixtures not containing Li_2S. In addition, post-test examinations of Li-Al/FeS_2 and Li-Al/NiS_2 cells (ANL-77-35, p. 48) have shown that Li_2S deposits form in the BN fabric separator. These two phenomena may occur through similar mechanisms, namely, the formation and transport of polysulfide ions (*e.g.*, $S_n^=$) in the electrolyte. Such ions could be reduced by Li-Al to form a Li_2S deposit in sealed cells or could be decomposed by heat to form $S^=$ ions and gaseous sulfur in unsealed mixtures. In calcium cells, the low solubility of CaS (see above) is suspected to result in less polysulfide formation and, consequently, good sulfur retention by the positive electrodes. In the present study, weight-loss experiments were conducted to measure the sulfur loss by vaporization for Li_2S and FeS_2 in LiCl-KCl, FeS_2 alone in E_3, and FeS_2 and CaS in E_3. The sample mixtures consisted of ∿0.5 g sulfides (equal volumes when two sulfides used) and ∿1.5 g electrolyte in graphite crucibles (1.27-cm ID). They were heated simultaneously at about 520°C in a helium-atmosphere furnace, and were occasionally removed, cooled, and weighed. Sulfur-to-iron ratios* for the three samples as a function of heating time are given in Fig. VIII-2. The data show that CaS has little effect on the loss of sulfur from FeS_2 and confirm the previous finding that Li_2S causes rapid sulfur loss from FeS_2.

A similar test was conducted with two samples, NiS_2 and NiS_2 plus CaS (equal volume of each sulfide), in the quaternary salt. Again, CaS had little effect on vaporization. Both samples exhibited losses of about 0.15 mole of sulfur per mole of nickel within 20 hr, and about 0.25 mole of sulfur per mole of nickel after 120 hr.

The above results indicate that FeS_2 and NiS_2 electrodes will probably retain sulfur reasonably well in calcium cells. This prediction has now been confirmed by examination of FeS_2 electrodes from previously operated calcium cells (discussed later).

---

*It was assumed that weight losses occurred exclusively through sulfur vaporization from the FeS_2.

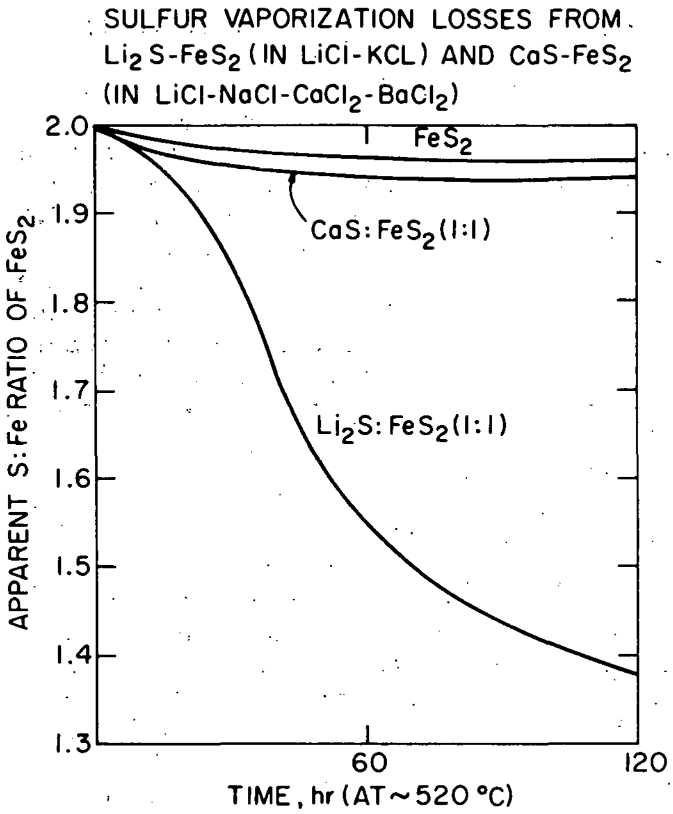

Fig. VIII-2. Sulfur Vaporization Losses From Li_2S-FeS_2 (in LiCl-KCl) and CaS-FeS_2 (in LiCl-NaCl-$CaCl_2$-$BaCl_2$)

3. Density

The densities of E_2 and E_3 were calculated from the liquid densities[3] of their components. For comparison, the density of LiCl-KCl was also calculated; densities for this eutectic have been experimentally determined by Van Artsdalen and Jaffe[4] (1.660 and 1.607 g/cm^3 at 427 and 527°C, respectively). The results of the calculations are given in Table VIII-2. The densities of the quaternary salts are 40% greater than the density of LiCl-KCl (a significant weight penalty).

Table VIII-2. Calculated Densities of Electrolytes

Electrolyte	Density, g/cm^3 427°C	527°C
E_2	2.380	2.327
E_3	2.331	2.278
LiCl-KCl	1.660	1.609

4. Conductivity

(H. Ohno,* Y. Iwadate,[†] and H. Shimotake)

The ionic conductivity of E_2 was measured over the temperature range 445-514°C. The conductance cell was a BN capillary (0.3-cm dia. and 1.5-cm long) described in Section V.C. The cell constant was experimentally measured using a molten LiCl-KCl eutectic mixture, and was about 13 cm^{-1}. The conductances were measured in the frequency range of 0.6 to 15 kHz. A polarization-free resistance can be obtained by a linear extrapolation of the resistance to infinite frequency on a resistance versus inverse frequency graph. The specific conductance (Ω^{-1}-cm^{-1}) for E_2 was calculated to be $-2.085 + 7.10 \times 10^{-3}T - 0.488 \times 10^{-6}T^2$, where T is the temperature in degrees centigrade. This conductivity is about two thirds that for LiCl-KCl eutectic.[4] Thus, calcium cells may require somewhat thinner electrodes than lithium cells for equivalent power.

5. Quaternary Salt Phases

(C. C. Sy, B. S. Tani‡)

An X-ray diffraction examination of various mixtures of LiCl, NaCl, $CaCl_2$ and $BaCl_2$ was conducted to aid in identifying the electrode phases present during cycling of calcium/metal sulfide cells. Mixtures of LiCl and NaCl (1:1 and 1:2 mole ratios, respectively) and $CaCl_2$ and $BaCl_2$ (1:1 mole ratio) were heated at 600°C for 10 hr. The X-ray diffraction analyses of these mixtures are given in Table VIII-3.

Table VIII-3. Phases in LiCl-NaCl and $CaCl_2$-$BaCl_2$ Samples

Sample	Major Phase	Minor Phase
LiCl:NaCl(1:1)	'LiCl'	'fcc'
LiCl:NaCl(1:2)	'NaCl'	'LiCl'
$CaCl_2$:$BaCl_2$(1:1)	$CaBaCl_4$	—

The compounds 'LiCl', 'NaCl' and 'fcc' in the table have lattice parameters lying between those of pure LiCl and NaCl. If the lattice parameter varies linearly with composition, then 'LiCl' contains 2 at. % NaCl, 'NaCl' contains 10 at. % LiCl, and 'fcc' is the known[5] compound $LiNa_2Cl_3$ and contains 68 at. %

---

[*] Research Associate from Japan Atomic Energy Research Institute, Japan.

[†] Exchange Student from Tokyo Institute of Technology, Japan.

[‡] Analytical Chemistry Laboratory, ANL.

NaCl. Since no $CaCl_2$ or $BaCl_2$ was detected in the $CaCl_2$: $BaCl_2$ sample, the X-ray pattern obtained was assumed to be that of the known[5] compound $CaBaCl_4$, for which X-ray data are not available.

The three eutectics of LiCl-NaCl-$CaCl_2$-$BaCl_2$--E_1, E_2, and E_3--were melted, slowly cooled, and examined by X-ray diffraction analyses. The results of these examinations are given in Table VIII-4.

Table VIII-4. Analyses of Quaternary Eutectics

Eutectic	Major Phases	Minor Phases
E_1	$CaBaCl_4$,'LiCl'[a]	$CaCl_2$
E_2	$CaBaCl_4$	$CaCl_2$
	'LiCl'[b]	'NaCl'[b]
E_3	$BaCl_2$,$CaBaCl_4$,'LiCl'[a]	$CaCl_2$

[a] These 'LiCl' phases contained 6-8 at.% NaCl.

[b] These are as described in previous table.

The eutectics E_2 and E_3 are true quaternaries since they have four crystallizing phases. Another phase, perhaps undetected in this sample, is required to complete the description of E_1.

The phases in FeS_2 electrodes of calcium cells having an electrolyte of E_2 or E_3 were identified with the aid of the above information. The phases were mixtures of CaS, iron-sulfur binary compounds, and salt phases.

B. Positive Electrode Development

1. Cell Studies

(L. E. Ross, S. K. Preto, C. C. Sy)

In the last report (ANL-78-94, p. 190), development work on negative-electrode materials was discussed. From those studies, the Ca-Si negative electrode ($CaSi_2$ uncharged; Ca_2Si charged) was selected for engineering-scale development. Recent studies have concentrated on development of three types of positive electrode--NiS_2, FeS_2 and FeS_2-CoS_2.* In later studies, FeS electrodes will be tested.

The test cells employed metal-disulfide electrodes (NiS_2, FeS_2, and $Fe_{0.93}Co_{0.07}S_2$) with theoretical capacities of about 4 A-hr. For each cell, the metal disulfide was packed in carbon foam and then placed within molybdenum sheet-and-screen housings (area, 3.25 cm^2; 0.8-cm thick). The

---

*In lithium cells, CoS_2 is normally added to the FeS_2 electrode to improve performance.

theoretical capacity densities were 1.00 A-hr/cm^2 for the NiS_2 electrode and 1.20 A-hr/cm^2 for the FeS_2 and FeS_2-CoS_2 electrodes. The negative electrode was a 7-10 A-hr $CaAl_2$ electrode in an iron housing (area, 16 cm^2). A reference electrode consisting of $CaAl_4$ and aluminum was used to control voltage limits. Zirconia cloth was used as a particle retainer and BN fabric as a separator, and the electrolyte was E_3 (purified by Anderson Physics Laboratories). The cells were operated at 460°C in alumina crucibles, the positive electrodes being cycled between voltages (IR included) of 2.1 V on charge and 1.0 V on discharge *versus* the reference electrode.

The achieved capacity densities for the NiS_2, FeS_2, and $Fe_{0.93}Co_{0.07}S_2$ electrodes are shown in Fig. VIII-3.

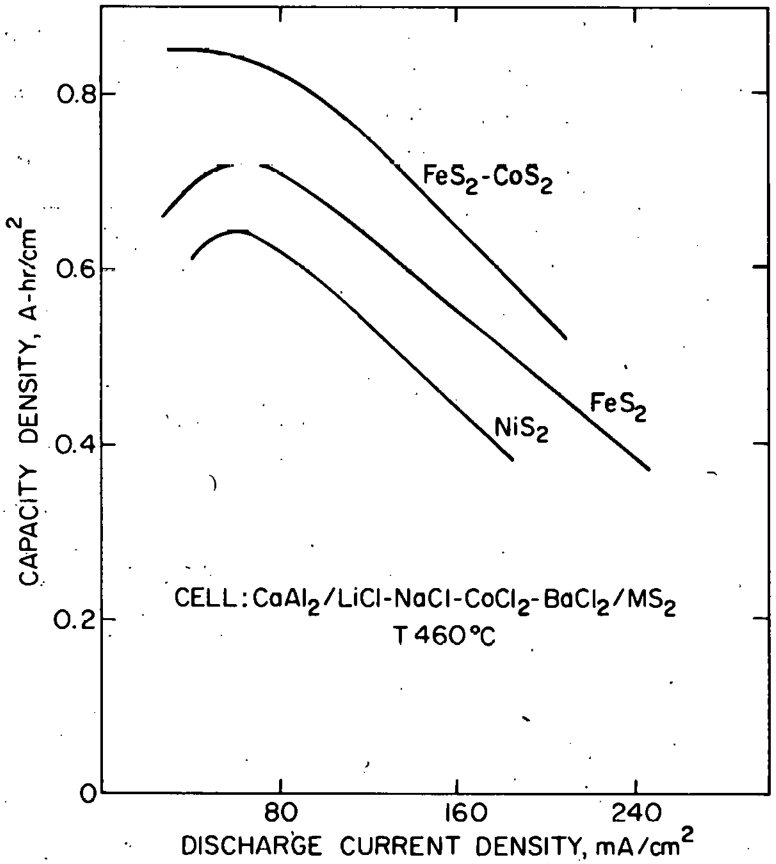

Fig. VIII-3. Capacity Density of Metal Disulfide Electrodes in LiCl-NaCl-$CaCl_2$-$BaCl_2$

The maximum electrode utilizations (theoretical capacity density divided by achieved capacity density) were very satisfactory--64% for NiS_2 and FeS_2 and 72% for $Fe_{0.93}Co_{0.07}S_2$. The beneficial effects of cobalt are evident from the high achieved capacity density of the Fe(Co)S_2 electrode. The achieved capacity of the Fe(Co)S_2 electrode in the above calcium cell is similar to that obtained in earlier LiAl/Fe(Co)S_2 cells (ANL-75-1, pp. 29-32). All three cells were operated for about 60 cycles with no decline in their coulombic efficiency, which was typically about 98%. However, the NiS_2 electrode exhibited a capacity decline with cycling; post-test examination revealed that the electrode retainers had loosened because of swelling. It is therefore believed that active material was lost in the NiS_2 electrode. Aside from this problem, no major difficulties were encountered with the cell operations.

2. Cyclic Voltammetry of Metal Disulfides

(S. K. Preto)

Previous studies of slow-scan (0.02 mV/sec) voltammograms (ANL-78-94, pp. 168-173, 188-190) were conducted to determine the electrochemical behavior of FeS_2, CoS_2, and NiS_2 electrodes in lithium-cell and calcium-cell electrolytes. In the present study, voltammograms at scan rates of 0.02 to 0.5 mV/sec were generated from these three metal disulfide electrodes in LiCl-KCl and E_3 electrolyte. In both electrolytes, the working electrodes were ∿100 mg of powdered metal disulfide (FeS_2, NiS_2, CoS_2) in carbon foam within a molybdenum housing (1 cm^2). The counter and reference electrodes were two-phase mixtures of LiAl and aluminum for the LiCl-KCl electrolyte, and $CaAl_4$ and aluminum for the LiCl-NaCl-$CaCl_2$-$BaCl_2$ electrolyte. The working electrodes were repeatedly cycled over a potential range of 1.0 V to 2.0 or 2.1 V *versus* the reference electrodes.

The data obtained from voltammograms were used to determine the peak current (i_p) and peak potential (E_p) for each of the major reactions of the individual electrodes; these reactions and their emf's are listed in Table VIII-5.* The results indicated that i_p and E_p vary linearly with the

Table VIII-5. Emf of Metal-Disulfide Electrode Reactions

	Emf, Volts	
	vs LiAl at 400°C	*vs* $CaAl_4$ at 460°C
$FeS_2 \rightarrow Fe_{1-x}S$	1.74[a]	1.78
$FeS \rightarrow Fe$	1.34[b]	1.39
$CoS_2 \rightarrow Co_3S_4$	1.74	1.79
$Co_3S_4 \rightarrow Co_9S_8$	1.63	1.68
$Co_9S_8 \rightarrow Co$	1.35	1.40
$NiS_2 \rightarrow Ni_{1-x}S$	1.75	1.81
$NiS \rightarrow Ni_7S_6$	1.60	1.65
$Ni_7S_6 \rightarrow Ni_3S_2$	1.56	1.59
$Ni_3S_2 \rightarrow Ni$	1.37	1.42

[a] In-cell reaction: $FeS_2 \rightarrow Li_3Fe_2S_4$.

[b] In-cell reaction: $Li_2FeS_2 \rightarrow Fe$.

---

[*] Previously reported in ANL-78-94, p.173 and 189.

square root of the scan rate; thus, ohmic effects are dominant in these electrode reactions. Figure VIII-4* shows the peak current as a function of peak potential for the major reactions of the three metal disulfide electrodes in LiCl-KCl, and Fig. VIII-5* shows the same type of plot for the reactions in the quaternary salt. As can be easily seen in these two figures, the curves are linear and intercept the voltage axis at voltages slightly above the reaction emf on charge and slightly below the reaction emf on discharge. The two closed symbols shown on the voltage axis for each reaction represent the scan-rate-independent potential at which the discharge peak and charge peak start; these symbols are located slightly below the discharge and slightly above the charge reaction emf.

From Figs. VIII-4 and -5, the following observations were made:

(1) The resistances, which are the reciprocals of the slopes, are generally much lower in the lithium than in the calcium system. This difference cannot be accounted for by differences in salt conductivity since LiCl-KCl at 400°C has about the same conductivity as the quaternary salt at 460°C. The high resistances in the quaternary salt (Fig. VIII-5) are believed to be caused by poorly conducting positive electrode phases (CaS in particular). Improved carbon additives, such as coke flour instead of carbon foam, may alleviate this problem.

(2) For a given electrode reaction, the charge resistance and discharge resistance often differ greatly. Ideally, these resistances should be equal and about the same for all reactions in a given electrode. The NiS_2 electrode in LiCl-KCl most closely approximates this condition. For the other electrodes, various resistance problems are evident. We are unable to account for all these resistive effects with a simple model. In later studies, the influence of positive-electrode additives (to improve electronic conduction) and electrolyte composition on the curve slopes should be assessed.

(3) The discontinuity between the point at which the charge and discharge curves for a given reaction intercept the voltage axis has been attributed to "crystallization overpotentials" of the type discussed by Vetter[6]. For example, in studies of metal electrodeposition, crystallization overpotentials have been found to range from ∿10 to ∿300 mV. In Figs. VIII-4 and -5, both the closed symbols and the voltage intercepts for a given reaction are separated by about 20 to 110 mV. This separation would be zero in the absence of crystallization problems. On the basis of their low crystallization overpotentials, the NiS_2 electrode in LiCl-KCl and the FeS_2 electrode in LiCl-NaCl-$CaCl_2$-$BaCl_2$ appear to be better than the other electrodes tested.

(4) Not evident from the figures, but very obvious during the studies, was the rapid loss with cycling in the capacity of the high-voltage reactions of the metal disulfide electrodes in LiCl-KCl electrolyte; this

---

*In these figures, data for charge are above the voltage axis, and data for discharge are below the axis. The open symbols represent the i_p and E_p for a given scan rate; the closer the symbol is to the voltage axis, the lower the scan rate.

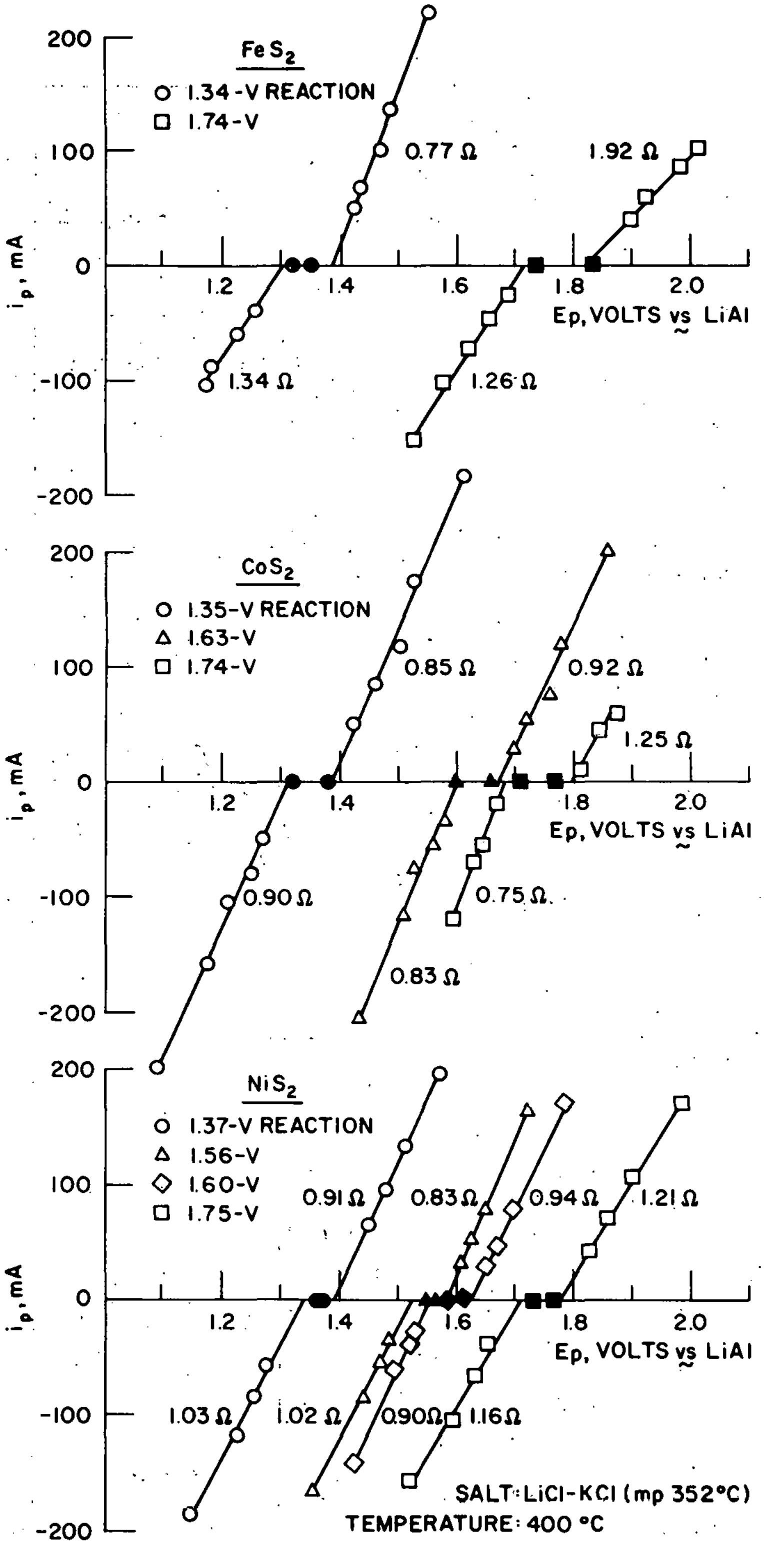

Fig. VIII-4. Peak Current *vs* Peak Potentials of Metal Disulfides in LiCl-KCl

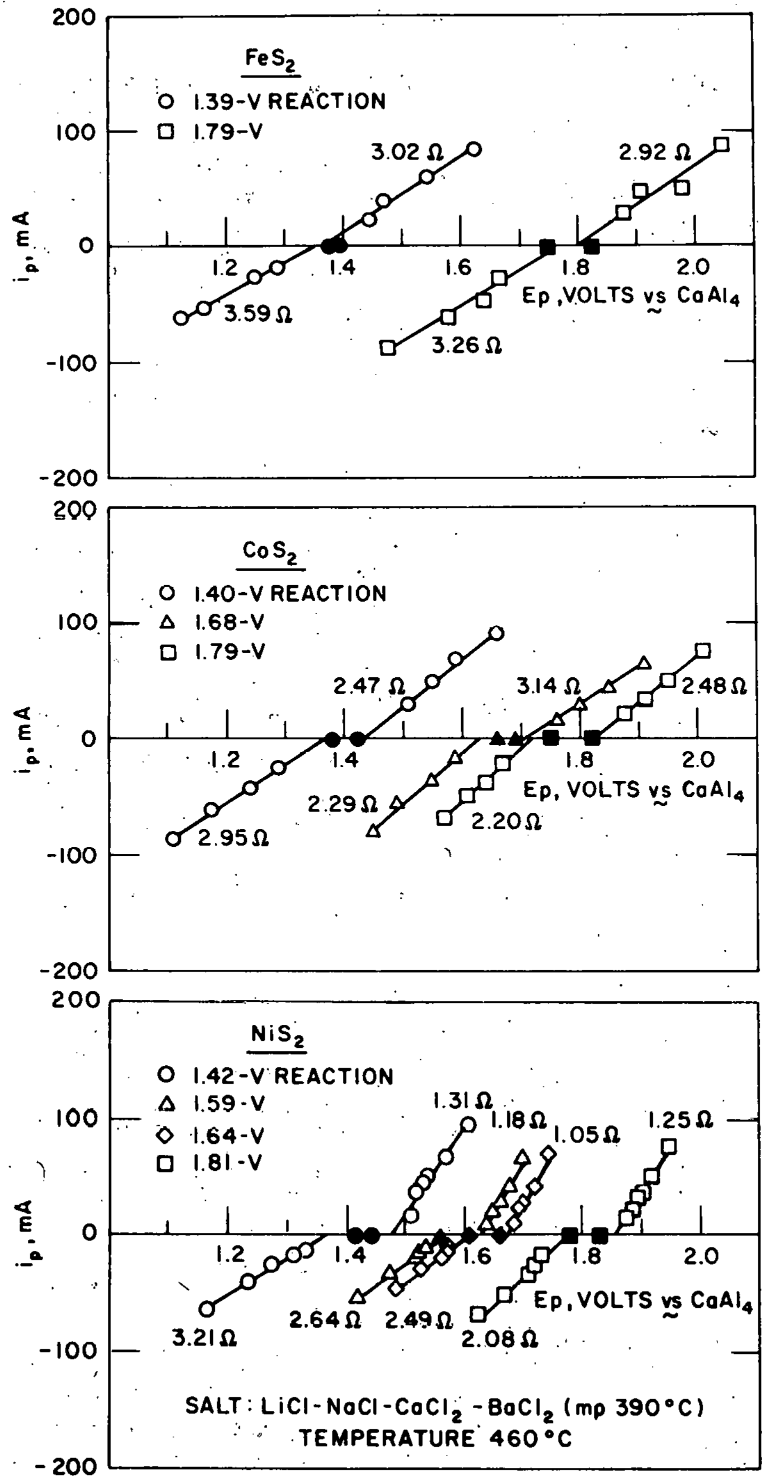

Fig. VIII-5. Peak Current *vs* Peak Potential of Metal Disulfides in $LiCl-NaCl-CaCl_2-BaCl_2$

effect is thought to be due to escape of sulfur from these electrodes. In comparison with the electrodes in the lithium system, the electrodes in LiCl-NaCl-$CaCl_2$-$BaCl_2$ did not exhibit this capacity loss even though their operating temperatures were higher. The low rate of capacity loss may be due to the low solubility of CaS.

In summary, in terms of their overall electrochemical properties, NiS_2 in LiCl-KCl and FeS_2 in the quaternary salt are the better electrode systems.

C. Large Cell Exploratory Studies

(L. E. Ross, L. G. Bartholme, P. F. Eshman, M. F. Roche)

Various electrodes and electrolytes have been tested in sealed, prismatic bicells of up to 300 A-hr capacity. Such cells provide more realistic data on performance capabilities than can be obtained from small-cell tests and also provide a convenient measure of progress toward the program goals.

The compositions of the last five cells are summarized in Table VIII-6. Cell CA-14 was operated in FY 1978 (see ANL-78-94, p. 186); CA-15 through CA-18 were operated in FY 1979. The cells were sealed, prismatic bicells having a metal-disulfide positive electrode sandwiched between two negative electrodes. The current collectors were honeycomb structures of iron for the negative electrode and molybdenum for the positive electrode. For additional current collection, either carbon fibers (CA-14), carbon foam (CA-16 through CA-18) or 7 mol % CoS_2 (CA-15 through CA-18) was added to the positive electrode. The separator was BN fabric for all cells except that of CA-18 which was BN felt. Typical cutoff voltages were 2.3-2.4 V on charge and 0.9-1.0 V on discharge.

Table VIII-7 presents performance data for the five cells. Figure VIII-6 shows the specific energies achieved by Cells CA-16, -17 and -18 along with a similarly constructed LiAl/FeS_2 cell, EP-I7-3.* These performance data show that significant progress has been made in the development of the calcium cell, but major improvements are still needed.

An early discharge (cycle 6) of Cell CA-16 is shown in Fig. VIII-7. Continued cycling led to elimination of the Ca_2Si/FeS_2 plateau and increased the CaSi plateaus to 90 A-hr (out of about 120 A-hr total). This effect, which occurred with Cells CA-16, -17, and -18, is attributed partly to improved utilization of the Ca-Si electrode with continued cycling and partly

---

*Fabricated by Eagle-Picher Industries.

Table VIII-6. Compositions of Calcium/Metal Sulfide Cells

Cell No.	Dimensions, cm	Weight, kg	Fully Charged Cell Comp.[a]	Electrolyte[b]	Theo. Capacity,[c] A-hr	Max. Utiliz.,[d] %
CA-14	13.5 x 13.5 x 2.5	1.3	$Ca_{1.2}Mg_2Si/NiS_2$	$LiCl-KCl-CaCl_2$	69	58
CA-15	13.5 x 13.5 x 3.6	2.2	$Ca_{1.34}Si/NiS_2$	E_3	214	45
CA-16	13.5 x 13.5 x 3.6	2.13	$Ca_{1.34}Si/FeS_2$	E_3	214	55
CA-17	13.5 x 13.5 x 3.6	2.3	$Ca_{1.28}Si/FeS_2$	E_2	214	66
CA-18	13.5 x 13.5 x 1.8	1.2	$CaSi/FeS_2$	E_2	107	72

[a] The cells were fabricated with one-third charged positive electrodes and either Mg_2Si or $CaSi_2$ negative electrodes.

[b] The CA-14 electrolyte was 7 mol % $CaCl_2$ in LiCl-KCl eutectic (m.p. ~340°C).

[c] Based on two-thirds of total sulfur in the positive electrode (the cells were designed to operate between one-third charged and full charge).

[d] Measured at low current density (13-16 mA/cm^2).

Table VIII-7. Cycling History of Calcium/Metal Sulfide Cells

Cell	Max. Spec. Energy,[a] W-hr/kg	Lifetime		A-hr Efficiency, %		Resistance, mΩ		Approx. Spec. Energy Decline, %/1000 hr	Normal Oper. Temp., °C
		Cycles	hr	Initial	Final	Initial	Final		
CA-14	42	120	1700	99	74	9	12	15[b]	450
CA-15	61	115	1200	90	97	10	25	35	470
CA-16	81	75	2250	88	100	8	16	20	460
CA-17	86	68	2000	93	85[c]	8	16	25	485
CA-18[d]	93	75	1200	96	65[e]	8	16	30[b,e]	480

[a] Measured at low charge-discharge current density (13-16 mA/cm^2).

[b] A large fraction of the decline is due to loss of A-hr efficiency.

[c] At cycle 60, thermal test (cycles 60-68) caused further decline to 73% A-hr efficiency.

[d] Cell is still being operated.

[e] This cell was severely overcharged near cycle 20, causing an abrupt decline in A-hr efficiency and specific energy.

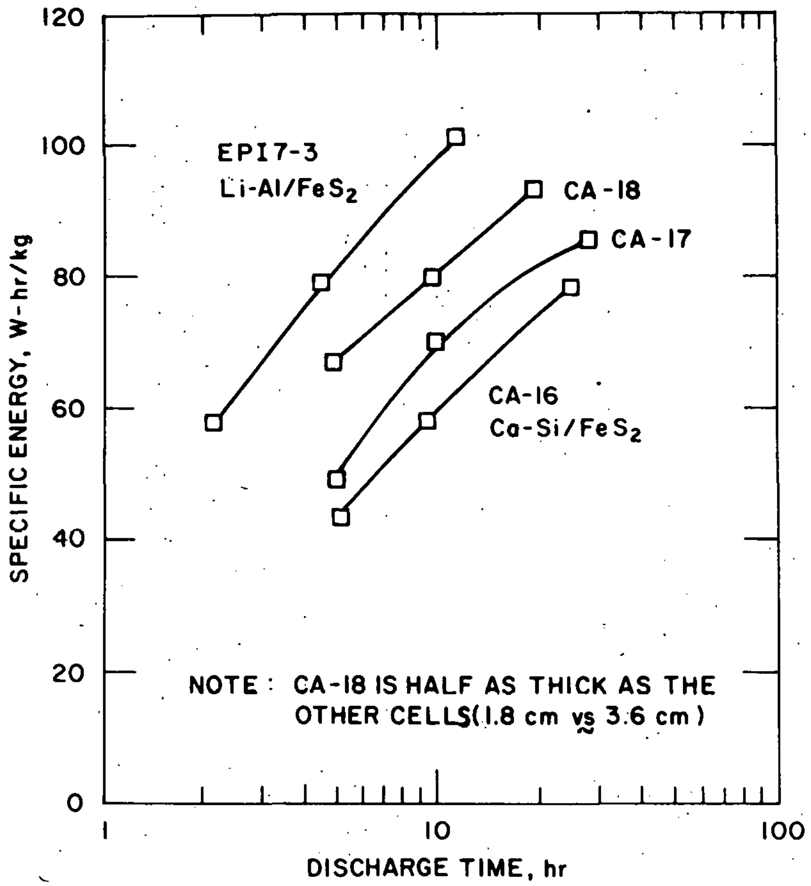

Fig. VIII-6. Performance of Three Ca-Si/FeS$_2$ Cells

to an irreversible loss of calcium through a reaction of Ca_2Si with the BN separator (based on post-test examinations). Furthermore, the effect was accompanied by an increase in cell resistance, which limited the cell performance.

To determine the effect of high temperature on the cells, the operating temperature was increased by about 20°C every cycle during the last eight cycles of Cell CA-17. As shown in Fig. VIII-8, the cell capacity increased until the temperature reached ~600°C, and then declined rapidly at 603°C and 623°C. Post-test examination showed that the cell had not leaked electrolyte, but that the unrestrained edges of the cell had bowed significantly. Thus, no catastrophic failure of the cell resulted from operation at very high temperatures; the cell failed by a gradual loss of capacity.

Detailed post-test examinations of Cells CA-16 and -17 are being conducted* to seek the causes of their increased resistance and capacity decline with cycling. Some of the significant early results of these examinations are:

---

*N. C. Otto, Chemical Engineering Division, ANL.

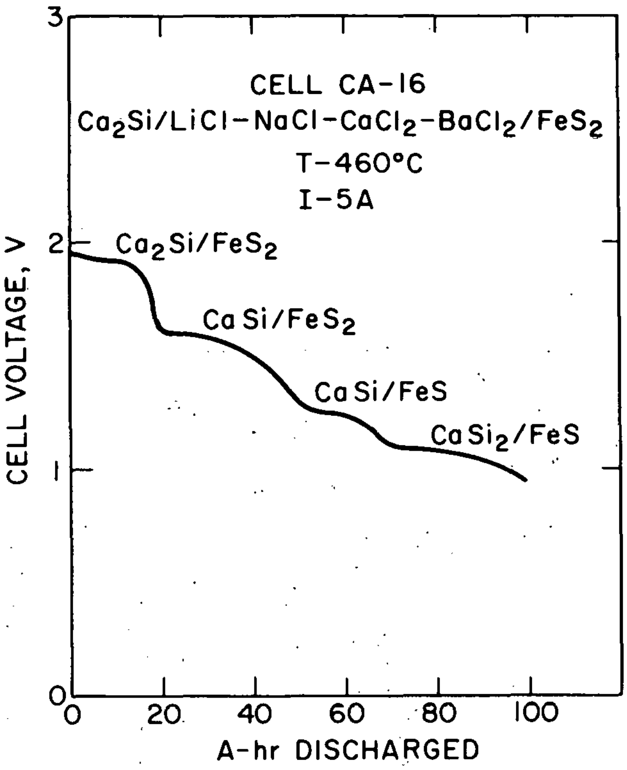

Fig. VIII-7. An Early Discharge (cycle #6) of a Ca_2Si/FeS_2 Cell Showing Multiple Discharge Reactions.

(1) The initially white BN separator of the cell had reacted to form a black material (not yet identified), and the reacted separator near the negative electrode had been crushed to form a very dense layer (a probable source of high resistance). This reaction is probably due to the high-calcium-activity compound, Ca_2Si, which was present during the early cycles of the cells (Fig. VIII-7).

(2) In CA-16, the iron current collector of the negative electrode was 5-10% corroded, forming a nonadherent reaction layer (another possible source of high resistance). The molybdenum current collector of the positive electrode was only slightly reacted (∿2%) and the reaction layer was adherent. Because of the very high temperatures during thermal testing, the current collectors of CA-17 were 50% corroded.

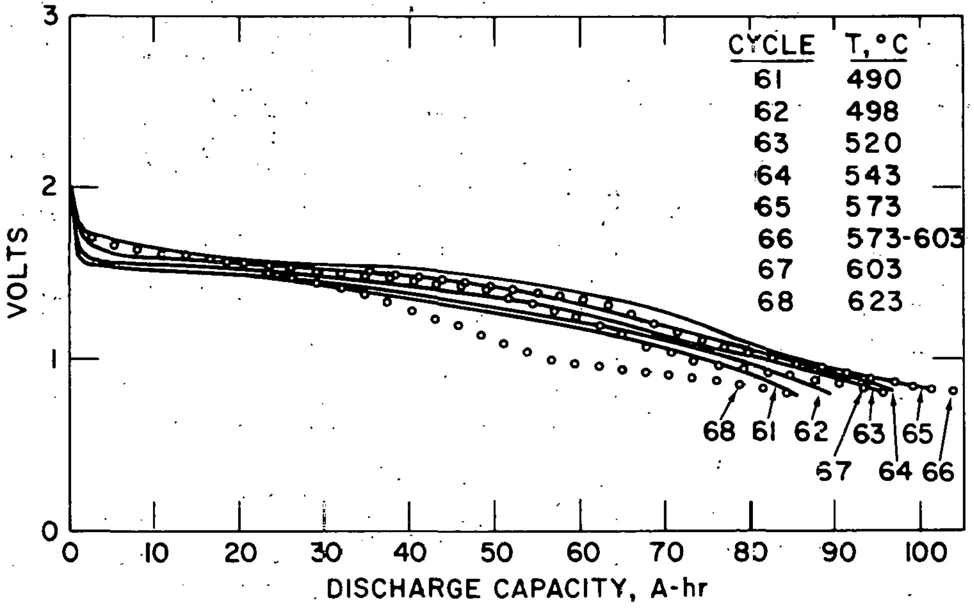

Fig. VIII-8. Thermal Tests of Cell CA-17

(3) No CaS was found by SEM examination of the BN separator of Cell CA-16, indicating good retention of sulfur by the FeS_2 electrode. However, salt taken from the reservoir on Cell CA-17 after its final cycle at 623°C contained 2.4 wt % sulfide,* indicating severe sulfur loss from the FeS_2 at very high temperatures.

According to Sharma and Bradley,[7] lithium-rich Li-Si compounds also react with BN, and Li-Si electrodes have been found to corrode current collectors.[8] Thus, the problems encountered here are not unique to calcium cells. Possible solutions to these problems that will be examined in future studies include modification of the negative electrode (*e.g.*, Ca-Mg-Si or Ca-Al negatives) or of the separator (*e.g.*, AlN). Better positive-electrode current collection may also be required to further improve the cell performance; alternatives to the carbon foam (*e.g.*, coke flour) will be tested in future studies.

---

*Analysis by C. Chow, Analytical Chemistry Laboratory, ANL.

REFERENCES

1. T. V. Tsyvenkova *et al.*, Rus. J. Inorg. Chem. *18*, 426 (1973).

2. M. L. Saboungi, J. J. Marr, M. Blander, J. Electrochem. Soc. *125*, 1567 (1978).

3. G. J. Janz, *Molten Salts Handbook*, Academic Press, NY (1967).

4. E. R. Van Artsdalen and I. S. Jaffe, J. Phys. Chem. *59*, 118 (1955).

5. E. M. Levin, C. R. Robbins, H. F. McMirode, *Phase Diagrams for Ceramists*, American Chemical Society, Ohio (1964, 1969 Suppl.).

6. K. J. Vetter, *Electrochemical Kinetics*, Academic Press, NY, pp. 671-674 (1967).

7. R. A. Sharma and T. G. Bradley, Fall Meeting of the Electrochemical Society, October 14-19, 1979, Extended Abstracts Vol, 79-2, Abstract No. 149 (1979).

8. R. K. Steunenberg and M. F. Roche, Proc. Symp. on Electrode Materials and Processes for Energy Conversion and Storage, pp. 869-889, Vol. 77-66, Princeton, NJ (1977).

APPENDIX A.

Performance Data on Gould Cells

Appendix A. Performance Data on Gould Cells

LIAl/FeS ENGINEERING CELL CHARACTERISTICS 9.'18/78

CELL NO. (PLATES)	THEOR. CAP (Ah) WT. (Kg) FAB. STATE	POSITIVE ELECTRODE AS BUILT HALF THICK. (In) (POROSITY)	(1) ADDITIVES	CURRENT COLLECTOR (THICKNESS) DENSITY	NEG. ELECTRODE AS BUILT HALF (THICK.-In.) w/o Li In LiAl(4)	SEPARATOR PKG (COMBINED ASS'Y FACE THICK.) FIBER DENSITY	ELECTROLYTE LOT NO. (w/o LiCl)	CELL RESIST. OPER. mOHMS @ 50% DISCH. T= 15 SEC.	FINAL FROZ. (OHM)	SPECIFIC ENERGY, Wh/Kg UTILIZATION, (%) @ CURRENT DENSITY (2) 20	40	60	80	CYCLE LIFE CYCLES	HOURS
X-41 (1)	163.7 2.13 Disch.	0.187 (40.70)	50% Fe. 1v/o Co. 3v/o C.	Ni. (0.013In.) 0.70g/Ah	8.2w/o H.P.P. (0.207) 8.20 (Disch.) 17.50 (Charged)	Carb. BN Felt 0.040 In. 73.2mg/sq cm	Blend (50.0)	4.560	380000	65.0 87.6	71.4 75.3	63.7 68.6	0.0 0.0	13.0 (6) (5)	591
X-42 (1)	170.7 2.07 Disch.	0.212 (40.81)	25% Fe. 1v/o Co. 3v/o C.	Ni. (0.013 In.) 0.64 g/Ah	8.2w/o H.P.P. (0.207) 8.20 (Disch.) 17.50 (Charged)	Carb. BN Felt 0.020 52.1mg/sq cm	#010 + #011 (50.0)	—	2.4	0.0 0.0	0.0 0.0	0.0 0.0	0.0 0.0	0.5 (5) (5)	98
X-43 (1)	166.6 2.16 Disch.	0.201 (40.85)	50% Fe. 1v/o Co. 3v/o C.	Ni. (0.013 In.) 0.66 g/Ah	8.2w/o H.P.P. (0.207) 8.20 (Disch.) 17.50 (Charged)	Carb. BN Felt 0.040 69.6mg/sq cm	#10 + #011 (52.0)	3.600	60000	65.1 89.6	75.9 82.1	73.9 77.2	0.0 0.0	10.5 (6) (5)	496
X-43A (1)	165.4 2.21 Disch.	0.212 (44.20)	50% Fe. 1v/o Co. 3v/o C.	Ni. (0.013 In.) 0.69 g/Ah	8.2w/o H.P.P. (0.206) 8.20 (Disch.) 17.50 (Charged)	Carb. BN Felt 0.040 69.6mg/sq cm	#010 + #011 (52.0)	5.380	0.2	57.1 61.0	42.9 47.3	48.1 52.7	0.0 0.0	10.5 (6) (5)	383
X-43B (1)	164.3 2.11 Disch.	0.216 (45.55)	50% Fe. 1v/o Co. 3v/o C.	Ni. (0.013 In.) 0.69 g/Ah	8.2w/o H.P.P. (0.176) 8.20 (Disch.) 17.50 (Charged)	Carb. BN Felt 0.040 62.5mg/sq cm	#011 (52.0)	4.100	.6	69.8 82.6	80.7 84.8	73.2 78.6	0.0 0.0	14.0 (7) (5)	644
X-44 (1)	166.4 2.31 Disch.	0.199 (40.31)	100% Fe. 1v/o Co. 3v/o C.	Ni. (0.013 In.) 0.66 g/Ah	8.2w/o H.P.P. (0.206) 8.20 (Disch.) 17.50 (Charged)	Carb. BN Felt 0.040 69.3mg/sq cm	#010 (53.6)	4.100	0	77.4 86.7	65.1 74.5	59.6 68.4	0.0 0.0	36.5 (6) (5)	790
X-45 (1)	167.7 2.15 Disch.	0.203 (41.05)	50% Fe. 1v/o Co. 3v/o C.	Ni. (0.013 In.) 0.66 g/Ah	8.2w/o H.P.P. (0.209) 8.20 (Disch.) 17.50 (Charged)	Carb. BN Felt 0.040 62.5mg/sq cm	#013 (48.0)	3.500	0.0	83.7 86.4	69.9 73.7	63.6 67.7	0.0 0.0	124.0 (6) (5)	1725
X-47 (1)	167.3 2.32 Disch.	0.203 (39.99)	50% Fe. 3v/o Co. 3v/o C.	Ni. (0.013 In.) 0.66 g/Ah	8.2w/o H.P.P. (0.205) 8.20 (Disch.) 17.50 (Charged)	Gould BN Felt 0.045 61.6mg/sq cm	#010 + #011 (52.0)	3.570	7.3^5	77.1 86.4	67.9 77.2	61.4 70.7	0.0 0.0	11.5 (6) (5)	426
X-46 (1)	184.6 2.33 Disch.	0.205 (36.70)	50% Fe. 3v/o Mo. 3v/o C.	Ni. (0.013 In.) 0.62 g/Ah	8.2w/o H.P.P. (0.210) 8.20 (Disch.) 17.50 (Charged)	Gould BN Felt 0.041 73.6mg/sq cm	#011 + #010 (52.0)	3.530	7.3	81.5 89.1	72.0 74.5	65.2 68.4	0.0 0.0	11.5 (7) (5)	426
X-49 (1)	162.6 2.35 Disch.	0.209 (36.26)	50% Fe. 3v/o Cr. 3v/o C.	Ni. (0.013 In.) 0.63 g/Ah	8.2w/o H.P.P. (0.212) 8.20 (Disch.) 17.50 (Charged)	Gould BN Felt 0.044 70.2mg/sq cm	#010 + #011 (52.0)	5.590	13000	57.7 60.2	52.1 55.4	50.4 53.7	0.0 0.0	11.9 (7) (5)	383

(1) FOR Fe.: w/o in excess of stoichiometric iron.
FOR OTHERS: v/o of active mix less electrolyte.
(2) [0.0] implies no test was run in this range to date.
(3) Ground Cast Iron (otherwise Pure Fe.)
(4) H.P.P.= Hot pressed powder, C.P.P.= Cold Pressed
(5) Cell shorted- Test terminated- Cell to Post Mortem
(6) Cell to ANL for Qualification Testing
(7) Cell to Life Test Facility
(8) Cell to Battery Assembly

Appendix A. (contd)

LiAl/FeS ENGINEERING CELL CHARACTERISTICS 9/18/79

CELL NO. (PLATES)	THEOR. CAP (Ah) WT: (Kg) FAB. STATE	POSITIVE ELECTRODE AS BUILT HALF THICK. (in) (POROSITY)	(1) ADDITIVES	CURRENT COLLECTOR (THICKNESS) DENSITY	NEG. ELECTRODE AS BUILT HALF (THICK.-in.) w/o Li in LiAl(4)	SEPARATOR PKG (COMBINED ASS'Y FACE THICK.) FIBER DENSITY	ELECTROLYTE LOT NO. (w/o LiCl)	CELL RESIST. OPER. mOHMS @ 50% DISCH. T= 15 SEC.	FINAL FROZ. (OHM)	SPECIFIC ENERGY, Wh/Kg UTILIZATION, (%) @ CURRENT DENSITY (2) 20	40	60	80	CYCLE LIFE CYCLES	HOURS
X-50 (1)	176.4 2.35 Disch.	0.210 (39.56)	50% Fe. 3v/o V. 3v/o C.	Ni. (0.013in.) 0.64g/Ah	6.2w/o H.P.P. (0.220) 6.20 (Disch.) 17.50 (Charged)	Gould BN Felt 0.041 in. 73.6mg/sq cm	#011+#010 (52.0)	3.570	74.7	76.2 82.2	68.1 74.9	61.2 68.7	0.0 0.0	11.5 (7) (5)	426
X-53 (1)	212.3 2.30 Half Ch.	0.205 (45.12)	25% Fe. 3v/o Co. 3v/o C.	Ni. (0.013 in.) 0.54 g/Ah	6.2w/o H.P.P. (0.266) 6.20 (Disch.) 17.50 (Charged)	Gould BN Felt 0.053 95.9mg/sq cm	#010+#011 (52.0)	3.630	7.2	67.9 76.2	71.7 63.5	60.7 54.7	0.0 0.0	15.5 (7) (5)	560
X-54 (1)	164.1 2.30 Half Ch.	0.199 (51.22)	25% Fe. 3v/o Co. 1v/o C.	Ni. (0.013 in.) 0.62 g/Ah	6+16w/o H.P.P. (0.234) 6.00 (Disch.) 17.50 (Charged)	Gould BN Felt 0.152 92.0mg/sq cm	#011 + LiCl (52.0)	4.210	14^5	66.0 66.1	73.9 75.7	61.5 63.6	0.0 0.0	11.0 (6) (5)	431
X-55 (1)	176.6 2.46 Disch.	0.217 (39.05)	100% Fe. 3v/o Zr. 1v/o C.	Ni. (0.013 in.) 0.64 g/Ah	6+16w/o H.P.P. (0.165) 6.00 (Disch.) 17.50 (Charged)	Gould BN Felt 0.124 59.9mg/sq cm	#011 + LiCl (52.0)	4.720	147	71.3 79.6	65.6 74.4	60.9 69.6	0.0 0.0	13.5 (7) (5)	620
X-56 (1)	162.1 2.47 Disch.	0.209 (37.12)	50% Fe. 2v/o ZrO2 3+1v/oC+Co	Ni. (0.013 in.) 0.62 g/Ah	6+16w/o H.P.P. (0.172) 6.00 (Disch.) 17.50 (Charged)	Gould BN Felt 0.143 99.3mg/sq cm	#011 + LiCl (52.0)	4.430	42000	0.0 0.0	0.0 0.0	0.0 0.0	0.0 0.0	11.0 (5) (5)	505
X-56A (1)	166.4 2.27 Disch.	0.207 (35.75)	50% Fe. 2v/o ZrO2 3+1v/oC+Co	Ni. (0.013 in.) 0.61 g/Ah	6+16w/o H.P.P. (0.172) 6.00 (Disch.) 17.50 (Charged)	Gould BN Felt 0.143 69.9mg/sq cm	#011 + LiCl (52.0)	4.430	42000	69.3 66.1	65.3 61.6	0.0 0.0	0.0 0.0	11.0 (7) (5)	505
X-57 (1)	168.2 2.46 Disch.	0.214 (40.44)	100% Fe(3) 2v/o ZrO2 1v/o Co.	Ni. (0.013 in.) 0.61 g/Ah	6+16w/o H.P.P. (0.190) 6.00 (Disch.) 17.50 (Charged)	Carb. BN Felt 0.175 59.9mg/sq cm	#011 + LiCl (52.0)	5.520	37.3	78.2 81.9	73.6 77.1	68.3 73.6	0.0 0.0	14.5 (7) (5)	623
X-58 (1)	145.4 2.45 Half Ch.	0.147 (46.60)	25% Fe. 3v/o Co. 3v/o C.	Ni. (0.013 in.) 0.76 g/Ah	6+16w/o H.P.P. (0.165) 6.00 (Disch.) 17.50 (Charged)	Carb. BN Felt 0.176 61.6mg/sq cm	#011 + LiCl (52.0)	—	4400	0.0 0.0	0.0 0.0	0.0 0.0	0.0 0.0	0.5 (5) (5)	60
X-59 (1)	143.9 1.98 Half Ch.	0.140 (44.50)	25% Fe. 3v/o Co. 3v/o C.	Ni. (0.013 in.) 0.79 g/Ah	6+16w/o H.P.P. (0.147) 6.50 (Disch.) 16.00 (Charged)	Carb. BN Felt 0.073 62.1mg/sq cm	#011 + LiCl (52.0)	—	52000	0.0 0.0	0.0 0.0	0.0 0.0	0.0 0.0	0.5 (5) (5)	60
X-60 (1)	155.0 1.93 Half Ch.	0.139 (41.76)	25% Fe. 3v/o Co. 3v/o C.	Ni. (0.013 in.) 0.74 g/Ah	6+16w/o H.P.P. (0.150) 6.50 (Disch.) 16.00 (Charged)	Carb. BN Felt 0.107 59.9mg/sq cm	#011 + LiCl (52.0)	—	56000	0.0 0.0	0.0 0.0	0.0 0.0	0.0 0.0	0.5 (5) (5)	60

(1) FOR Fe.: w/o in excess of stoichiometric iron.
FOR OTHERS: v/o of active mix less electrolyte.
(2) [0.0] implies no test was run in this range to date.
(3) Ground Cast Iron (otherwise Pure Fe.)
(4) H.P.P.= Hot pressed powder, C.P.P.= Cold Pressed
(5) Cell shorted- Test terminated- Cell to Post Mortem
(6) Cell to ANL for Qualification Testing
(7) Cell to Life Test Facility
(8) Cell to Battery Assembly

Appendix A. (contd)

LiAl/FeS ENGINEERING CELL CHARACTERISTICS 9/18/78

CELL NO. (PLATES)	THEOR. CAP (Ah) WT. (Kg) FAB. STATE	POSITIVE ELECTRODE AS BUILT HALF THICK. (in) (POROSITY)	(1) ADDITIVES	CURRENT COLLECTOR (THICKNESS) DENSITY	NEG. ELECTRODE AS BUILT HALF (THICK.-in.) w/o Li in LiAl(4)	SEPARATOR PKG (COMBINED ASS'Y FACE THICK.) FIBER DENSITY	ELECTROLYTE LOT NO. (w/o LiCl)	CELL RESIST. OPER. mOHMS @ 50% DISCH. T= 15 SEC.	FINAL FROZ. (OHM)	SPECIFIC ENERGY, Wh/Kg UTILIZATION, (%) @ CURRENT DENSITY (2)				CYCLE LIFE	
										20	40	60	80	CYCLES	HOURS
X-62 (1)	121.1 1.93 Half Ch.	0.142 (45.41)	100w/o F 1v/o Co. 3v/o C.	Ni. (0.013in.) 0.95g/Ah	8+18w/o H.P.P. (0.146) 8.50 (Disch.) 18.00 (Charged)	Carb. BN Felt 0.110 in. 58.9mg/sq cm	#011 +LiCl (52.0)	—	8	0.0 0.0	0.0 0.2	0.2 0.0	0.0 0.0	0.5 (5) (6)	60
X-63 (1)	170.4 2.09 Disch.	0.200 (38.16)	50% Fe. 1v/o Co. 3v/o C.	Ni. (0.013 in.) 0.67 g/Ah	6+16w/o H.P.P. (0.194) 6.00 (Disch.) 17.50 (Charged)	Carb. BN Felt 0.126 58.9mg/sq cm	#011 + LiCl (52.0)	3.100	2.4	97.9 85.6	94.3 94.3	0.0 0.0	0.0 0.0	15.0 (5) (5)	1330
X-64 (1)	165.0 2.11 Disch.	0.200 (38.96)	50%Fe. (3) 1v/o Co. (3)	Ni. (0.013 in.) 0.62 g/Ah	6+16w/o H.P.P. (0.194) 6.00 (Disch.) 17.50 (Charged)	Carb. BN Felt 0.195 58.9mg/sq cm	#011 + LiCl (52.0)	—	1.0	0.0 0.0	0.0 0.0	0.0 0.0	0.0 0.0	0.5 (5) (6)	140
X-65 (1)	172.0 2.24 Half Ch.	0.180 (53.62)	50Fe.(3) 1v/o Co. 2v/o C.	Ni. (0.013 in.) 0.66 g/Ah	8+16w/o H.P.P. (0.210) 6.00 (Disch.) 17.50 (Charged)	Carb. BN Felt 0.100 19.7mg/sq cm	#011 + LiCl (52.0)	—	——	0.0 0.0	0.0 0.0	0.0 0.0	0.0 0.0	1.5 (5) (5)	153
X-66 (1)	176.6 2.26 Half Ch.	0.179 (46.86)	50Fe.(3) 1v/o Co. 2v/o C.	Ni. (0.013 in.) 0.64 g/Ah	6+16w/o H.P.P. (0.212) 6.00 (Disch.) 17.50 (Charged)	Carb. BN Felt 0.111 31.2mg/sq cm	#011 + LiCl (52.0)	4.400	——	67.9 89.4	65.1 87.9	76.6 82.6	0.0 0.0	17.0 (7) (6)	400
X-68 (1)	177.5 2.17 Half Ch.	0.164 (48.18)	50Fe.(3) 1v/o Mo. 2v/o C.	Ni. (0.013 in.) 0.64 g/Ah	8+18w/o H.P.P. (0.209) 6.00 (Disch.) 17.50 (Charged)	Carb. BN Felt 0.115 42.4mg/sq cm	#011 + LiCl (52.0)	4.640	76	92.3 90.6	87.0 86.8	84.7 86.0	0.0 0.0	17.0 (7) (5)	392
X-70 (1)	175.9 2.27 Half Ch.	0.177 (46.61)	50Fe.(3) 1v/o Mo. 2v/o C.	Ni. (0.013 in.) 0.64 g/Ah	6+16w/o H.P.P. (0.209) 6.00 (Disch.) 17.50 (Charged)	Carb. BN Felt 0.123 41.5mg/sq cm	#011 + LiCl (52.0)	4.400	646	88.6 90.7	84.9 89.0	85.9 90.9	0.0 0.0	17.0 (7) (5)	400
X-77 (1)	72.5 1.54 HALF CH.	0.084 (58.60)	10% Fe. 2v/o Co. 1v/o C.	Ni. (0.013 in.) 1.15 g/Ah	14.5w/o H.P.P. (0.065) 6.00 (Disch.) 17.50 (Charged)	Carb. BN Felt 0.066 73.4mg/sq cm	#013 + LiCl (52.0)	4 300	——	56.7 94.2	54.5 93.3	49.6 68.7	29.0 56.1	349.5 (7) (5)	4512
X-78 (1)	178.1 2.22 Half Ch.	0.189 (51.47)	50Fe.(3) 1v/o Mo. 2v/o C.	Ni. (0.013 in.) 0.63 g/Ah	8+14.5w/o H.P.P. (0.214) 6.10 (Disch.) 16.00 (Charged)	*Carb BN Felt 0.111 68.5mg/sq cm	13 + LiCl (52.0)	5.000	——	91.1 90.4	87.0 88.7	83.1 86.4	0.0 0.0	12.0 (7) (6)	480
X-63 (2)	213.6 2.26 Half Ch.	0.085 (44.92)	10Fe.(3) 1v/o Mo. 2v/o C.	Ni. (0.010 in.) 0.85 g/Ah	6+16w/o H.P.P. (0.204) 6.20 (Disch.) 16.00 (Charged)	BN Cloth Cups 0.070 325.6mg/sq cm	#013 +LiCl (52.0)	—	——	0.0 0.0	0.0 0.0	0.0 0.0	0.0 0.0	3.0 (5) (5)	142

(1) FOR Fe.: w/o in excess of stoichiometric iron.
FOR OTHERS: v/o of active mix less electrolyte.
(2) [0.0] implies no test was run in this range to date.
(3) Ground Cast Iron (otherwise Pure Fe.)
(4) H.P.P.= Hot pressed powder, C.P.P.= Cold Pressed
(5) Cell shorted– Test terminated– Cell to Post Mortem
(6) Cell to ANL for Qualification Testing
(7) Cell to Life Test Facility
(8) Cell to Battery Assembly

Appendix A. (contd)

LIAl/FeS ENGINEERING CELL CHARACTERISTICS 9/18/78

CELL NO. (PLATES)	THEOR. CAP (Ah) WT. (Kg) FAB. STATE	POSITIVE ELECTRODE AS BUILT HALF THICK. (In) (POROSITY)	(1) ADDITIVES	CURRENT COLLECTOR (THICKNESS) DENSITY	NEG. ELECTRODE AS BUILT HALF (THICK.-In.) w/o Li in LiAl(4)	SEPARATOR PKG (COMBINED ASS'Y FACE THICK.) FIBER DENSITY	ELECTROLYTE LOT NO. (w/o LiCl)	CELL RESIST. OPER. mOHMS @ 50% DISCH. T= 15 SEC.	FINAL FROZ. (OHM)	SPECIFIC ENERGY, Wh/Kg UTILIZATION, (%) @ CURRENT DENSITY (2) 20	40	60	80	CYCLE LIFE CYCLES	HOURS
X-84 (2)	225.5 2.26 Half Ch.	0.088 (47.44)	10Fe.(3) 1v/o Mo. 2v/o C.	Ni. (0.010in.) 0.60g/Ah	6+16v/o H.P.P. (0.210) 6.20 (Disch.) 16.00 (Charged)	BN Cloth Cups 0.081 in. 306.5mg/sq cm	#013 + LiCl (52.0)	3.450	14	106.0 90.7	80.4 88.6	86.1 86.0	0.0 0.0	27.5 (7) (5)	564
X-85 (1)	120.0 1.41 Half Ch.	0.112 (46.15)	10Fe.(3) 1v/o Mo. 2v/o C.	Ni. (0.010 in.) 0.70 g/Ah	6+16v/o H.P.P. (0.100) 5.20 (Disch.) 16.00 (Charged)	*Carb BN Felt 0.067 63.1mg/sq cm	#013 + LiCl (52.0)	3.250	———	0.0 0.0	0.0 0.0	0.0 0.0	0.0 0.0	2.5 (5) (5)	102
X-86 (2)	238.6 2.34 Half Ch.	0.113 (46.65)	10Fe.(3) 1v/o Mo. 2v/o C.	Ni. (0.010 in.) 0.60 g/Ah	6+16v/o H.P.P. (0.210) 5.20 (Disch.) 16.00 (Charged)	*Carb BN Felt 0.067 68.5mg/sq cm	#013 + LiCl (52.0)	3.700	0.4	112.0 69.1	86.6 66.4	86.7 66.5	0.0 0.0	31.5 (7) (5)	600
X-88 (2)	241.5 2.47 Half Ch.	0.111 (45.64)	10Fe.(3) 1v/o Mo. 2v/o C.	Ni. (0.010 in.) 0.67 g/Ah	6+16v/o H.P.P. (0.204) 5.20 (Disch.) 16.00 (Charged)	*Carb BN Felt 0.073 70.5mg/sq cm	Lithco (52.0)	3.100	———	109.5 67.0	86.7 67.4	86.8 66.7	0.0 0.0	28.5 (6) (7)	365
X-89 (1)	110.7 1.61 Half Ch.	0.110 (45.44)	10Fe(3) 1v/o Mo. 2v/o C.	Ni. (0.010 in.) 0.67 g/Ah	Al +16w/o H.P.P. (0.107) 5.20 (Disch.) 16.20 (Charged)	*Carb BN Felt 0.060 68.7mg/sq cm	Lithcoa (52.0)	——	64	74.1 70.8	66.5 74.3	70.7 60.4	0.0 0.0	25.0 (7) (5)	505
X-90 (1)	120.0 1.60 Half Ch.	0.115 (47.45)	10Fe.(3) 1v/o Mo. 2v/o C.	Ni. (0.010 in.) 0.67 g/Ah	Al +16w/o C.P.P. (0.113) 6.20 (Disch.) 16.00 (Charged)	*Carb BN Felt 0.067 68.0mg/sq cm	Lithcoa (52.0)	4.400	300	81.7 85.1	80.7 85.7	77.4 85.6	0.0 0.0	16.5 (7) (7)	265
D-1 (2)	235.6 2.39 Half Ch.	0.112 (47.55)	10Fe.(3) 1v/o Mo. 2v/o C.	Ni. (0.010 in.) 0.69 g/Ah	Al +16w/o C.P.P. (0.216) 5.20 (Disch.) 16.00 (Charged)	*Carb BN Felt 0.061 67.4mg/sq cm	Lithcoa (52.0)	2.600	0.6	91.6 76.5	0.0 0.0	0.0 0.0	0.0 0.0	16.0 (7) (5)	362
D-2 (2)	228.0 1.93 Half Ch.	0.111 (46.46)	10Fe.(3) 1v/o Mo. 2v/o C.	Ni. (0.010 in.) 0.70 g/Ah	Al + 16w/o C.P.P. (0.220) 5.20 (Disch.) 16.00 (Charged)	*Carb BN Felt 0.046 68.9mg/sq cm	Anderson (52.0)	2.300	0.7	86.2 67.4	0.0 0.0	0.0 0.0	0.0 0.0	14.5 (7) (5)	350
D-4 (2)	243.6 2.42 Half Ch.	0.109 (45.50)	10w/o Fe 1v/o Mo. 2v/o C.	Ni+Fe- (0.010 in.) 1.55 g/Ah	6+16v/o H.P.P. (0.206) 5.20 (Disch.) 16.00 (Charged)	*Carb BN Felt 0.065 66.9mg/sq cm	Lithcoa (52.0)	2.500	———	117.0 86.3	104.9 91.6	105.9 93.0	0.0 0.0	23.5 (7) (7)	646

(1) FOR Fe.: v/o in excess of stoichiometric iron.
FOR OTHERS: v/o of active mix less electrolyte.
(2) [0.0] implies no test was run in this range to date.
(3) Ground Cast Iron (otherwise Pure Fe.)
(4) H.P.P.= Hot pressed powder, C.P.P.= Cold Pressed
(5) Cell shorted- Test terminated- Cell to Post Mortem
(6) Cell to ANL for Qualification Testing
(7) Cell to Life Test Facility
(8) Cell to Battery Assembly

Appendix A. (contd)

LiAl/FeS ENGINEERING CELL CHARACTERISTICS 3/10/79

CELL NO. (PLATES)	THEOR. CAP (Ah) WT. (Kg) FAB. STATE	POSITIVE ELECTRODE AS BUILT HALF THICK. (In) (POROSITY)	(1) ADDITIVES	CURRENT COLLECTOR (THICKNESS) DENSITY	NEG. ELECTRODE AS BUILT HALF (THICK.-In.) w/o Li in LiAl(4)	SEPARATOR PKG (COMBINED ASS'Y FACE THICK.) FIBER DENSITY	ELECTROLYTE LOT NO. (w/o LiCl)	CELL RESIST. OPER. mOHMS @ SEC DISCH. To 15 SEC.	FINAL FROZ. (OHM)	SPECIFIC ENERGY, Wh/Kg UTILIZATION, (%) @ CURRENT DENSITY (2) 20	40	60	80	CYCLE LIFE CYCLES	HOURS
E-1 (1)	110.6 1.57 Half Ch.	0.106 (47.50)	10w/o Fe 1v/o Mo. 2v/o C.	Ni. (0.010in.) 0.72g/Ah	6+16w/o H.P.P. (0.111) 5.20 (Disch.) 16.00 (Charged)	*Carb BN Felt 0.077 in. 68.9mg/sq cm	Lithcoa (52.0)	3.500	----	67.6 100.3	0.0 0.0	64.7 88.3	77.6 93.7	27.0 (7) (7)	550
E-2 (1)	115.1 1.41 Half Ch.	0.112 (46.90)	10Fe.(3) 1v/o Mo. 2v/o C.	Ni.(BN Ret (0.010 in.) 0.70 g/Ah	Al+16w/o C.P.P. (0.112) 5.20 (Disch.) 16.00 (Charged)	*Carb BN Felt 0.049 34.2mg/sq cm	Lithcoa (52.0)	3.600	3.0	66.0 67.0	67.3 67.1	74.0 76.4	0.0 0.0	15.5 (7) (5)	370
E-3 (1)	116.7 1.43 Half Ch.	0.105 (44.46)	10% Fe. 1v/o Mo. 2v/oC (GW)	Ni. (0.010 in.) 0.69 g/Ah	Al+18w/o C.P.P. (0.102) 5.20 (Disch.) 16.00 (Charged)	*Carb BN Felt 0.066 71.1mg/sq cm	Lithcoa (52.0)	3.500	----	85.3 93.4	65.4 66.0	61.6 64.6	0.0 0.0	50.0 (7) (7)	1000
E-4 (1)	115.4 1.43 Half Ch.	0.111 (47.62)	10% Fe. 1v/o Mo. 2v/oC.(GW)	Ni. (0.010 in.) 0.70 g/Ah	Al+16w/o C.P.P. (0.102) 5.20 (Disch.) 16.00 (Charged)	*Carb BN Felt 0.060 70.6mg/sq cm	Lithcoa (52.0)	---	----	81.5 82.1	80.9 82.6	61.9 65.5	0.0 0.0	32.5 (7) (7)	650

(1) FOR Fe.: w/o in excess of stoichiometric iron.
FOR OTHERS: v/o of active mix less electrolyte.
(2) [0.0] implies no test was run in this range to date.
(3) Ground Cast Iron (otherwise Pure Fe)
(4) H.P.P.= Hot pressed powder, C.P.P.= Cold Pressed
(5) Cell shorted— Test terminated— Cell to Post Mortem
(6) Cell to ANL for Qualification Testing
(7) Cell to Life Test Facility
(8) Cell to Battery Assembly

Appendix A. (contd)

LiAl/FeS ENGINEERING CELL CHARACTERISTICS 5 July 1979

CELL NO.	THEOR. CAP (Ah) WT. (Kg)	POSITIVE ELECTRODE AS BUILT HALF THICK. (in) (POROSITY)	(1) ADDITIVES	CURRENT COLLECTOR (THICKNESS) DENSITY	NEG. ELECTRODE AS BUILT HALF (THICK.-in.) COMPOSITION	SEPARATOR PKG (COMBINED) FACE THICK. FIBER DENSITY	ELECTROLYTE LOT NO. (w/o LiCl)	CELL RESIST. OPER. mOHMS @ 50% DISCH. T= 15 SEC.	FINAL FROZ. (OHM)	SPECIFIC ENERGY, Wh/Kg UTILIZATION, (%) @ CURRENT DENSITY (2) 20	40	60	80	CYCLE LIFE CYCLES	HOURS
Q-1	117.6 1.591	0.114 (47.93)	10% Fe. 1v/o Mo. 2v/o C.	Ni. w/Tab (0.010in.) 0.66g/Ah	Hot pr. Powder (0.103) 12.000w/o Li	BN Felt 0.076 in. 70.2mg/sq cm	#013 + LiCl (52.0)	5.000	10^5	62.7 67.7	0.0 0.0	0.0 0.0	0.0 0.0	3.5	125
Q-2	117.8 1.592	0.106 (43.87)	10% Fe. 1v/o Mo. 2v/o C.	Ni w/Tab (0.010 in.) 0.67 g/Ah	Hot pr. Powder (0.103) 12.000w/o Li	BN Felt 0.062 68.5mg/sq cm	#013 + LiCl (52.0)	5.000	10^5	74.7 83.4	0.0 0.0	0.0 0.0	0.0 0.0	3.5	125
Q-3	115.5 1.584	0.104 (43.93)	10% Fe. 1v/o Mo. 2v/o C.	Ni. w/Tab (0.010 in.) 0.69 g/Ah	Hot pr. Powder (0.105) 12.000w/o Li	BN Felt 0.062 69.3mg/sq cm	#013 + LiCl (52.0)	5.000	10^5	62.8 68.3	0.0 0.0	0.0 0.0	0.0 0.0	4.5	147
Q-4	119.3 1.493	0.107 (43.71)	10% Fe. 1v/o Mo. 2v/o C.	Ni. w/Tab (0.010 in.) 0.67 g/Ah	Hot pr. Powder (0.103) 12.000w/o Li	BN Felt 0.061 72.8mg/sq cm	Ander.+LiCl (52.0)	4.800	10^5	64.5 63.2	0.0 0.0	0.0 0.0	0.0 0.0	4.5	147
Q-5	116.8 1.493	0.106 (44.39)	10% Fe. 1v/o Mo. 2v/o C.	Ni. w/Tab (0.010 in.) 0.69 g/Ah	Hot pr. Powder (0.104) 12.000w/o Li	BN Felt 0.061 66.9mg/sq cm	Ander.+LiCl (52.0)	4.200	10^5	67.3 68.9	0.0 0.0	0.0 0.0	0.0 0.0	4.5	147
Q-6	117.5 1.598	0.110 (45.89)	10% Fe. 1v/o Mo. 2v/o C.	Ni. w/Tab (0.010 in.) 0.69 g/Ah	Hot pr. Powder (0.112) 12.000w/o Li	BN Felt 0.070 67.6mg/sq cm	#013 + LiCl (52.0)	5.000	10^5	70.4 76.6	70.5 77.0	70.7 78.2	0.0 0.0	3.5	125
Q-7	112.8 1.575	0.108 (47.34)	10% Fe. 1v/o Mo. 2v/o C.	Ni. w/Tab (0.010 in.) 0.70 g/Ah	Hot pr. Powder (0.107) 12.000w/o Li	BN Felt 0.076 66.5mg/sq cm	#013 + LiCl (52.0)	5.000	10^5	69.0 77.1	68.2 77.6	68.9 79.7	0.0 0.0	3.5	125
Q-8	115.0 1.560	0.108 (45.21)	10% Fe. 1v/o Mo. 2v/o C.	Ni. w/Tab (0.010 in.) 0.70 g/Ah	Hot pr. Powder (0.107) 12.000w/o Li	BN Felt 0.076 66.5mg/sq cm	#013 + LiCl (52.0)	5.000	10^5	73.7 81.0	73.3 80.6	71.9 80.5	0.0 0.0	3.5	125
Q-9	116.4 1.592	0.104 (43.49)	10% Fe. 1v/o Mo. 2v/o C.	Ni. w/Tab (0.010 in.) 0.69 g/Ah	Hot pr. Powder (0.107) 12.000w/o Li	BN Felt 0.060 66.3mg/sq cm	Ander.+LiCl (52.0)	5.000	10^5	77.6 84.9	77.0 84.6	76.0 83.7	0.0 0.0	3.5	125
Q-10	117.8 1.628	0.105 (43.36)	10% Fe. 1v/o Mo. 2v/o C.	Ni. w/Tab (0.010 in.) 0.66 g/Ah	Hot pr. Powder (0.107) 12.000w/o Li	BN Felt 0.079 66.1mg/sq cm	Ander.+LiCl (52.0)	5.000	10^5	66.1 74.3	64.4 73.0	60.4 69.6	0.0 0.0	3.5	125

(1) FOR Fe.: w/o in excess of stoichiometric iron.
FOR OTHERS: v/o of active mix less electrolyte.
(2) [0.0] implies no test was run in this range to date.

GOULD, INC.

APPENDIX B.

Performance Data on ANL Li/MS Cells

Appendix B. Performance Data on ANL Li/MS Cells

Cell Description[a]	Max. Performance @ Indicated Rate		Rates, hr		Initial Eff., %		Life Characteristics						Remarks
									% Decline in				
	A-hr	W-hr	Disch.	Charge	A-hr	W-hr	Days[b]	Cycles[b]	Capacity	Energy	A-hr Eff.	W-hr Eff.	
R-36, Li-Al/NiS_2-CoS_2, 180/150 A-hr, 1.8 kg	100 70	146 84	13.5 3.0	13.5 8.0	99	79	506	1319	35	32	35	20	Carbon fiber added to NiS_2 positive electrode. Terminated.
R-41, Li-Al/FeS-Cu_2S, 180/103 A-hr, 1.7 kg	76	100	3.3	8.8	>99	83	180	351	2	13	2	1.2	BN felt separator treated with $LiAlCl_4$. Terminated.
R-42, Li-Al/FeS-Cu_2S, 160/113 A-hr, 1.7 kg	61	75	3.0	6.0	60	42	103	253	21	23.5	35	46	Similar to R-41 but with $LiAlCl_4$ in positive electrode. Terminated.
R-43, Li-Al/FeS, 150/134 A-hr, 1.8 kg	83	96	5	0	100	83	127	240	14.6	32.3	20	22	This cell had BN felt separator with $LiAlCl_4$, LiCl-rich electrolyte, high-temperature carbon added. Terminated.
R-44, Li-Al/FeS, 180/133 A-hr, 1.8 kg	80	98	4	10	99	82	>210	>326	0	0	0	0	This cell has BN felt separator with $LiAlCl_4$, LiCl-rich electrolyte, high-temperature carbon added to positive, and iron current collector.
R-46, Li-Al/Fe, 180/133 A-hr, 1.8 kg	56.5	65.0	7.2	7.25	98.5	79.5	70	121	20	18	11	7	This cell has BN felt separator with $LiAlCl_4$, high-termperature carbon, LiCl-rich electrolyte, and Fe rod current collector with no sheet. Terminated.
R-47, Li-Al/FeS, 210/144 A-hr, 1.78 kg	90.3	108.4	4.5	14.5	99.8	84.5	>277	>409	9	8	0	0	This cell has BN felt separator with $LiAlCl_4$, high-temperature carbon, LiCl-rich electrolyte, and Ni current collector.
R-48, Li-Al/FeS, 210/144 A-hr, 1.78 kg	82	100	4.0	10.8	100	87.5	>249	>404	0	2	2	5	Similar to R-47, but with all iron current collector.
R-49, Li-Al/FeS, 185/144 A-hr, 1.68 kg	84	102	4.2	11.2	99.9	84.9	181	310	19	17	5	8	Similar to R-48, with only one electrode frame around positive electrode. Terminated.
R-50, LiAl/FeS, 141/103 A-hr, 1.40 kg	71 68	82 85	4.4 4.0	9.4 9.0	99 99	85 80	174	326	24	31	50	47	Similar to R-47, but thinner positive electrode. Terminated.

(contd)

Appendix B. (contd)

	Max. Performance @ Indicated Rate		Rates, hr		Initial Eff., %		Life Characteristics						
									% Decline in				
Cell Description^a	A-hr	W-hr	Disch.	Charge	A-hr	W-hr	Days^b	Cycles^b	Capacity	Energy	A-hr Eff.	W-hr Eff.	Remarks
R-51, LiAl/FeS, 86/62.5 A-hr, 0.95 kg	36 38	43.8 52	1.8 4.0	5.8 5.8	99 99	85 90	>139	>338	0	0	0	0	Similar to R-48, but with a 60 % thinner positive electrode.
R-52, LiAl/FeS, 119/93 A-hr, 1.50 kg	44	51	2.2	6.0	93	75	30	82	-	-	-	-	One layer of BN felt separator, LiCl-rich electrolyte, and a rigid-edge current-collector. Shorted and terminated.
R-53, LiAl/FeS, 145.3/145.3 A-hr, 1.6 kg	69	83.2	3.5	9.4	99	83	>49	>77	0	0	0	0	Similar to R-48 but with an ANL alloy current collector and a positive-to-negative capacity ratio of 1.
R-54, LiAl/FeS, 208/145 A-hr, 1.68 kg	80	98	4.0	10	99	80	>30	>41	0	0	0	0	Similar to R-48 but with a LiF-LiCl-KCl salt (mp 395°C).
R-55, LiAl/FeS + TiS_2, 210/141 A-hr, 1.6 kg	80	90	4.0	10	99	84	>10	>16	0	0	0	0	Similar to R-48 but with 10 wt % TiS_2 in positive electrode.
M-8, Li-Al/FeS, 155/113 A-hr,1.55 kg	83 74	101 88	8 3.8	8.5 7.5	97	84	197	347	9	10	0	0	Design: BN felt separator/retainer, LiCl-rich electrolyte (Anderson), positive loading of 1.41 A-hr/cm^3. 3.5 mΩ cell resistance. Terminated.
M-10, Li-Al/FeS, 155/115 A-hr, 1.56 kg	56 43	65 50	2.8 1.4	5.5 4.5	99 99	83 83	100	300	18	15	9	0	Design: BN felt separator/retainer, LiCl-KCl eutectic, positive loading of 1.40 A-hr/cm^3. Terminated.
M-11, Li-Al/FeS, 174/132 A-hr, 1.52 kg	71 60	80 67	3.5 2	7 6	99 99	79 77	130	365	18	15	0	0	Design: BN felt separator/retainer, LiCl-rich electrolyte (Anderson), positive loading of 1.61 A-hr/cm^3. 3.5 mΩ cell resistance. Terminated.
M-12, Li-Al/FeS-Cu_2S, 155/121 A-hr, 1.55 kg	67	80	3.3	6.8	98	83.6	83	202	44	41	6	6	Design: BN felt separator/retainer, LiCl-KCl eutectic, positive loading of 1.40 A-hr/cm^3. 3.5 mΩ cell resistance. Terminated.

(contd)

Appendix B. (contd)

	Max. Performance @ Indicated Rate		Rates, hr		Initial Eff., %		Life Characteristics						
									% Decline in				
Cell Description[a]	A-hr	W-hr	Disch.	Charge	A-hr	W-hr	Days[b]	Cycles[b]	Capacity	Energy	A-hr Eff.	W-hr Eff.	Remarks
M-13, Li-Al/FeS, 174/105 A-hr, 1.38 kg	88 75 67	109 87 76	8.7 3.7 2.2	9 7.5 6.7	99 99 98	89 82 80	16	28	0	0	0	0	This cell has cold-pressed electrodes, LiCl-rich electrolyte, BN-felt separator, positive-electrode theor. cap. density of 1.2 A-hr/cm^3. Voluntarily terminated.
M-14, Li-Al/FeS, 174/128 A-hr, 1.40 kg	94 75 66	115 88 76	9.5 3.6 2.2	9.5 7.6 6.7	99 99 98	87 83 81	25	30	0	0	0	0	This cell has cold-pressed electrodes, LiCl-rich electrolyte, BN-felt separator, and positive-electrode theor. cap. density of 1.5 A-hr/cm^3. Voluntarily terminated.
M-MP-3, Li-Al/FeS, 420/346 A-hr, 4.68 kg	265 239	327 285	8.8 4	9 8	99 98	87 86	128	230	7	7	40	37	This cell had cold pressed electrodes (three positive, four negative), LiCl-electrolyte, BN-felt separators. Cell resistance at 50% discharge is 1.14 mΩ. Terminated.
M-8-PWD, LiAl/FeS, 170/120 A-hr, 1.5 kg	85 73 63	103 86 69	8.5 3.6 2.1	8.8 7.3 6.3	99 98 98	85 83 77	59	100	8	8	20	21	MgO powder separator in M-series design cell. LiCl-rich electrolyte. Terminated.
M-8WB, LiAl/FeS, 174/122 A-hr, 1.39 kg	80 69 61	98 82 69	8 3.5 2	8 7 6.5	99 98 96	85 84 76	30	50	1	-	0	0	Similar in design to M-8. Positive terminal split into a "wishbone" configuration. Specific power was 65 W/kg at 50% DOD. Voluntarily terminated.
M-8-NP, LiAl/FeS, 120/120 A-hr, 1.42 kg	83 76 64	101 89 73	8.3 3.8 2.1	8.7 8 6.8	94 95 94	81 78 74	>98	>184	7	7	1	1	This cell has cold-pressed electrodes, LiCl-rich electrolyte, BN-felt separators. Cell resistance at 50% discharge is 4.3 mΩ. Suspended.
M-8-PW-0, LiAl/FeS, 170/122 A-hr, 1.5 kg	85 73 63	103 86 69	8.5 3.6 2.1	8.8 7.3 6.3	99 98 98	85 83 77	>33	>55	3	2	0	0	MgO powder separator in M-series design cell. LiCl-rich electrolyte. Cell resistance at 50% is 5.5 mΩ.
MP-PW-1, Li-Al/FeS, 530/388 A-hr, ∿6.0 kg	301.5	374.1	15	15	96	82.3	7	7	0	0	0	0	Multiplate cell with vibratory loaded MgO powder and LiCl-rich electrolyte. Assembled semi-charged with positive loading density of 1.1 A-hr/cm^3. Internal resistance is 2.2 to 2.5 mΩ. Terminated.

(contd)

Appendix B. (contd)

	Max. Performance @ Indicated Rate		Rates, hr		Initial Eff., %		Life Characteristics						
									% Decline in				
Cell Description[a]	A-hr	W-hr	Disch.	Charge	A-hr	W-hr	Days[b]	Cycles[b]	Capacity	Energy	A-hr Eff.	W-hr Eff.	Remarks
LC-1, LiAl/FeS, 180/120 A-hr, 1.34 kg	94 80	121 101	10 4	10 8	99	86	98	176	2	2	0	0	Low-cost design with BN felt separator and no screens, honeycomb or frames. Carbon-bonded FeS (1.4 A-hr/cc) *vs* cold-pressed LiAl. Shorted abruptly.
LC-2, LiAl/FeS, 180/120 A-hr, 1.265 kg	96 80	124 98	10 4	10 8	99	87	55	95	15	15	20	20	Duplicate of LC-1 with only 1-mm thick BN felt separator. Terminated.
LC-3, Li-Al/FeS, 180/120 A-hr (shimmed cell)	100	117	20	20	96	79	70	151	20.0	23.0	0	2	Low-cost cell design consisting of BN-felt separator, perforated sheet current collector, carbon-bonded positive electrode, cold-pressed negative electrodes, and "electrolyte starved" state. Initial cycles showed low capacity. Shorted abruptly.
EPRE-1, LiAl/FeS, 97 A-hr, 1.3 kg	90	108	5	10	>99	86	>122	>244	22.2	22.7	0	0	Reference-electrode bicell built with hardware similar to Eagle-Picher bicell with fading capacity on cycling.
KK-15, Li-Al/FeS, 150/133 A-hr, 1.54 kg	101 87 77.5	128 108 93.5	10 4.5 2.5	10 8 7	99	89	143	245	5	5	0	0	This cell has carbon-bonded FeS electrode (1.4 A-hr/cm^3), hot-pressed LiAl electrodes, LiCl-rich electrolyte, BN-felt separator. Resistance is 2.8 mΩ. Terminated after accidental overcharge.
KK-17, LiAl/FeS, 170/115 A-hr, 1.34 kg	102 86	129 104	10 4	10 8	99	87	>18	>25	0	0	0	0	Cell design: BN-felt separator, carbon-bonded FeS (1.4 A-hr/cc) *vs.* cold-pressed LiAl.
K-MP-1, Li-Al/FeS, 420/333 A-hr, 4 kg	276 263 246	344 313 279	9 4.3 2.7	9 8 7	95	82	60	42	5	5	0	0	Multiplate cell: BN-felt separator, no electrode frames, carbon-bonded positive electrode (1.4 A-hr/cc) and pressed negative. Achieved a very high specific power: 101 W/kg at 50% discharge. Feedthrough short-circuited.

(contd)

Appendix B. (contd)

Cell Description[a]	Max. Performance @ Indicated Rate		Rates, hr		Initial Eff., %		Life Characteristics						Remarks
									% Decline in				
	A-hr	W-hr	Disch.	Charge	A-hr	W-hr	Days[b]	Cycles[b]	Capacity	Energy	A-hr Eff.	W-hr Eff.	
PW-9, Li-Al/FeS, 216/144 A-hr, 1.94 kg	94 69 55.8	114 82.6 65.84	18.4 6.9 3.7	18.4 9.3 7.4	99	82	>451	>793	0	0	0	2.3	Design: hot-pressed MgO powder separator; screen and frame on negative electrodes. M-series cell design. Resistance 8-10 mΩ. Addition of electrolyte returned performance to initial rate.
PW-12, Li-Al/FeS 190/134 A-hr, 1.6 kg	65	79.3	6.5	8.5	97	87	78	103	22	19	34	39	Hot-press MgO powder separator (2-cm thick, 70 wt % salt). Resistance is 4.6-6.4 mΩ.
PW-13, Li-Al/FeS, 175/144 A-hr, 1.7 kg	83	96.6	11	11	99	80	125	188	47	48	28	29	MgO powder separator. Cell temporarily short circuited in early stages, but was later repaired. Cell terminated after 188 cycles.
PW-16, Li-Al/FeS, 173/131 A-hr, 1.8 kg	106 65 83	129 71 96	12 2.1 4.2	14 8.7 11	99	78	162	330	22	22.4	0	0	Design: vibratory loaded MgO powder separator, LiCl-rich electrolyte, positive loading of 1.1 A-hr/cm^3. Leak developed in cell container, then voluntarily terminated.
PW-17, LiAl/FeS, 175/120 A-hr, 1.3 kg	330	39	4.2	16.2	95	70	9	11	0	0	0	0	Similar to PW-16. Terminated due to a short circuit in feedthrough.
PW-18, LiAl/FeS, 175/125 A-hr, 1.3 kg	73	97	8.8	13.6	95	78	30	59	-	-	-	-	Similar to PW-16. Terminated.
PW-19, LiAl/FeS, 175/122 A-hr, 1.3 kg	71	85	8.8	8.8	100	85	>56	>101	3	3	0	0	MgO powder separator.
PW-20, LiAl/FeS, 175/122 A-hr, 1.3 kg	80	99	10	10	98	83	>30	>53	2	2	0	0	MgO powder separator.
PW-24, LiAl/FeS, 1.0 kg	70	84	8.8	8.8	99	84	4	10	0	0	0	0	MgO powder separator. Terminated.
PW-25, LiAl/FeS, 1.3 kg	65	78	8.8	8.8	99	84	>23	>53	0	0	0	0	MgO powder separator.

(contd)

Appendix B. (contd)

Cell Description[a]	Max. Performance @ Indicated Rate		Rates, hr		Eff., %		Life Characteristics						Remarks
									% Decline in				
	A-hr	W-hr	Disch.	Charge	A-hr	W-hr	Days[b]	Cycles[b]	Capacity	Energy	A-hr Eff.	W-hr Eff.	
SM8F01, LiAl/FeS, 174/120 A-hr, 1.39 kg	82	94	4	8.2	99	82	>36	>74	0	0	0	0	BN felt separator status cell; similar in design to M-8.
SM8F02, LiAl/FeS, 174/120 A-hr, 1.40 kg	40	47	4	4.5	87	66	9	20	0	0	0	0	Same design as SM8F01.
SM8F03, LiAl/FeS, 174/120 A-hr, 1.38 kg	83	100	4	8.5	98	84	>82	>163	2	1	1	0	Same design as SM8F01.
SM8F05, LiAl/FeS, 174/120 A-hr, 1.39 kg	81	96	4	7.8	99	84	>80	>200	20	20	1	5	Same design as SM8F01.
SM8F06, LiAl/FeS, 174/120 A-hr, 1.40 kg	81	96	4	8	99	83	>15	>23	0	0	0	0	Same design as SM8F01.
SM8F07, LiAl/FeS, 174/120 A-hr, 1.39 kg	70	82	4	6.4	99	83	>52	>99	0	0	0	0	Same desing as SM8F01.
SM8F08, LiAl/FeS, 174/120 A-hr, 1.39 kg	82	96	4	8	99	81	>36	>66	3	4	1	5	Same design as SM8F01.
SM8F09, LiAl/FeS, 173/119 A-hr, 1.39 kg	81	95	4	8	99	80	>35	>70	2	2	1	1	Same design as SM8F01.
SM8F10, LiAl/FeS, 173/120 A-hr, 1.40 kg	82	96	4	8	99	81	>33	>50	7	8	1	1	Same design as SM8F01.
SP6P19, LiAl/FeS, 175/122 A-hr, 1.3 kg	65	75	8	8	100	85	86	155	15	15	0	0	MgO powder separator status cell; similar to PW-16.
SP6P20, LiAl/FeS, 175/122 A-hr, 1.3 kg	65	77	8	8	98	83	>60	>106	40	56	5	5	Same design as SP6P19.
SP6P22, LiAl/FeS, 175/122 A-hr, 1.3 kg	80	99	10	10	98	83	>111	>229	20	20	0	2	Same design as SP6P19.
SP6P23, LiAl/FeS, 175/122 A-hr, 1.3 kg	69	62	8.8 4.5	8.8 8	98	83	39	57	0	0	0	0	Same design as SP6P19.

---

[a] Cell description includes cell number, composition of negative and positive electrodes, theoretical capacity, and cell weight; these cells are of the bicell design unless otherwise indicated.

[b] The "greater than" symbol denotes continued operation.

APPENDIX C.

Performance Data on Contractors' Cells Tested at ANL

Appendix C. Performance Data on Contractors' Cells Tested at ANL

	Max. Performance @ Indicated Rate		Rates, hr		Initial Eff., %		Life Characteristics						
									% Decline in				
Cell Description[a]	A-hr	W-hr	Disch.	Charge	A-hr	W-hr	Days[b]	Cycles[b]	Capacity	Energy	A-hr Eff.	W-hr Eff.	Remarks
I-8-H-40, Li-Al/FeS_2-CoS_2, 148/117 A-hr, 1.20 kg	73	100	6	18	99	84	461	521	21.9	24	26	25	Eagle-Picher (EP) bicell used to test the effect of low-temperature operation on cell lifetime. Terminated.
G-04-003, Li-Al/FeS_2-CoS_2, 96 A-hr, 2.08 kg	73	103	4	12	>99	78	203	327	32	34	23	28	Gould upper-plateau FeS_2 bicell used for lifetime testing. Terminated after 327 cycles.
REV-9A, Li-Si/FeS, 171 A-hr, 1.99 kg	88	110	6.8	6.8	85	79	43	88	26	27	3	5	Rockwell International Li-Si/FeS bicell. Terminated.
X-40 Li-Al/FeS, 165 A-hr	143	182	14	14	98	87	6	5	-	-	-	-	Gould experimental bicell with positive additives of iron, carbon, and cobalt and a BN felt separator. Short-circuited.
X-41, Li-Al/FeS, 165 A-hr	-	-	-	-	-	-	-	-	-	-	-	-	Gould experimental bicell with positive additives of iron, carbon and cobalt and a BN felt separator. Short-circuited at startup.
X-43, Li-Al/FeS, 165 A-hr	-	-	-	-	-	-	-	-	-	-	-	-	Gould experimental bicell with positive additives of iron, carbon, and cobalt and a BN felt separator. Short-circuited at startup.
X-43A, Li-Al/FeS, 167 A-hr, 2.10 kg	-	-	-	-	-	-	-	-	-	-	-	-	Gould experimental bicell with positive additives of iron, carbon, and cobalt and a BN felt separator. Short-circuited during first cycle.
X-44, Li-Al/FeS, 167 A-hr, 2.28 kg	99	101	3.3	6.6	98	82	12	27	0	0	0	0	Gould experimental bicell with positive additives of iron, cobalt, and, and carbon and a BN felt separator; short-circuited.
X-45, Li-Al/FeS, 167 A-hr, 2.13 kg	104	125	3.3	6.6	>99	84	51	113	8	1.0	13	15	Gould experimental bicell with positive additives of iron, cobalt, and carbon and a BN felt separator; terminated due to declining A-hr efficiency.

(contd)

Appendix C. (contd)

	Max. Performance @ Indicated Rate		Rates, hr		Initial Eff., %		Life Characteristics						
									% Decline in				
Cell Description[a]	A-hr	W-hr	Disch.	Charge	A-hr	W-hr	Days[b]	Cycles[b]	Capacity	Energy	A-hr Eff.	W-hr Eff.	Remarks
X-47, Li-Al/FeS, 165 A-hr, 2.1 kg	156	198	12	12	98	86	-	-	-	-	-	-	Gould experimental bicell with positive additives of cobalt, carbon and iron and with BN felt separator; short-circuited on second cycle.
X-78, Li-Al/FeS, 177 A-hr, 2.2 kg	150	178	10	5	99	85	13	18	0	0	0	0	Gould experimental bicell with positive additives of iron molybdenum and carbon and Carborundum BN felt separator; terminated due to short circuit
X-88, Li-Al/FeS-LiS-Fe, 237 A-hr, 2.4 kg	212	245	4	8	>99	85	18	25	0	0	0	0	Gould experimental multiplate cell with BN felt separator and positive additives of cobalt, carbon and molybdenum; abruptly short-circuited.
C-1, LiAl/FeS, 198 A-hr, 2.1 kg	119	144	6.8	7.8	99	83	152	242	24	24	18	16	Gould baseline FeS cell with BN cloth separator and Ni current collector; no positive additives. Difficult to initiate deep cycling. Short-circuited.
C-2, Li-Al/FeS, 195 A-hr, 2.0 kg	74	87	4	4	99	-	>189	>547	27.0	28.7	0.4	-	Same basic design as C-1. Difficult to initiate deep cycles.
C-3, LiAl/FeS, 200 A-hr, 2.1 kg	110	130	7.4	7.4	>99	82	>148	>327	42	42	1.1	3.1	Same basic design as C-1. Difficult to initiate deep cycles.
C-4A, Li-Al/FeS, 195 A-hr, 2.0 kg	28.5	36.5	-	-	99	-	62	367	-	-	-	-	Same basic design as C-1. Difficult to initiate deep cycling. Terminated.
C-7, Li-Al/FeS, 171 A-hr, 2.17 kg	103	125	6.9	6.9	>99	>83	>231	>456	20.3	20.0	0.3	0	Gould baseline FeS cell with BN cloth separator, Hastelloy B collector sheet, and positive additives of Fe, Co, and C.
C-8, Li-Al/FeS, 171 A-hr, 2.24 kg	118	145	7.9	7.9	>99	>85	30	59	2.5	3.4	2	3	Same design as C-7 except nickel collector sheet; short-circuited.
C-10A, Li-Al/FeS, 171 A-hr, 2.20 kg	121	151	8.0	8.0	>99	>86	301	303	2.5	3.3	6.0	4.0	Same design as C-7 except nickel collector sheet; short-circuited.

(contd)

Appendix C. (contd)

Cell Description[a]	Max. Performance @ Indicated Rate		Rates, hr		Initial Eff., %		Life Characteristics						Remarks
									% Decline in				
	A-hr	W-hr	Disch.	Charge	A-hr	W-hr	Days[b]	Cycles[b]	Capacity	Energy	A-hr Eff.	W-hr Eff.	
Q-1, Li-Al/FeS, 115 A-hr (shimmed cell)	73	86	2.5	5.0	99	83	33	93	0.5	0.5	7.0	6.3	Gould bicell with BN felt separator and positive additives of Fe, Mo, and C. Incorporates features expected to be used for Mark II cells. Short-circuited.
Q-2, Li-Al/FeS, 115 A-hr (shimmed cell)	74	88	2.5	5.0	>99	>84	>51	>138	0	0	0	0	Same basic design as Cell Q-1.
Q-3, Li-Al/FeS, 115 A-hr (shimmed cell	69	81	2.5	5.0	99	83	>50	>173	0	0	0	0	Same basic design as Cell Q-1.
Q-4, Li-Al/FeS, 115 A-hr (shimmed cell)	83	97	2.5	5.0	99	84	>29	>86	0	0	0	0	Same basic design as Cell Q-1. Best performing cell in this series, 72% positive-electrode utilization.
Q-5, Li-Al/FeS, 115 A-hr (shimmed cell)	71	83	2.5	5.0	98	83	>29	>99	0	0	0	0	Same basic design as Cell Q-1.
Q-6, Li-Al/FeS, 115 A-hr (shimmed cell)	79	94	2.5	5.0	98	83	>28	>93	0	0	0	0	Same basic design as Cell Q-1.
Q-7, Li-Al/FeS, 115 A-hr (shimmed cell)	62	73	2.5	5.0	98	81	>28	>139	0	0	0	0	Same basic design as Cell Q-1.
Q-8, Li-Al/FeS, 115 A-hr (shimmed cell)	67	79	2.5	5.0	98	82	>24	>96	0	0	0	0	Same basic design as Cell Q-1.
Q-9, Li-Al/FeS, 115 A-hr (shimmed cell)	66	78	2.5	5.0	97	82	19	>64	0	0	0	0	Same basic design as Cell Q-1.
EMP-DC-1, LiAl/FeS-Cu_2S, 148/145 A-hr (shimmed cell)	114	138	4	8	>99	84	37	75	27	29	16	14	Bicell built from cell components of Matrix C cells. Terminated due to declining efficiency.

(contd)

Appendix C. (contd)

Cell Description[a]	Max. Performance @ Indicated Rate		Rates, hr		Initial Eff., %		Life Characteristics						Remarks
									% Decline in				
	A-hr	W-hr	Disch.	Charge	A-hr	W-hr	Days[b]	Cycles[b]	Capacity	Energy	A-hr Eff.	W-hr Eff.	
EMP-DC-3, LiAl/FeS-Cu_2S, 296/145 A-hr (shimmed cell)	103	124	4	8	>99	84	-	78	35	36	36	35	Same design as EMP-DC-1 except that the negative electrode capacity was doubled; terminated.
EMP-DC-4, LiAl/FeS-Cu_2S, 296/145 A-hr (shimmed cell)	106	128	4	8	99	84	55	123	35	36	22	20	Same design as DC-3; terminated.
EMP-DC-5, LiAl/FeS-Cu_2S, 444/435 A-hr, 3.7 kg	335	395	4	8	>99	82	31	59	25	25	10	10	Multiplate cell built with Matrix C cell components; terminated.
EPMP-7-020 LiAl/FeS-Cu_2S, 400 A-hr, 3.7 kg	264	299	4	8	>99	71	25	45	20	17	0	8	Eagle-Picher multiplate (EPMP) cell with 15 w/o Cu_2S added to positive electrode, screen retainer only. Restarted after modifications. Testing terminated.
EPMP-7-022, LiAl/FeS-Cu_2S, 398 A-hr, 3.7 kg	316	358	4	8	97	77	40	86	28	27	0	0	Cell design: 20 wt % Cu_2S added to positive electrode and Y_2O_3 felt retainer on positive. Terminated.
EPMP-7-024, LiAl/FeS-Cu_2S, 405 A-hr, 3.7 kg	328	386	4	8	>99	>83	23	33	21	23	53	53	Cell design: 15 wt % Cu_2S in positive electrode, Y_2O_3felt retainer on positive. Terminated.
EPMP-7-027, Li-Al/FeS-CuS_2, 405 A-hr, 3.69 kg	341	381	4	8	>99	77	42	87	58	61	72	74	Cell design: 15% Cu_2S in positive and Ni current collector and rod. Terminated.
EPMP-7-028, LiAl/FeS-Cu_2S, 405 A-hr, 3.64 kg	329	374	4	8	>97	>73	47	78	20	23	10	11	Cell design: 15 wt % Cu_2S in positive electrode, Y_2O_3 felt retainer on positive. Terminated.
EPMP-7-029, Li-Al/FeS-CuS_2, 405 A-hr, 3.62 kg	311	355	4	8	>99	78	82	172	30	31	28	29	Cell design 0.005" Fe-ribbon positive current collector and rod. Terminated. Operated after failure.
EPMP-7-030, Li-Al/FeS-CuS_2, 405 A-hr, 3.73 kg	340	396	4	8	>99	>82	36	59	16	15	0	0	Cell design: 15 wt % Cu_2S in positive, Y_2O_3 felt retainer on positive and negative. Terminated to run another cell.

(contd)

Appendix C. (contd)

Cell Description[a]	Max. Performance @ Indicated Rate		Rates, hr		Initial Eff., %		Life Characteristics						Remarks
									% Decline in				
	A-hr	W-hr	Disch.	Charge	A-hr	W-hr	Days[b]	Cycles[b]	Capacity	Energy	A-hr Eff.	W-hr Eff.	
EPMP-7-032, Li-Al/FeS, 402 A-hr, 3.94 kg	358	405	4	8	>98	>77	35	60	20	21	13	14	Cell design: LiCl-rich electrolyte, Y_2O_3 felt retainer on both faces. Terminated.
EPMP-7-033, Li-Al/FeS, 402 A-hr, 3.25 kg	325	393	8	8	>98	>81	81	145	13	13	10	15	Cell design similar to -032. Terminated discharged.
EPMP-7-035, Li-Al/FeS, 402 A-hr, 3.96 kg	333	385	4	8	>98	>79	52	102	9	9	5	5	Cell design: LiCl-rich electrolyte, Y_2O_3 felt on both faces, nickel-honeycomb current collector (instead of usual iron). Testing terminated for post-test analysis.
EPMP-7-036, Li-Al/FeS, 402 A-hr, 3.92 kg	343	379	4	8	>98	>74	31	78	9	7	7	5	Cell design similar to -035. Terminated.
EPMP-7-050, LiAl/FeS-Cu_2S, 408 A-hr, 3.8 kg	307	353	4	8	98	78	28	53	24	26	30	31	Cell design: 20 wt % Cu_2S in positive electrode and Y_2O_3 felt on positive face. Terminated because cell leaked.
EPMP-7-055, Li-Al/FeS, 402 A-hr, 3.8 kg	325	393	4	8	99	82	153	320	17	25	10	20	Filled with LiCl-rich electrolyte. Terminated.
EPMP-7-059, Li-Al/FeS, 403 A-hr, 3.8 kg	322	390	4	8	98	82	28	50	4	7	14	15	Similar to -055. Shorted.
EPMP-060, Li-Al/FeS, 403 A-hr, 3.8 kg	240	271	4	8	99	76	96	172	(6)	(7)	(44)	(43)	Similar to -055. Study of cell reversal after cell shorted.
EPMP-7-067, Li-Al/FeS-Cu_2S, 409 A-hr, 3.8 kg	302	352	4	8	99	82	42	70	14	13	41	41	Filled with LiCl-rich electrolyte. Shorted.
EPMP-7-068, Li-Al/FeS-Cu_2S, 409 A-hr, 3.8 kg	318	376	4	8	98	81	34	69	31	30	39	37	Similar to -067. Shorted.
EPMP-7-069, Li-Al/FeS, 409 A-hr, 3.8 kg	329	384	4	8	98	81	5	4	-	-	-	-	Filled with LiCl-rich electrolyte. Cell shorted.
EPMP-7-070, Li-Al/FeS-Cu_2S, 387 A-hr, 3.7 kg	303	342	4	8	>99	77	46	123	33	47	12	8	15 wt % Cu_2S in positive and filled with LiCl-rich electrolyte. Used for equalization studies. Shorted.

(contd)

Appendix C. (contd.)

Cell Description[a]	Max. Performance @ Indicated Rate		Rates, hr		Initial Eff., %		Life Characteristics						Remarks
									% Decline in				
	A-hr	W-hr	Disch.	Charge	A-hr	W-hr	Days[b]	Cycles[b]	Capacity	Energy	A-hr Eff.	A-hr Eff.	
EPMP-7-071, Li-Al/FeS-Cu_2S, 387 A-hr, 3.7 kg	308	341	4	8	99	75	67	118	16	14	48	47	15 wt % Cu_2S in positive and filled with LiCl-rich (410°C liquidus) electrolyte. Used for J-227 driving profile tests. Shorted.
EPMP-7-091, Li-Al/FeS-Cu_2S, 387 A-hr, 3.8 kg	323	376	4	8	99	80	92	199	31	31	25	20	Same as -070, used for power pulse tests. Terminated.
EPMP-7-094, Li-Al/FeS-Cu_2S, 387 A-hr, 3.8 kg	268	302	4	8	98	78	40	74	25	62	65	-	Design as -070. Shorted.
EPMP-7-106, Li-Al/FeS-Cu_2S, 425 A-hr, 4 kg	278	325	4	8	99	84	116	245	21	26	28	38	Type of cell used in Mark IA battery. Terminated due to short circuit.
EMP-224, LiAl/FeS-Cu_2S, 430/425 A-hr, 3.9 kg	308	366	4	8	99	84	42	68	25	27	19	18	Type of cell used in Mark IA battery. Cycled on driving profile. Terminated.
EPMP-7-338, Li-Al/FeS-Cu_2S, 425 A-hr, 4 kg	331	411	8	8	99	87	70	96	37	39	30	32	Type of cell used in Mark IA. Terminated due to short circuit. Tested at constant power.

[a] Cell description includes cell number, composition of negative and positive electrodes, theoretical capacity, and cell weight; all EPMP-series cells are of the multiplate design and fabricated by Eagle-Picher Industries.

[b] The "greater than" symbol denotes continued operation.

APPENDIX D.

Summary of Post-Test Examinations of Multiplate Cells

Appendix D. Summary of Post-Test Examinations of Multiplate Cells

Cell Description[a]	Lifetime		Reason Terminated	Comments
	Cycles	Days		
EPMP-5-001, Li-Al/FeS, E	8	5	Equipment malfunction	Electrodes showed uniform thickness, no extrusion, and no bulging of cell can. Separator showed considerable deficiency of electrolyte.
EPMP-5-003, Li-Al/FeS, E	60	39	End of test	Examination showed minor variations in electrode thickness, minor agglomeration of Li-Al in lower portion of negative electrodes, deficiency of electrolyte in separator. No extrusion of electrodes. Negative electrodes swelled by about 25% in thickness.
EPMP-5-005, Li-Al/FeS-Cu_2S, E	94	55	End of test	This cell showed a cold resistance of 0.3 mΩ, indicating a short circuit. Negative electrode thickness was non-uniform; negative electrodes swelled by 25-40% in thickness. Short circuit was attributed to the migration of Li-Al from the negative electrode and the deposition of copper and iron (from positive electrode) in the open interstices of the BN fabric separator. Separator was more completely filled with electrolyte; but not completely filled.
EPMP-5-009, Li-Al/FeS-Cu_2S, E	75	39	End of test	Cell resistance was 9 Ω (cold). Electrode thickness was uniform. Minor extrusion at top. Very minor agglomeration of Li-Al. Some unreacted Li-Al in outside electrodes. Negative electrodes showed 15-20% swelling in thickness.
EPMP-5-018, Li-Al/$CuFeS_2$-Fe, E	68	38	Declining A-hr efficiency	A partial short circuit was formed due to cracked lower insulator in feedthrough. Electrolyte deficiency in negative electrodes and separator. Major LiAl agglomeration in negative electrode center.
EPMP-7-022, Li-Al/FeS-Cu_2S, E	4	6	Short circuit	Multiple short circuits caused by ruptures in separator and screens, which, in turn, were caused by the electrodes being broken during cell assembly.
EPMP-7-026, Li-Al/FeS-Cu_2S, E	58	37	Short circuit	Short circuit caused by extrusion of positive electrode material through ruptures in screens and separators at bottom of cell. Cell thickness expanded by 20-25% (loose retainer plate bolts) and was refilled with electrolyte. Edge of cell bulged. Electrolyte filling of separators and electrodes was good. Little evidence of agglomeration in Li-Al.
EPMP-7-030, Li-Al/FeS-Cu_2S, E	59	33	Short circuit	The feedthrough developed a short circuit on cycle 49, which was isolated, and the cell was operated an additional 10 cycles. Short was in top of feedthrough and caused by electrolyte from external source.
EPMP-7-032, Li-Al/FeS-Cu_2S, E	60	35	Short circuit	Short circuit caused by upward extrusion of one positive electrode, which ruptured retainer screen and separator fabric and forced screen into contact with top cover plate. Negative-electrode thickness in center of cell was very non-uniform, with some areas showing 50-60% expansion. Some areas were slightly compressed. Extensive agglomeration of Li-Al was present in the negative electrode. Separator was deficient in electrolyte.
EPMP-7-033, Li-Al/FeS, LR	145	81	Declining A-hr efficiency	Minor agglomeration of Li-Al in negative electrode. Negative electrode showed both compression and expansion. Very non-uniform thickness in center of cell. Edges of cell can were severely bulged.

(contd)

Appendix D. (contd.)

Cell Description[a]	Lifetime Cycles	Lifetime Days	Reason Terminated	Comments
EPMP-7-034, Li-Al/FeS, LR	0	0	Short circuit	Short circuit developed during electrolyte filling, when 100 g of liquid $LiAlCl_4$ was added to cell followed by LiCl-rich electrolyte. Short was apparently caused by metallic deposits (from the $LiAlCl_4$) within the separator, which was completely filled with electrolyte. Results indicate that $LiAlCl_4$ should not be added as a liquid and that amount should be minimized.
EPMP-7-035, Li-Al/FeS, LR	101	55	Declining A-hr efficiency	Short circuit caused by extrusion of positive electrode material through rupture in screen and separator at bottom of cell. Edge of cell bulged. Minor agglomeration of Li-Al. Electrode thickness was uniform and expanded by ∿25%. Deficiency of electrolyte in negative electrode and separator.
EPMP-7-036, Li-Al/FeS, LR	78	29	Declining A-hr efficiency	Cause of short circuit same as -035. Negative electrodes expanded ∿25%, and showed some non-uniformity and minor Li-Al agglomeration; edge of cell bulged.
EPMP-7-048, Li-Al/FeS, E	0	0	Short circuit	Separators were pretreated with wetting agent of $LiAlCl_4$. The amount used was excessive. Short circuit was attributed to metallic deposits across the separator from the $LiAlCl_4$. Because of the nature of the fabric, the $LiAlCl_4$ was concentrated in these areas.
EPMP-7-055, Li-Al/FeS, LR	320	153	Declining A-hr efficiency	Decline in A-hr efficiency was due to extrusion of positive electrode material. Cell exhibited stable capacity for ∿300 cycles. Less porosity and agglomeration were observed in the negative electrode.
EPMP-7-059, Li-Al/FeS, E	50	27	Declining A-hr efficiency	Cause of short circuit same as -035. Electrode thickness was very uniform. Considerable deficiency of electrolyte in separator and negative electrode. Original Li-Al particles in center of negative electrode (unreacted). Negative electrodes expanded 20-25%.
EPMP-7-060, Li-Al/FeS, E	172	94	Short circuit	This cell ran for 113 cycles with steadily declining coulombic efficiency. Fifty-nine subsequent cycles were run with the cell in voltage reversal. Substantial reaction of the BN cloth was observed. Short circuit was caused by extrusion of center positive electrode at bottom of cell.
EPMP-7-068, Li-Al/FeS-Cu_2S, LR	69	36	Declining A-hr efficiency	The short circuit was between one pair of electrodes (a positive and the adjacent negative) about one inch from the bottom. The retainer screen of the positive electrode was ruptured in this area and it appears that a broken wire penetrated the separator and contacted the negative electrode. Electrode thickness was very uniform. Minor agglomeration of Li-Al. The two center negative electrodes had extruded through ruptures in the retainer screens at the bottom. Deficiency of electrolyte in separator. Expansion in thickness of negative electrodes by 20 to 30%.
EPMP-7-069, Li-Al/FeS-Cu_2S, E	4	∿5	Short circuit	The electrical feedthrough short circuited. The short was caused by electrolyte corrosion at the top of the upper insulator. The electrolyte was from an external source and did not leak through the feedthrough.

(contd)

Appendix D. (contd.)

Cell Description[a]	Lifetime		Reason Terminated	Comments
	Cycles	Days		
EPMP-7-071, Li-Al/FeS-Cu_2S, LR	118	67	Short circuit	Short circuit was caused by rupture in separator near the edge in the center positive electrode; Li-Al agglomeration was observed in the center portion of the negative electrodes. Areas of excessive corrosion of the current collectors were observed, which indicate higher temperature operation (>450°C) or some overcharging. Negative electrode expansion was 30%.
EPMP-7-091, Li-Al/FeS-Cu_2S, E	199	92	Short circuit	Short circuit was caused by extrusion of positive electrode material at bottom and along one side of the cell.
EPMP-7-094, Li-Al/FeS-Cu_2S, E	74	48	Short circuit	Short circuit was caused by a metallic bridge across insulator of the feedthrough; this problem was brought about by corrosion due to the accidental spill of electrolyte in this area. The BN powder seal in the feedthrough was effective. Minor agglomeration observed in negative electrode. Inner negative electrodes showed 7% compression, while outer negative electrodes showed 20% expansion. Positive electrodes showed 80% expansion. Cell was fully discharged.
EPMP-7-129, Li-Al/FeS-Cu_2S, E	78	40	Short circuit	This cell and EPMP-7-131 (below) were run together as part of a 6-V battery. The short circuit was due to the formation of a metallic bridge across the upper insulator of the feedthroughs caused by electrolyte moving up through the BN seal. Metallographic examination of the external copper negative electrode strip showed that it contained multiple fractures throughout all areas. This is the result of using a high oxygen (0.2%) containing copper in a reducing atmosphere. All future external copper components should be made only from oxygen-free copper.
EPMP-7-131, Li-Al/FeS-Cu_2S, E	78	40	Short circuit	Same as EPMP-7-129.
EPMP-7-164, Li-Al/FeS-Cu_2S, E	5	3	Declining A-hr efficiency	Poor A-hr efficiency was caused by a loop in the positive screen penetrating the separator at one edge, which resulted in a partial short circuit. Electrolyte filling was very good in the electrodes and fair in the separators.
EPMP-7-166, Li-Al/FeS-Cu_2S, E	0	0	Short circuit	Cell was accidentally overheated (>600°C). Short circuit caused by molten Li-Al penetrating the separator.
EPMP-7-287, Li-Al/FeS-Cu_2S, E	0	0	Short circuit	Short circuit was caused by accidental overcharge in electrolyte filling operation which resulted in metallic iron deposits across the separator.
EPMP-7-292, Li-Al/FeS-Cu_2S, E	0	0	Short circuit	Same as EPMP-7-287.

(contd)

Appendix D. (contd)

Cell Description[a]	Lifetime		Terminated	Comments
	Cycles	Days		
K-MP-1, Li-Al/FeS (carbon bonded), LR	88	54	Short circuit	The short circuit was due to the absence of BN felt at the top of the cell between one negative electrode and the adjoining positive electrode; this condition allowed metallic material from both electrodes to bridge the separator gap. Elimination of picture frames in this cell showed no undesirable effects. Care must be taken not to deviate too far from this electrode capacity and loading density or problems in material extrusion or separator failure may develop.
M-MP-3, Li-Al/FeS, LR	230	128	Short circuit	This ANL multiplate cell was constructed for performance comparison against the EPMP cells. This cell had an excess of electrolyte (1 cm tall) above all the electrodes, which may have contributed significantly to the excellent capacity retention. During the building of this cell, some LiAl particles inadvertently slipped between the picture frame and the 200-mesh screen, and subsequent cycling caused these particles to break up and move across the separator to form a short circuit.

---

[a] Cell description includes cell number, composition of negative and positive electrodes, and electrolyte composition (the symbols E and LR represent the eutectic and LiCl-rich electrolyte compositions, respectively).

APPENDIX E.

Post-Test Examination of Bicells

Appendix E. Post-Test Examination of Bicells

Cell Description	Lifetime Cycles	Lifetime Days	Reason Terminated	Comments
DC-1, Li-Al/FeS-Cu_2S	75	37	Short circuit	Cell DC-1 (and DC-3 below) was built at ANL using EPMP hardware to learn methods of improving cell capacity stability and transferring it to the multiplate designs. The short circuit in these two cells was caused by the sideward expansion of the positive electrode, with a resulting fracture in the 200-mesh screen which caused the separator to be torn and positive electrode material to contact the cell housing.
DC-3, Li-Al/FeS-Cu_2S	78	36	Short circuit	Same as DC-1.
EP-I3B-1, Li-Al/FeS-Cu_2S	896	417	Short circuit	Short circuit caused by the honeycomb current collector of the positive electrode cutting through the separator. Positive electrode showed non-uniform swelling.
EP-I3B-2, Li-Al/FeS-Cu_2S	505	333	Short circuit	Short circuit caused by the honeycomb current collector of the positive electrode cutting through the separator. Also, metallic copper deposited within the separator. Negative electrode showed 40% expansion.
EP-I8L-035, Li-Al/FeS_2 -CoS_2	94	83	End of test	Cell had been subjected to vibration testing. The microstructure of the positive and negative electrodes was the same as observed in non-vibrated cells, indicating that the vibration testing had no effect on electrode morphology. A Li_2S deposit found in the separator. Negative electrode showed 40% expansion; positive electrode showed 7% compression.
EP-I8H-036, Li-Al/FeS_2-CoS_2	106	104	Declining capacity	Cause of failure not identified. Typical deposit of Li_2S was observed in the separator. Negative electrode showed 80% expansion. Positive electrode showed 8% expansion, 90 vol % active material (10 vol % electrolyte), and was about half discharged.
G04-019A, Li-Al/FeS_2	20	18	Short	Metallographic examination showed massive intrusions of positive electrode material into the BN fabric separator, and this appears to be the cause of the short circuit. A Li_2S deposit found in separator. Positive electrode was deficient in electrolyte, and expanded by 60%.
G-0080-9, Li-Al/FeS	0	2	Short circuit	This cell used a copper current collector in the positive electrode. The short circuit was caused by copper deposition across the separator between the positive bus bar (copper) and the housing bracket at the negative electrode potential. Corrosion of the copper current collector ranged from 270 to 566 mils/yr penetration.
GQ-1 Li-Al/FeS-Mo-C	93	33	Short circuit	Short circuit was caused by rupture of the positive electrode retainer screen and subsequent extrusion of active material. Significant corrosion of the nickel current collector had occurred.

(contd)

Appendix E. (contd)

Cell Description	Lifetime Cycles	 Days	Reason Terminated	Comments
GX-45, Li-Al/FeS	113	51	Short circuit	Short circuit was caused by rupture in BN felt separator, which in turn was caused by the gross non-uniform expansion of the negative electrode and compression of the positive electrode in localized areas.
GX-88, Li-Al/FeS-Mo-C, LR	25	18	Short circuit	The short circuit in this cell was caused by the moderate sideward expansion of the positive electrode which in turn caused the side bracket to tilt and cut the BN separator and finally contact the cell housing. The Li-Al particles in the front 0.3 mm of the negative electrodes have been converted to $LiAlO_2$. These electrodes were formed in a dry room and formation time and/or subsequent storage protection was not adequate to prevent the formation of this oxide layer before cell operation.
HC-2, $Li-Al/FeS_2$	144	111	Short circuit	Cell assembled in air, with Li_2FeS_2 used as starting material in the positive electrode. Examination showed $LiAlO_2$ in the negative electrode top, indicating air reaction with the Li-Al alloy. Short circuit caused by sulfide deposits in the separator and conductive ZrO_2 contacting both electrodes.
JS-3, $Li-Al/FeS-Cu_2S$	8	10	Short circuit	Short circuit was caused by extrusion of positive material through the overlap point of the separator at the top of the positive electrode. The negative electrodes showed ∿100% expansion in this area. The positive electrode showed excessive expansion at the bottom (>50%), whereas the negative electrodes were severely compressed.
KK-6, $Li-Al/FeS_2-CoS_2$	313	183	End of test	Lithium sulfide deposits typical of FeS_2 cells were observed within the separator. Also, Li_2S or Al_2S_3 was observed in the negative electrodes. The negative electrodes were cast plates with 11 wt % Li. These electrodes expanded by more than 100% in thickness, and the back 1/3 was α-Al(Li-Al depleted of Li), with the remainder LiAl. This indicates non-uniform reaction.
KK-14, $Li-Al/FeS-Cu_2S$	301	151	Declining A-hr efficiency	The cause for the declining A-hr efficiency (∿75%) was not identified. Possible contributing factors are: six freeze-thaw cycles, metallic copper deposits within separators, and non-uniform utilization of the negative electrodes (bottom portions were depleted of Li, while the upper portions contained normal LiAl for charged electrodes). Boron nitride felt was compressed from 6 to ∿1.9 mm. Electrodes showed excessive expansion.
M-7, $Li-Al/FeS_{1.44}$	136	85	Declining A-hr efficiency	The cause of the declining coulombic efficiency (85%) was not identified. The Y_2O_3 felt separator showed evidence of reaction with the positive electrode to form Y_2O_2S. Negative electrode showed expansion of almost 100%. The 6-mm thick separator was compressed to ∿1.4 mm. A Li_2S deposit found within the separator. Utilization was non-uniform in the negative electrode.

(contd)

Appendix E. (contd)

Cell Description	Lifetime		Reason	Comments
	Cycles	Days	Terminated	
M-8, Li-Al/FeS	347	197	End of test	Negative electrodes had expansion of about 100%. The BN felt separator had been compressed from 6 to 2.4 mm. The corrosion of the electrodes was somewhat greater than normal.
M-9, Li-Al/FeS-Cu_2S	240	132	Declining capacity	Specific cause of failure not identified. Negative electrodes showed agglomeration in back positions ($\sim$90 vol % Li-Al), the front portions being $\sim$50 vol % Li-Al. Positive electrode very dense looking (50-70 vol %) for a charged condition. Metallic copper was deposited within separator. BN felt separator was compressed from 6 to 1.5-1.7 mm. Negative electrodes showed excessive expansion (>50%).
M-11, Li-Al/FeS	365	130	End of test	Cell used BN felt separators and was a test of effects of the initial A-hr loadings in positive electrode on utilization and cell performance. 1.6 A-hr/cm^3 in positive electrode. The positive electrode showed $\sim$33% expansion and was mostly Li_2FeS_2 + Fe with FeS, J and Li_2FeS_2 at the electrode face. Some agglomeration in back position of negative electrode.
M-13, Li-Al/FeS	27	16	End of test	Same as M-11. 1.2 A-hr/cm^3 in positive electrode. Positive electrode showed $\sim$33% expansion and was mostly FeS with minor Li_2FeS_2. Back portion of negative electrode was not utilized (cycled).
M-14, Li-Al/FeS	28	22	End of test	Same as M-11. 1.5 A-hr/cm^3 in positive electrode. Positive electrode showed $\sim$50% expansion and contained only FeS. Back portion of negative electrode was not utilized (cycled).
M-15, Li-Al/FeS	57	30	End of test	Same as M-11. 1.0 A-hr/cm^3 in positive electrode. Positive electrode contained only FeS and showed no expansion. Back portion of negative electrode was not utilized (cycled).
PW-8, Li-Al/FeS	673	280	End of test	Negative electrodes showed excessive expansion in thickness and the positive electrode was severely compressed. The MgO powder separator was 3-mm thick on one face of the positive electrode and 5-mm thick on the other face. Also, MgO powder was observed inside the positive electrode (see Cell PW-14). The positive electrode showed some evidence of non-uniform reaction from top (mostly Li_2FeS_2) to bottom (mostly J phase).
PW-14, Li-Al/FeS-Cu_2S	26	22	Short circuit	Short circuit was caused by a defective feedthrough. This cell used a MgO powder separator (-60 + 120 mesh) and was more densely loaded in the bottom portion ($\sim$50 vol %) than in the top (>40 vol %). Also, a considerable amount of MgO was present within the positive electrode. This apparently occurred during vibratory loading of the MgO powders.
R-31, Li-Al/NiS_2-CoS_2	1040	378	Short circuit	Short circuit was caused by extrusion of positive electrode material around the folded BN fabric separator at the top of the cell. The positive electrode was severely compressed in this area by expansion of the negative electrodes. Dimensional uniformity of the electrodes was poor.

(contd)

Appendix E. (contd)

Cell Description	Lifetime Cycles	 Days	Reason Terminated	Comments
R-37, Li-Al/FeS	669	305	End of test	This cell was constructed without the customary screen over the positive electrode. Examination showed no adverse effects on particle migration into the separator by omission of the screen. This electrode did not include a honeycomb current collector. Without a screen at the separator face, a honeycomb current collector would cut through the separator with a resulting short circuit.
R-38, Li-Al/FeS-C	172	94	Short circuit	Failure caused by the extrusion of positive electrode material past the overlap in the separator at the top of the electrode; appearance of the electrodes indicated non-uniform utilization of the electrodes from top to bottom.
R-40, Li-Al/FeS-C	109	63	Short circuit	Short circuit occurred in the feedthrough. Examination showed that electrolyte leaked from the cell through the BN powder seal. This condition allowed corrosion to occur at the top of the feedthrough with the formation of a metallic bridge across the upper insulator. Boron nitride powder (-325 mesh) was inadvertently used for the seal rather than the -40 + 325 powder which forms a better seal.
R-41, Li-Al/FeS-Cu_2S	351	180	Short circuit	Short circuit caused by the electrode frames at the top of the cell cutting through the BN felt separator. This was caused by the excessive swelling of the positive electrode (50-100% expansion). Metallic copper was deposited within the separator. A band of α-$LiAlO_2$ was observed at the top of the negative electrodes, indicating exposure to oxygen during assembly or operation.
R-44, Li-Al/FeS	412	259	Declining A-hr efficiency	The one unusual characteristic of this cell was the presence of a 2-5 mm layer of $LiAlO_2$ at the very top edge of both negative electrodes. This suggests that this unsealed cell had been exposed to oxygen for some period of its operating life.

Distribution for ANL-79-94

Internal:

W. E. Massey
P. R. Fields
S. A. Davis
B. R. T. Frost
G. T. Garvey
J. J. Roberts
K. E. Anderson
J. D. Arntzen
B. Bandyopadhyay
J. Barghusen
D. L. Barney (25)
L. Bartholme
J. E. Battles
E. C. Berrill
L. Burris
F. A. Cafasso
A. A. Chilenskas (25)
M. Contos
P. Cunningham
W. DeLuca
P. A. Eident
R. Elliott
P. Eshman
M. K. Farahat
A. K. Fischer
E. C. Gay
J. D. Geller
J. E. A. Graae
J. Harmon
E. R. Hayes
F. Hornstra
A. A. Jonke
T. D. Kaun
R. W. Kessie
J. E. Kincinas
V. M. Kolba
W. Kremsner
M. L. Kyle
W. W. Lark
R. F. Malecha
F. J. Martino
C. A. Melendres
A. Melton
W. E. Miller
F. Mrazek
K. M. Myles
Z. Nagy
P. A. Nelson (50)
N. Otto
E. G. Pewitt
R. B. Poeppel
S. Preto
G. Redding
K. A. Reed
M. F. Roche
L. E. Ross
M. Saboungi-Blander
W. W. Schertz
J. L. Settle
H. Shimotake
M. A. Slawecki
J. A. Smaga
R. K. Steunenberg
S. Susman
B. Swaroop
C. A. Swoboda
C. Sy
Z. Tomczuk
R. Varma
D. R. Vissers
S. Vogler
D. S. Webster
S. E. Wood
N. P. Yao
A. B. Krisciunas
ANL Contract File
ANL Libraries (5)
TIS Files (6)

External:

DOE-TIC, for distribution per UC-94cb (334)
Manager, Chicago Operations and Regional Office, DOE
Chief, Office of Patent Counsel, DOE-CORO
V. Hummel, DOE-CORO
W. R. Frost, DOE-CORO
President, Argonne Universities Association
Chemical Engineering Division Review Committee:
  C. B. Alcock, U. Toronto
  R. C. Axtmann, Princeton U.
  J. T. Banchero, U. Notre Dame
  T. Cole, Ford Motor Corp.
  P. W. Gilles, U. Kansas
  R. I. Newman, Warren, N. J.
  H. Perry, Resources for the Future, Washington
  G. M. Rosenblatt, Pennsylvania State U.
  W. L. Worrell, U. Pennsylvania
E. Adler, Hughes Aircraft Co., El Segundo
J. G. Ahlen, Illinois Legislative Council, Springfield
J. W. Alpha, Corning Glass Works, Corning, N. Y.
J. Ambrus, Naval Surface Weapons Center, Silver Spring, Md.
J. N. Anand, Dow Chemical Co., Walnut Creek, Calif.

F. Anson, California Inst. Technology
B. Askew, Gould Inc., Rolling Meadows, Ill.
P. Auh, Brookhaven National Lab.
H. Balzan, Tennessee Valley Authority, Chattanooga
K. F. Barber, Div. Electric and Hybrid Vehicle Systems, USDOE
H. J. Barger, Jr., U. S. Army MERDC, Fort Belvoir
R. W. Barnes, Lithium Corp. of America, Gantonia, N. C.
T. R. Beck, Electrochemical Technology Corp., Seattle
M. Benedict, Massachusetts Inst. Technology
D. N. Bennion, U. California, Los Angeles
J. Birk, Electric Power Research Inst.
J. Braunstein, Oak Ridge National Lab.
M. Breiter, GE Research & Development Center, Schenectady
J. O. Brittain, Northwestern U.
R. Brodd, Parma Technical Center, Union Carbide Corp.
J. J. Brogan, Div. Highway Systems, USDOE
E. Brooman, Battelle Memorial Inst., Columbus
B. D. Brummet, McGraw-Edison Co., Bloomfield, N. J.
M. C. Burton, Delco Remy, Anderson, Ind.
D. M. Bush, Sandia Laboratories
E. Buzzelli, Westinghouse Electric Corp., Pittsburgh
E. J. Cairns, Lawrence Berkeley Lab.
E. Carr, Eagle-Picher Industries, Joplin
P. Carr, Energy Development Associates, Madison Heights, Mich.
Chloride Systems (U. S. A.) Inc., North Haven, Conn.
C. Christenson, Gould Inc., Rolling Meadows, Ill.
M. Cohen, U. Chicago
A. R. Cook, Int'l Lead Zinc Research Organization, Inc., New York City
G. Coraor, E. I. duPont de Nemours & Co., Wilmington
D. R. Craig, Hooker Chemical Corp., Orchard Park, N. Y.
G. Cramer, Southern California Edison, Rosemead
F. M. Delnick, Sandia Labs.
H. Dietrich, Fiber Materials, Inc., Biddeford, Mass.
D. L. Douglas, Electric Power Research Inst.
E. Dowgiallo, MERADCOM, Ft. Belvoir
J. Dunning, General Motors Research Lab., Warren, Mich.
P. Eggers, Battelle Memorial Inst., Columbus
M. Eisenberg, Electrochimica Corp., Mountain View, Calif.
R. P. Epple, Div. Materials Sciences, USDOE
H. R. Espig, Gould Inc., Rolling Meadows, Ill.
D. T. Ferrell, Jr., ESB Inc., Yardley, Pa.
P. L. Fleischner, National Beryllia Corp., Haskell, N. J.
J. H. B. George, Arthur D. Little, Inc., Cambridge, Mass.
J. Giner, Giner, Inc., Waltham, Mass.
G. Goodman, Globe-Union, Inc., Milwaukee
G. Gorten, Gorten and Associates, Sherman Oaks, Calif.
H. Grady, Foote Mineral Co., Exton, Pa.
S. Gratch, Birmingham, Mich.
D. Gregory, Inst. Gas Technology, Chicago
N. Gupta, Ford Motor Co., Dearborn, Mich.
N. Hackerman, Rice U.
G. Hagey, Div. of Environmental Impacts, USDOE
R. Hamilton, Carborundum Co., Niagara Falls
W. Hassenzahl, Los Alamos Scientific Laboratory
L. A. Heredy, Atomics International

B. Higgins, Eagle-Picher Industries, Joplin
R. Hudson, Eagle-Picher Industries, Joplin
J. R. Huff, U. S. Army Mobility Equipment R&D Center, Fort Belvoir
R. A. Huggins, Stanford U.
R. A. Huse, Public Service Electric & Gas Co., Newark, N. J.
S. D. James, U. S. Naval Surface Weapons Center, Silver Spring, Md.
M. A. Jansen, Allegheny Power Service Corp., Greensburgh, Pa.
G. Janz, Rensselaer Polytechnic Inst.
H. Jensen, C&D Batteries, Plymouth Meeting, Pa.
F. Kalhammer, Electric Power Research Institute
C. Kamienski, Lithium Corp. of America, Gastonia, N. C.
M. Katz, Div. Energy Storage Systems, USDOE
K. Kinsman, Ford Motor Co., Dearborn, Mich.
R. Kirk, Div. of Electric and Hybrid Vehicle Systems, USDOE
K. W. Klunder, Div. of Energy Storage Systems, USDOE
J. Kollar, Northfield, Ill.
J. Lagowski, Detroit Edison Utility Co.
H. Laitinen, U. Florida
J. J. Lander, Air Force Aero Propulsion Lab., Wright-Patterson AFB
A. Landgrebe, Div. of Energy Storage Systems, USDOE (6)
C. E. Larson, Bethesda, Md.
S. H. Law, Northeast Utilities, Hartford, Conn.
C. A. Levine, Dow Chemical Co., Walnut Creek, Calif.
D. Linden, U. S. Army Electronics Command, Fort Monmouth, N. J.
R. Llewellyn, Indiana State U.
P. S. Lykoudis, Purdue Univ.
J. Mathers, U. Maryland
C. J. Mazac, PPG Industries, Corpus Christi
J. McKeown, Office of Resource Management, USDOE
F. McLarnon, Lawrence Berkeley Lab.
C. McMurty, Carborundum Co., Niagara Falls
D. Meighan, C&D Batteries, Plymouth Meeting, Pa.
R. C. Miller, Kawecki Berylco Industries, Inc., Boyertown, Pa.
R. Minck, Ford Motor Co., Dearborn, Mich.
R. Murie, General Motors Corp., Warren, Mich.
E. M. Murman, Flow Research Co., Kent, Wash.
G. Murray, Detroit Edison Utility Co.
J. Newman, U. California, Berkeley
J. Nowabilski, Union Carbide Co., Tonawanda
C. Pax, Div. Electric and Hybrid Vehicle Systems, USDOE (6)
G. F. Pezdirtz, Div. of Energy Storage Systems, USDOE
R. Pollard, U. California, Berkeley
R. K. Quinn, Sandia Labs.
L. H. Raper, Eureka Co., Bloomington, Ill.
R. Rightmire, Standard Oil of Ohio, Cleveland
P. F. Ritterman, TRW Inc., Redondo Beach
R. Rizzo, Globe-Union, Inc., Milwaukee
N. Rosenberg, Transportation Systems Center, Cambridge, Mass.
P. N. Ross, Lawrence Berkeley Lab.
R. Rubischko, Chloride Inc., Tampa
A. J. Salkind, Rutgers U.
A. F. Sammells, Inst. Gas Technology, Chicago
W. Schaefer, Commonwealth Edison, Maywood, Ill.
G. Scharbach, American Motors General Corp., Wayne, Mich.
T. Schneider, Public Service Electric & Gas Co., Newark, N. J.

R. I. Schoen, National Science Foundation
J. R. Schorr, Battelle Memorial Inst., Columbus
D. R. Schramm, Public Service Electric & Gas Co., Newark, N. J.
H. J. Schwartz, NASA Lewis Research Center
J. R. Selman, Illinois Inst. Technology
J. A. Shropshire, Exxon Research and Engineering Co., Linden, N. J.
R. Singleton, U. S. Bureau of Mines, Washington
A. I. Snow, Atlantic Richfield Co., Harvey, Ill.
W. Spindler, Electric Power Research Inst.
S. Srinivasan, Brookhaven National Lab.
D. Stakem, Catalyst Research Corp., Baltimore
E. Steeve, Commonwealth Edison Co., Chicago
R. H. Strange II, National Science Foundation
R. L. Strombotne, U. S. Dept. Transportation, Washington
S. Sudar, Atomics International
R. H. Swoyer, Pennsylvania Power and Light Co., Allentown
P. C. Symons, Energy Development Assoc., Madison Heights, Mich.
R. Szwarc, General Electric Co., St. Petersburg
F. Tepper, Catalyst Research Corp., Baltimore
L. Thaller, NASA Lewis Research Center
G. M. Thur, Div. Highway Systems, USDOE
C. W. Tobias, U. California, Berkeley
L. Topper, Div. of Res. & Technical Assessment, USDOE
W. Towle, Globe-Union, Inc., Milwaukee
A. A. Uchiyama, Jet Propulsion Lab.
J. Vanderryn, Office of International Affairs, USDOE
J. V. Vinciguerra, Eagle-Picher Industries, Joplin
J. B. Wagner, Arizona State U.
R. D. Walker, Jr., U. Florida
C. O. Wanvig, Jr., Globe-Union, Inc., Milwaukee
S. A. Weiner, Ford Motor Co., Dearborn, Mich.
J. Werth, ESB Inc., Yardley, Pa.
C. Wienlein, Globe-Union, Inc., Milwaukee
F. Will, General Electric R&D Center, Schenectady
A. Williams, Dow Chemical Co., Midland, Mich.
J. Withrow, Chrysler Corp., Detroit
S. E. Wood, El Paso, Tex.
T. Wydeven, NASA Ames Research Center
L. S. Yao, U. Illinois
O. Zimmerman, Portland General Electric Co., Portland, Ore.
M. Zlotnick, Energy Technology, USDOE
Chloride Technical Limited, Manchester, England
L. Pearce, Admiralty Materials Lab., Holten Heath, England
E. Voss, Varta Batterie A. G., Kelkhern, Germany
E. Aiello, U. Chicago
W. J. Argersinger, Jr., U. Kansas
K. J. Bell, Oklahoma State U.
R. Blanco, Oak Ridge National Lab.
C. F. Bonilla, Columbia U.
W. Brandt, U. Wisconsin, Milwaukee
A. E. Dukler, U. Houston
W. J. Frea, Michigan Technological U.
J. E. Linehan, Marquette U.
Maine Univ., Prof. in charge of Chem. Engr. Lib.
Marquette U., Dept. of Chemistry

Michigan Technological U., Library
N. R. Miller, United Nuclear Industries, Richland
G. Murphy, Iowa State U.
E. A. Peretti, U. Notre Dame
G. W. Preckshot, U. Missouri
H. Rosson, U. Kansas
C. Sanathanan, U. Illinois—Chicago Circle
A. Sesonske, Purdue U.
USDOE, Director, Office of Safeguards and Security
B. W. Wilkinson, Michigan State U.
Comision Nacional de Energia Atomica, Library, Argentina
J. A. Sabato, Com. Nac. de Energia Atomica, Buenos Aires, Argentina
J. O. B. Carioca, Nucleo de Fontes Nao Convencionais de Energia da UFCE, Fortaleza-Ceara, Brazil
C. H. Cheng, National Tsing Hua Univ., China
National Radiological Protection Board, Library, Harwell, England
L. Kemmerich, Ges. fur Kernforschung, Karlsruhe, Germany
F. Weigel, Inst. fur Anorganische Chemie der U. Munich, Germany
N. Saratchandran, Bhabha Atomic Research Centre, Bombay, India
K. Fujimiya, U. of Tokyo, Japan
Japan Atomic Energy Research Inst., Tokai-mura, Japan
K. Matsuda, Inst. of Physical & Chemical Res., Yamato-machi, Japan
S-S. Lee, Korea Advanced Institute of Science, Korea
Korean Atomic Energy Research Institute, Korea
R. Nordberg, Sahlgren's Hospital, Göteborg, Sweden
T. Wallin, Royal Inst. Technology, Stockholm